Report
R-20-08
January 2022

Modelling of radionuclide transport and retention in the regolith above a hypothetical SFL repository location in the Laxemar area

Alvaro Sáinz-García
Diego Sampietro
Elena Abarca
David García
Jorge Molinero

SVENSK KÄRNBRÄNSLEHANTERING AB

SWEDISH NUCLEAR FUEL
AND WASTE MANAGEMENT CO

Box 3091, SE-169 03 Solna
Phone +46 8 459 84 00
skb.se

SVENSK KÄRNBRÄNSLEHANTERING

ISSN 1402-3091
SKB R-20-08
ID 1936898

January 2022

Modelling of radionuclide transport and retention in the regolith above a hypothetical SFL repository location in the Laxemar area

Alvaro Sáinz-García, Diego Sampietro, Elena Abarca,
David García, Jorge Molinero

Amphos 21 Consulting S.L.

This report concerns a study which was conducted for Svensk Kärnbränslehantering AB (SKB). The conclusions and viewpoints presented in the report are those of the authors. SKB may draw modified conclusions, based on additional literature sources and/or expert opinions.

This report is published on www.skb.se

© 2022 Svensk Kärnbränslehantering AB

Summary

The present work was initiated as part of the SFL safety evaluation (SE-SFL). It examines radionuclide transport in the near-surface system using the COMSOL Multiphysics® modelling platform. The near-surface system is located in the regolith where radionuclide transport can be affected by retardation and dispersion.

A central objective of this study is to investigate the influence of regolith characteristics on the transport and retention of a series of radionuclides in a simulated groundwater flow field. The radionuclide transport and retention in the near-surface are quantified at different scales by two numerical models: 1) a large-scale distributed K_d model; and 2) a more detailed distributed reactive transport model that focuses on a smaller portion of the K_d model's domain.

The distributed K_d model is a hydrogeological three-dimensional distributed K_d model that simulates unsaturated groundwater flow through the regolith while accounting for the solute transport of ^{36}Cl, ^{135}Cs, ^{59}Ni, ^{226}Ra and ^{93}Mo. Radionuclide retention in the regolith has been quantified according to a linear sorption model (K_d). Radioactive decay is included in the simulations for ^{93}Mo and ^{226}Ra. All modelling is completed using COMSOL Multiphysics® (COMSOL 2015).

Retention processes affecting the mobility of Sr, Cs, Ni and Ra in a smaller section of the regolith are modelled using a distributed reactive model. This is completed using iCP (Nardi et al. 2014) an interface between PhreeqC (Parkhurst and Appelo 2013) and COMSOL Multiphysics®.

Results from both models highlight the importance of groundwater in estimating the transport and accumulation patterns of the radionuclides considered in this study. Insights from this kind of detailed modelling can be used to help improve transport modelling and inform parameters for the biosphere transport models.

Sammanfattning

Detta arbete inleddes i anslutning till säkerhetsutvärderingen för SE-SFL. I rapporten redovisas undersökningar av radionuklidtransport i det ytnära grundvattensystemet med hjälp av modelleringsverktyget COMSOL Multiphysics®. Det ytnära grundvattensystemet befinner sig i regoliten där radionuklidtransport kan påverkas av fördröjning och dispersion.

Ett centralt syfte med denna studie är att utforska hur regolitegenskaperna kan påverka transport av ett flertal radionuklider i ett simulerat grundvattenflödesfält. I denna studie används två olika modelleringsmetoder för modellering av radionuklidtransport: 1) en storskalig distribuerad K_d-modell; och 2) en mer detaljerad, reaktiv transportmodell som fokuserar på en mindre del av området som modellerades i K_d-modellen.

Den distribuerade K_d-modellen är en 3D-numerisk modell som simulerar omättade vattentflöden i regoliten samt transport av de löste ämnena ^{36}Cl, ^{135}Cs, ^{59}Ni, ^{226}Ra and ^{93}Mo. Fördröjning av radionuklider räknas enligt en linjär sorptionsmodell (K_d). Sönderfall av radionuklider ingår i beräkningar för ^{93}Mo och ^{226}Ra. K_d-modelleringen utförs i COMSOL Multiphysics® (COMSOL 2015).

Retentionsprocesser som påverkar transporten av Sr, Cs, Ni och Ra utreds med hjälp av den distribuerade reaktivtransportmodellen som fokuserar på en mindre del av K_d-modellens modellområde. Modelleringen utförs i iCP (Nardi et al. 2014) vilket är en gränsyta mellan PhreeqC, ett geokemiskt modelleringsverktyg (Parkhurst och Appelo 2013), och COMSOL Multiphysics®.

Resultaten från bägge modellerna illustrerar att grundvattnets kemiska egenskaper har en stor betydelse vid beräkning av radionuklidens transport- och depositionsmönster i regoliten. Insikter från modelleringsövningar, såsom den som genomfördes i denna studie, kan hjälpa till att förbättra metodiken för modellering av radionuklidtransport i sin helhet, samt på ett bättre sätt informera kring de parametrar som kommer att användas i transportmodelleringen för biosfären.

Contents

1 Introduction 7
1.1 Modelling strategy 7
1.2 Objectives 8
1.3 Outline of the report 8

2 Data compilation 9
2.1 Basin delineation 9
2.2 Regolith description 11
2.3 Water flow at the regolith surface 12
2.4 Flow from the crystalline rock 13
2.5 Radionuclide discharge points 14
2.6 Radionuclides half-life 15
2.7 Values of the solid/liquid partition coefficients ($\boldsymbol{K}_d$) 15
2.8 Geochemical system 17
2.8.1 Mineral chemistry 17
2.8.2 Water chemistry 18

3 Description of the distributed $\boldsymbol{K}_d$ model with radioactive decay 23
3.1 Model geometry and spatial discretization 23
3.2 Regolith materials 24
3.3 Model equations 27
3.3.1 Unsaturated groundwater flow 27
3.3.2 Solute transport with linear sorption and decay 28
3.4 Initial and boundary conditions 29
3.4.1 Groundwater flow with variable saturation 29
3.4.2 Solute transport with linear sorption and decay 31

4 Results of the distributed $\boldsymbol{K}_d$ model with radioactive decay 33
4.1 Hydrogeological model 33
4.2 K_d model with radioactive decay 37
4.2.1 Chlorine-36 37
4.2.2 Nickel-59 41
4.2.3 Cesium-135 44
4.2.4 Radium-226 47
4.2.5 Molybdenum-93 50
4.3 Summary and conclusions from the $\boldsymbol{K}_d$ model with radioactive decay 53

5 Description of the distributed reactive model 57
5.1 Model geometry and spatial discretization 57
5.2 Regolith materials 59
5.3 Model equations 60
5.3.1 Groundwater flow 60
5.3.2 Solute transport 60
5.3.3 Reactive transport 60
5.4 Initial and boundary conditions 61
5.4.1 Groundwater flow 61
5.4.2 Solute transport 61

6 Results of the distributed reactive model 65
6.1 Groundwater flow 65
6.2 Radionuclide transport and retention 67
6.2.1 Strontium 67
6.2.2 Cesium 68
6.2.3 Nickel 69
6.2.4 Radium 70
6.2.5 Summary and conclusions from the distributed reactive model 71

7 Discussion and conclusions from the two modelling approaches 73

References 75

Appendix A Validation of the implementation of the advective-dispersive transport equation with linear sorption and decay 79

Appendix B Selected results from $\boldsymbol{K}_d$ model with radioactive decay 83

Appendix C 1D distributed reactive model of radionuclides retention processes in the till and clay 93

Appendix D Selected results distributed reactive model 125

1 Introduction

SKB plans to dispose of long-lived low- and intermediate-level nuclear waste in the SFL repository. The waste comprises waste from the operation and decommissioning of the Swedish nuclear power plants, legacy waste from the early research in the Swedish nuclear program, and smaller amounts of waste from hospitals, industry and research. The long-lived low- and intermediate-level waste from the nuclear power plants consists of neutron-irradiated components and control rods. For further details on the planned waste profile for SFL see Elfwing et al. (2013).

This work focusses on improving the understanding of radionuclide transport in the near-surface system above a hypothetical SFL repository location in the Laxemar area. Special emphasis is placed on improving the spatial and temporal representation of radionuclide migration in the Quaternary sediments (regolith) and the interface between the bedrock and regolith.

1.1 Modelling strategy

The radionuclide transport and retention in the near-surface are quantified at different scales by two numerical models: 1) a large-scale model using a partition coefficient, or "K_d approach", to evaluate the retention of the radionuclides; and 2) a sub-domain modelled in more detail by means of a distributed reactive model.

The three-dimensional distributed model used for the K_d approach examines the fate and transport of radionuclides (^{36}Cl, ^{135}Cs, ^{59}Ni, ^{226}Ra and ^{93}Mo) through the regolith at a regional scale. In the K_d approach, the retained amount of each radionuclide is accounted by a linear relation with the aqueous concentration as dictated by a partition coefficient K_d. In this model, the regolith materials are not defined by a geometrical entity, i.e., there is no plane or volume delimiting each material. The corresponding properties of each material are assigned directly to the model mesh. All modelling for the K_d approach is conducted using COMSOL Multiphysics (COMSOL 2015).

For the distributed reactive model, a sub-domain the of the model used for the K_d approach is used to examine the transport of radionuclides Sr, Cs, Ni and Ra. The aim of this model is to test the retention capacity of the regolith through a reactive transport model implemented in iCP (interface COMSOL-Phreeqc) (Nardi et al. 2014). This model accounts for retention via sorption (cation exchange and surface complexes) and by precipitation of solid-solutions and uses a more detailed description of the regolith in order to examine the flux of both water and radionuclides between specific regolith materials. Radio-active decay is not considered in this model.

Both models, the K_d approach and the distributed reactive model, examine the fate and transport of radionuclides imparted by a steady-state solution of the groundwater flow-field as modelled in COMSOL Multiphysics. Model parameters and boundary conditions for the hydrological model are based on the MIKE SHE hydrological modelling performed by Johansson and Sassner (2019).

Geological data from the Laxemar area is used to represent the regolith above the hypothetical SFL location. Data from previous SKB projects are used for the definition of the regolith geometry (SKB 2008) and hydrological conditions (Johansson and Sassner 2019). The chemical system used for the implementation of the regolith retention capacity is based on the Forsmark site, which has more available data (Andersson et al. 2003, Tröjbom and Söderbäck 2006, Sheppard et al. 2009, 2011).

1.2 Objectives

The main objective of this work is to investigate the radionuclide transport and retention in the regolith materials under temperate climate conditions. The specific objectives of the project are:

- build a 3D model of Laxemar near-surface system above the hypothetical SFL repository location with available hydrogeological and geometric data,
- examine radionuclide transport through the regolith,
- examine the retention capacity of the regolith for a number of radionuclides,
- examine the pros and cons of a K_d model compared to a reactive transport model to the extent it is possible given the framework of the study, and
- improve understanding of the processes affecting radionuclide transport and retention in the regolith.

1.3 Outline of the report

Chapter 1 provides a short introduction to the contents of the report.

Chapter 2 describes the literature review of relevant hydrological and chemical data.

Chapter 3 provides an overview on the mathematical methods applied to solve flow and transport equations in the distributed K_d model. The objects, parameters and boundary and initial conditions implemented in the model are described.

Chapter 4 presents the main results of the distributed K_d model with linear sorption and radioactive decay. The transport of radionuclides towards the discharge areas on the ground surface and retention in the regolith layers are analyzed.

Chapter 5 presents the distributed reactive model. The detailed model geometry of the selected discharge area in basin 206 and the chemical processes implemented in the reactive transport model are described.

Chapter 6 analyses the results of the distributed reactive model.

Appendix A presents two benchmark exercises to validate the implementation of the advective-dispersive transport equation with linear sorption and decay in COMSOL Multiphysics that is used in the distributed K_d model.

Appendix B presents selected results of the distributed K_d model to be used to help in the discussion of results.

Appendix C explores the retention processes occurring in the till and clay chemical systems in a simplified 1D geometry. These processes are the same as the processes implemented in the 3D distributed reactive model.

Appendix D presents selected results of the distributed reactive model to be used to help in the discussion of results.

2 Data compilation

This chapter summarizes the data compiled from different sources that are integrated into the definition of the conceptual hydrological model, the distributed K_d model with radioactive decay and the distributed reactive model. The data used in the construction of the models consists of geometrical and geographical information on the basins in the Laxemar area (digital elevation model (DEM), geographic information system (GIS), geological characterization data) and hydrological and geochemical information. The data used to inform the models is listed below:

- Basin delineation at Laxemar.
- Traces of the faults at the bedrock-regolith contact extracted from the bedrock geological map reported in Laaksoharju et al. (2009).
- The delineation of the present-day arable land objects at Laxemar.
- The regolith description from Nyman et al. (2008).
- Groundwater recharge and discharge fluxes at the ground surface at Laxemar according to results from the MIKE SHE hydrological model (Johansson and Sassner 2019).
- Bedrock groundwater fluxes in an out of the regolith at Laxemar according to results from the MIKE SHE hydrological model (Johansson and Sassner 2019).
- Exit points at the bedrock/regolith interface of particles released in the repository. Particle trajectories have been simulated with the regional hydrological model developed in ConnectFlow (Joyce et al. 2019).
- K_d coefficients for the regolith materials (Sheppard et al. 2009, 2011).
- The aqueous chemical composition and mineralogy of the regolith materials at Forsmark (Andersson et al. 2003, Tröjbom and Söderbäck 2006, Piqué et al. 2010).

The coordinate system of all data presented in this section is RT90. The location of the repository, as presented in Abarca et al. (2019), is referenced throughout the report, however a representation of the repository itself is not implemented in the model.

2.1 Basin delineation

Geographical information of the basins at Laxemar has been compiled from previous reports (SKB 2008, Laaksoharju et al. 2009, Abarca et al. 2019). The delineation and numeration of the basins at Laxemar is presented below in Figure 2-1. Basin 210 and basin 206 are selected for this study (cf Synthesis report SKB (2008)). Basin 210 is situated above the hypothetical location of the SFL repository. Basin 206 is situated northwest of the repository.

Basin 206 has an extent of 60.91 ha, while the basin 210 covers 185.80 ha. Both basins contain arable and forest lands but consist predominately of forest (Figure 2-2). The arable lands tend to be located above faults in the bedrock (Figure 2-3) as the faults coincide with topographic depressions and valleys which also tend to coincide with arable lands (SKB 2008). For the analyses presented herein, it is the projected arable land that is of greatest importance as it is here where potential exposure does to future civilizations are generally estimated to be the highest.

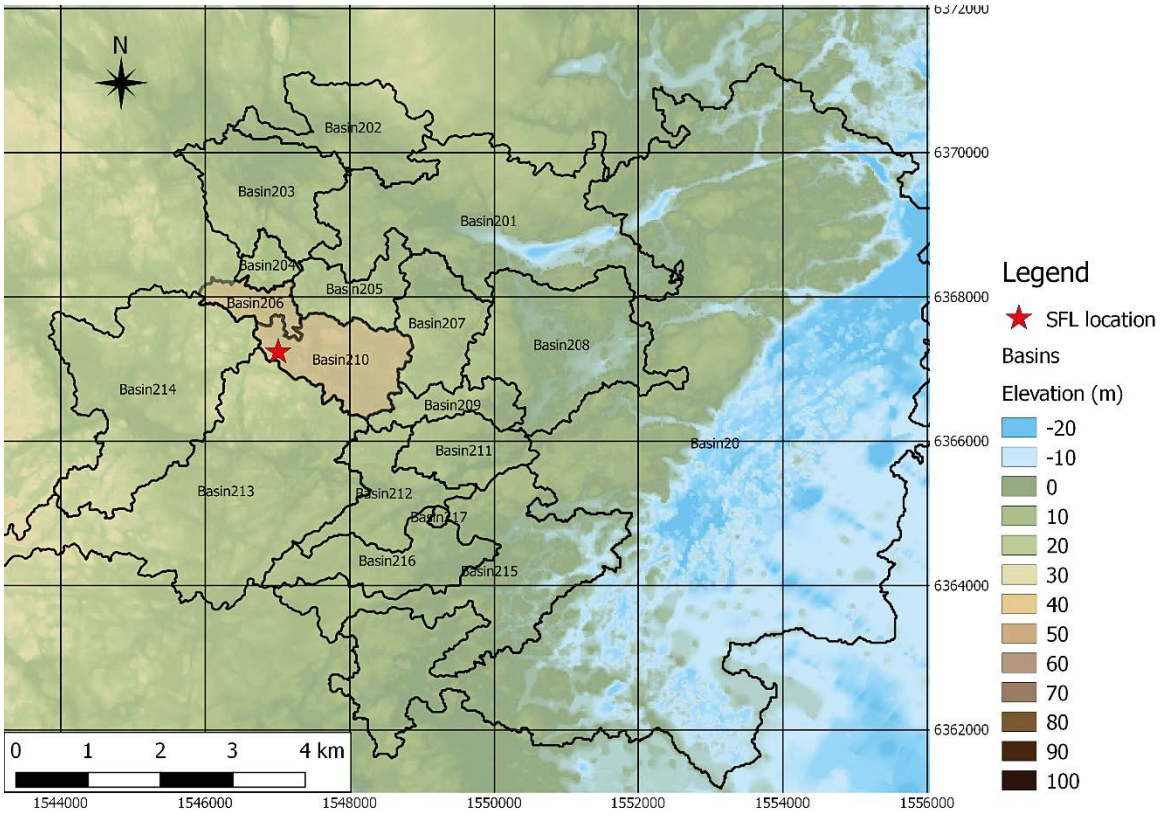

Figure 2-1. *Location of the hydrological basins at Laxemar. Basins 206 and 210, selected for this study, are plotted in red.*

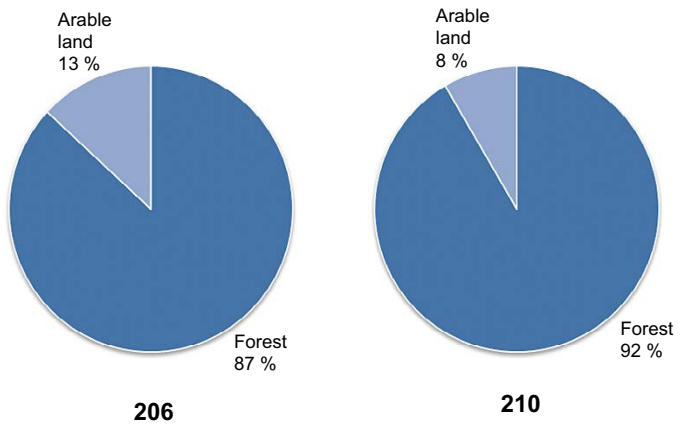

Figure 2-2. *Proportions of arable land and forest within basins 206 and 210.*

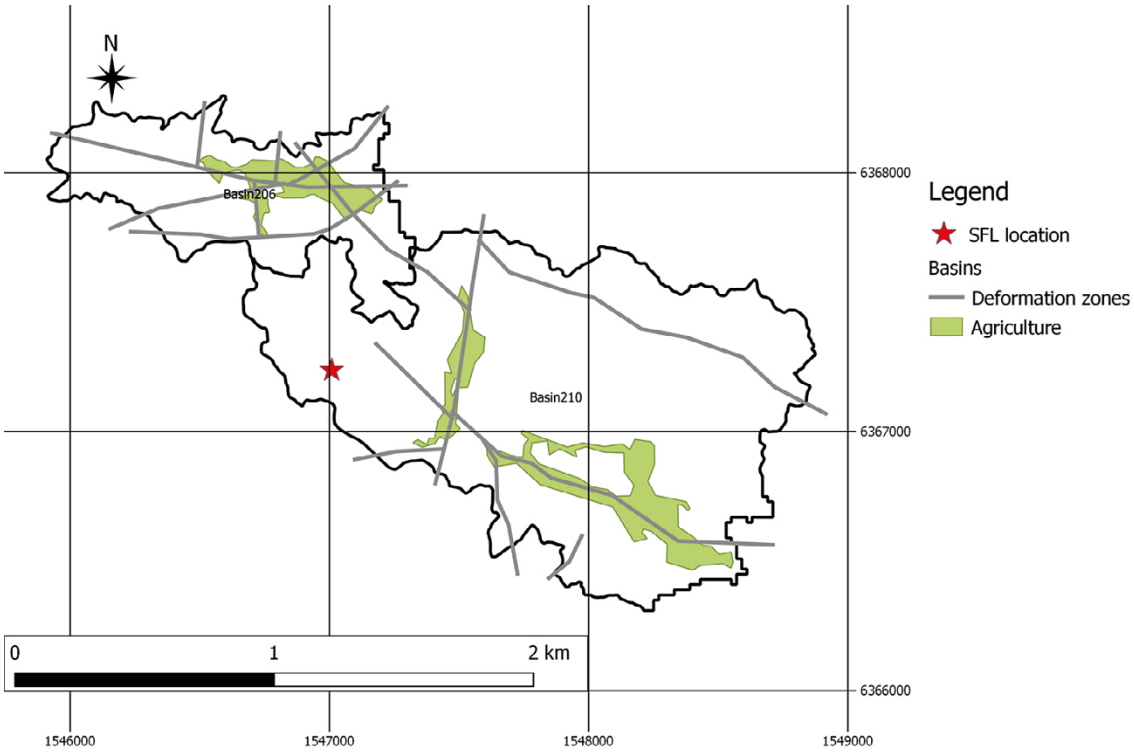

Figure 2-3. *Map of basins 210 and 206. The arable land objects (green polygons), the forest area (white surface) and the deformation zones in the underlying bedrock (grey lines) are displayed. The red star shows the hypothetical position of the SFL repository used in SE-SFL (Abarca et al. 2019).*

2.2 Regolith description

The term regolith applies to all unconsolidated deposits overlying the bedrock. An exhaustive description of the genesis and distribution of the regolith materials can be found in Lindström et al. (2000). The thickness of the regolith is generally related to the bedrock morphology; decreased thickness in the elevated areas where bedrock outcrops and increased thickness in the depressions where material accumulated during earlier stages of landscape development.

The regolith model in the study area consists of five different sediment materials: till, glacial clay, postglacial sand, clay-gyttja and peat (Nyman et al. 2008). The sediments are divided into two main categories according to the environment in which they were formed: glacial and postglacial deposits. The glacial deposits include till and glacial clay. Till is generally characterized as being poorly sorted and glacial clay deposits are generally characterized as being well sorted. Both till and glacial clay are assumed to contain little or no organic matter (OM). The postglacial deposits are clay, sand and peat. These deposits often contain OM and tend to dictate the location of arable lands.

A digital elevation model (DEM) with a 20 × 20 m resolution is used to define the regolith surface (Strömgren and Brydsten 2008). Regolith materials are implemented using raster files, with the same spatial resolution of the DEM, to denote the elevation of the bottom surface of each layer (Nyman et al. 2008). In the study area, the calculated mean thickness of the regolith is 4 m with a maximum thickness of 23 m under the arable lands. The descending order of the regolith stratigraphy, as defined by the raster surface data, is as follows:

- Top of regolith: land-surface topography as defined by the DEM.
- Surface Z2: bottom of the peat.
- Surface Z3: bottom of clay gyttja.
- Surface Z4: bottom of postglacial sand.
- Surface Z5: bottom of glacial clay.
- Surface Z6: bottom of till.

2.3 Water flow at the regolith surface

Surface hydrological conditions are obtained from the results of a surface hydrological model implemented in MIKE SHE (Johansson and Sassner 2019). The following results from the MIKE SHE model are used in the definition of the upper boundary condition of the COMSOL model:

- Average annual flux from the saturated to the unsaturated zone (Figure 2-4).
- Average annual discharge from the saturated zone to surface water/surface runoff.

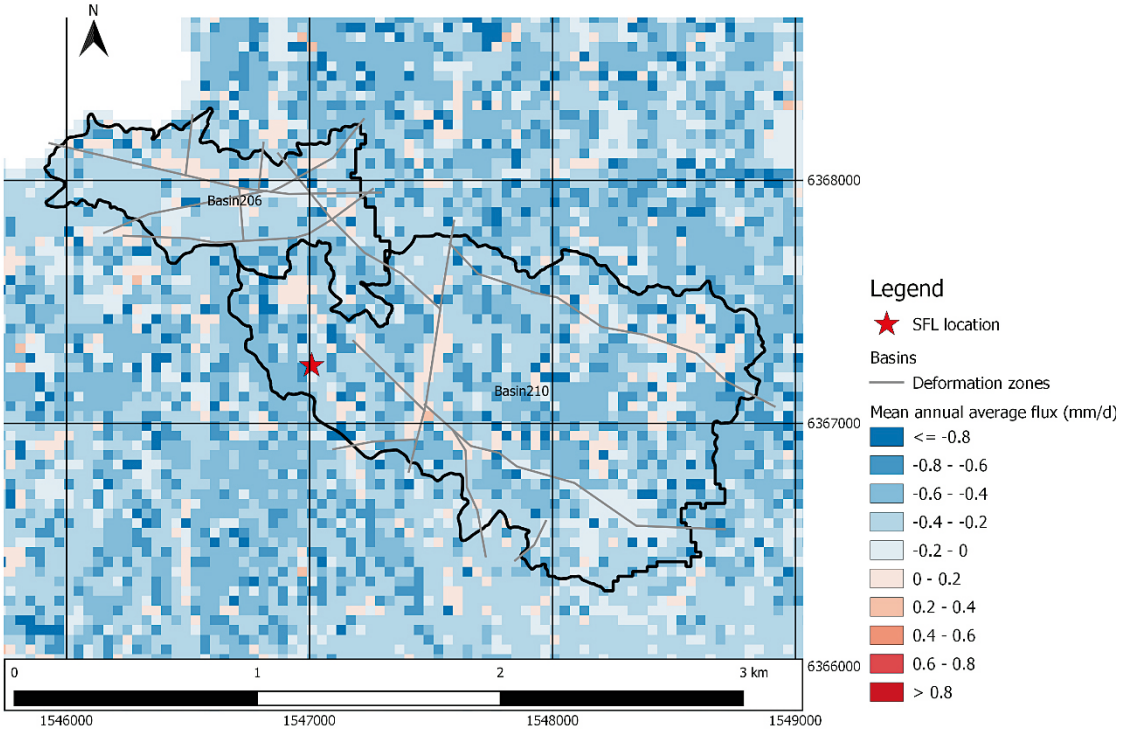

Figure 2-4. *Distribution of the yearly averaged vertical fluxes ($mm \cdot d^{-1}$) between the unsaturated (UZ) and saturated zone (SZ) of the MIKE SHE model. Positive values (red) indicate upward flow (water discharge) and negative values (blue), downward flow (water recharge). The red star shows the hypothetical position of the SFL repository used in SE-SFL (Abarca et al. 2019).*

2.4 Flow from the crystalline rock

Groundwater fluxes at the interface between the regolith and bedrock at Laxemar area are obtained from the hydrological model carried out with MIKE SHE (Johansson and Sassner 2019). Average annual vertical groundwater fluxes from the MIKE SHE model (Figure 2-5) are used in the definition of the lower boundary condition of the COMSOL model.

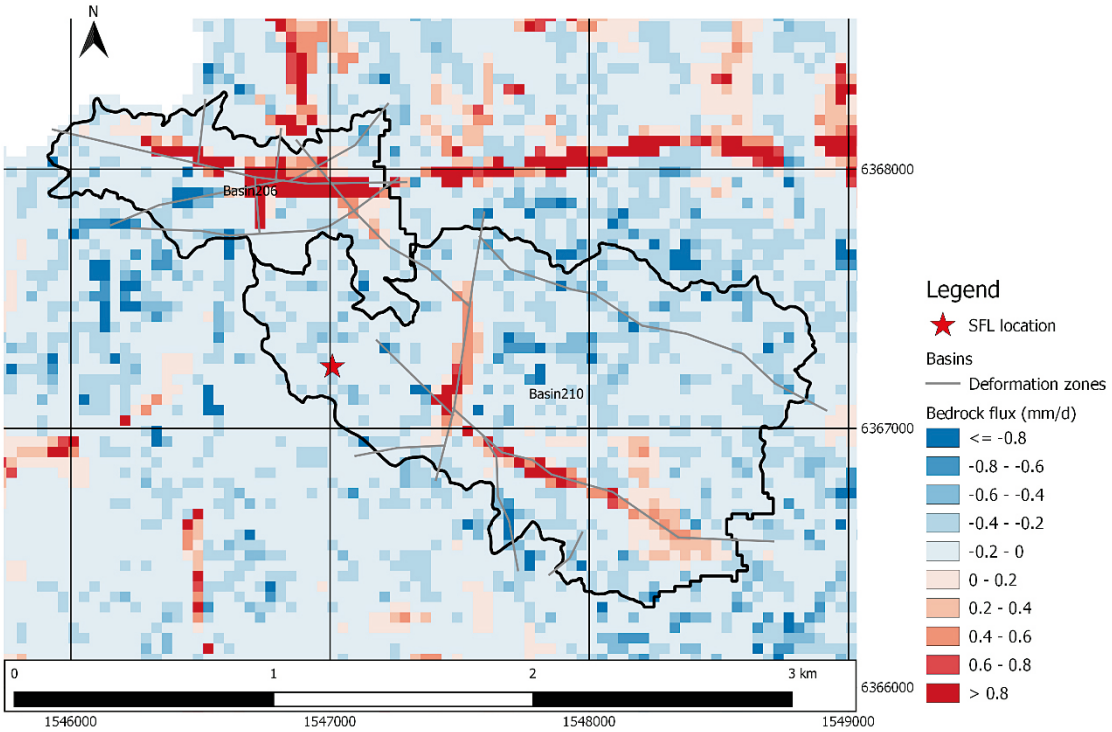

Figure 2-5. *Distribution of the yearly averaged vertical fluxes between the bedrock and the regolith in the MIKE SHE model. Positive values indicate upward flow (inflow to the regolith) and negative values, downward flow (outflow). The red star shows the hypothetical position of the SFL repository used in SE-SFL (Abarca et al. 2019).*

2.5 Radionuclide discharge points

Particle transport simulations were carried out with the regional hydrogeological model in ConnectFlow (Joyce et al. 2019). The positions of the particles at the bedrock-regolith interface (Figure 2-6) are used to specify the locations of radionuclide inflows at the bottom boundary of the model domain.

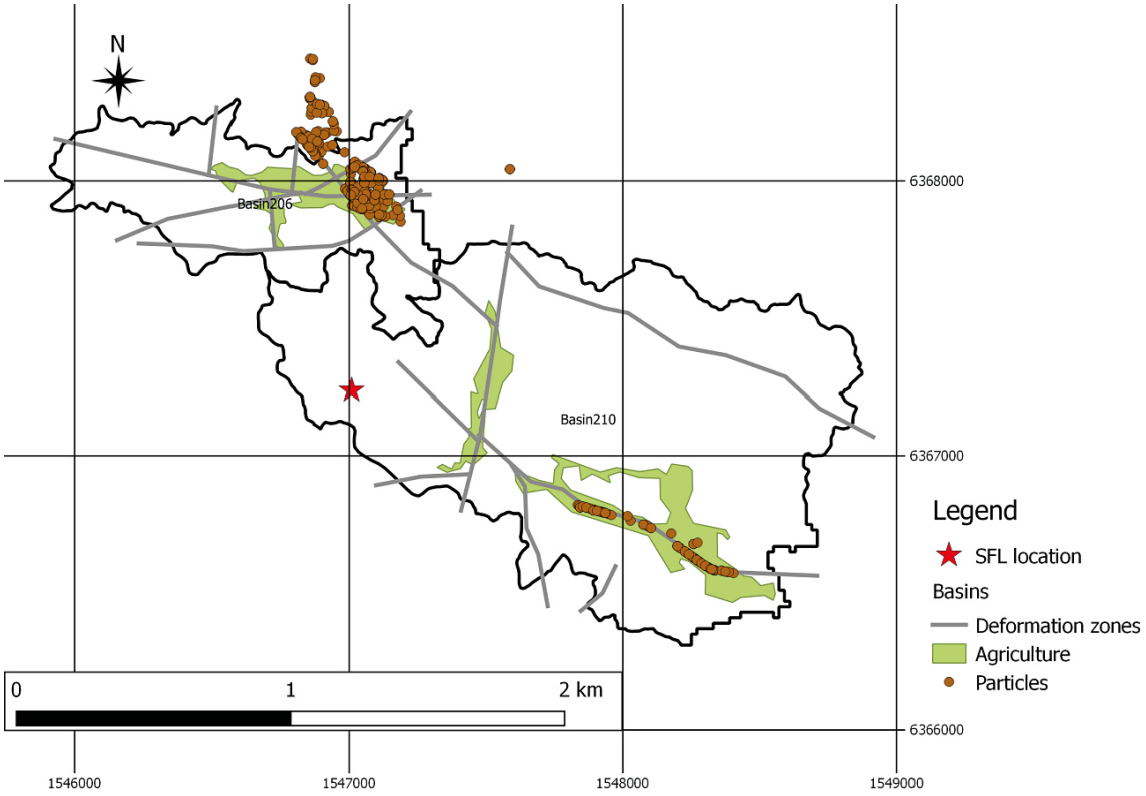

Figure 2-6. *Positions of particles originating from the SFL repository that have arrived at the bedrock-regolith interface according to the particle transport modelling in ConnectFlow (Joyce et al. 2019). Arable lands in the regolith and deformation zone areas of the bedrock are also displayed. The red star shows the hypothetical position of the SFL repository used in SE-SFL (Abarca et al. 2019).*

2.6 Radionuclides half-life

Radioactive decay is only considered for ^{93}Mo and ^{226}Ra due to the large half-life of the other radionuclides in comparison with the characteristic time of the transport models (the total time of transport simulation is 1×10^4 years) (Table 2-1). The decay applies to the aqueous and sorbed species.

Table 2-1. Selected radionuclides and their half-life. Data from Firestone et al. (1998).

	^{93}Mo	^{36}Cl	^{59}Ni	^{226}Ra	^{135}Cs
Half-life (y)	4×10^3	3×10^5	7.6×10^4	1.6×10^3	2.3×10^6

2.7 Values of the solid/liquid partition coefficients (K_d)

A significant effort was made by SKB to compile and evaluate K_d data for both Laxemar and Forsmark. However, K_d values specific to Forsmark are used in this study. This is justified model, considering: Forsmark values are in good agreement with Laxemar values for clay gyttja, till and cultivated peat (Figure 2-7), the assessment of the uncertainties surrounding the K_d values at Forsmark is more extensive (Figure 2-8) and K_d values are available for all of the regolith materials examined in the present study (Figure 2-8). The K_d values used in this study are given in Table 2-2. It should be noted that the K_d values used for the current study differ with those used in the SE-SFL analyses, see Tröjbom et al. (2013).

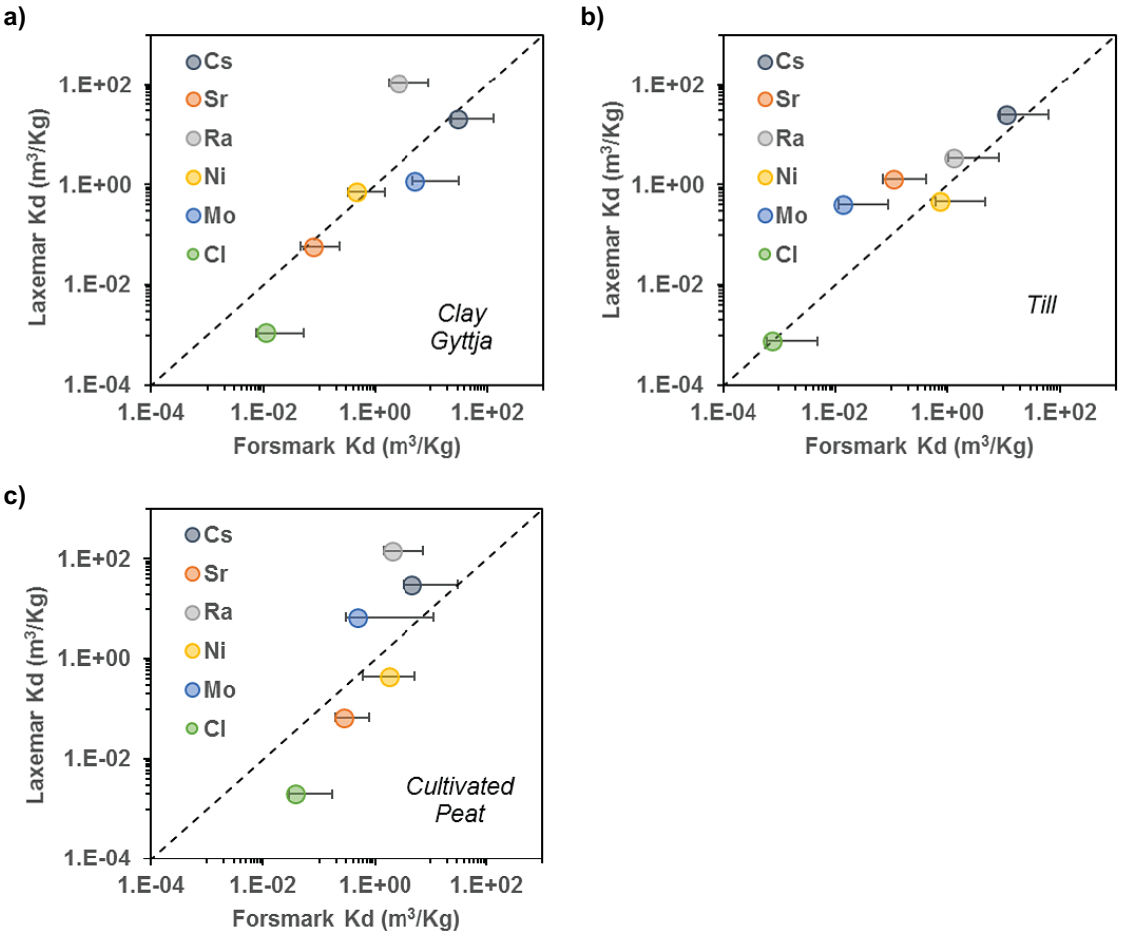

Figure 2-7. Relationship between K_d ($m^3 \cdot kg^{-1}$) values from three different deposits (Clay gyttja, till and cultivated peat) in Forsmark and Laxemar sites. Note that the dashed line stands for a 1:1 K_d ratio. Forsmark K_d values and associated uncertainties are taken from Sheppard et al. (2011); Laxemar K_d values are taken from Sheppard et al.(2009). Note the logarithmic scales on both axes.

Table 2-2. Selected radionuclide K_d ($m^3 \cdot kg^{-1}$) values for the different materials studied in the current work. All values selected based on the data presented in Sheppard et al. (2011). Values presented are the mean K_d value for each material.

	Peat	Clay-gyttja	Postglacial/Glacio fluvial sediments	Glacial clay	Till
Mo	0.4	5.06	0.045	0.2125	0.014
Cl	0.038	0.0114	0.0005	0.0048	0.0008
Ni	1.8	0.4551	0.13	5.0792	0.75
Ra	2	2.6	3.1	5.5	1.3
Cs	4.5	30	0.53	170	11

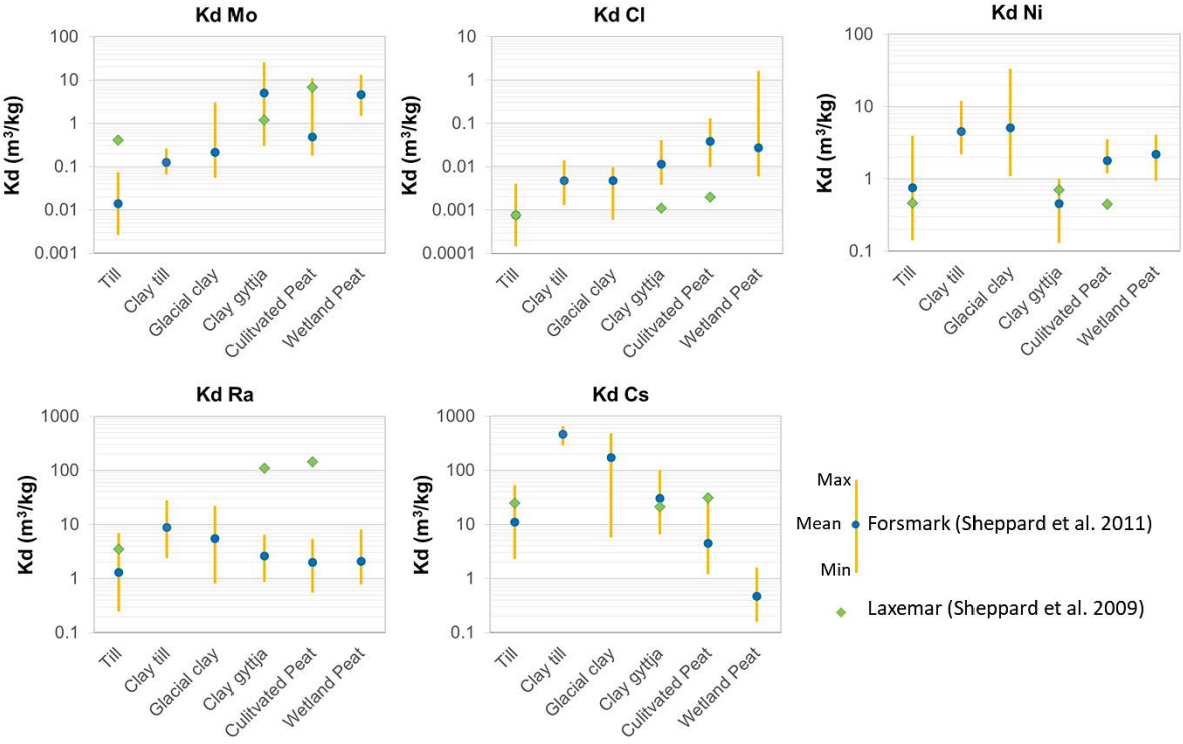

Figure 2-8. *K_d ($m^3 \cdot kg^{-1}$) values and associated uncertainties for Mo, Cl, Ni, Ra, Cs at different regolith materials for Forsmark (Sheppard et al. 2011) and for Laxemar (Sheppard et al. 2009). Note the logarithmic scale on the y axis and that scales differ among elements that differ among elements.*

2.8 Geochemical system

In the K_d model with radioactive decay, the individual chemical processes acting to change the sorbed and aqueous concentrations of the radionuclides are all lumped into a single, dimensionless solid/liquid partition coefficient K_d (see Section 2.7). In the distributed reactive model, however, the fate and transport of the radionuclides is affected by the chemistry of the pore-water and its interaction with the regolith materials. The mineral and water composition and the chemical reactions presented in this section are implemented in the distributed reactive transport model.

The chemistry implemented corresponds with the Forsmark conditions for consistency with the selected K_d values in the distributed K_d model. The mineral and pore-water system are equilibrated through preliminary PHREEQC (Parkhurst and Appelo 2013) batch calculations. The thermodynamic database used for all the chemical reactions in this study is the Nagra/PSI TDB 01/01 (Hummel et al. 2002). No mechanistic model for retention of radionuclides on organic matter is considered due to the lack of thermodynamic data for this type of reactions. These types of retention mechanisms are, currently, better represented using the K_d approach.

2.8.1 Mineral chemistry

The radionuclide retention capacity of the regolith depends on the mineralogical composition of the sediments. The till and glacial clay mineralogy is based on previous reports (Piqué et al. 2010, 2013). It is assumed that the postglacial sand and the clay gyttja-peat layer have the same chemical system as the glacial clay, except for the absence of illite in the postglacial sand. The chemical processes implemented in the clay gyttja-peat layer are equal to those of the glacial clay.

In these systems, radionuclides can be chemically retained by sorption/exchange (in illite or ferrihydrite) or by precipitation of solid-solutions ($(Ca,Sr)CO_3$ and $(Ba,Ra)SO_4$).

Till

The mineralogy of the till system is based on previous reports (Pique et al. 2010, 2013) (Table 2-3). To ensure that the system is in equilibrium at its initial stage, the following mineral composition has been considered:

- Calcite, implemented in the numerical model with trace amounts of strontium forming a $(Ca,Sr)CO_3$ non-ideal solid-solution.
- Barite, implemented in the numerical model with trace amounts of radium forming a $(Ba,Ra)SO_4$ ideal solid-solution.
- Ferrihydrite, implemented in the numerical model in thermodynamic equilibrium. Surface complexation of several ionic species into the surface of this mineral are accounted for through the reactions detailed in Table 2-7.
- Illite, implemented in the numerical model as a cation exchange but also as a surface complexation mineral. Reactions taking place in the exchange and surface positions of this phase are detailed in Table 2-5 and Table 2-8.
- Siderite ($FeCO_3$), allowed to precipitate/dissolve in thermodynamic equilibrium within the numerical model.

The adopted concentration of cation exchange sites (CES) in the till deposit is 67 $mmol \cdot l_{medium}$. A great variability on cation exchange capacity of the regolith materials is observed in Laxemar (Sohlenius et al. 2006, Lundin et al. 2007, Söderbäck and Lindborg 2009) as well as in Forsmark sites (Lundin et al. 2005, Hedenström and Sohlenius 2008). The value used in this study agree reasonably well with previous studies (Table 2-6). The total amount of CES is distributed as three different sites: Planar, Type II and Frayed Edge (FE) sites, following Bradbury and Baeyens (2000) model. Planar sites, considered as "low affinity sites", are the most abundant (~80 % of CES), followed by Type II (20 %) and FES (0.25 %).

Clay

The mineralogy of the clay system applies to glacial clay, glacial gyttja-peat and postglacial (except for the absence of illite in the postglacial sand) materials. The mineralogy (Table 2-3) corresponds to that used in previous reports (Pique et al. 2010, 2013) with some modifications to ensure that the system is in equilibrium at its initial stage (see bullet points below). Minerals considered in the model are the same as in the till case except for ferrihydrite that is not present in the clay system.

- Calcite, implemented in the numerical model with trace amounts of strontium forming a (Ca,Sr) CO_3 non-ideal solid-solution.
- Barite, implemented in the numerical model with trace amounts of radium forming a (Ba,Ra)SO_4 ideal solid-solution.
- Illite, implemented in the numerical model as a cation exchange but also as a surface complexation mineral. Reactions taking place in the exchange and surface positions of this phase are detailed in Table 2-5 and Table 2-8. In the postglacial sand no illite is considered and, therefore, no exchange or surface complexation occur.
- Siderite ($FeCO_3$) and pyrite (FeS_2), both allowed to precipitate/dissolve in thermodynamic equilibrium within the numerical model.

The adopted concentration of cation exchange sites (CES) in the clay deposit is 226 $mmol \cdot l_{medium}$. The value used in this study agree reasonably well with previous studies (Table 2-6). The amount of surface complexation sites is distributed between planar, Type II and Frayed Edge sites calculated as previously explained for the till system.

2.8.2 Water chemistry

Four different groundwater types with unique chemical characteristics are used in the distributed reactive model (Table 2-4). The chemical characteristics of the groundwater types are considered representative of typical porewater found at Forsmark and are classified according to the solid material with which the porewater is in chemical equilibrium.

Till groundwater composition

The chemistry of the groundwater in equilibrium with the till deposit is obtained after equilibration in PHREEQC of a sample from the Forsmark groundwater monitoring well SFM0002 (Tröjbom and Söderbäck 2006) with (Ca,Sr)CO_3 and (Ba,Ra)SO_4 solid-solution, siderite and ferrihydrite. The original iron and strontium concentrations are slightly modified by the equilibrium with ferrihydrite and strontium solid-solution. The redox state of the solution is controlled by the Fe^{2+}/ferrihydrite pair.

Clay groundwater composition

The composition of the initial clay porewater results from the equilibration of the water sample collected at site PFM000117 (Andersson et al. 2003) with pyrite, siderite and calcite. The redox state of clay porewaters is expected to be controlled by microbial activity. Given that 1) a relatively reducing environment in the lake bottom sediments is expected (Percival et al. 2001, Outridge et al. 2005), and 2) that at Forsmark these sediments are relatively rich in calcite (Hedenström 2004).

Deep groundwater

The composition of the reference water that represents the deep groundwater results from the equilibrium of the water sampled in the Forsmark soil pipe SFM0023 with pyrite, calcite and barite. This equilibrium produces a slight shift in the pH of the water and in the concentrations of Ca, C and Ba. The selected groundwater is that used previously in Piqué et al. (2010). Ra natural concentration assumed in this groundwater is that reported in Tröjbom and Grolander (2010).

Radionuclides-rich deep groundwater

The radionuclide-rich groundwater composition is the same as the deep groundwater, except for radionuclide concentrations (Table 2-4). Repository-derived radionuclide concentrations are calculated considering: 1) no retention capacity over radionuclides at the geosphere and 2) instantaneous travel time between the repository and the regolith (i.e., no decay is assumed). These assumptions are conservative as lead to higher repository-derived radionuclide concentrations at the bedrock-regolith interface. The repository-derived radionuclides are labelled as RD to distinguish them from the naturally occurring isotopes. Ra is not labelled because natural Ra is considered below the detection limit.

The concentrations of RDSr and RDNi are calculated by assuming equilibrium of the deep groundwater with their solubility limiting phases ($SrSO_4$ (celestite) and NiS (millerite)), following the methodology described in Duro et al. (2006). The concentrations of RDSr and RDNi in the deep groundwater are 1.56×10^{-3} mol·l^{-1} and 4.16×10^{-7} mol·l^{-1}, respectively (Table 2-4). Since the solubility limiting phases for Ra and RDCs in the near-field are difficult to define, Sena et al. (2008) calculated the corresponding concentrations from the radioactive release doses estimated in the near-field: 9.15×10^{-11} mol·l^{-1} and 3.4×10^{-7} mol·l^{-1}, respectively (SKB 2006). The solubility limits used correspond to that calculated for the spent nuclear fuel repository as SFL specific solubility limit values are not available.

Table 2-3 Initial concentration of the minerals for the till and the clay chemical systems. * are constituents of the $(Ca,Sr)CO_3$ and $(Ba,Ra)SO_4$ solid-solutions.

	Till	Clay
Species	**mol·l$_{water}^{-1}$**	
Siderite	4.60×10^{-4}	0
Pyrite	-	4
Ferrihydrite	5.00×10^{-3}	-
Calcite*	1	1
Strontianite*	1.74×10^{-5}	1.34×10^{-5}
RDStrontianite*	8.28×10^{-13}	2.14×10^{-12}
Barite$^{\neq}$	1.80×10^{-8}	2.66×10^{-8}
$RaSO_4^{\neq}$	2.36×10^{-16}	1.43×10^{-16}

Table 2-4. Chemistry of the selected porewaters. Concentrations are mol·l^{-1}. * denotes low arbitrary concentrations to reduce the concentration gradient between waters.

	Till	Clay	Deep	Radionuclide-rich deep
pH	7.12	7.75	6.86	6.86
Eh(mV)	2.7	−232	−152	−152
Pe	0.05	−3.94	−2.58	−2.58
Na	1.23×10^{-3}	2.63×10^{-4}	6.13×10^{-2}	6.13×10^{-2}
K	1.23×10^{-4}	5.17×10^{-5}	8.00×10^{-4}	8.00×10^{-4}
Ca	2.84×10^{-3}	1.17×10^{-3}	1.82×10^{-2}	1.82×10^{-2}
Mg	3.60×10^{-4}	1.16×10^{-4}	4.73×10^{-3}	4.73×10^{-3}
C(IV)	5.51×10^{-3}	2.49×10^{-3}	4.72×10^{-3}	4.72×10^{-3}
Cl	1.90×10^{-3}	1.53×10^{-4}	1.04×10^{-1}	1.04×10^{-1}
SO_4^{2-}	2.41×10^{-4}	6.39×10^{-5}	2.21×10^{-3}	2.21×10^{-3}
Si	9.74×10^{-5}	4.63×10^{-5}	5.63×10^{-4}	5.63×10^{-4}
Fe_{total}	1.51×10^{-5}	8.34×10^{-7}	5.80×10^{-5}	5.80×10^{-5}
Sr	2.14×10^{-6}	6.19×10^{-7}	5.24×10^{-5}	5.24×10^{-5}
U	2.20×10^{-8}	1.12×10^{-9}	1.13×10^{-8}	1.13×10^{-8}
Cs	6.53×10^{-11}	4.50×10^{-11}	3.65×10^{-9}	3.65×10^{-9}
Ra	5.09×10^{-15}	5.19×10^{-15}	5.03×10^{-15}	9.15×10^{-11}
Ba	8.45×10^{-7}	2.08×10^{-6}	4.38×10^{-7}	4.38×10^{-7}
Ni	4.18×10^{-8}	4.89×10^{-9}	7.17×10^{-9}	7.17×10^{-9}
RDSr	1.02×10^{-13}*	9.87×10^{-14}*	1.00×10^{-13}*	1.56×10^{-3}
RDCs	1.00×10^{-13}*	9.97×10^{-14}*	1.00×10^{-13}*	3.40×10^{-7}
RDNi	9.48×10^{-14}*	9.99×10^{-14}*	1.00×10^{-13}*	4.96×10^{-7}

Table 2-5. Cation exchange reactions and Gaines-Thomas coefficients in the illite interlayer.

Reaction	logK (25 °C)	Reference
$X^- + Na^+ \leftrightarrow NaX$	0.0	Bradbury and Baeyens 2000
$X^- + K^+ \leftrightarrow KX$	1.1	Bradbury and Baeyens 2000
$X^- + Cs^+ \leftrightarrow CsX$	1.6	Bradbury and Baeyens 2000
$2X^- + Sr^{2+} \leftrightarrow SrX_2$	1.5	Cole et al. 2000
$2X^- + Ca^{2+} \leftrightarrow CaX_2$	1.3	Tournassat et al. 2007
$2X^- + Mg^{2+} \leftrightarrow MgX_2$	1.5	Tournassat et al. 2007
$2X^- + Ni^{2+} \leftrightarrow NiX_2$	1.1	Bradbury and Baeyens 2009
$X^{II-} + Na^+ \leftrightarrow NaX^{II}$	0.0	Bradbury and Baeyens 2000
$X^{II-} + K^+ \leftrightarrow KX^{II}$	2.1	Bradbury and Baeyens 2000
$X^{II-} + Cs^+ \leftrightarrow CsX^{II}$	3.6	Bradbury and Baeyens 2000
$X^{FES-} + Na^+ \leftrightarrow NaX^{FES}$	0.0	Bradbury and Baeyens 2000
$X^{FES-} + K^+ \leftrightarrow KX^{FES}$	2.4	Bradbury and Baeyens 2000
$X^{FES-} + Cs^+ \leftrightarrow CsX^{FES}$	7	Bradbury and Baeyens 2000
$X^{FES-} + NH_4^+ \leftrightarrow NH_4X^{FES}$	3.5	Bradbury and Baeyens 2000

Table 2-6. CES (mmol·l_{medium}) values for till and clay deposit in this study, Lundin et al. (2007) and Sena et al. (2008).

	This study	Lundin et al. (2007)	Sena et al. (2008)
Till	67	89–93	40
Clay	226	54–140	200

Table 2-7. Complexation reactions on ferrihydrite surface and corresponding thermodynamic constants.

Reaction	logK (25 °C)	References
$\equiv HFO^sOH + H^+ \leftrightarrow \equiv HFO^sOH^{2+}$	6.51	Waite et al. 1994
$\equiv HFO^sOH \leftrightarrow \equiv HFO^sO^- + H^+$	−9.13	Waite et al. 1994
$\equiv HFO^sOH + UO_2^{2+} \leftrightarrow \equiv (HFO^sO)_2UO_2 + 2H^+$	−2.57	Waite et al. 1994
$\equiv HFO^sOH + UO_2^{2+} + CO_3^{2-} \leftrightarrow \equiv (HFO^sO)_2UO_2CO_3^{2-} + 2H^+$	3.67	Waite et al. 1994
$\equiv HFO^sOH + CO_3^{2-} + 2H^+ \leftrightarrow \equiv HFO^sCO_3H + H_2O$	19.50	Waite et al. 1994
$\equiv HFO^sOH + CO_3^{2-} + H^+ \leftrightarrow \equiv HFO^sCO_3^- + H_2O$	11.51	Waite et al. 1994
$\equiv HFO^sOH + Ni^{2+} \leftrightarrow \equiv HFO^sONi^+ + H^+$	0.37	Dzombak and Morel 1990
$\equiv HFO^wOH + H^+ \leftrightarrow \equiv HFO^wOH_2^+$	6.51	Waite et al. 1994
$\equiv HFO^wOH \leftrightarrow \equiv HFO^wO^- + H^+$	−9.13	Waite et al. 1994
$\equiv HFO^wOH + UO_2^{2+} \leftrightarrow \equiv (HFO^wO)_2UO_2 + 2H^+$	−6.28	Waite et al. 1994
$\equiv HFO^wOH + UO_2^{2+} + CO_3^{2-} \leftrightarrow \equiv (HFO^wO)_2UO_2CO_3^{2-} + 2H^+$	−0.42	Waite et al. 1994
$\equiv HFO^wOH + CO_3^{2-} + 2H^+ \leftrightarrow \equiv HFO^wCO_3H + H_2O$	19.50	Waite et al. 1994
$\equiv HFO^wOH + CO_3^{2-} + H^+ \leftrightarrow \equiv HFO^wCO_3^- + H_2O$	11.51	Waite et al. 1994
$\equiv HFO^wOH + Ni^{2+} \leftrightarrow \equiv HFO^wONi^+ + H^+$	−2.50	Dzombak and Morel 1990

Table 2-8. Complexation reactions on illite surface and corresponding thermodynamic constants.

Reaction	logK (25 °C)	References
$\equiv SO^sOH + H^+ \leftrightarrow \equiv SO^sOH^{2+}$	4.0	Bradbury and Baeyens 2009
$\equiv SO^sOH \leftrightarrow \equiv SO^sO^- + H^+$	−6.2	Bradbury and Baeyens 2009
$\equiv SO^sOH + UO_2^{2+} \leftrightarrow \equiv SO^sOUO_2^+ + H^+$	2.6	Marques Fernandes et al. 2012
$\equiv SO^sOH + UO_2^{2+} + H_2O \leftrightarrow \equiv SO^sOUO_2OH + 2H^+$	−3.6	Marques Fernandes et al. 2012
$\equiv SO^sOH + UO_2^{2+} + 2H_2O \leftrightarrow \equiv SO^sOUO_2(OH)_2^- + 3H^+$	−10.3	Marques Fernandes et al. 2012
$\equiv SO^sOH + UO_2^{2+} + 3H_2O \leftrightarrow \equiv SO^sOUO_2(OH)_3^{2-} + 4H^+$	−17.5	Marques Fernandes et al. 2012
$\equiv SO^sOH + UO_2^{2+} + CO_3^{2-} \leftrightarrow \equiv SO^sUO_2CO_3^- + H^+$	9.8	Marques Fernandes et al. 2012
$\equiv SO^sOH + UO_2^{2+} + 2CO_3^{2-} \leftrightarrow \equiv SO^sUO_2(CO_3)_2^{3-} + H^+$	15.5	Marques Fernandes et al. 2012
$\equiv SO^sOH + U^{4+} \leftrightarrow \equiv SO^sOU^{3+} + H^+$	7.4	Bradbury and Baeyens 2005
$\equiv SO^sOH + U^{4+} + H_2O \leftrightarrow \equiv SO^sOUOH^{2+} + 2H^+$	7.3	Bradbury and Baeyens 2005
$\equiv SO^sOH + U^{4+} + 2H_2O \leftrightarrow \equiv SO^sOU(OH)_2^+ + 3H^+$	−2.4	Bradbury and Baeyens 2005
$\equiv SO^sOH + U^{4+} + 3H_2O \leftrightarrow \equiv SO^sOU(OH)_3 + 4H^+$	−8.8	Bradbury and Baeyens 2005
$\equiv SO^sOH + U^{4+} + 4H_2O \leftrightarrow \equiv SO^sOU(OH)_4^- + 5H^+$	−15.3	Bradbury and Baeyens 2005
$\equiv SO^sOH + Ni^{2+} \leftrightarrow \equiv SO^sONi^+ + H^+$	0.7	Bradbury and Baeyens 2011
$\equiv SO^sOH + Ni^{2+} + H_2O \leftrightarrow \equiv SO^sONiOH + 2H^+$	−8.2	Bradbury and Baeyens 2011
$\equiv SO^sOH + Ni^{2+} + 2H_2O \leftrightarrow \equiv SO^sONi(OH)_2^- + 3H^+$	−17.3	Bradbury and Baeyens 2011
$\equiv SO^sOH + Fe^{2+} \leftrightarrow \equiv SO^sOFe^+ + H^+$	0.7	Bradbury and Baeyens 2011
$\equiv SO^sOH + Fe^{2+} + H_2O \leftrightarrow \equiv SO^sOFeOH + 2H^+$	−8.2	Bradbury and Baeyens 2011
$\equiv SO^sOH + Fe^{2+} + 2H_2O \leftrightarrow \equiv SO^sOFe(OH)_2^- + 3H^+$	−17.3	Bradbury and Baeyens 2011
$\equiv SO^{wa}OH + H^+ \leftrightarrow \equiv SO^{wa}OH_2^+$	4.0	Bradbury and Baeyens 2009
$\equiv SO^{wa}OH \leftrightarrow \equiv SO^{wa}O^- + H^+$	−6.2	Bradbury and Baeyens 2009
$\equiv SO^{wa}OH + Fe^{2+} \leftrightarrow \equiv SO^{wa}OFe^+ + H^+$	−1.8	Bradbury and Baeyens 2011
$\equiv SO^{wa}OH + UO_2^{2+} \leftrightarrow \equiv SO^{wa}OUO_2^+ + H^+$	0.1	Marques Fernandes et al. 2012
$\equiv SO^{wa}OH + UO_2^{2+} + H_2O \leftrightarrow \equiv SO^{wa}OUO_2OH + 2H^+$	−5.3	Marques Fernandes et al. 2012
$\equiv SO^{wa}OH + UO_2^{2+} + CO_3^{2-} \leftrightarrow \equiv SO^{wa}UO_2CO_3^- + H^+$	9.3	Marques Fernandes et al. 2012
$\equiv SO^{wa}OH + Ni^{2+} \leftrightarrow \equiv SO^{wa}ONi^+ + H^+$	−1.8	Bradbury and Baeyens 2011
$\equiv SO^{wb}OH + H^+ \leftrightarrow \equiv SO^{wb}OH_2^+$	8.5	Bradbury and Baeyens 2009
$\equiv SO^{wb}OH \leftrightarrow \equiv SO^{wb}O^- + H^+$	−10.5	Bradbury and Baeyens 2009

3 Description of the distributed K_d model with radioactive decay

The main characteristics of the distributed K_d model are presented in this chapter.

3.1 Model geometry and spatial discretization

The model geometry limits are based on the basin contours, the topography (DEM) and the bedrock-regolith contact presented in Section 2. The numerical models use a local reference system were $X = X_{RT90} - 1\,539\,000$ m and $Y = Y_{RT90} - 6\,360\,000$.

The short vertical extension compared the horizontal extent poses challenges to the domain discretization. The model surface is of around $2\,000 \times 3\,000$ meters in the x-y direction, while the vertical extent is less than 43 meters. For that reason, the mesh built in the COMSOL model is formed by 15 layers of triangular prisms in the vertical direction (Figure 3-1).

Ground surface plots, vertical 2D cross sections and 1D vertical profiles are used to present the model results; the location of the cross sections and vertical profiles is presented in Figure 3-2. The location of the cross sections is considered to adequately represent the regolith geomorphology of the two basins in the model domain. Vertical profiles are placed in the areas where the model showed the highest concentration of chlorine-36.

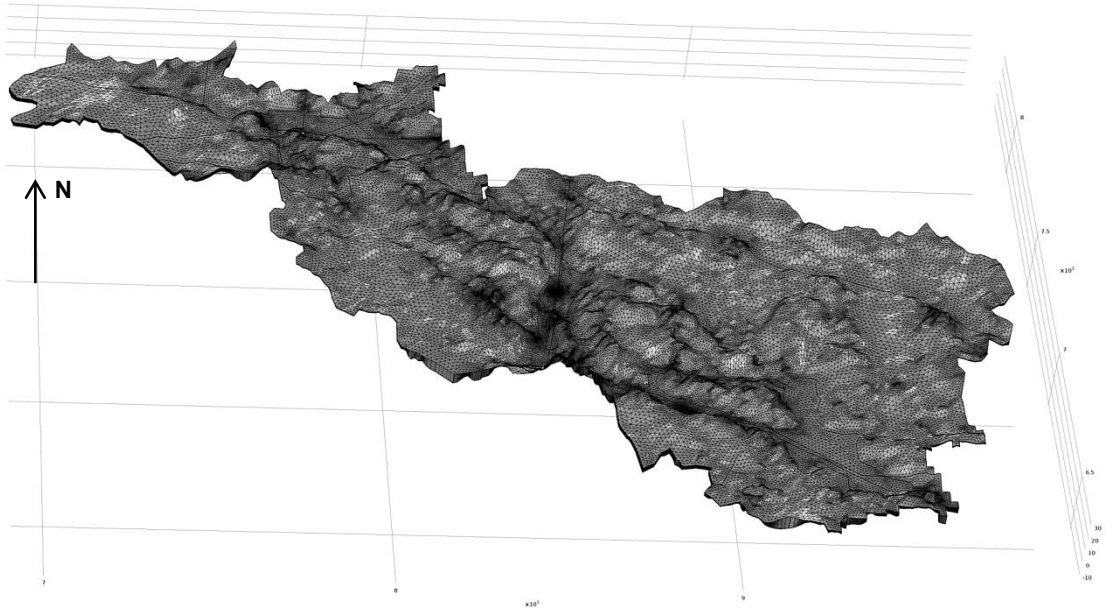

Figure 3-1. *3D view of model mesh with 1 402 890 triangular prisms. Vertical discretization is composed of 15 layers.*

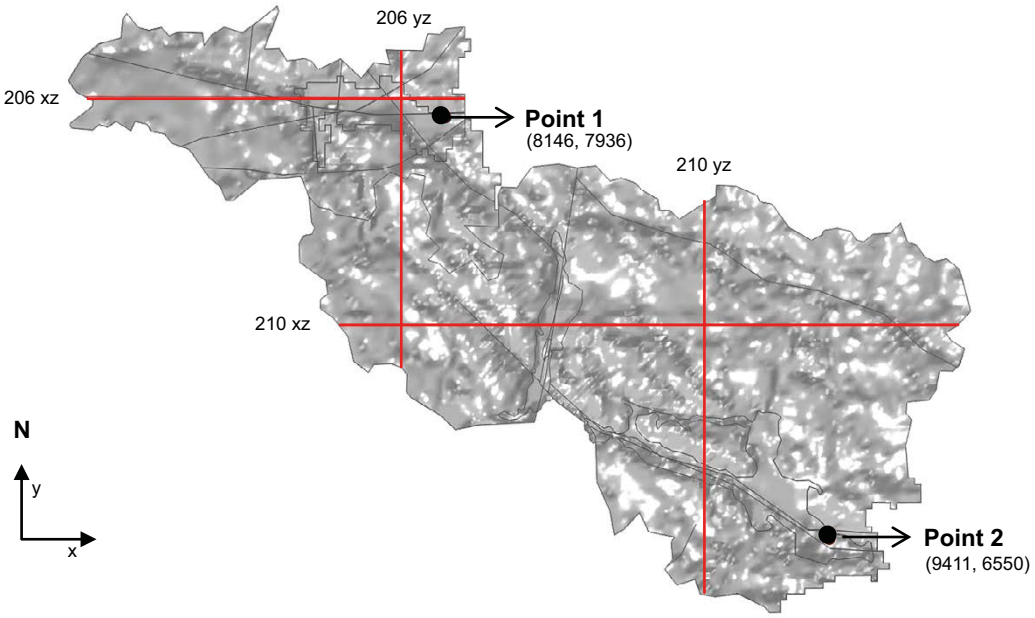

Figure 3-2. *Locations of the vertical 2D cross-sections (red lines) and vertical 1D profiles (black dots).*

3.2 Regolith materials

Geological data from Laxemar (Section 2.2) is used to represent the regolith in the model. Figure 3-3, Figure 3-4 and Figure 3-5 show the distribution of materials in the model.

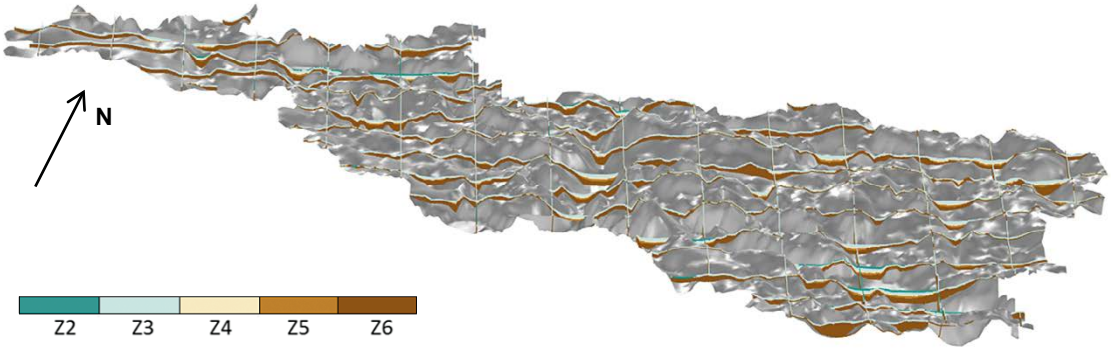

Figure 3-3. *Vertical cross-sections showing the distribution of the regolith materials in the model domain. Z2 refers to peat, Z3 to clay gyttja, Z4 to postglacial sand, Z5 to glacial clay and Z6 to till.*

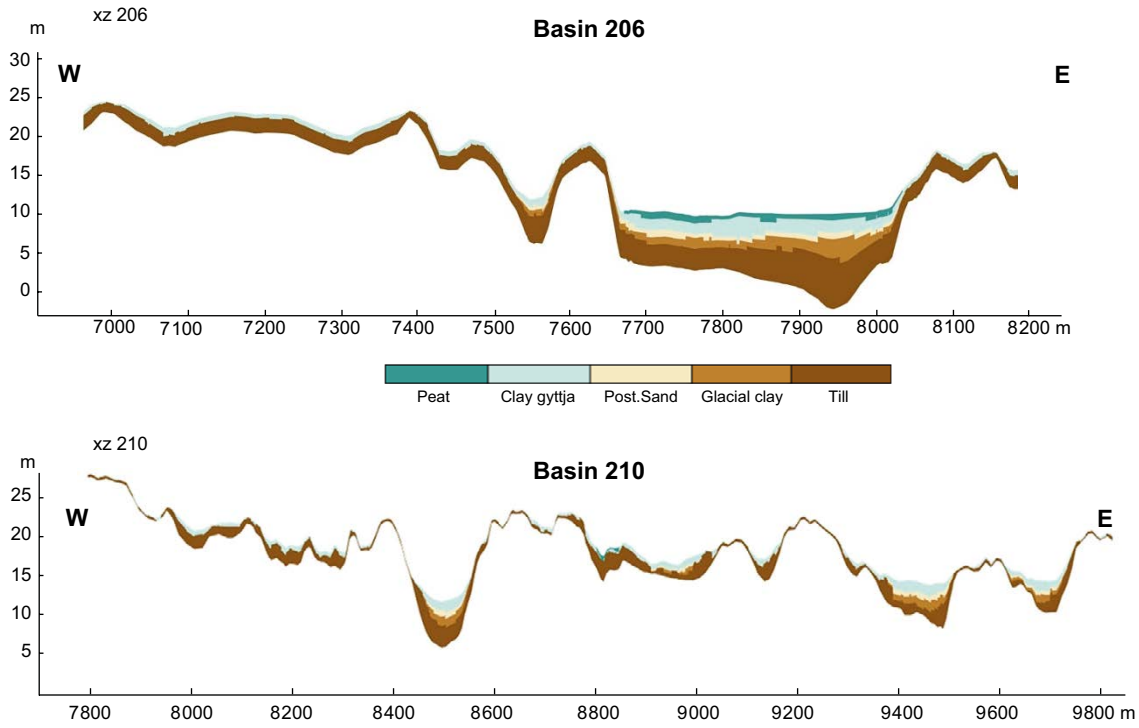

Figure 3-4. *Vertical cross-section in the west–east direction showing the regolith materials in basins 206 and 210. Z2 refers to peat, Z3 to clay gyttja, Z4 to postglacial sand, Z5 to glacial clay and Z6 to till.*

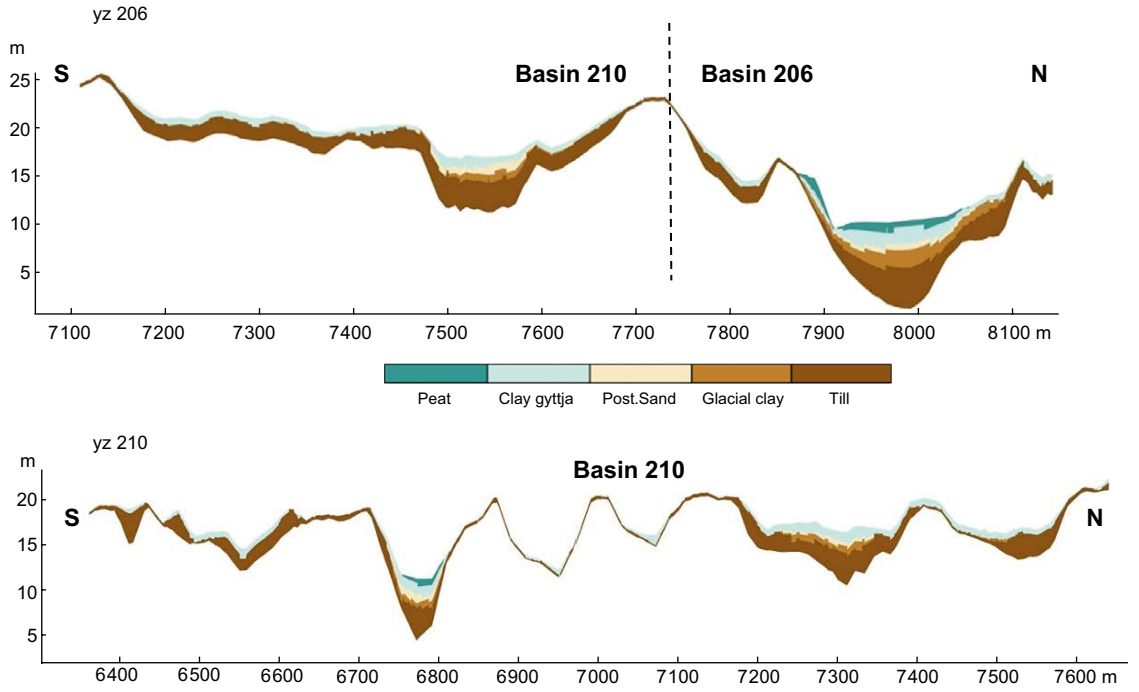

Figure 3-5. *Vertical cross-section in the south–north direction showing the regolith materials in basins 206 and 210. Z2 refers to peat, Z3 to clay gyttja, Z4 to postglacial sand, Z5 to glacial clay and Z6 to till.*

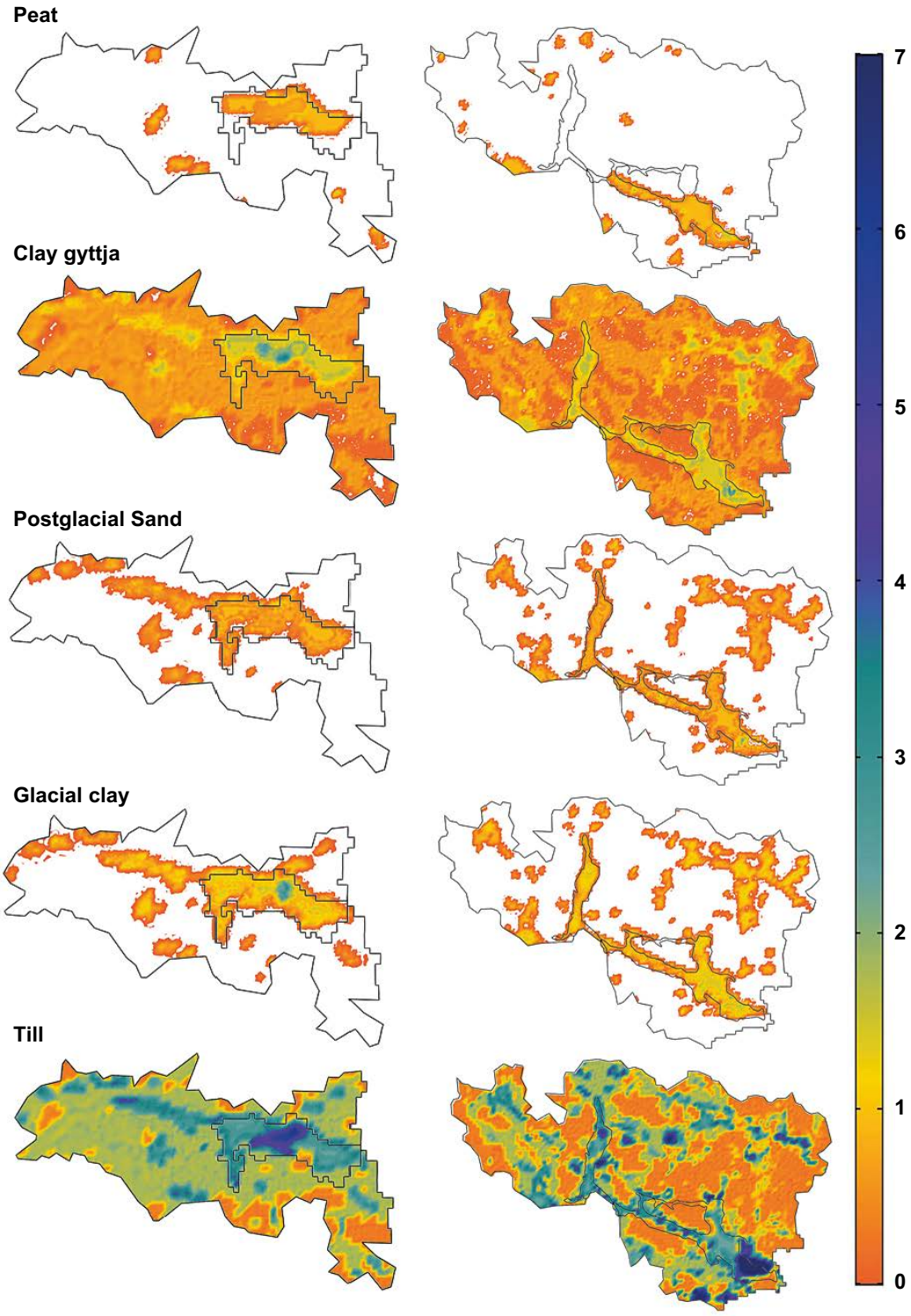

Figure 3-6. *Thickness (m) of the regolith materials in the basins 206 and 210.*

The regolith materials are not defined by a geometrical entity, i.e., there is no plane or volume delimiting each material. The corresponding hydrological and transport properties of each material are assigned directly to the model mesh. The values of the hydraulic parameters for assigned to each material are reported in Table 3-1 and Table 3-2.

3.3 Model equations

3.3.1 Unsaturated groundwater flow

Groundwater flow through variably saturated porous media is calculated using Richards' equation (Richards 1931). The Richards' equation solved by COMSOL Multiphysics is:

$$\rho\left(\frac{C_m}{\rho g}+S_eS\right)\frac{\partial \boldsymbol{p}}{\partial t}+\nabla\rho\left(-\frac{k_s}{\mu}k_r(\nabla \boldsymbol{p}+\rho g\nabla z)\right)=Q_m \qquad \text{Equation (3-1)}$$

where $\boldsymbol{p}$ is the directionally dependent pressure (Pa). ρ is the fluid density (kg·m^{-3}), C_m represents the specific moisture capacity, S_e denotes the effective saturation, S is the storage coefficient, k_s gives the hydraulic permeability (m^2), μ is the fluid dynamic viscosity (Pa·s), k_r denotes the relative permeability, g is acceleration of gravity (9.8 m·s^{-2}), z represents the elevation (m), and Q_m is volumetric flow-rate (kg·m^{-3}·s^{-1}).

The model follows the van Genuchten soil-moisture retention model (van Genuchten 1980):

$$H_p=\boldsymbol{p}/\rho g \qquad \text{Equation (3-2)}$$

$$\theta=\begin{cases}\theta_r+S_e(\theta_s-\theta_r) & H_p<0\\ \theta_s & 0\le H_p\end{cases} \qquad \text{Equation (3-3)}$$

$$S_e=\begin{cases}\frac{1}{[1+|\alpha H_p|^n]^m} & H_p<0\\ 1 & 0\le H_p\end{cases} \qquad \text{Equation (3-4)}$$

$$C_m=\begin{cases}\frac{\alpha m}{1-m}(\theta_s-\theta_r)S_e^{\frac{1}{m}}\left(1-S_e^{\frac{1}{m}}\right)^m & H_p<0\\ 0 & 0\le H_p\end{cases} \qquad \text{Equation (3-5)}$$

where θ (-) is the water content of the porous medium, θ_r is the residual water content (-), θ_s is the saturated water content (-), H_p is the static water pressure head (m), α is a scale parameter inversely proportional to the mean pore diameter (m^{-1}), and n and m are shape parameters characteristic of the porous medium where $m = 1- 1/n$, $0 < m < 1$. The volume of liquid per porous medium volume, θ ranges from the saturated water content θ_s to the residual water content θ_r. Saturation is assumed when water pressure is equal to atmospheric pressure (i.e., when $H_p = 0$).

In this study, the Richards' equation is solved under stationary conditions (i.e., at steady-state). Therefore, the temporal derivatives in Equation (3-1) are zero.

The dependence of the relative permeability on the degree of saturation has been calculated with a cubic exponential law (Pintado et al. 2002, Saaltink et al. 2005, Åkesson et al. 2010, Villar et al. 2012).

$$k_r=\begin{cases}{S_e}^3 & H_p<0\\ 1 & 0\le H_p\end{cases} \qquad \text{Equation (3-6)}$$

The groundwater velocity is given by the Darcy Law for non-saturated medium:

$$\boldsymbol{u}=-\frac{k_s}{\mu}k_r(\nabla \boldsymbol{p}+\rho g\nabla z) \qquad \text{Equation (3-7)}$$

where $\boldsymbol{u}$ is the flux vector or Darcy velocity (m·s^{-1}).

Saturated hydraulic properties of the regolith are given in Table 3-1. Parameterization of the retention curve properties for each regolith material are the same as those used in Bosson et al. (2009), Rhén et al. (2009) and Sheppard et al. (2011) (Table 3-2).

3.3.2 Solute transport with linear sorption and decay

The fate and transport of radionuclides is accounted using an advection-dispersion model with radionuclide sorption and decay. This model is written as:

$$(\theta + \rho_b K_d)\frac{\partial c}{\partial t} + \nabla(c\boldsymbol{u}) = \nabla[(\boldsymbol{D_D} + \theta D_L)\nabla c] - (\theta + \rho_b K_d)\lambda c \qquad \text{Equation (3-8)}$$

where c is the aqueous activity concentration of the radionuclide in question (Bq·m^{-3}), $\boldsymbol{u}$ is the directionally dependent Darcy's velocity (m·s^{-1}), θ is the effective porosity (-), ρ_b is the bulk density (kg·m^{-3}), K_d is the solid/liquid partition coefficient (m^3·kg^{-1}) for sorption process, $\boldsymbol{D_D}$ is the dispersion tensor array (m^2·s^{-1}), D_L is the liquid phase diffusion coefficient (m^2·s^{-1}) and λ is the radioactive decay constant which can be written as:

$$\lambda = \frac{\ln(2)}{t_{1/2}} \qquad \text{Equation (3-9)}$$

where $t_{1/2}$ is the radionuclide half-life (years).

The solid-phase activity concentration C_p (Bq·kg^{-1}) of the immobile solid phase can be written as:

$$C_P = K_d c \qquad \text{Equation (3-10)}$$

The dispersion tensor array $\boldsymbol{D_D}$ can be written as:

$$\begin{aligned}
D_{Dxx} &= \alpha_1 \frac{u^2}{|\boldsymbol{u}|} + \alpha_2 \frac{v^2}{|\boldsymbol{u}|} + \alpha_3 \frac{w^2}{|\boldsymbol{u}|} \\
D_{Dyy} &= \alpha_1 \frac{v^2}{|\boldsymbol{u}|} + \alpha_2 \frac{u^2}{|\boldsymbol{u}|} + \alpha_3 \frac{w^2}{|\boldsymbol{u}|} \\
D_{Dzz} &= \alpha_1 \frac{w^2}{|\boldsymbol{u}|} + \alpha_2 \frac{u^2}{|\boldsymbol{u}|} + \alpha_3 \frac{v^2}{|\boldsymbol{u}|} \\
D_{Dxy} &= D_{Dyx} = (\alpha_1 - \alpha_2)\frac{uv}{|\boldsymbol{u}|} \\
D_{Dxz} &= D_{Dzx} = (\alpha_1 - \alpha_3)\frac{uw}{|\boldsymbol{u}|} \\
D_{Dyz} &= D_{Lzy} = (\alpha_1 - \alpha_3)\frac{vw}{|U\boldsymbol{u}|}
\end{aligned} \qquad \text{Equation (3-11)}$$

where w, u, and v are the directional (x, y and z respectively) components of the Darcy velocity (m·s^{-1}) and α_1 is the longitudinal and α_2, α_3 the transversal dispersivities (m).

Dispersivity has been shown to be both dependent on the spatial scale (Gelhar et al. 1992) and the scale of the heterogeneities present in the porous media (Gelhar and Axness 1983). Only the dependence on spatial scale is considered when estimating the directional dependent dispersivities in the present study due to the substantial uncertainties associated with the spatial heterogeneities of the regolith. The dispersivities used in this study are defined as $\alpha_1 = 3$h and $\alpha_2 = \alpha_3 = 3$h/5, where h is the length of the model grid element parallel to the direction of flow (m).

The liquid phase diffusion D_L coefficient is assumed to be equal to the molecular diffusion of Cl^- in fresh water (1×10^{-9} m^2·s^{-1}) (Yuan-Hui and Gregory 1974) multiplied by the porosity of the porous medium. Other transport properties of the regolith are given in Table 3-1.

The equations for radionuclide sorption and decay are implemented in COMSOL Multiphysics using the built-in equation for "transport of diluted species in porous media". Prior to the implementation of the 3D distributed model, two benchmark exercises have been developed to validate the transport of a radionuclide decay chain subject to linear adsorption with K_d. The description and results of the benchmark exercises are presented in Appendix A.

Table 3-1. Saturated hydraulic and transport properties of the regolith materials are the same as in Bosson et al. (2009), Rhén et al. (2009) and Sheppard et al. (2011). The conductivity can be calculated from the hydraulic permeability (k_s) following $K = k_s \rho g/\mu$.

Materials	K (m·s^{-1})	Effective Porosity	ρ_b (kg·m^{-3})
Peat	3.0×10^{-6}	0.24	240
Clay gyttja	1.0×10^{-7}	0.03	670
Postglacial sand	1.0×10^{-3}	0.25	1400
Glacial clay	1.0×10^{-8}	0.25	1300
Till	4.5×10^{-5}	0.05	1400

Table 3-2. Unsaturated parameters of the regolith materials for the Van-Genuchten model.

Materials	α (m^{-1})	n	m	θ_r	θ_s	References
Peat	1.408	0.955	0.165	0.024	0.24	Hallema et al. 2015
Clay gyttja	1.5	1.1	0.09	0.003	0.03	MDH Engineered Solutions Corp 2003
Postglacial sand	12	2.7	0.63	0.025	0.25	MDH Engineered Solutions Corp 2003
Glacia clay	1.5	1.1	0.09	0.025	0.25	MDH Engineered Solutions Corp 2003
Till	1.5	1.1	0.09	0.005	0.05	MDH Engineered Solutions Corp 2003

3.4 Initial and boundary conditions

3.4.1 Groundwater flow with variable saturation

Groundwater flow in and out of the bedrock is defined as a boundary condition of the model in this study. Fluxes in and out of the bottom domain are defined using results from the MIKE SHE simulations (Section 2.4) and are equal to the fluxes shown in Figure 2-5 and Figure 3-7).

A Cauchy boundary condition is used for the top boundary condition. Flux through the surface (u' in m·s^{-1}) is evaluated as:

$$u' = \beta(z_T - h) + u_0 \qquad \text{Equation (3-12)}$$

where z_T is the ground surface elevation (m), h is the hydraulic head (m), u_0 (m·s^{-1}) is the yearly averaged vertical downward (negative) fluxes at the surface of the MIKE SHE hydrogeological model, see Figure 2-4 and Figure 3-8. β is the hydraulic conductance at the boundary (s^{-1}),

$$\begin{cases} \beta = \frac{K}{L} & for\ h > z_T \\ \beta = 0 & for\ h < z_T \end{cases} \qquad \text{Equation (3-13)}$$

where K is the saturated hydraulic conductivity (m·s^{-1}) of the porous material and L is the length factor (m). The hydraulic conductance β is subject to calibration. In this study, β is 10 for forest and 25 for arable lands.

A Cauchy boundary condition distinguishes between the recharge zones and discharge zones depending on the hydraulic head. In locations where the hydraulic head is higher than the ground surface elevation a flux leaving the model is implemented.

A no-flow condition is considered at the lateral boundaries except for at the basin outlets, see Figure 3-9. A Cauchy boundary condition (Equations (3-12) and (3-13)) is applied at the outlets where β is assumed proportional to the saturated hydraulic conductivity of the porous material at the outlet and the length factor L equal to 1 m. The water table is assumed to be one meter below the ground based on field observations in Rhén et al. (2009). The z_T is therefore assumed to be $z_T - 1$ m at the basin's outlets.

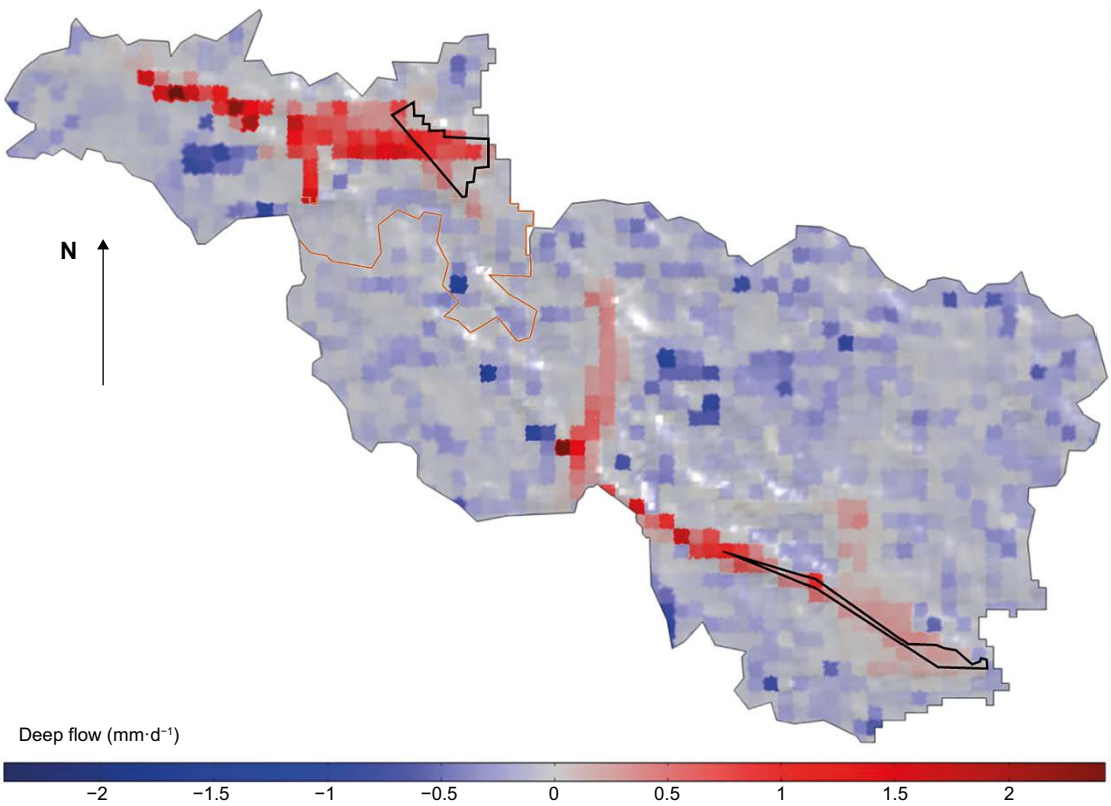

Figure 3-7. *Prescribed fluxes (mm·d^{-1}) at the model's bottom boundary (i.e., the regolith-bedrock interface). Positive values indicate an inflow to the model from the bedrock and negative indicate an outflow from the model towards the bedrock. The black contours show the areas where a radionuclide flux from the bedrock is prescribed in the basin scale model.*

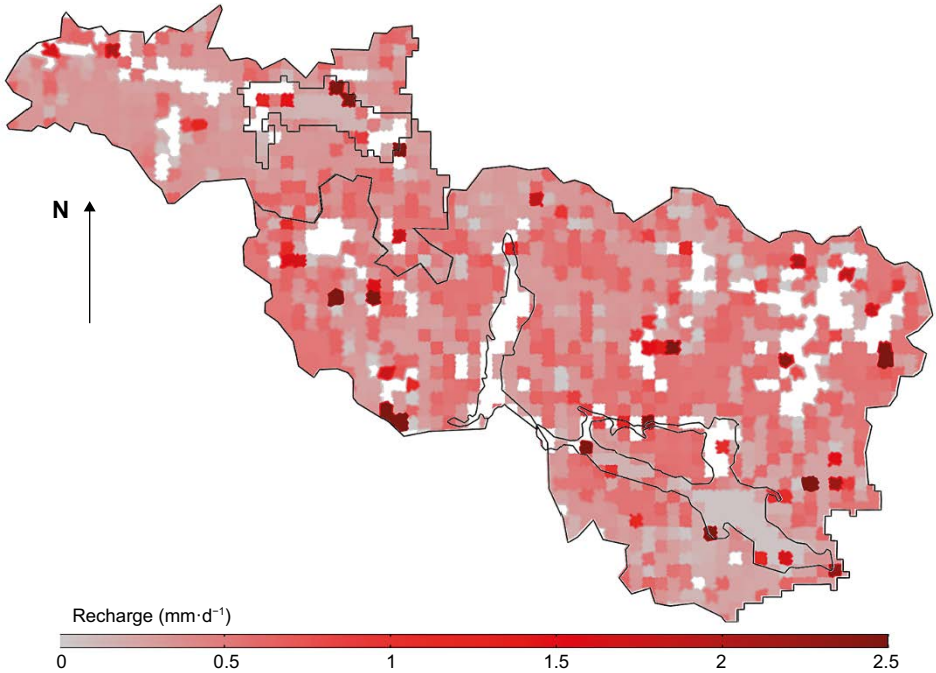

Figure 3-8. *Downward flux, or recharge, at the model's top boundary (i.e., ground surface) (mm·d^{-1}). White area shows the area where there is no inflow prescribed.*

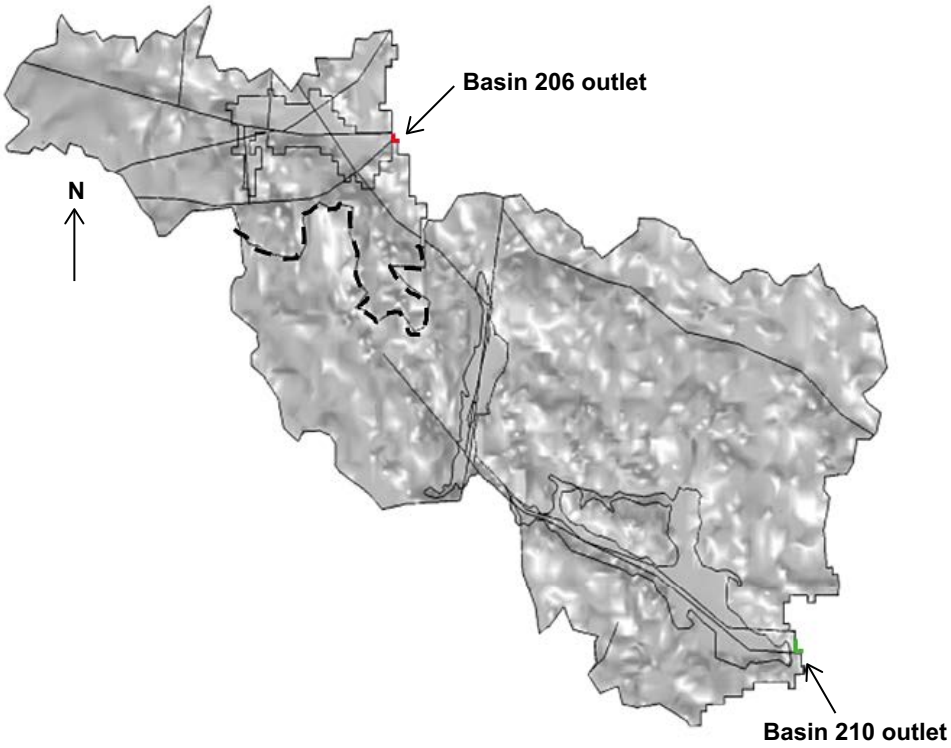

Figure 3-9. *Location of basin outlets. Outflow from the outlets is applied as boundary condition. A no-flow boundary condition is assumed in the rest of the lateral boundaries. The dashed line indicates the border between basin 206 (north) and 210 (south).*

3.4.2 Solute transport with linear sorption and decay

The initial state of the model contains no radionuclides. Radionuclides enter the domain as a prescribed mass flux within the areas defined in Figure 3-7. These areas coincide with the results from the particle transport modelling in ConnectFlow (Joyce et al. 2019), see Figure 2-6. A radionuclide mass flux of 1 Becquerel per year is assumed for each basin resulting in a total of 2 $Bq \cdot yr^{-1}$ for the entire model domain. A return flux of radionuclides from the regolith to the bedrock is not permitted within these areas and inflows to the model outside of these areas are assumed to contain no radionuclides. An open boundary condition is applied to the remaining bedrock-regolith interface, the basin outlets (Figure 3-9) and the model surface. The open boundary allows the radionuclides to leave the model domain through advection, dispersion, and diffusion. At the remaining the lateral boundaries, radionuclides can leave the domain only by diffusion.

4 Results of the distributed K_d model with radioactive decay

This chapter presents a brief overview of the results of the basin scale hydrogeological model and the K_d model. Pressure heads and flows are calculated according to Section 3.3.1 in the hydrological model. The flow-field, or array of directionally-dependent darcy velocities, calculated in the hydrogeological model are used as inputs to the advection-dispersion model with linear adsorption, or "K_d model" (Equation (3-8)).

4.1 Hydrogeological model

The calculated groundwater heads along streamlines illustrating the groundwater flow field are shown in Figure 4-1.

The modelled groundwater flow divide does not coincide with the surface water divide as estimated by the DEM; the modelled groundwater flow divide is located south of the surface water divide which separates basins 206 and 210, see Figure 4-1 and Figure 4-2. Modelled groundwater discharge areas are located at topographic depressions (where the hydraulic heads are lower) (Figure 4-3) . Groundwater flows leave also the basins via the basin outlets, see Figure 3-9 and Figure 4-1. The water balances of the basins are shown in Table 4-1. In general, groundwater flows in each basin are moving towards the basin outlets with the exception of the western part of basin 210 where a small portion of the groundwater flows to the north towards the outlet of basin 206.

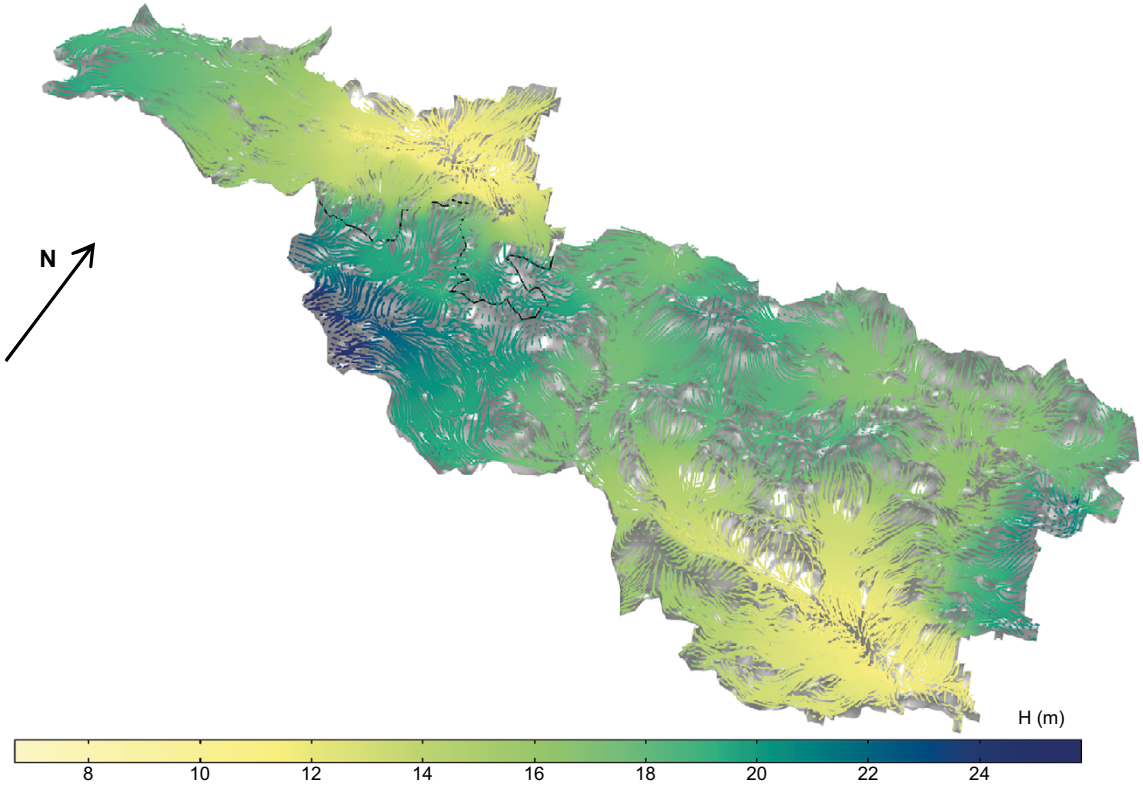

Figure 4-1. *3D plot of the groundwater flow streamlines, showing the flow paths and the discharge areas. The color shows the local groundwater head in m a.s.l. The black line indicates the border between basin 206 (north) and 210 (south).*

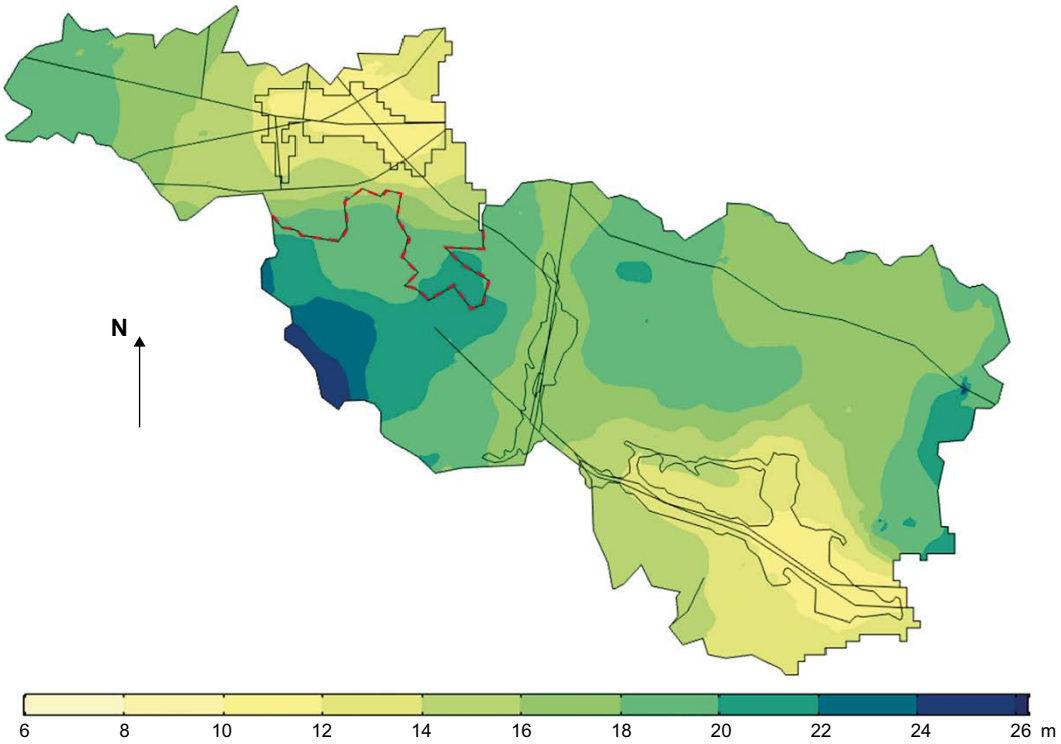

Figure 4-2. *Modelled groundwater head elevation in m a.s.l. The dashed red line indicates the watershed divide that separates basin 206 (north) from 210 (north).*

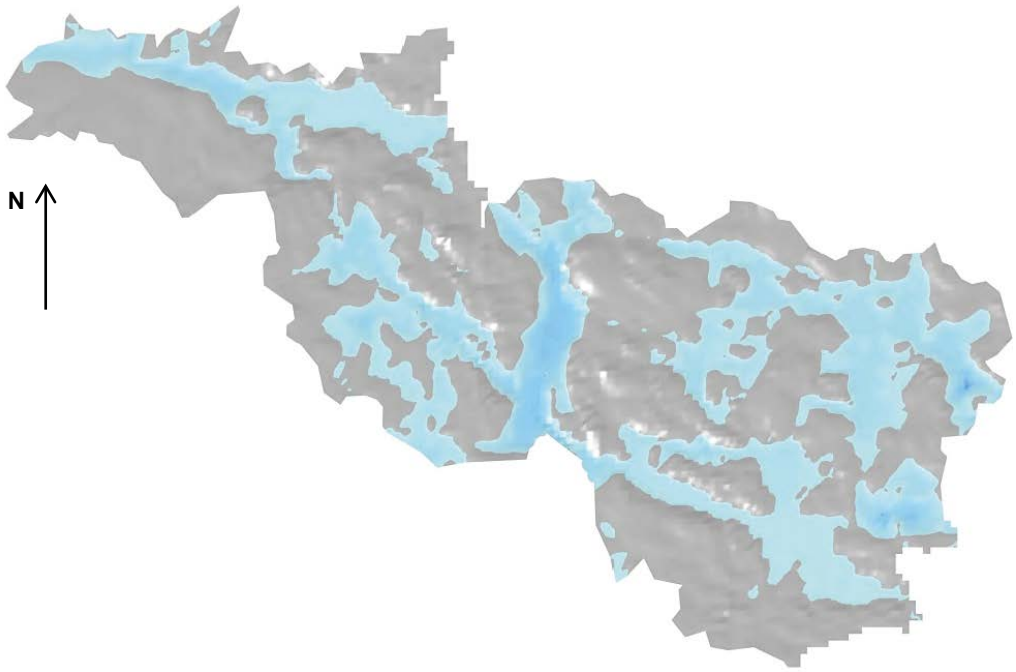

Figure 4-3. *Areas with modelled groundwater discharge at the ground surface of the regolith (light blue).*

Table 4-1. Distributed K_d model water balance (×10^3 m^3·year^{-1}). The outflow through the ground surface and the lateral boundaries are model outputs.

	Bottom surface	Ground surface	Lateral boundaries
Inflow	54.8	380.6	-
Outflow	102	331.1	0.42

2D vertical cross-sections of the groundwater flow field in is shown in Figure 4-4, Figure 4-5 and Figure 4-6. The locations of these cross-sections are shown in Figure 3-2.

All cross-sections show the same general pattern: horizontal flows occur primarily in the more permeable till and post-glacial sand layers and vertical flows occur primarily in the less permeable peat, clay gyttja and glacial clay layers. The magnitude of the flow-field vectors is largest in the postglacial sand and till layers (Figure 4-4, Figure 4-5 and Figure 4-6) which indicates that the majority of the flow within the modelled area is horizontal. The clay act as an aquitard confining the groundwater in the till. The inflection of the flow in the till layer occurs at the areas without or with thinner clay layer (e.g., at the basins borders) (Figure 4-4).

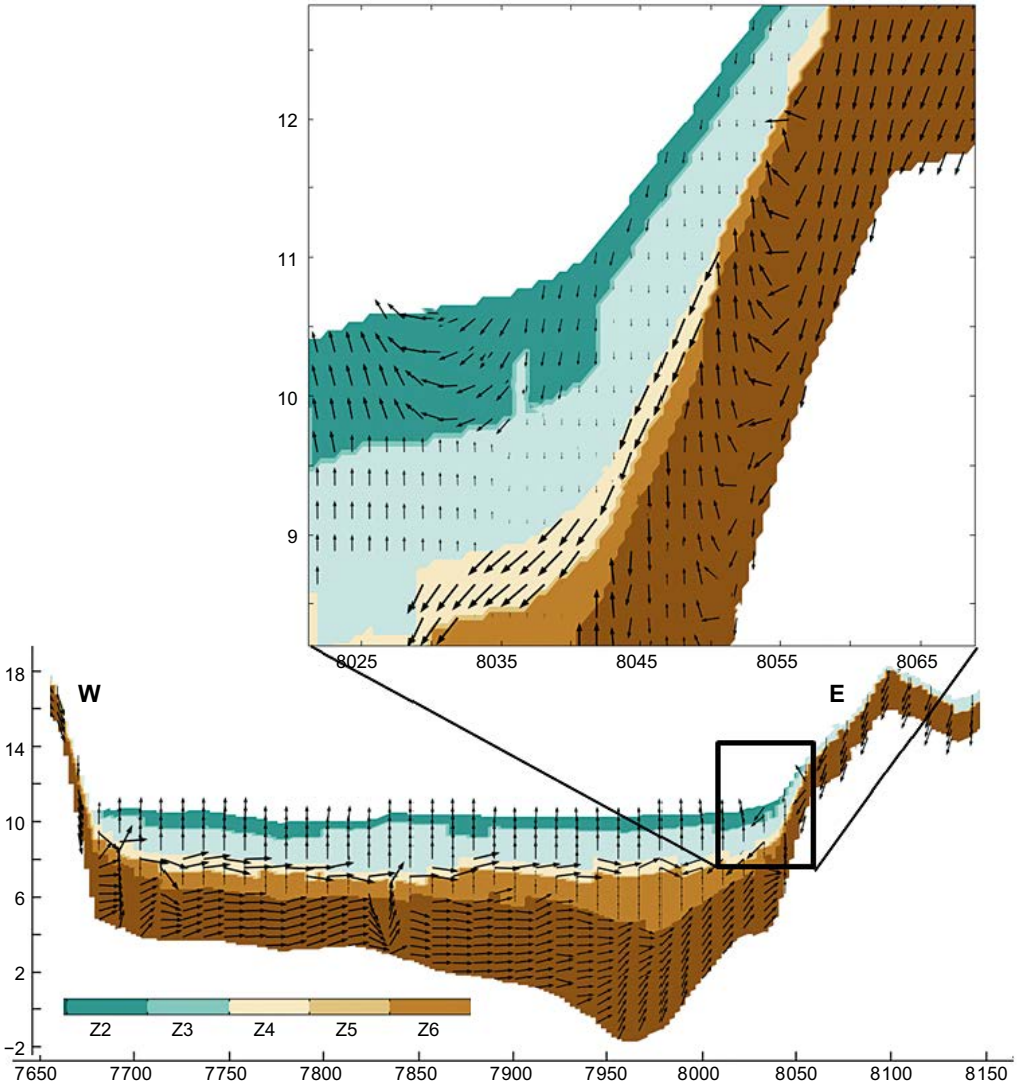

Figure 4-4. *Detail of the cross-section 206 xz showing the groundwater velocity vectors. The magnitude of the vector is proportional to the Darcy velocity. Colors illustrate the materials: Z2 refers to peat, Z3 to clay gyttja, Z4 to postglacial sand, Z5 to glacial clay and Z6 to till.*

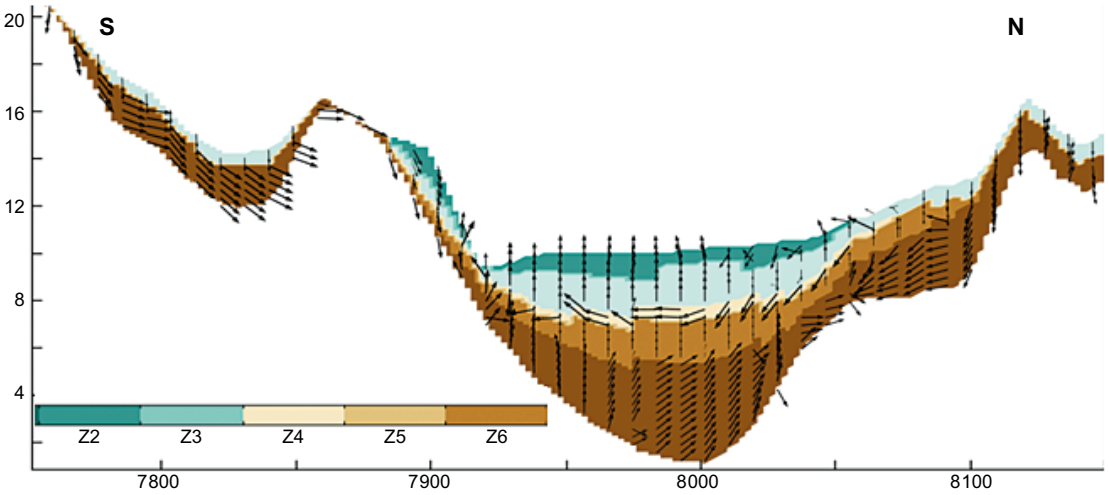

Figure 4-5. *Detail of the cross-section 206 yz showing the groundwater velocity vectors. The size of the vector is proportional to the Darcy velocity magnitude. Colors illustrate the materials: Z2 refers to peat, Z3 to clay gyttja, Z4 to postglacial sand, Z5 to glacial clay and Z6 to till.*

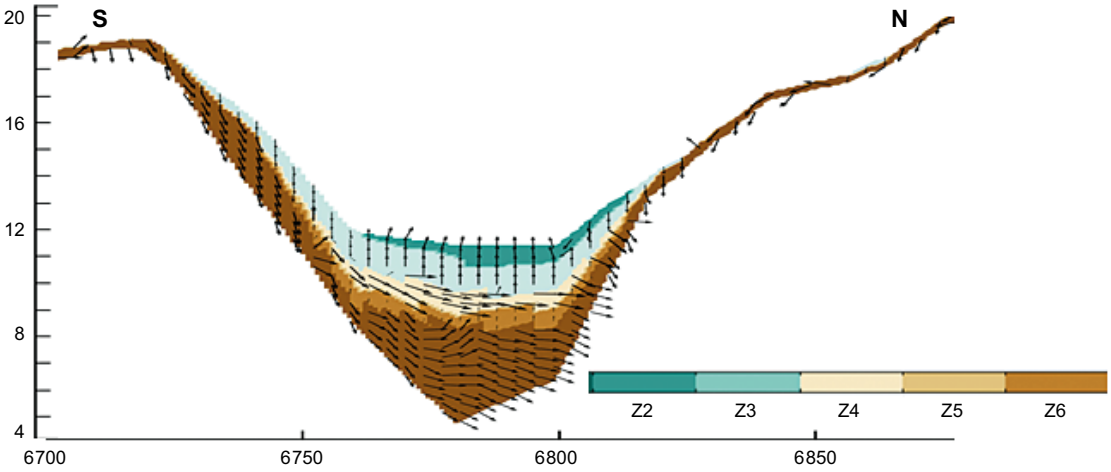

Figure 4-6. *Detail of the cross-section 210 yz showing the groundwater velocity vectors. The size of the vector is proportional to the Darcy velocity magnitude. Colors illustrate the materials: Z2 refers to peat, Z3 to clay gyttja, Z4 to postglacial sand, Z5 to glacial clay and Z6 to till.*

The direction of the flow is further explored at the location of the vertical 1-D profiles (see Figure 3-2) by examining the flow ratio R (-) of the modelled vertical and horizontal flows in each geological layer using Equation (4-1):

$$R = \log_{10} \frac{|q_w|}{max(|q_u|,|q_v|)} \qquad \text{Equation (4-1)}$$

where q_u, q_v and q_w are the components of the Darcy velocity vector in the directions x, y and z, respectively.

The flow ratios for each geological layer, calculated at the positions of the vertical 1-D profiles in Figure 3-2, are presented in Figure 4-7. At these points, all horizontal flow occurs within the till and postglacial sand layers with exception of the peat layer in basin 210.

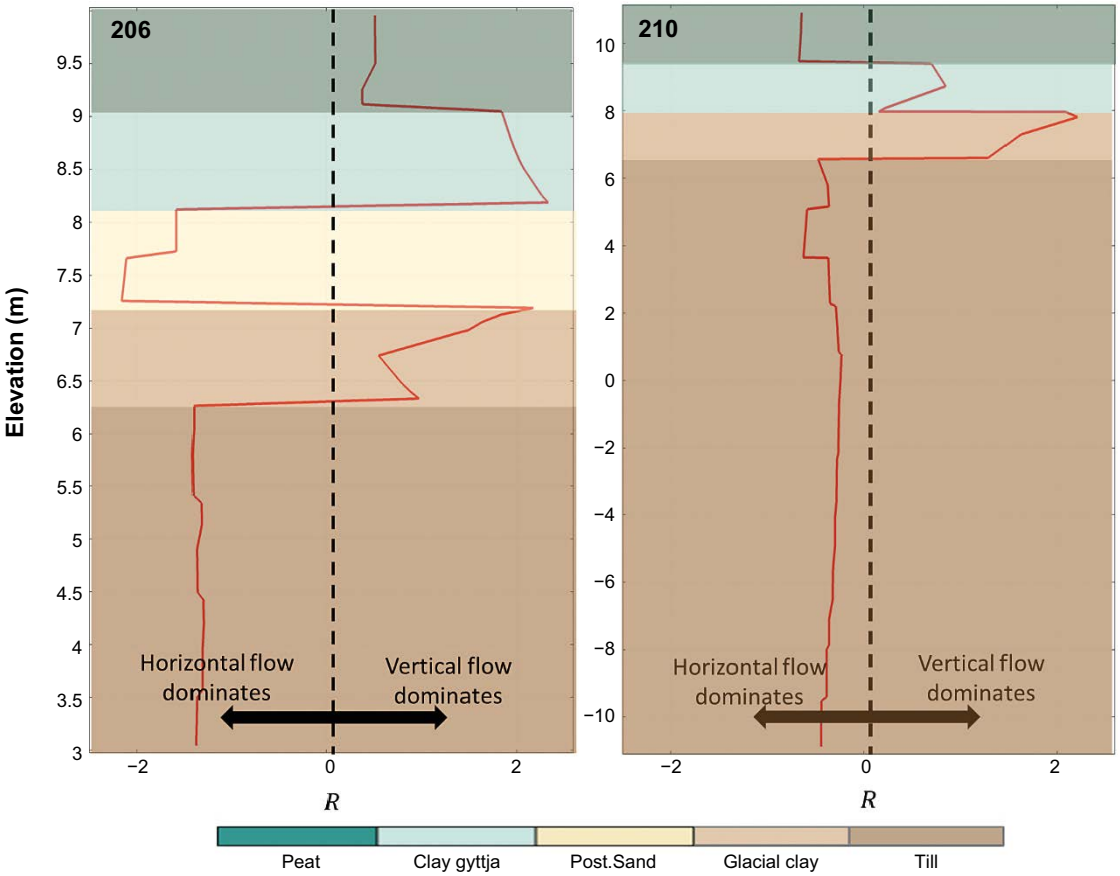

Figure 4-7. *Vertical profiles of the vertical/horizontal flow ratio in points 1 (object 206) and point 2 (object 210) see Figure 3-2. The ratio is computed as in Equation (4-1).*

4.2 K_d model with radioactive decay

This section details the results of the distributed K_d model as presented in Equation (3-8). The directionally-dependent darcy velocities and the dispersion tensor is calculated using the results of the hydrogeological model (see Section 4.1). Radionuclide transport is modelled for each radionuclide irrespective of the other radionuclides considered in this report.

4.2.1 Chlorine-36

Chlorine-36 (^{36}Cl) is treated as a conservative tracer in this study due to its relatively long half-life and its low affinity for sorption compared to other radionuclides (see Table 2-1 and Table 2-2). Any microbiological metabolization of chlorine that may take place in organic soils (e.g. like those discussed in Bastviken et al. 2007 and Svensson et al. 2012) are disregarded in this study. Differences in aqueous- and solid concentrations between ^{36}Cl and that of the other radionuclides examined in this study are attributed to differences in the sorption affinity and/or decay rate of the radionuclides being compared.

After a period of 10 000 years, the modeled maximum ^{36}Cl aqueous activity concentration at model surface (peat surface) is around 1.18×10^{-4} Bq·m$^3_{water}$. This activity concentration is located in the south–eastern part of basin 210 (Figure 4-9). In basin 206, the maximum aqueous ^{36}Cl activity concentration is around 3.16×10^{-5} Bq·m$^{-3}_{water}$ and it is located at the contact between the arable land and the forest in the eastern part of the basin. The maximum activities concentrations occur above the area where the radionuclides enter the regolith in the till and glacial clay layers (see Figure 2-6, Figure 4-8 and Figure 4-9). The lowest aqueous ^{36}Cl concentraton occurs at the postglacial sand (see also Figure B-3) due to the large water flow at this layer that leads to water mixing and, consequently, dilution.

The glacial clay acts as an aquitard (see Section 4.1) suggesting that flow rates within the clay layer would be substantially lower than those in the more permeable till and sand layers. This suggests that role of diffusive transport is likely more significant in the clay layers than in the surrounding till and sand layers.

The maximum sorbed activity concentration of ^{36}Cl occurs in the till and the glacial clay layers and the minimum occurs in the postglacial sand (Figure 4-8 and Figure 4-9).

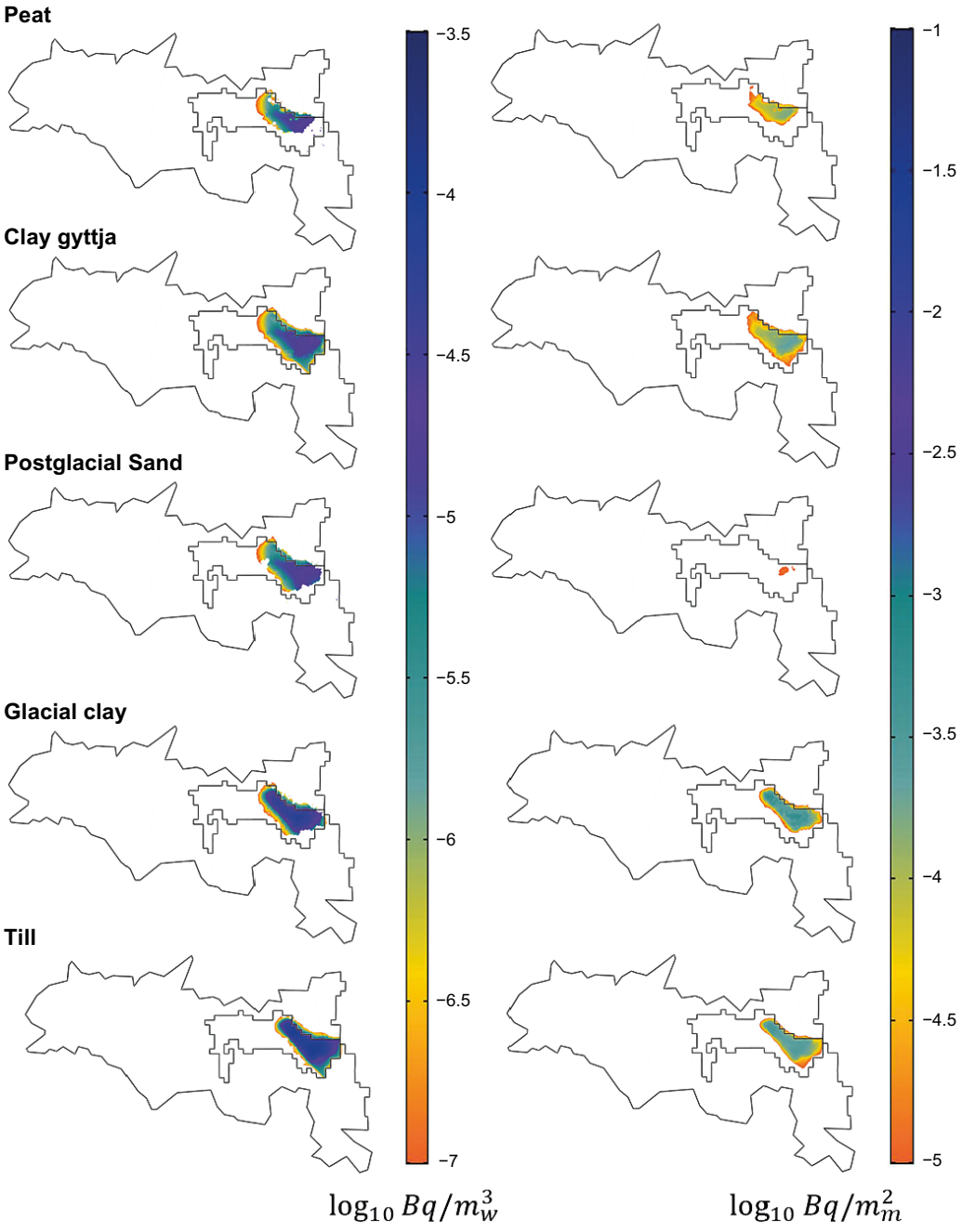

Figure 4-8. *Spatial distribution of ^{36}Cl aqueous activity concentration ($Bq \cdot m_{water}^{-3}$) (left) and sorbed activity concentration per unit area ($Bq \cdot m_{medium}^{-2}$) (right) in the regolith materials after 10 000 years in object 206. The aqueous concentration is the average concentration of the regolith layers. Note that aqueous values below 1×10^{-7} ($Bq \cdot m_w^{-3}$) and sorbed values below 1×10^{-5} ($Bq \cdot m_m^{-2}$) are not plotted in the figure. Note that concentrations are displayed on a logarithmic scale.*

The relatively low sorbed activity concentration of ^{36}Cl in the postglacial sand is caused by the low aqueous activity concentration in the pore water and the low K_d (i.e., low sorption capacity) of the postglacial sand (see Table 2-2). The clay gyttja and the peat show relatively high sorbed ^{36}Cl activities concentrations due to their high K_d values (see Table 2-2).

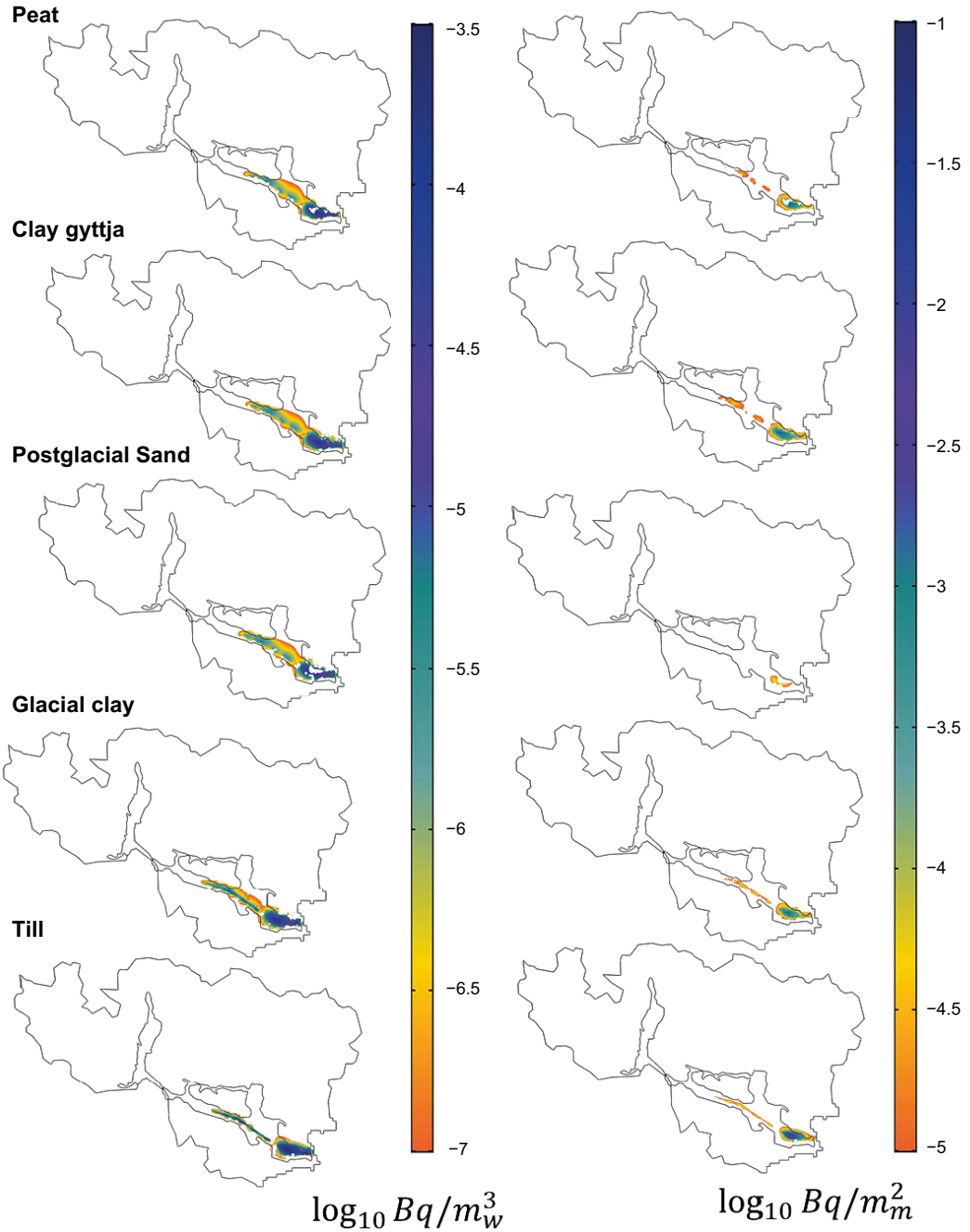

Figure 4-9. *Spatial distribution of ^{36}Cl aqueous activity concentration ($Bq \cdot m_w^{-33}$) (left) and sorbed activity concentration per unit area ($Bq \cdot m_m^{-2}$) (right) in the regolith materials after 10 000 years in object 210. The aqueous concentration is the average concentration of the regolith layers. Note that aqueous values below 1×10^{-7} ($Bq \cdot m_w^{-3}$) and sorbed values below 1×10^{-5} ($Bq \cdot m_m^{-2}$) are not plotted in the figure. Note that concentrations are displayed on a logarithmic scale.*

Figure 4-10 and Figure 4-11 show the mass balance distribution of the normalized ^{36}Cl activity concentration throughout the simulation. In both objects 206 and 210, almost all of the ^{36}Cl activity exits the model domain, either via the bottom or the surface of the model domain. The amount of ^{36}Cl retained in the system is negligible. Part of the ^{36}Cl that leaves the model domain into the bedrock may return to the regolith at another position. This phenomenon is however not currently capable of being captured given the current delineation of the model domain. The modelled system appears to have reached an equilibrium state in less than 1 000 years of simulation time, see Figure B-1 and Figure B-2.

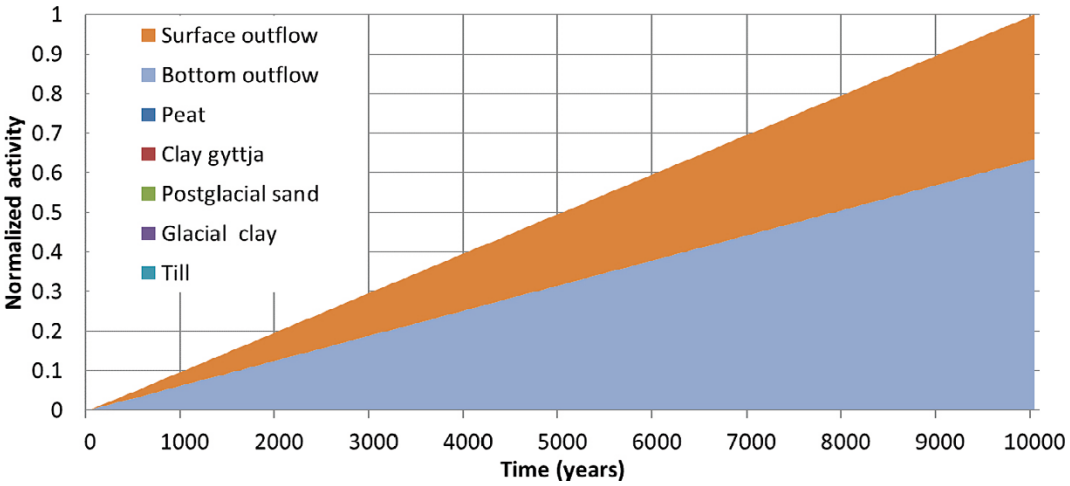

Figure 4-10. *Temporal development of the activity of ^{36}Cl in the regolith materials (till, glacial clay, postglacial sand, clay gyttja and peat) and accumulated activity that exit the model through the ground surface (surface outflow) and the bottom (bottom outflow) boundaries in basin 206. ^{36}Cl is normalized with the total amount introduced in the system during the simulation.*

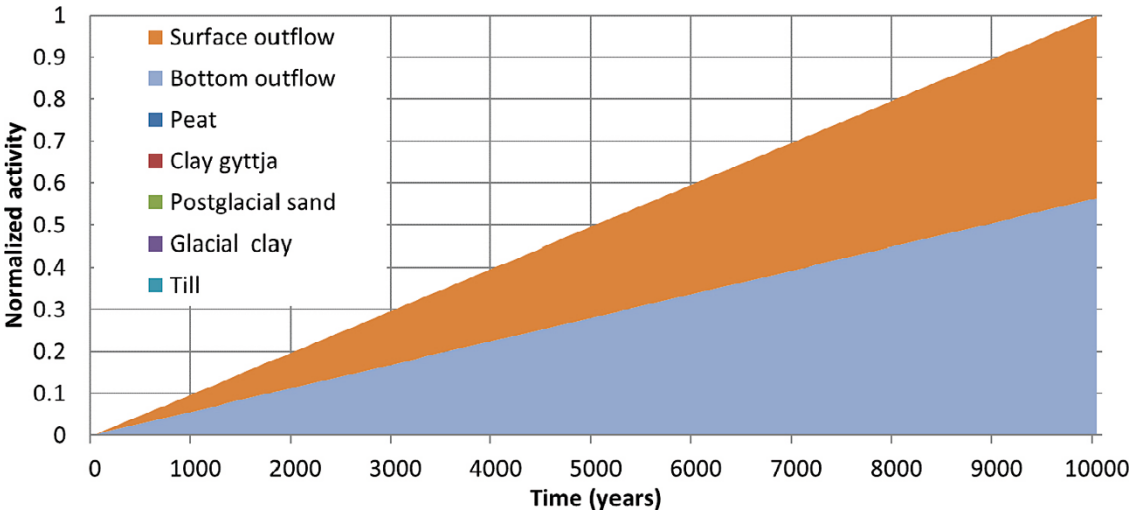

Figure 4-11. *Temporal development of the activity of ^{36}Cl in the regolith materials (till, glacial clay, postglacial sand, clay gyttja and peat) and accumulated activity that exit the model through the ground surface (surface outflow) and the bottom (bottom outflow) boundaries in basin 210. ^{36}Cl is normalized with the total amount introduced during the simulation.*

4.2.2 Nickel-59

After 10 000 years of simulation, the maximum nickel-59 (^{59}Ni) aqueous activity concentration at the model surface is around 2.61×10^{-5} Bq·m$^{-3}_{water}$. The maximum activity concentration occurs at the contact between the arable land and the forest in the eastern part of basin 206 (Figure 4-12). Similar values are found in the south–eastern part of basin 210 (around 1.5×10^{-5} Bq·m$^{-3}_{water}$) along the permanent river in the arable land of basin 210 (Figure 4-13). The activity concentration of the aqueous ^{59}Ni and sorbed in basin 206, follow similar trends as the ^{36}Cl (Figure 4-12). The higher activity concentrations of aqueous ^{59}Ni occur at the till and glacial clay (around 6.5×10^{-5} Bq·m$^{-3}_{water}$). There is also a relevant dilution due to the water mixing conveyed by the postglacial sand.

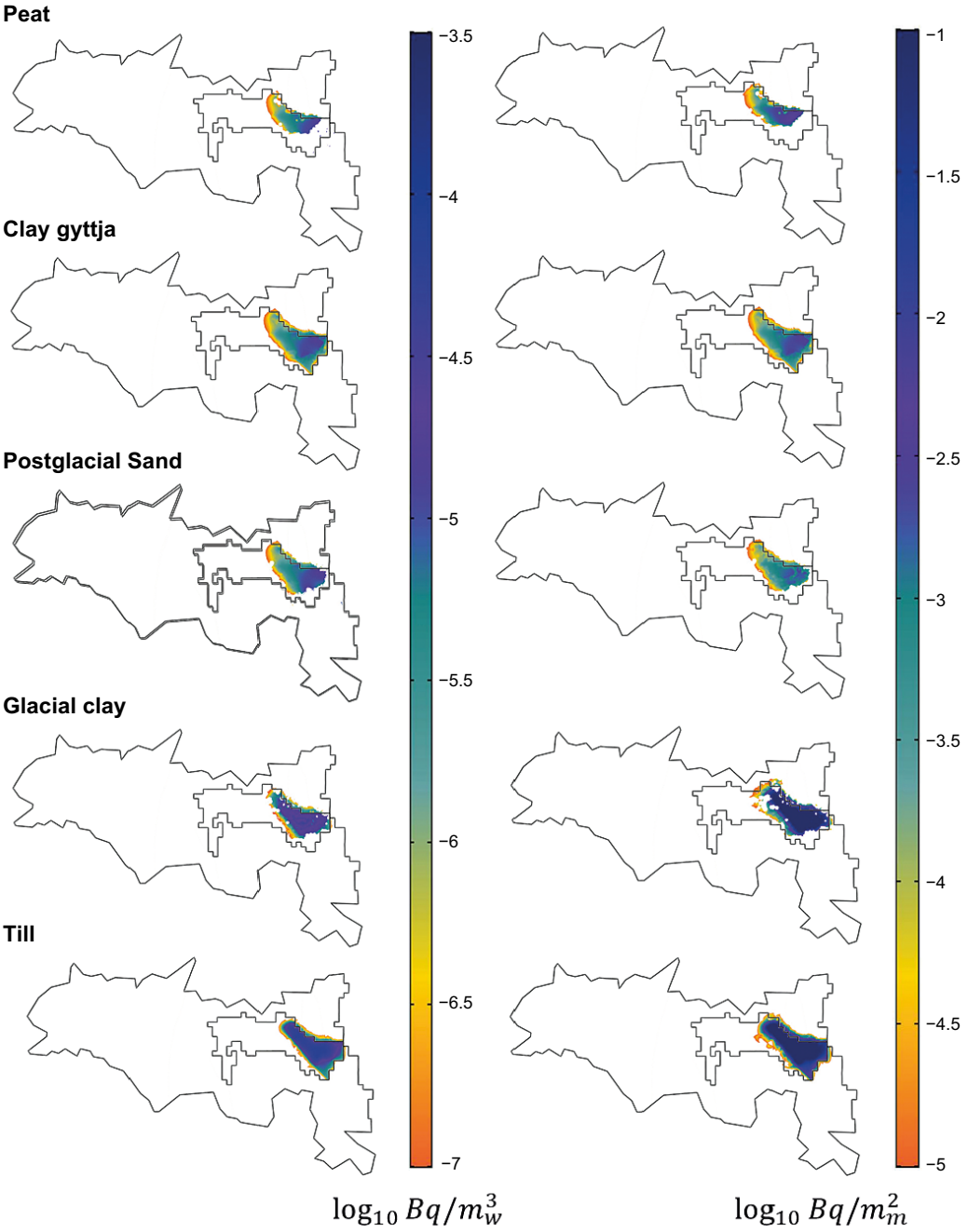

Figure 4-12. *Spatial distribution of Ni-36 aqueous activity concentration (Bq·m$_w^{-3}$) (left) and sorbed activity concentration per unit area (Bq·m$_m^{-2}$) (right) in the regolith materials after 10 000 years in object 206. The aqueous concentration is the average concentration of the regolith layers. Note that aqueous values below 1×10^{-7} (Bq·m$_w^{-3}$) and sorbed values below 1×10^{-5} (Bq·m$_m^{-22}$) are not plotted in the figure. Note that concentrations are displayed on a logarithmic scale.*

After 10 000 years of simulation, the sorption capacity of the glacial clay does not appear to be saturated suggesting that sorbed concentrations are likely to continue to increase (see Figure B-4 and Figure B-5). During the simulation time, most of the ^{59}Ni is adsorbed in the glacial clay leading to lower activity concentrations in the upper regolith materials (postglacial sand, clay gyttja and peat). In basin 206, almost all the activity concentration is sorbed on regolith the materials (see Figure B-4 and Figure B-5), with the aqueous ^{59}Ni activity concentration being around four orders of magnitude less than the sorbed activity concentrations.

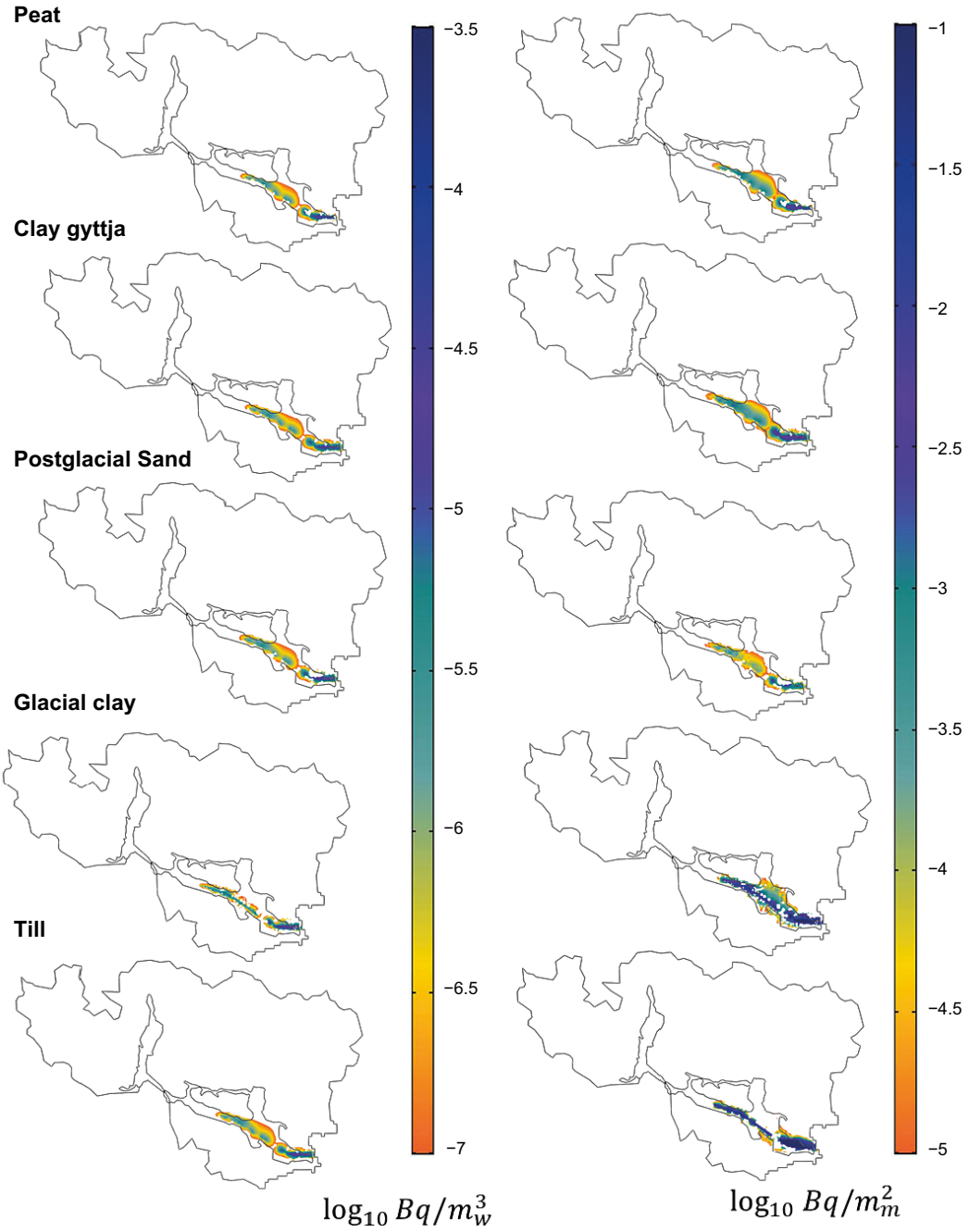

Figure 4-13. *Spatial distribution of Ni-36 aqueous activity concentration ($Bq \cdot m_w^{-3}$) (left) and sorbed activity concentration per unit area ($Bq \cdot m_m^{-2}$) (right) in the regolith materials after 10 000 years in object 210. The aqueous concentration is the average concentration of the regolith layers. Note that aqueous values below 1×10^{-7} ($Bq \cdot m_w^{-3}$) and sorbed values below 1×10^{-5} ($Bq \cdot m_m^{-2}$) are not plotted in the figure. Note that concentrations are displayed on a logarithmic scale.*

Figure 4-14 and Figure 4-15 show the mass balance distribution of the normalized ^{59}Ni activity concentration throughout the simulation. At early times, most of the activity concentration is in the till. After 10 000 years the till in basin 210 retains more ^{59}Ni (53 %) than in basin 206 (27 %), due to the larger volume of regolith present in basin 210. Over the simulation time, most of the ^{59}Ni is retained in the till and glacial clay. Most of the ^{59}Ni leaving the model domain leaves through the bottom surface of the model suggesting that it may be capable of re-entering the regolith outside of the model domain. The retention capacity of the regolith is not depleted after 10 000 years. The modelled system appears to be nearing an equilibrium state at the vertical profile basin 206 between 5 000 and 10 000 years of simulation time, see Figure B-4 and Figure B-5.

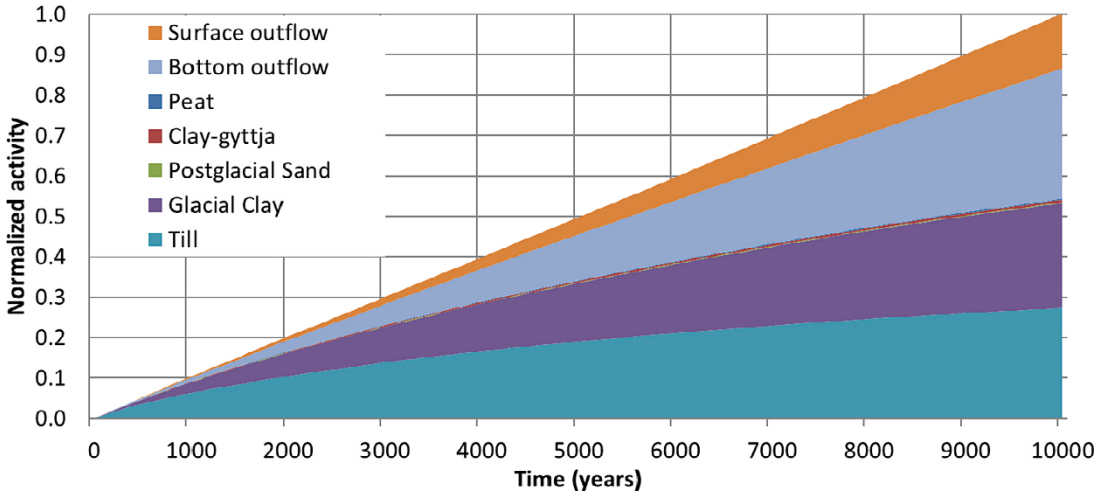

Figure 4-14. *Temporal development of the activity of ^{59}Ni in the regolith materials (till, glacial clay, postglacial sand, clay gyttja and peat) and accumulated activity that exit the model through the ground surface (surface outflow) and the bottom (bottom outflow) boundaries in basin 206. ^{59}Ni is normalized with the total amount introduced in the system.*

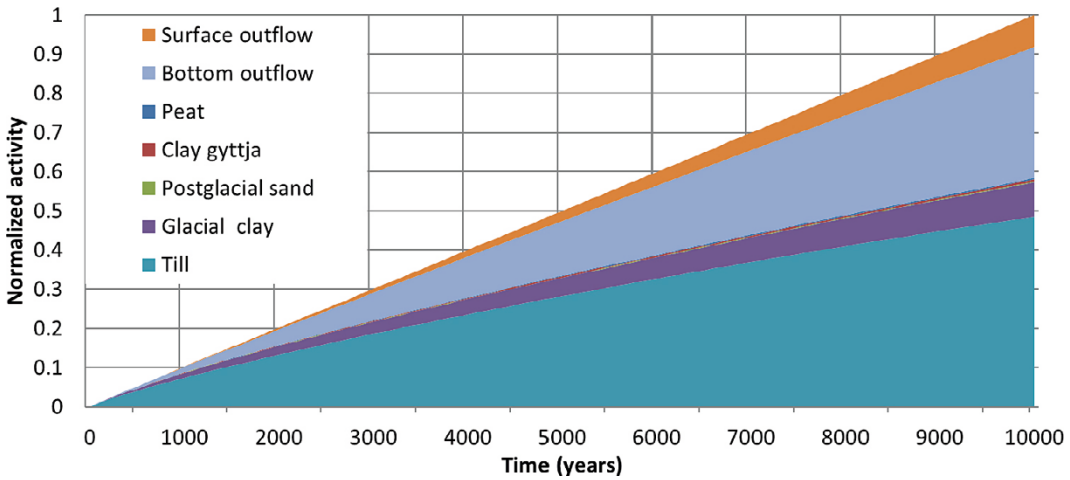

Figure 4-15. *Temporal development of the activity of ^{59}Ni in the regolith materials (till, glacial clay, postglacial sand, clay gyttja and peat) and accumulated activity that exit the model through the ground surface (surface outflow) and the bottom (bottom outflow) boundaries in basin 210. ^{59}Ni is normalized with the total amount introduced in the system at the end of the simulation.*

4.2.3 Cesium-135

After 10 000 years of simulation, the highest cesium-135 (^{135}Cs) activity concentrations are located in the till layer at the bottom of the regolith in the contact with the bedrock (Figure 4-16, Figure 4-17 and Figure B-9), with a highest aqueous activity concentration at model surface of of 2.21×10^{-5} Bq·m$^{-3}{}_{water}$ occurring in the object 210 (Figure 4-17). ^{135}Cs is characterized by a relatively high sorption affinity to the regolith materials examined in this study (Table 2-2). The highest sorbed activity concentration (3.55×10^{-2} Bq·m$^{-2}{}_{medium}$) occurs at the bottom of the till in object 210 where the repository-derived ^{135}Cs enters the regolith (Figure 4-17). High sorbed activity concentrations also occur at the bottom of the glacial clay, which K_d is over an order of magnitude higher than that of the till.

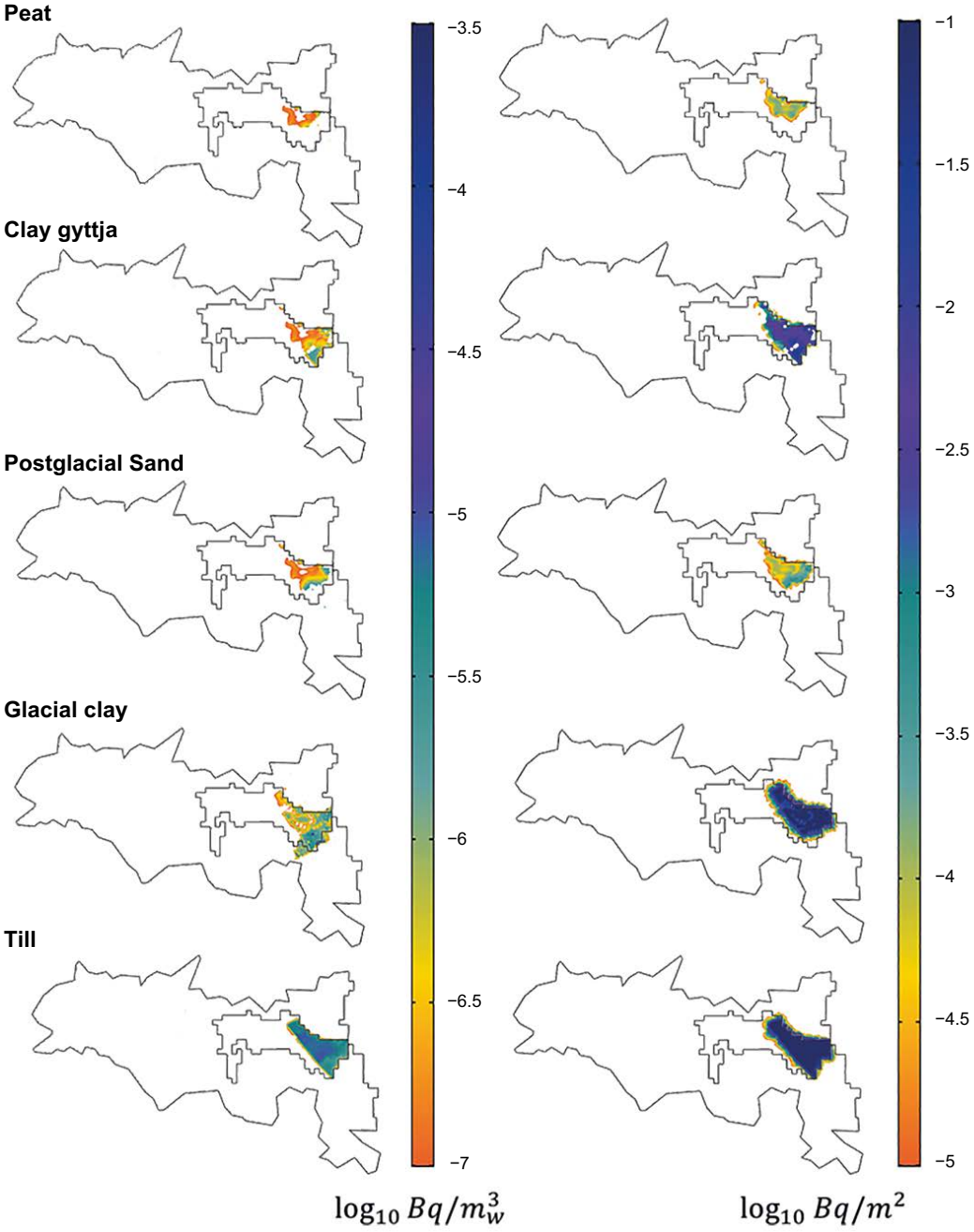

Figure 4-16. *Spatial distribution of ^{135}Cs aqueous activity concentration (Bq·m$_w^{-3}$) (left) and sorbed activity concentration per unit area (Bq·m$_m^{-2}$) (right) in the regolith materials after 10 000 years in object 206. The aqueous concentration is the average concentration of the regolith layers. Note that aqueous values below 1×10^{-7} (Bq·m$_w^{-3}$) and sorbed values below 1×10^{-5} (Bq·m$_m^{-2}$) are not plotted in the figure. Note that concentrations are displayed on a logarithmic scale.*

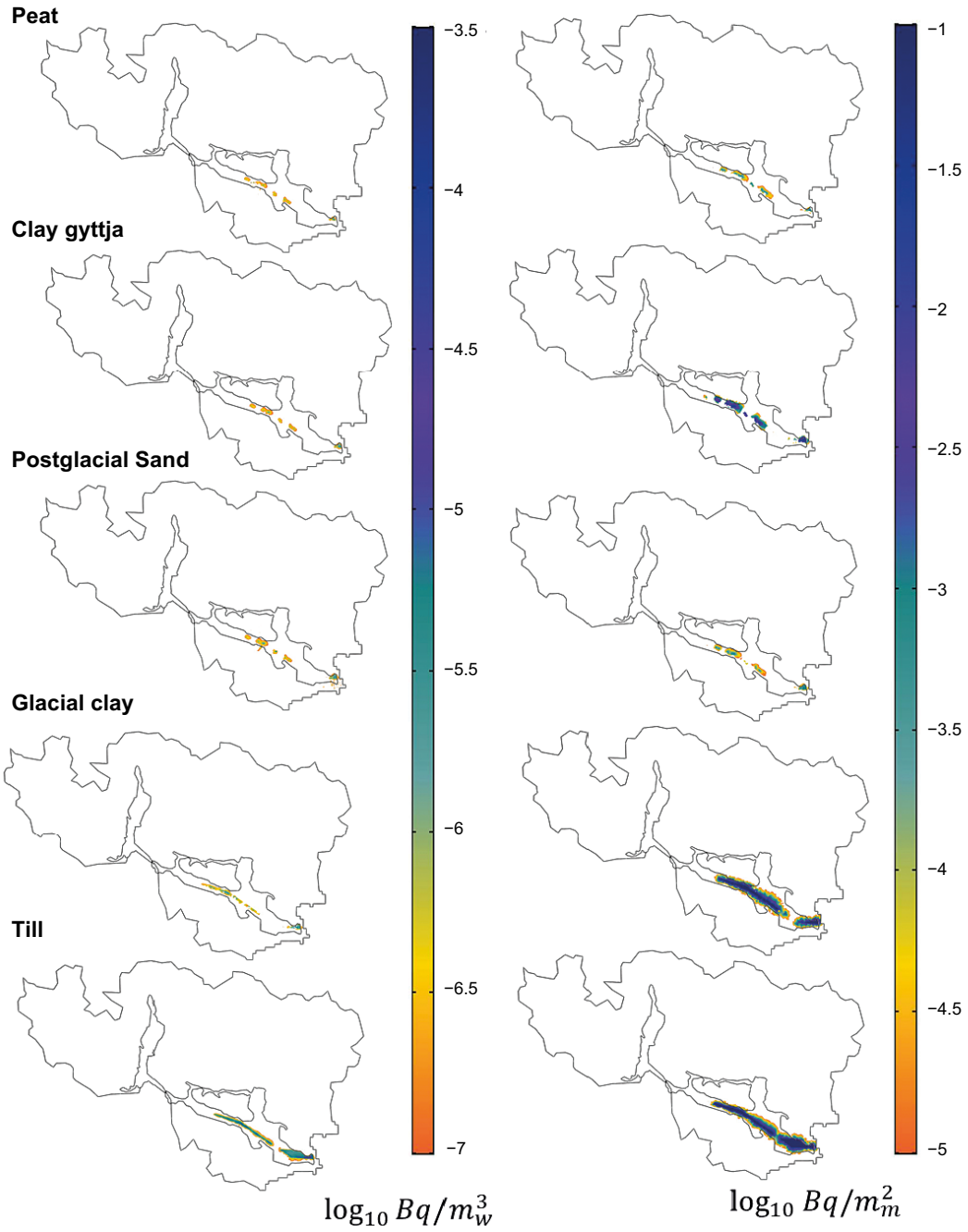

Figure 4-17. *Spatial distribution of ^{135}Cs aqueous activity concentration ($Bq \cdot m_w^{-3}$) (left) and sorbed activity concentration per unit area ($Bq \cdot m_m^{-2}$) (right) in the regolith materials after 10 000 years in object 210. The aqueous concentration is the average concentration of the regolith layers. Note that aqueous values below 1×10^{-7} ($Bq \cdot m_w^{-3}$) and sorbed values below 1×10^{-5} ($Bq \cdot m_m^{-2}$) are not plotted in the figure. Note that concentrations are displayed on a logarithmic scale.*

Most of the ^{135}Cs is retained in the till after 10 000 years: 58 % and 73 % of the total ^{135}Cs released into basins 206 and 210 respectively is retained in the till layers of each object (Figure 4-18 and Figure 4-19). More ^{135}Cs is retained in the till layer of object 210 due to the thicker till layer present here. Glacial clay retains 33 % and 17 % of the ^{135}Cs in basins 206 and 210 respectively. The amount of ^{135}Cs sorbed in the clay gyttja is 2 % and 1 % in objects 206 and 210 respectively. Only a small amount of ^{135}Cs leaves the domain through the bottom surface of the model domain after 10 000 years of simulation (6 % in basin 206 and 9 % in basin 210). Even less of the ^{135}Cs leaves the model domain through the top surface (1 % in basin 206 and < 1 % in basin 210). Results suggest that the retention capacity of the regolith materials may not be exhausted after 10 000 years (Figure B-7 and Figure B-8). The vertical section of basin 206 appears to have reached an equilibrium state in less than 1 000 years of simulation time, see Figure B-7.

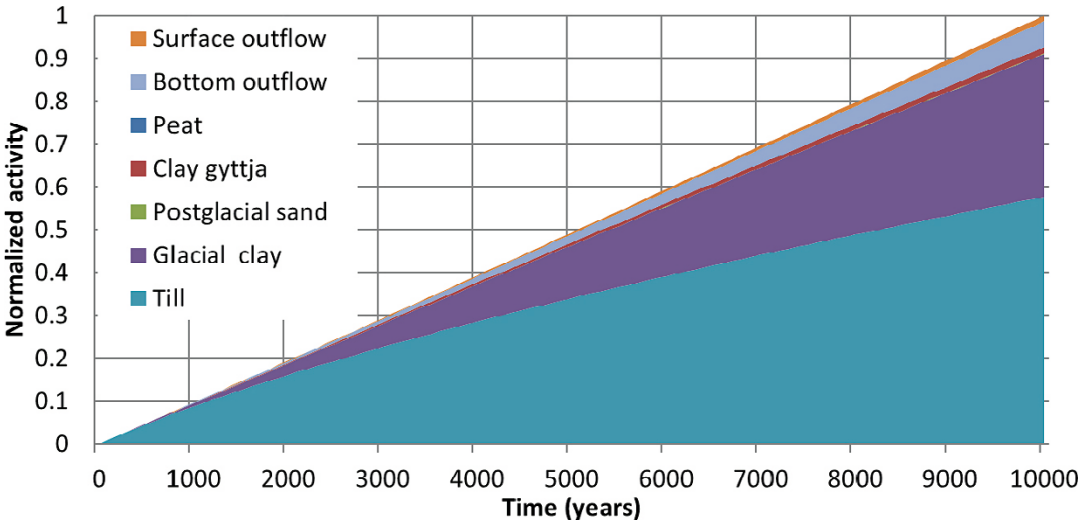

Figure 4-18. *Temporal development of the activity of ^{135}Cs in the regolith materials (till, glacial clay, postglacial sand, clay gyttja and peat) and accumulated activity that exit the model through the ground surface (surface outflow) and the bottom (bottom outflow) boundaries in basin 206. ^{135}Cs is normalized with the total amount introduced in the system at the end of the simulation.*

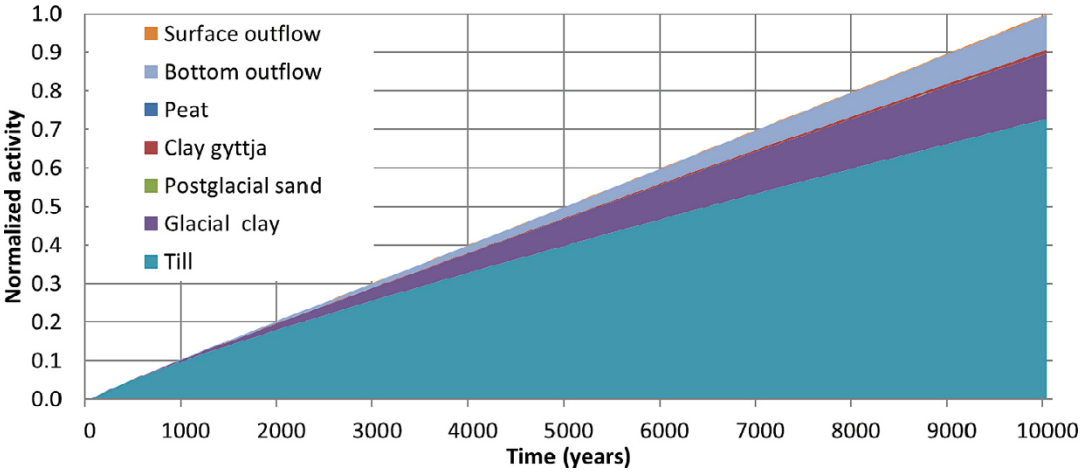

Figure 4-19. *Temporal development of the activity of ^{135}Cs in the regolith materials (till, glacial clay, postglacial sand, clay gyttja and peat) and accumulated activity that exit the model through the ground surface (surface outflow) and the bottom (bottom outflow) boundaries in basin 210. ^{135}Cs is normalized with the total amount introduced in the system at the end of the simulation.*

4.2.4 Radium-226

The decay rate of radium-226 (^{226}Ra) (1 600 years) is included in the distributed K_d model as it is on a scale relevant to the simulation time (see Section 2.6). After 10 000 years of simulation, the maximum aqueous activity concentration of ^{226}Ra at model surface is of around 1×10^{-6} Bq·m$^{-3}_{water}$. The maximum aqueous concentrations are located in the eastern part of basin 206 and in the south–eastern part of basin 210. The relatively low penetration of ^{226}Ra into the upper regolith layers is due to the high sorption affinity of ^{226}Ra and its relatively fast decay rate.

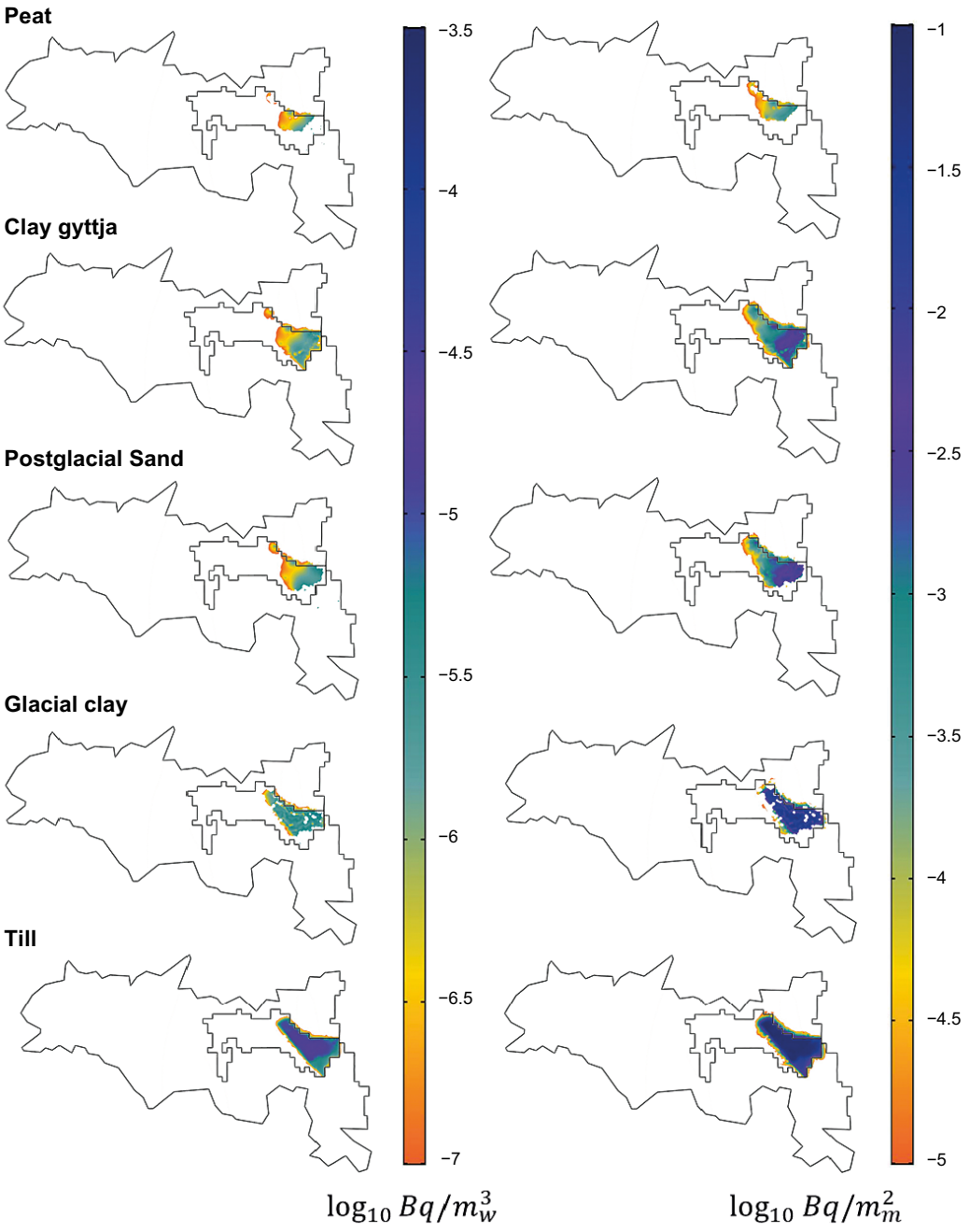

Figure 4-20. *Spatial distribution of ^{226}Ra aqueous activity concentration (Bq·m$_w^{-3}$) (left) and sorbed activity concentration per unit area (Bq·m$_m^{-2}$) (right) in the regolith materials after 10 000 years in object 206. The aqueous concentration is the average concentration of the regolith layers. Note that aqueous values below 1×10^{-7} (Bq·m$_w^{-3}$) and sorbed values below 1×10^{-5} (Bq·m$_m^{-2}$) are not plotted in the figure. Note that concentrations are displayed on a logarithmic scale.*

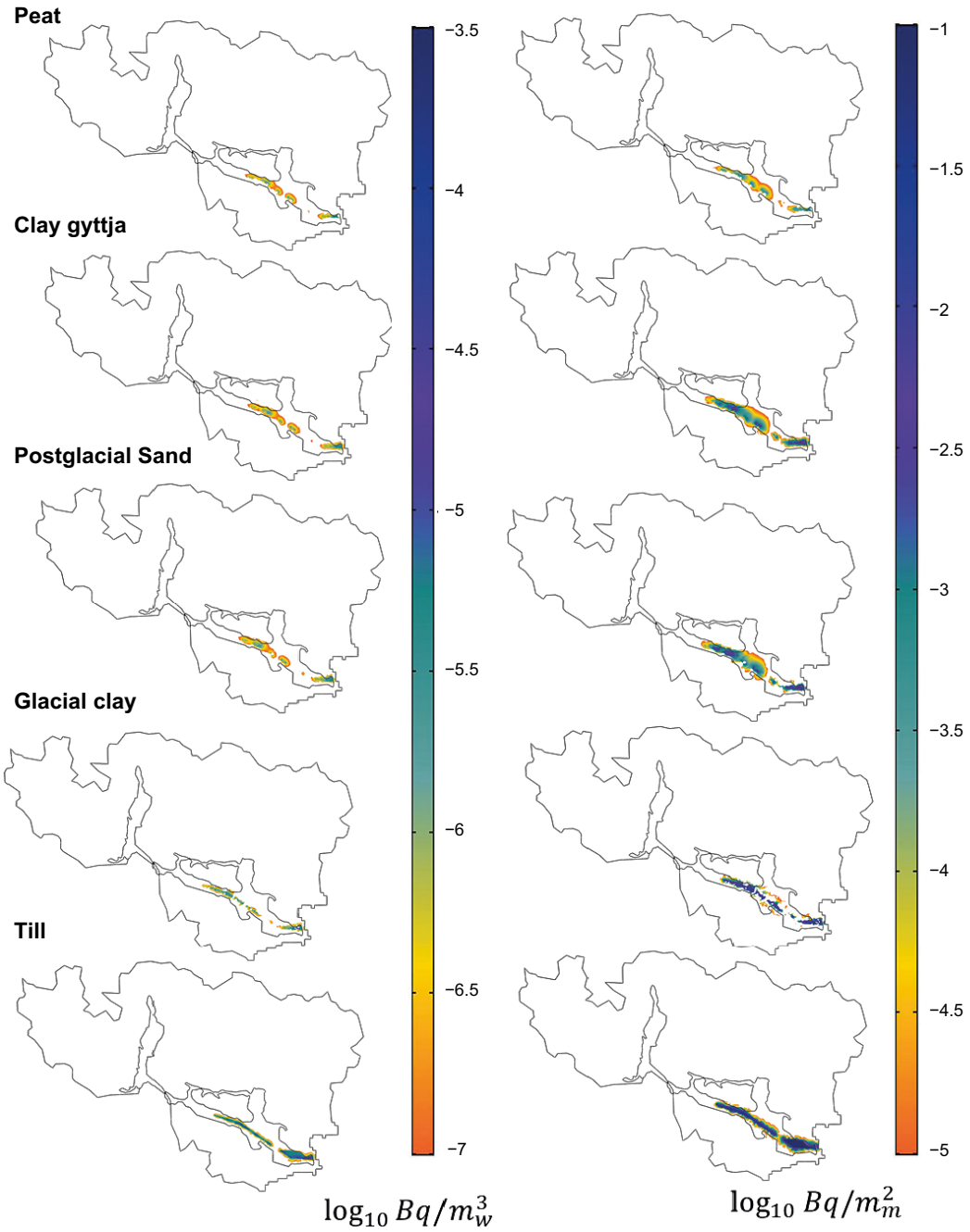

Figure 4-21. *Spatial distribution of ^{226}Ra aqueous activity concentration ($Bq \cdot m_w^{-3}$) (left) and sorbed activity concentration per unit area ($Bq \cdot m_m^{-2}$) (right) in the regolith materials after 10 000 years in object 210. The aqueous concentration is the average concentration of the regolith layers. Note that aqueous values below 1×10^{-7} ($Bq \cdot m_w^{-3}$) and sorbed values below 1×10^{-5} ($Bq \cdot m_m^{-2}$) are not plotted in the figure. Note that concentrations are displayed on a logarithmic scale.*

After 10 000 years most of the ^{226}Ra is removed from the system via radioactive decay: 62 % of the total ^{226}Ra is removed from basin 206 via radioactive decay and 53 % in basin 210. 14 % and 23 % of the activity concentration leaves the model through the bottom boundary for basins 206 and 210 respectively. 4 % and 2 % of the activity concentration leaves through the top boundary in basins 206 and 210 respectively. The retention as sorbed ^{226}Ra is of a 14 % of the ^{226}Ra and the glacial clay 5 % after 10 000 years in basin 206. The retention in basin 210 is of 19 % in the till and a 2 % in the glacial clay after the same amount of time. The retention capacity of the materials in this basin seems to be exhausted (see Figure B-10 and Figure B-11). The modelled system appears to have reached a state of chemical equilibrium between 5 000 and 10 000 years of simulation time, see Figure B-10 and Figure B-11.

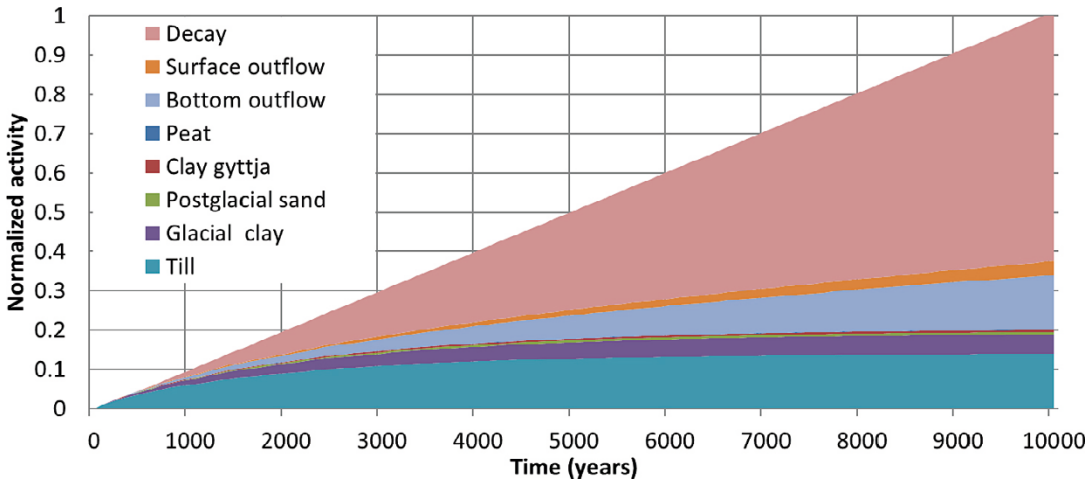

Figure 4-22. *Temporal development of the activity of the ^{226}Ra in the regolith materials (till, glacial clay, postglacial sand, clay gyttja and peat) and accumulated activity that exit the model through the ground surface (surface outflow) and the bottom (bottom outflow) boundaries in basin 206. ^{226}Ra is normalized with the total amount introduced in the system at the end of the simulation.*

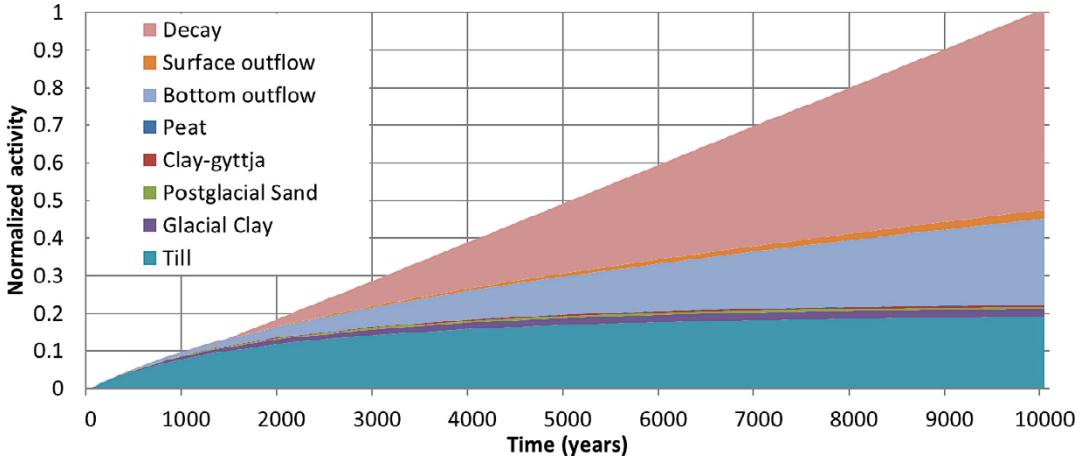

Figure 4-23. *Temporal development of the ^{226}Ra in the regolith materials (till, glacial clay, postglacial sand, clay gyttja and peat) and accumulated activity that exit the model through the ground surface (surface outflow) and the bottom (bottom outflow) boundaries in basin 210. ^{226}Ra is normalized with the total amount introduced in the system at the end of the simulation.*

4.2.5 Molybdenum-93

The decay rate of molybdenum-93 (^{93}Mo) (4×10^3 years) is included in the distributed K_d model as it is on a scale relevant to the simulation time (see Section 2.6). The modelled maximum aqueous activity concentration at the model surface of ^{93}Mo is 5.5×10^{-5} Bq·m$^{-3}_{water}$ and is estimated to occur in the arable land in the south–eastern part of basin 210 (Figure 4-25). The radioactive decay of ^{93}Mo decreases the activity reaching the surface regolith layers. Much of the ^{93}Mo is retained in the clay and till materials (Figure 4-24 and Figure 4-25). The maximum sorbed activity concentration in object 210 of 0.369 Bq·m$_m^{-2}$ takes place at the clay gyttja, which has a K_d value one order of magnitude higher than any other regolith material (Table 2-2).

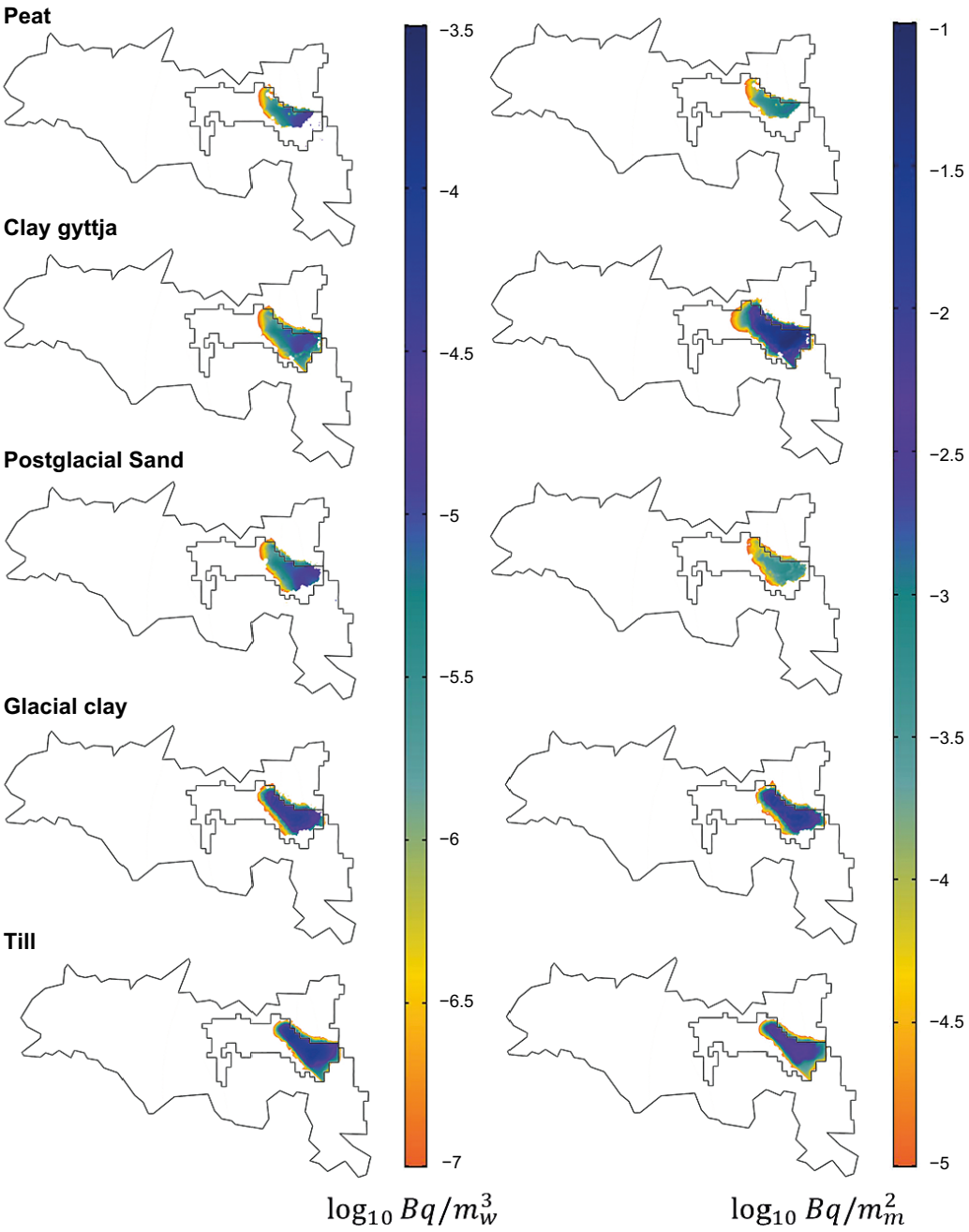

Figure 4-24. *Spatial distribution of ^{93}Mo aqueous activity concentration (Bq·m$_w^{-3}$) (left) and sorbed activity concentration per unit area (Bq·m$_m^{-2}$) (right) in the regolith materials after 10 000 years in object 206. The aqueous concentration is the average concentration of the regolith layers. Note that aqueous values below 1×10^{-7} (Bq·m$_w^{-3}$) and sorbed values below 1×10^{-5} (Bq·m$_m^{-2}$) are not plotted in the figure. Note that concentrations are displayed on a logarithmic scale.*

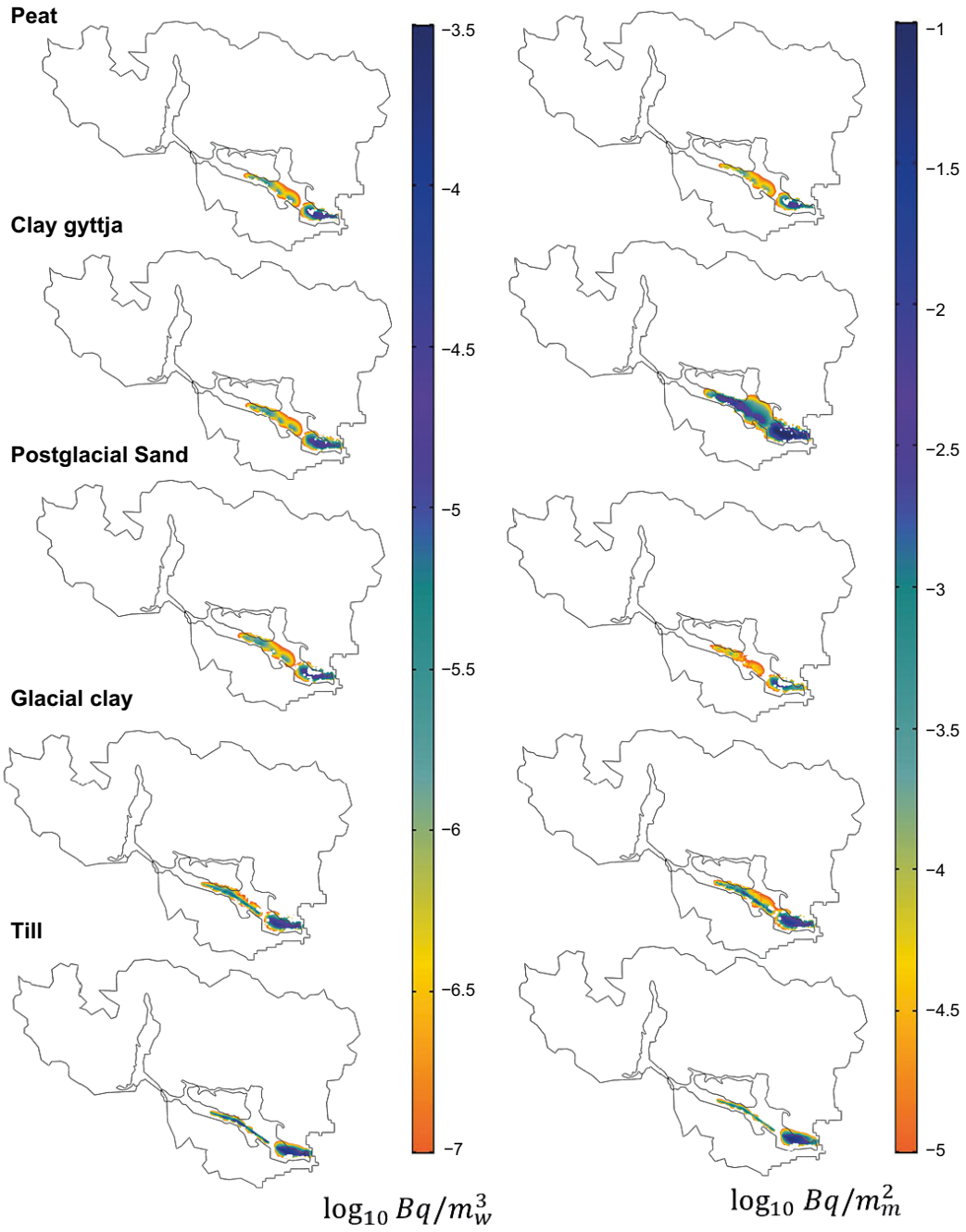

Figure 4-25. *Spatial distribution of ^{93}Mo aqueous activity concentration ($Bq \cdot m_w^{-3}$) (left) and sorbed activity concentration per unit area ($Bq \cdot m_m^{-2}$) (right) in the regolith materials after 10 000 years in object 210. The aqueous concentration is the average concentration of the regolith layers. Note that aqueous values below 1×10^{-7} ($Bq \cdot m_w^{-3}$) and sorbed values below 1×10^{-5} ($Bq \cdot m_m^{-2}$) are not plotted in the figure. Note that concentrations are displayed on a logarithmic scale.*

The retention of ^{93}Mo is relatively low after 10 000 years with only 10 % being retained in basin 206 and 16 % in basin 210 (Figure 4-26 and Figure 4-27). After 5 000 years the sorption capacity of the regolith is depleted (see Figure B-13 and Figure B-14). The amount of ^{93}Mo that has decayed after 10 000 years is 13 % in basin 206 and 16 % in basin 210. Most of the ^{93}Mo leaves the system through the model boundaries with the majority leaving through the bottom boundary (57 % in basin 206 and 48 % in basin 210). The modelled system appears to have reached state of chemical equilibrium before 5 000 years of simulation time, see Figure B-13 and Figure B-14.

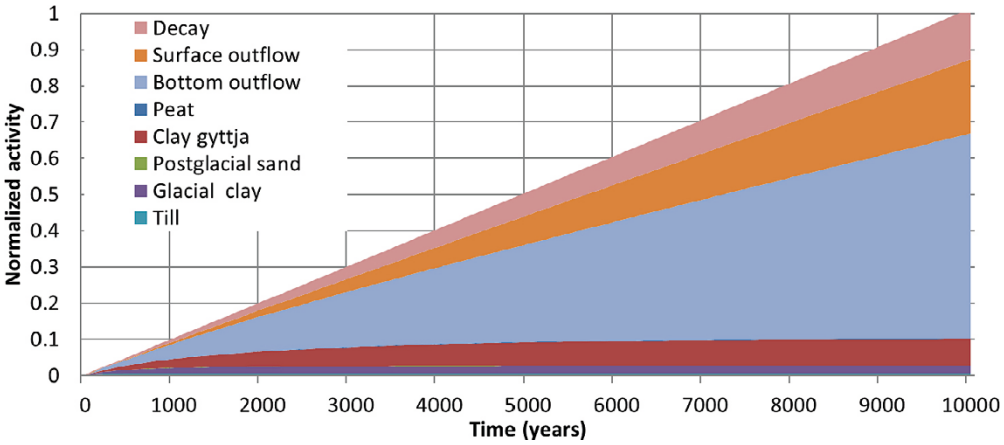

Figure 4-26. *Temporal development of the activity of the ^{93}Mo in the regolith materials (till, glacial clay, postglacial sand, clay gyttja and peat) and accumulated activity that exit the model through the ground surface (surface outflow) and the bottom (bottom outflow) boundaries in basin 206. ^{93}Mo is normalized with the total amount introduced in the system at the end of the simulation.*

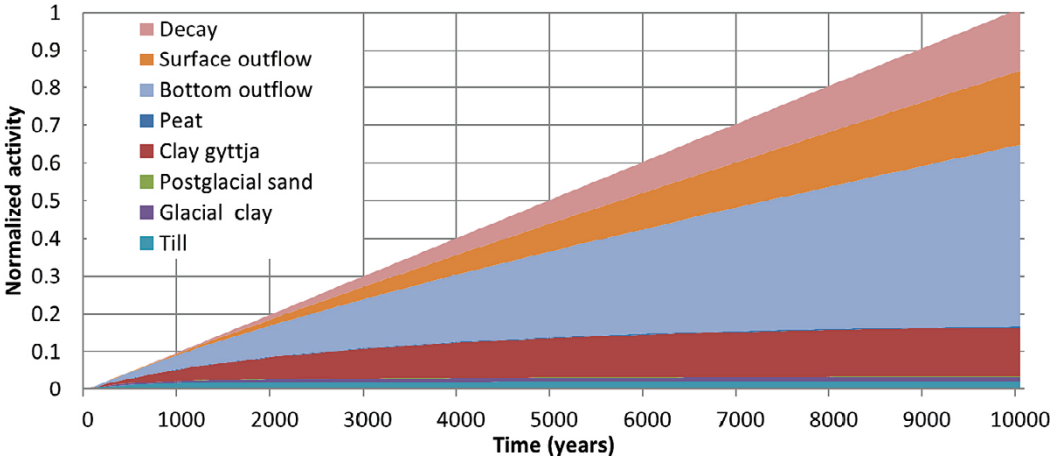

Figure 4-27. *Temporal development of the activity of the ^{93}Mo in the regolith materials (till, glacial clay, postglacial sand, clay gyttja and peat) and accumulated activity that exit the model through the ground surface (surface outflow) and the bottom (bottom outflow) boundaries in basin 210. ^{93}Mo is normalized with the total amount introduced in the system at the end of the simulation.*

4.3 Summary and conclusions from the K_d model with radioactive decay

In basin 206, the till layer presents the highest aqueous activity concentration for all the radionuclides (Figure 4-28). This is due to its proximity to the source of radionuclides and the mixing in the upper layers promoted by the postglacial sand that increases the dilution in these layers. The layers below the postglacial sand (till and glacial clay) have little water mixing and dilution.

Retention characteristics of the radionuclides are compared to those of ^{36}Cl due to the relatively low sorption affinity of ^{36}Cl. In general, aqueous concentrations of all other radionuclides are all smaller than those of ^{36}Cl. Likewise, the sorbed concentrations of all other radionuclides are larger than that of ^{36}Cl. ^{135}Cs and ^{226}Ra have the lowest modelled aqueous concentrations in all modelled regolith layers (Figure 4-28 and Figure 4-29). In object 206, ^{135}Cs and ^{226}Ra have the highest sorbed concentrations in the till and glacial clay layers, ^{226}Ra and ^{59}Ni in the post glacial sand and ^{93}Mo and ^{59}Ni in the gyttja and peat layers (Figure 4-28). For object 210, ^{93}Mo and ^{59}Ni have the highest sorbed concentrations throughout most of the regolith profile with the exception of ^{135}Cs being dominant in the lowest parts of the till (Figure 4-29).

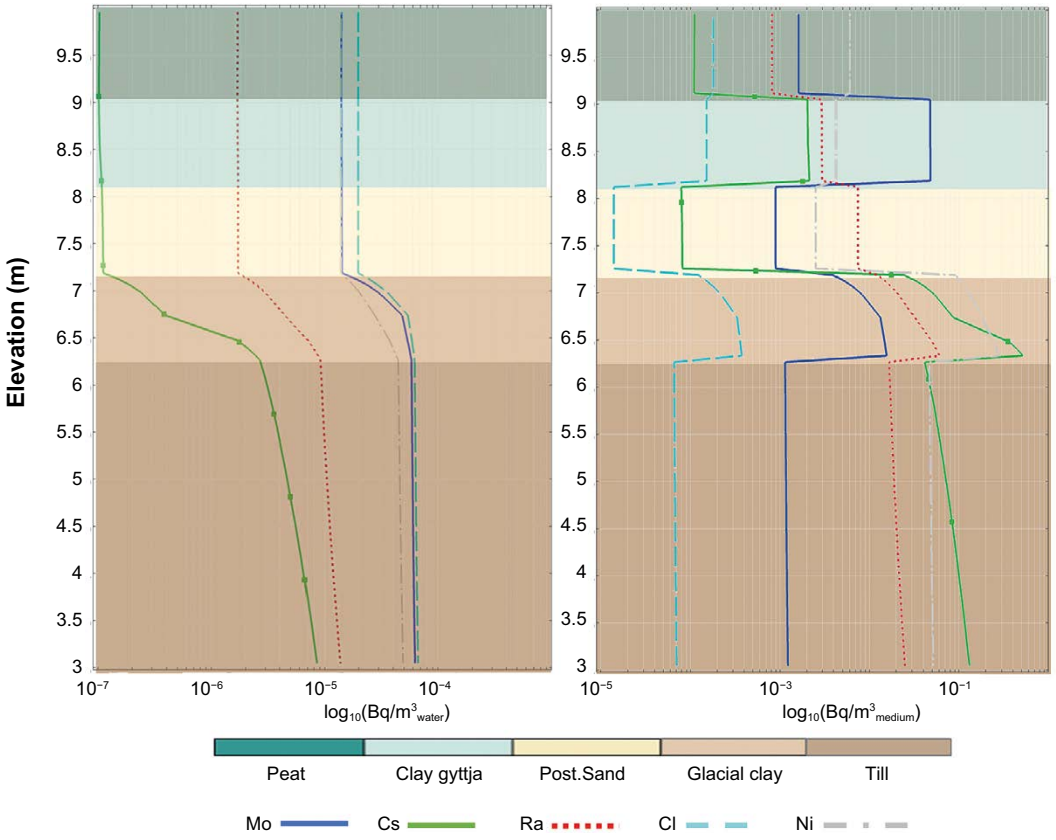

Figure 4-28. *Aqueous (left) and sorbed (right) activity concentrations of radionuclides in the vertical profile located at point 1 in basin 206 (see Figure 3-2) after 10 000 years of simulation.*

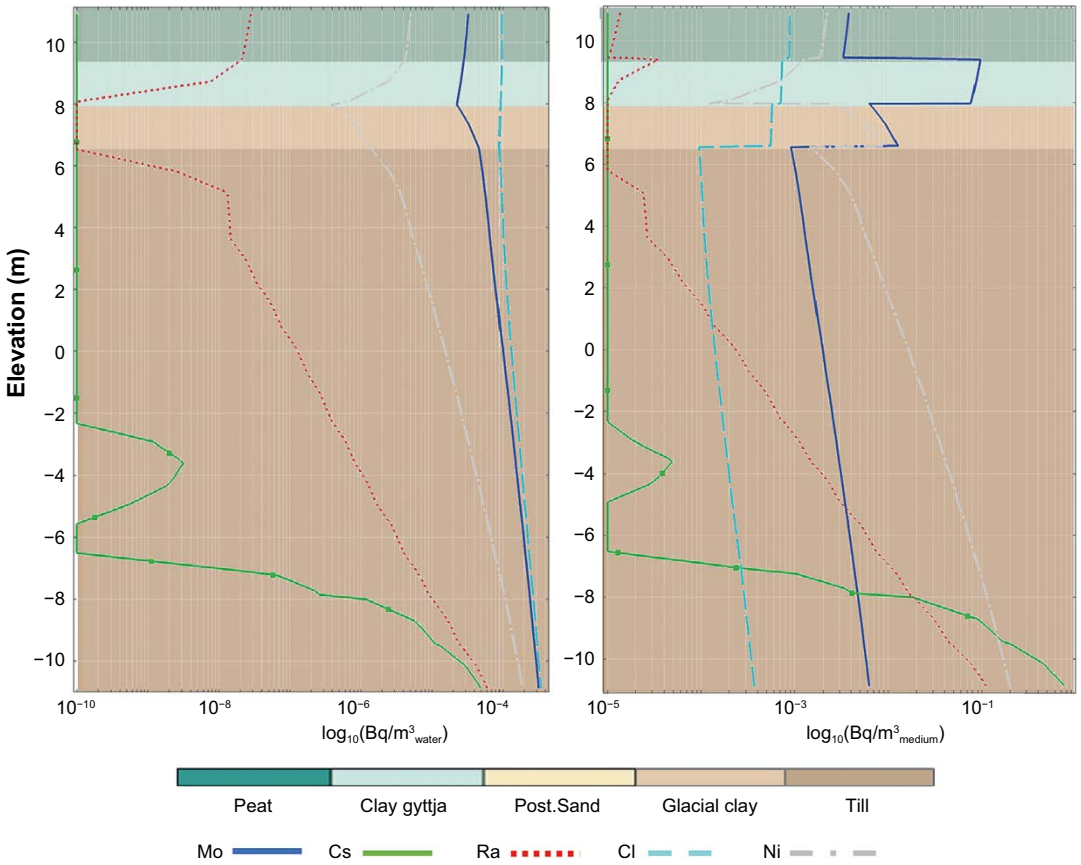

Figure 4-29. *Aqueous (left) and sorbed (right) activity concentrations the radionuclides in the vertical profile located at point 2 in basin 210 (see Figure 3-2) after 10 000 years of simulation.*

The fates of the radionuclides in the basins after 10 000 years of simulation are summarized in Figure 4-30 and Figure 4-31. According to the K_d model with radioactive decay, ^{135}Cs has the highest retention in the regolith after 10 000 years and ^{93}Mo is the least retained (excluding ^{36}Cl). In general, radionuclide retention patters are similar for basins 206 and 210, but there are some differences. Radionuclides with a relatively high sorption affinity (^{135}Cs) or decay rate (^{226}Ra) are more uniformly distributed in basin 206 than in basin 210. In basin 210, most of the ^{135}Cs is retained in the till due to its relatively large thickness resulting in decreased activity concentrations in the upper layers of the regolith. The percentages of ^{226}Ra and ^{93}Mo removed via radioactive decay are higher in basin 210 than in 206, indicating that radionuclides remain longer in the regolith of this basin. Outflow through the model's bottom surface is generally higher in basin 210 than in 206 with the exception of ^{93}Mo.

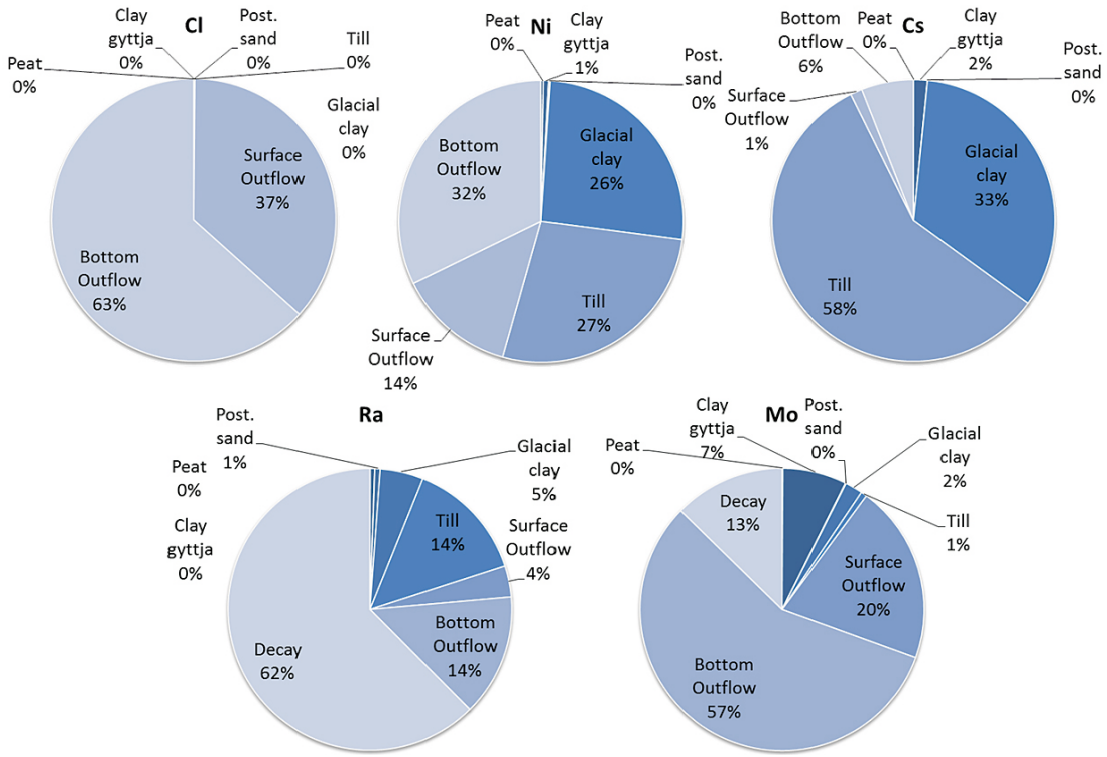

Figure 4-30. *Distribution of the activity of the radionuclides in the regolith materials (till, glacial clay, postglacial sand, clay gyttja and peat) and accumulated activity that exit the model through the ground surface (surface outflow) and the bottom (bottom outflow) at 10 000 years for basin 206.*

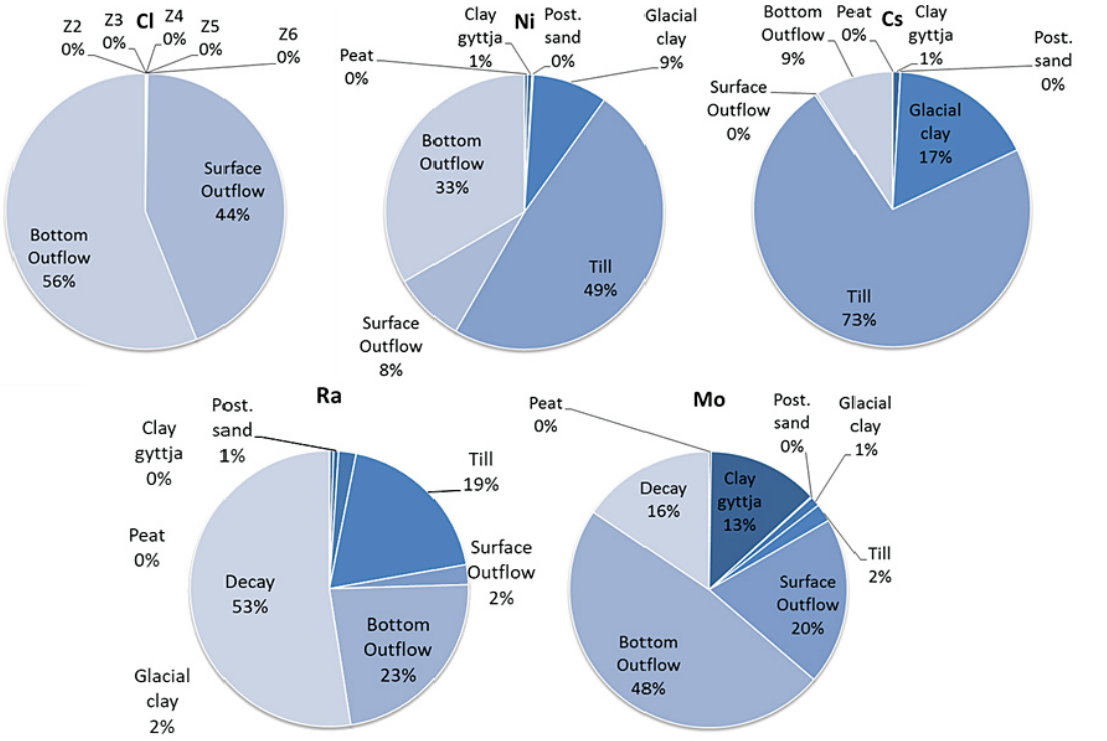

Figure 4-31. *Distribution of the activity of the radionuclides in the regolith materials (till, glacial clay, postglacial sand, clay gyttja and peat) and accumulated activity that exit the model through the ground surface (surface outflow) and the bottom (bottom outflow) at 10 000 years for basin 210.*

5 Description of the distributed reactive model

The retention processes affecting radionuclides Ni, Ra, Sr and Cs is implemented in a 3D reactive transport model. Unsaturated groundwater flow, solute transport, sorption and solid solution precipitation are considered in this model. Reactive transport models are complex and highly computational demanding. It is therefore applied to a smaller area of the model area used in the K_d modelling approach. The radionuclides Cl and Mo are not examined in the reactive transport model as, currently, there is no conceptual model of the reactive transport of these elements which adequately accounts for the role of organic matter. The radionuclide Sr is added to the study due to there being a well-developed conceptual model available for the radionuclide.

The concentrations of repository-derived radionuclides entering the model domain are calculated based on the solubility limits at the spent nuclear fuel near field (Duro et al. 2006, Sena et al. 2008) as specific SFL values are not available. The migration of radionuclides from the near-field towards the bedrock-regolith interface is considered instantaneous (i.e., no decay is considered) and without radionuclide retention. These assumptions led to higher radionuclides concentrations than expected. Therefore, inflow concentrations are conservative and model results should be seen as a test for regolith retention capacity.

5.1 Model geometry and spatial discretization

The distributed reactive model of the retention processes in the regolith is implemented in a smaller section basin 206. This section is located in one of the arable areas that receive groundwater discharge within object 206 (Figure 5-1). The mean and maximum regolith thicknesses in the domain are 6 and 12 m, respectively.

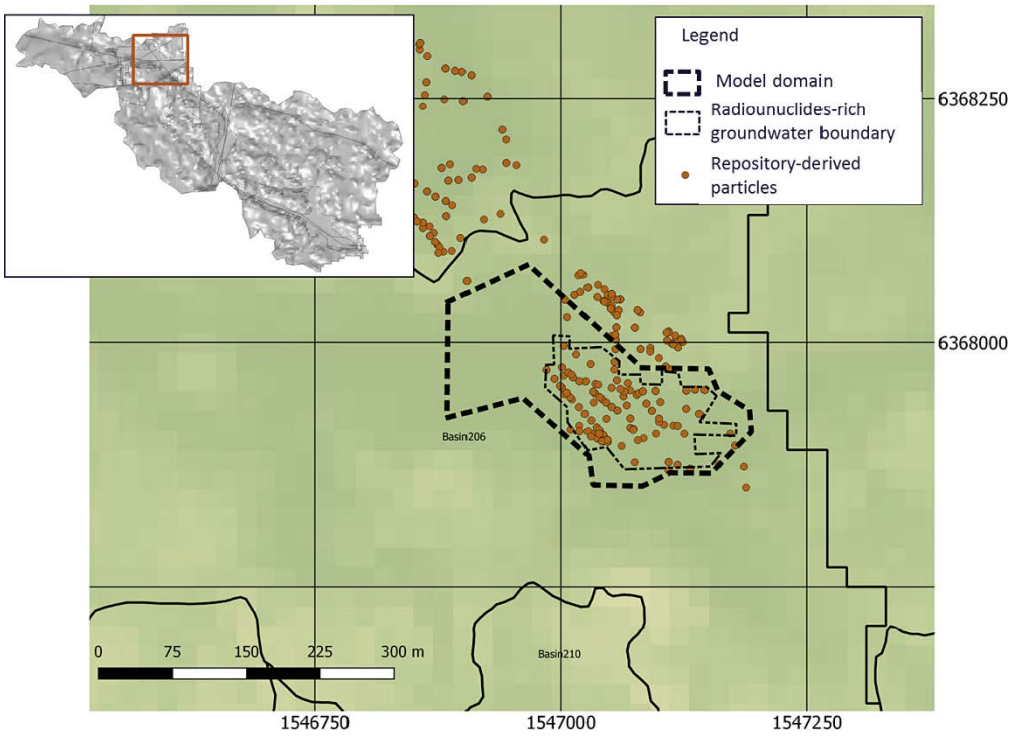

Figure 5-1. *Location of the distributed reactive model, the area where radionuclides-rich groundwater enters the model at the regolith/bedrock interface and exit points of repository-derived particles from SFL according to the ConnectFlow model (Joyce et al. 2019).*

The numerical model is implemented using a mesh with 38 790 prism elements (Figure 5-2). The regolith is represented with 21 vertical layers. The total simulated time is 1 000 years with a time step varying from 1 day (early in the simulation) up to 10 years.

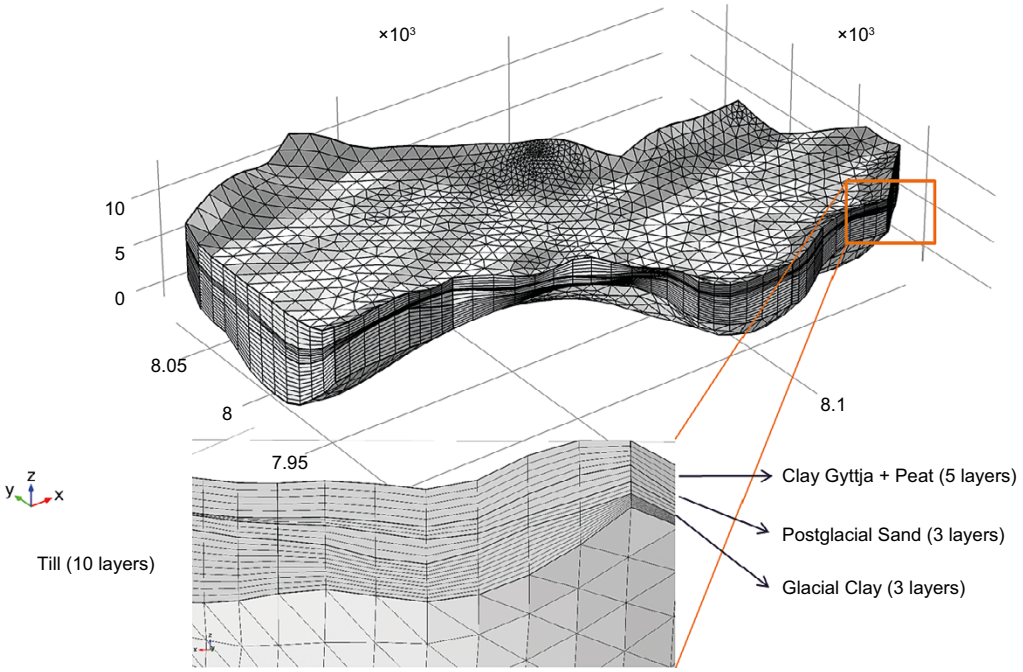

Figure 5-2. *Finite element mesh of triangular prisms showing the vertical discretization of the regolith materials. The vertical scale is exaggerated 5 times. North is aligned with the y axis.*

5.2 Regolith materials

A 3D representation of the conceptual model boundaries and delineation of the regolith layers is presented in Figure 5-3. The upper and lower boundaries of the model (i.e. the ground surface and the top of the bedrock) as well as the delineation of the regolith layers of the distributed reactive model are those described in Section 2.2. There is little peat within the model area. In order to avoid difficulties in the solution of the numerical method, the clay gyttja and peat layers are combined into one layer. In some areas of the model domain there is no glacial clay or postglacial sand. In these areas the till and the clay gyttja/peat layers are in direct connection with one another.

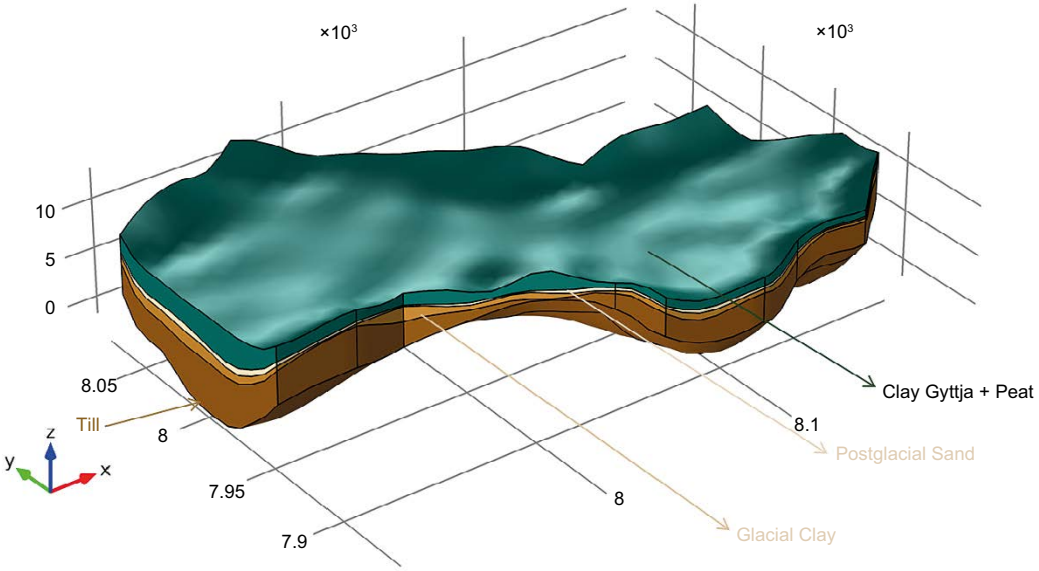

Figure 5-3. *3D representation of the model domain and regolith materials; all dimensions in units of meters. North is aligned with the y axis.*

5.3 Model equations

5.3.1 Groundwater flow

The groundwater flow model of the discharge area is updated to recreate a flow field consistent with the geometrical description of the regolith material properties. This groundwater flow model is based on the distributed K_d model and has the same conceptualization of the recharge and discharge fluxes through the ground surface and the bedrock/regolith interface. A steady groundwater flow through a variably saturated porous medium is solved with the Richards' equation in COMSOL (Equation (3-1)). Section 3.3 explains all the details of the model equations.

The hydraulic properties (Table 5-1) of the till, glacial clay, and postglacial sand materials are those of the regional scale model used for the K_d modelling approach see Table 3-1 and Table 3-2).

Table 5-1. Hydraulic and transport properties of the regolith materials for the distributed reactive model. h refers to the mesh element size.

Materials	K (m/s)	Effective Porosity	$\alpha_{1,2}$ (m)	α_3 (m)	D_L (m^2/s)
Clay gyttja-Peat	1.0×10^{-7}	0.25	h/5	h/25	1.0×10^{-9}
Postglacial sand	1.0×0^{-3}	0.25	h/5	h/25	1.0×10^{-9}
Glacial clay	1.0×0^{-8}	0.25	h/5	h/25	1.0×10^{-9}
Till	4.5×10^{-5}	0.05	h/5	h/25	1.0×10^{-9}

5.3.2 Solute transport

Solute transport is solved disregarding radioactive decay. The equation solved can be written as:

$$\theta_s S_w \frac{\partial c_i}{\partial t} + \boldsymbol{u}\,\nabla(c_i) = \nabla[(\boldsymbol{D_D} + \theta_s \boldsymbol{D_L})\nabla c_i] \qquad \text{Equation (5-1)}$$

where c_i is the concentration of species i ($kg \cdot m^{-3}$), $\boldsymbol{u}$ is the Darcy's velocity field ($m \cdot s^{-1}$), θ_s is the saturated effective porosity of the regolith material (-), S_w is the water saturation (-), $\boldsymbol{D_D}$ is the dispersion tensor ($m^2 \cdot s^{-1}$) and $\boldsymbol{D_L}$ is the diffusion coefficient ($m^2 \cdot s^{-1}$). The Darcy velocity field is evaluated in the groundwater flow following the Equation (3-7). The dispersion tensor depends on dispersivities (m), longitudinal (α_1) and transversal (α_2 and α_3) as in Equation (3-11). The effective porosity of the gyttja-peat layer is similar to that of the peat and equal to the glacial clay and postglacial sand to favor the model convergence. The diffusion coefficient ($\boldsymbol{D_L}$) and the longitudinal (α_1) and transversal ($\alpha_{2,3}$) dispersivities are assumed equal for all materials and solutes (Table 5-1).

5.3.3 Reactive transport

The interface COMSOL-PhreeqC (iCP) (Nardi et al. 2014) is used for the numerical simulation of the reactive transport. iCP is an interface that couples COMSOL Multiphysics with the geochemical simulator PHREEQC (Parkhurst and Appelo 2013). In iCP, the reactive transport equations are solved with a sequential non-iterative approach (SNIA) (Yeh and Tripathi 1989, Saaltink et al. 2000, 2001). The conservative solute transport is computed in the first step with COMSOL while geochemistry is solved in a second step with PhreeqC.

The geochemical reactions modelled in the reactive transport model are described in Section 2.8 and summarized in Table 5-2. The implementation of 3D reactive transport models in a realistic geometry it is complex. As a first step towards the implementation of the reactive transport 1D models with idealized geometry are developed (Appendix C). The results of the 1D models helps to better interpret the results of the distributed reactive transport model and the interactions between different water types.

Table 5-2. Chemical reactions, initial water and mineralogical composition types for the different regolith materials considered in this study. A full explanation of the water and mineralogical composition types is presented in Section 2.8.

Materials	Initial water	Minerals in equilibrium	Exchanger	Surface complexation
Clay gyttja-peat	Clay water	Clay	Illite	Illite
Postglacial sand	Clay water	Clay	-	-
Glacial clay	Clay water	Clay	Illite	Illite
Till	Till water	Till	Illite	Illite/Ferrihydrite

5.4 Initial and boundary conditions

5.4.1 Groundwater flow

The boundary and initial conditions of groundwater flow are derived from the regional groundwater model used for the distributed K_d model (Section 3.4); the bottom surface flux come from a previous modelling exercise (Johansson and Sassner 2019), a Cauchy boundary condition is imposed for the model's top boundary (i.e. the ground surface) and the Darcy velocity and the pressure fields from the regional hydrological model are used to define the groundwater fluxes entering through the lateral boundaries as well as the initial groundwater pressure heads (see Section 4.1).

5.4.2 Solute transport

Initial conditions

The initial state of the water and mineralogical composition for the clay gyttja/peat, postglacial sand, glacial clay and the till is defined in Table 5-2. The glacial clay, postglacial sand and clay gyttja-peat domains are assumed to have the initial water composition of a clay system and the till is assumed to have the initial water composition of a till chemical system (see Section 2.8 and Table 2-4).

The initial mineral composition considered in the reactive model are assumed to be in equilibrium with the porewater in its initial state, see Section 2.8 and Table 2-3. Equilibrium with the initial porewater is also assumed for the initial composition of the exchanger and surface positions of the different materials, see Table 5-3, Table 5-4 and Table 5-5.

Table 5-3. Initial compositions of the illite interlayer for the till and the clay chemical systems.

	Till	Clay
Species	**mol·l_{water}^{-1}**	
NaX	3.93×10^{-3}	8.91×10^{-4}
KX	4.94×10^{-3}	2.21×10^{-3}
CsX	8.31×10^{-9}	6.06×10^{-9}
SrX_2	3.03×10^{-4}	1.60×10^{-4}
CaX_2	4.06×10^{-1}	2.78×10^{-1}
MgX_2	3.27×10^{-2}	1.91×10^{-2}
NiX_2	2.24×10^{-6}	4.65×10^{-7}
NaX^{II}	1.64×10^{-2}	5.83×10^{-3}
KX^{II}	2.06×10^{-1}	1.44×10^{-1}
CsX^{II}	3.46×10^{-6}	3.96×10^{-6}
NaX^{FES}	1.04×10^{-4}	3.60×10^{-5}
KX^{FES}	2.62×10^{-3}	1.78×10^{-3}
CsX^{FES}	5.54×10^{-5}	6.15×10^{-5}

Table 5-4. Initial compositions of the ferrihydrite surface for the till chemical system.

Species	mol·l_{water}^{-1}
≡$HFO^{s}OH$	7.48×10^{-5}
≡$HFO^{s}OH^{2+}$	9.26×10^{-6}
≡$HFO^{s}O^{-}$	1.45×10^{-6}
≡$(HFO^{s}O)_2UO_2$	9.64×10^{-7}
≡$(HFO^{s}O)_2UO_2CO_3^{2-}$	1.36×10^{-5}
≡$HFO^{s}CO_3H$	2.82×10^{-5}
≡$HFO^{s}CO_3^{-}$	7.53×10^{-6}
≡$HFO^{s}ONi^{+}$	2.96×10^{-5}
≡$HFO^{w}OH$	5.39×10^{-2}
≡$HFO^{w}OH_2^{+}$	6.67×10^{-3}
≡$HFO^{w}O^{-}$	1.04×10^{-3}
≡$(HFO^{w}O)_2UO_2$	1.35×10^{-7}
≡$(HFO^{w}O)_2UO_2CO_3^{2-}$	7.97×10^{-7}
≡$HFO^{w}CO_3H$	2.03×10^{-2}
≡$HFO^{w}CO_3^{-}$	5.43×10^{-3}
≡$HFO^{w}ONi^{+}$	2.88×10^{-5}

Table 5-5. Initial compositions of the illite surface for the till and the clay chemical systems.

	Till	Clay
Species	mol·l_{water}^{-1}	
≡$SO^{s}OH$	4.72×10^{-5}	4.01×10^{-5}
≡$SO^{s}OH^{2+}$	1.33×10^{-8}	7.13×10^{-9}
≡$SO^{s}O^{-}$	1.05×10^{-3}	1.42×10^{-3}
≡$SO^{s}OUO_2^{+}$	2.54×10^{-9}	5.46×10^{-11}
≡$SO^{s}OUO_2OH$	5.68×10^{-8}	1.94×10^{-9}
≡$SO^{s}OUO_2(OH)_2^{-}$	4.01×10^{-7}	2.17×10^{-8}
≡$SO^{s}OUO_2(OH)_3^{2-}$	8.94×10^{-7}	7.71×10^{-8}
≡$SO^{s}UO_2CO_3^{-}$	6.01×10^{-7}	4.10×10^{-9}
≡$SO^{s}UO_2(CO_3)_2^{3-}$	4.49×10^{-6}	9.74×10^{-9}
≡$SO^{s}OU^{3+}$	4.83×10^{-24}	2.15×10^{-19}
≡$SO^{s}OUOH^{2+}$	1.36×10^{-16}	9.58×10^{-12}
≡$SO^{s}OU(OH)_2^{+}$	9.57×10^{-19}	1.08×10^{-13}
≡$SO^{s}OU(OH)_3$	1.35×10^{-17}	2.41×10^{-12}
≡$SO^{s}OU(OH)_4^{-}$	1.51×10^{-16}	4.28×10^{-11}
≡$SO^{s}ONi^{+}$	2.95×10^{-5}	3.81×10^{-5}
≡$SO^{s}ONiOH$	1.31×10^{-6}	2.70×10^{-6}
≡$SO^{s}ONi(OH)_2^{-}$	3.69×10^{-8}	1.21×10^{-7}
≡$SO^{s}OFe^{+}$	8.36×10^{-3}	5.58×10^{-3}
≡$SO^{s}OFeOH$	3.72×10^{-4}	3.95×10^{-4}
≡$SO^{s}OFe(OH)_2^{-}$	1.05×10^{-5}	1.77×10^{-5}
≡$SO^{wa}OH$	8.27×10^{-3}	4.06×10^{-3}
≡$SO^{wa}OH_2^{+}$	2.34×10^{-6}	7.22×10^{-7}
≡$SO^{wa}O^{-}$	1.85×10^{-1}	1.44×10^{-1}
≡$SO^{wa}OFe^{+}$	4.63×10^{-3}	1.79×10^{-3}
≡$SO^{wa}OUO_2^{+}$	1.41×10^{-9}	1.75×10^{-11}
≡$SO^{wa}OUO_2OH$	1.98×10^{-7}	3.91×10^{-9}
≡$SO^{wa}UO_2CO_3^{-}$	3.33×10^{-5}	1.31×10^{-7}
≡$SO^{wa}ONi^{+}$	1.64×10^{-5}	1.22×10^{-5}
≡$SO^{wb}OH$	1.99×10^{-2}	2.26×10^{-2}
≡$SO^{wb}OH_2^{+}$	1.78×10^{-1}	1.27×10^{-1}
≡$SO^{wb}O^{-}$	2.23×10^{-5}	4.03×10^{-5}

Boundary conditions

Two types of boundary conditions are applied for the transport equation: open boundary condition where mass may both enter and leave the system, and outflow boundary condition where mass may only leave the system The open boundary condition applies to all aqueous species and is defined using Equation (5-2):

$$\begin{aligned} -\mathbf{n}\cdot(\boldsymbol{D_D}+\theta_s\tau^{-1}\boldsymbol{D_L})\nabla c_i = 0 \quad & if \quad \mathbf{n}\cdot\mathbf{u}\geq 0 \\ c_i = c_{\mathrm{ext,i}} \quad & if \quad \mathbf{n}\cdot\mathbf{u}<0 \end{aligned} \qquad \text{Equation (5-2)}$$

Where c_{ext} is a prescribed pore-water concentration at the model boundaries. This boundary condition switches between a prescribed concentration (c_{ext}) where water enters the model domain and outflow boundary condition (Neumann type) when water leaves the model domain. The concentration of the water leaving the model domain is calculated by the model.

The lateral boundaries of the till and glacial clay layers have an outflow boundary condition (Figure 5-4). All the rest boundaries of the model are open boundary conditions. The composition of the prescribed pore-water concentration (c_{ext}) of the open boundary conditions depends on the location and the regolith material in contact with the boundary condition (Figure 5-4). Three types of prescribed pore-water concentration are used. The composition of these waters is described in Section 2.8.2 (Table 2-4):

- *Deep groundwater* which is assumed to be free of radionuclides. This water enters the model domain through part of the bottom boundary.
- *Radionuclide-rich deep groundwater* which has the same chemical composition of the *deep groundwater* but with the addition of repository-derived radionuclide particles originating from the hypothetical SFL repository. The radionuclide particles reach the bedrock/regolith interface according to the ConnectFlow model (Joyce et al. 2019) and enters the model domain through part of the bottom boundary as shown in Figure 5-1. The mass rate of radionuclides entering the domain at this location is 1.78×10^{-7}, 4.16×10^{-13}, 8.78×10^{-13} and 1.04×10^{-14} mol·s for RDSr, RDCs, RDNi and Ra respectively.
- *Clay water* which is pore-water assumed to be in equilibrium with clay minerals . This water enters the model domain through the top boundary and at the lateral boundaries of the postglacial sand and clay gyttja-peat layers. It is assumed that rainwater entering the model through the top boundary of the model is instantaneously equilibrated with the pore-water in the regolith thus ignoring any reactions in the uppermost part of the regolith as a result of infiltrating rainwater. This is a reasonable assumption considering the time frame of the model and considering that the reactions in the uppermost part of the regolith are not relevant when modelling the fate and transport of radionuclides in these layers.

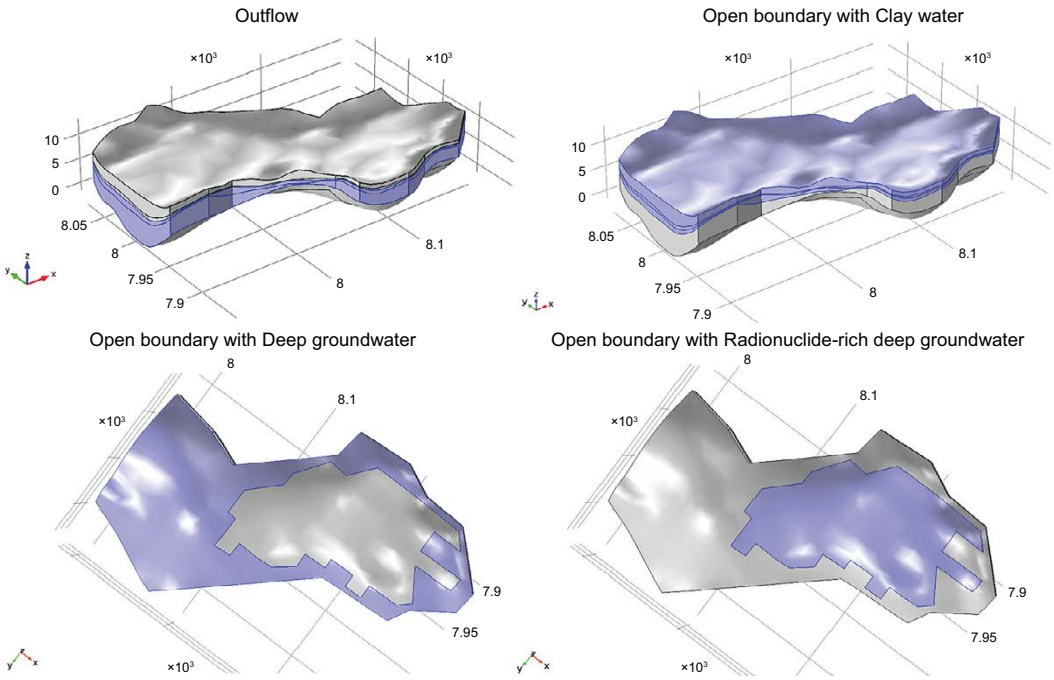

Figure 5-4. *Location and type of the boundary conditions and their respective boundary water (c_{ext}) applied to the solute transport physics in the distributed reactive model. North is aligned with the positive y axis. The bottom two figures show the bottom boundary as being viewed from below the domain looking up.*

6 Results of the distributed reactive model

6.1 Groundwater flow

Most of the ground surface of the model has water discharge, with small areas of recharge, as depicted in red in Figure 6-1.

The hydraulic head at the ground surface is larger at the lateral boundaries of the model than in the middle of the domain (Figure 6-2) suggesting that the general direction of the groundwater flows is towards the center of the domain. The lowest hydraulic heads are located in a topographically depressed area at the south–eastern part of the domain where the highest discharge fluxes occur.

The normalized flow in Figure 6-2 shows a clear upward flow component in the low permeable materials: glacial clay and clay gyttja-peat. On the contrary, the horizontal component is more significant in the high permeable layers (till and postglacial sand), see Figure 6-2.

The three-dimensional flow field is also illustrated by groundwater flow streamlines (Figure 6-3). Streamlines show the path followed by 400 particles released evenly distributed along the bedrock-regolith interface. Most of the particles enter the postglacial sand and then move horizontally towards the south–eastern boundary of the domain. Once there, the vertical hydraulic gradient increases and water migrates upwards through the clay gyttja-peat upwards eventually discharging to the surface. The glacial clay hinders the infiltration of recharge water in the lower material layers (till), while the overlying highly permeable postglacial materials control groundwater flow in the upper system and promote water mixing. However, preferential vertical paths appear where the glacial clay is very thin. These areas concentrate most of the advective flow between the till and the postglacial sand, acting as preferential flow and transport paths generating chimneys of upwards solute migration.

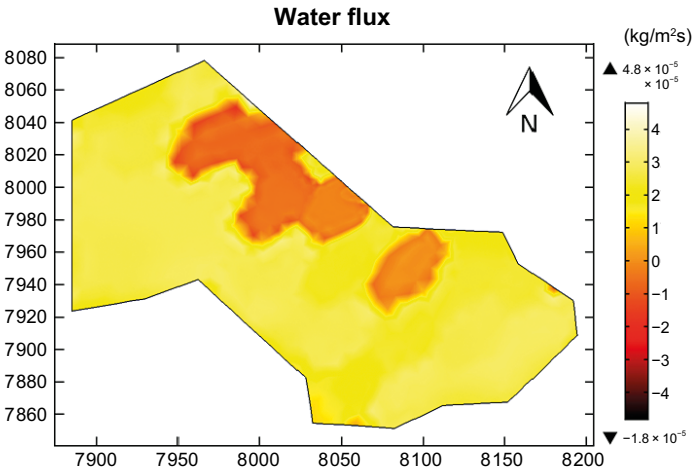

Figure 6-1. *Upward water flux ($kg \cdot m^{-2} \cdot s^{-1}$) at the ground surface of the model. Negative values (in red) indicate recharge areas. Positive values (in yellow) show discharge areas.*

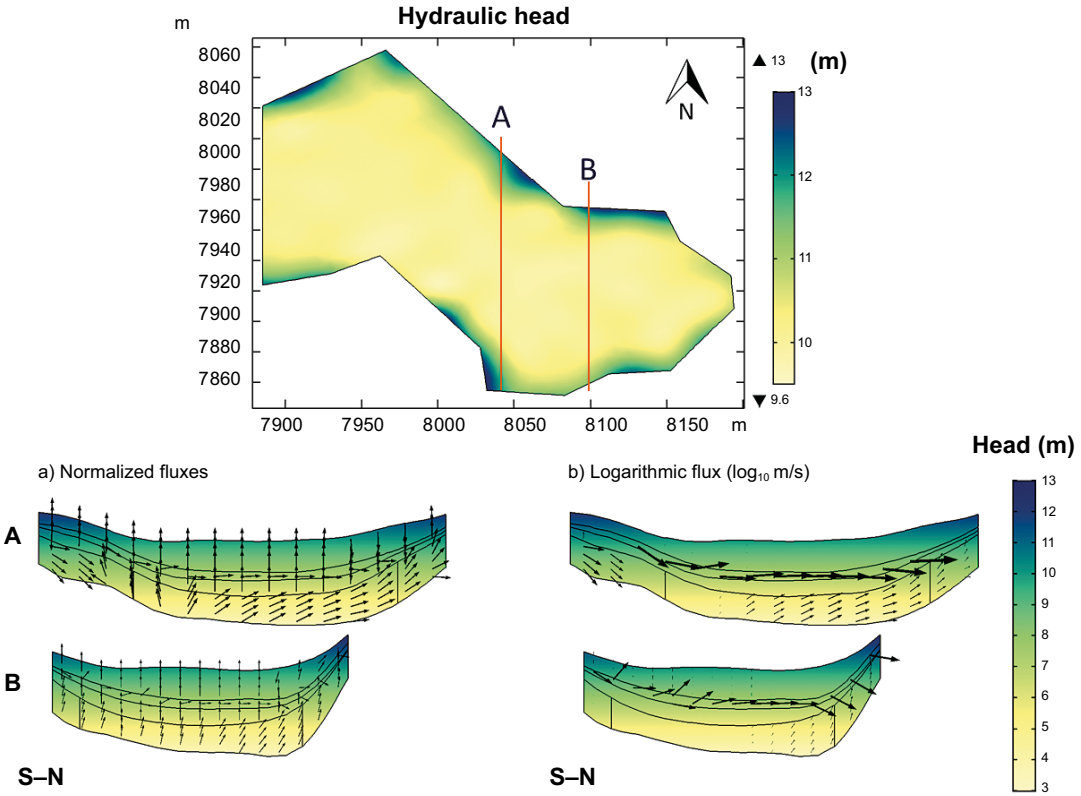

Figure 6-2. *Hydraulic head (m) at the ground surface of the model (top) and cross-sections showing both the hydraulic head with (a) normalized (unit length) and b) logarithmic velocity vectors (bottom). The locations of cross-sections A and B are shown in the top figure. Cross-sections are displayed from south to north. The vertical lines within the till layer show the boundaries of the radionuclide-rich deep groundwater zone (see Figure 5-4).*

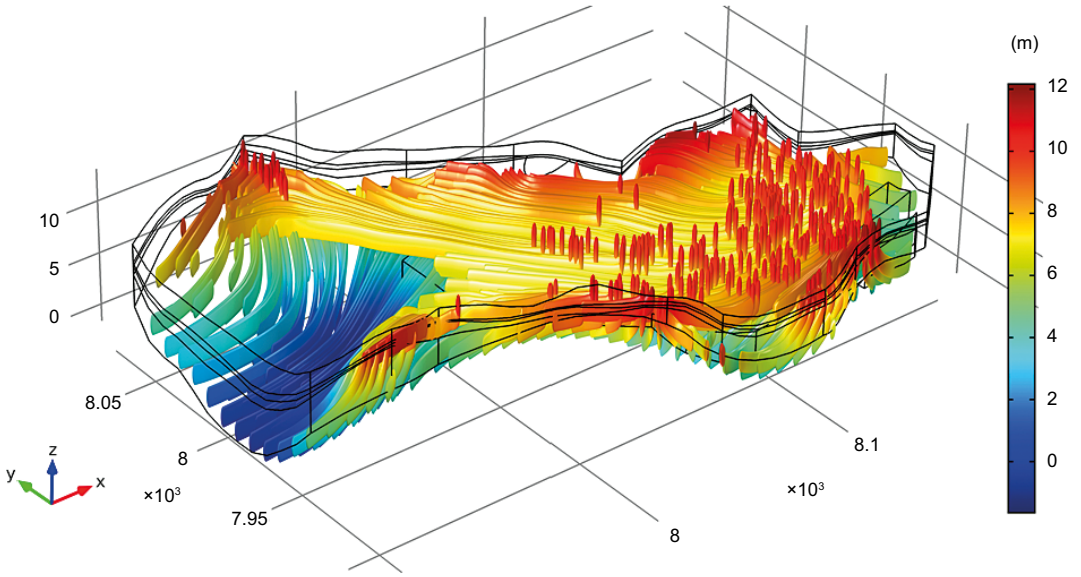

Figure 6-3. *Streamlines of groundwater flow in the distributed reactive model. The color indicates the elevation (meters above sea level) of the streamline. The vertical scale is exaggerated 5 times. North is aligned with the y axis.*

6.2 Radionuclide transport and retention

In this section the main results arising from the reactive transport model are presented. Relevant transport and retention processes affecting radioactive Ni, Ra, Sr, and Cs in the regolith materials in object 206 are analyzed. Here, the superscript "RD" is applied in front of the radionuclide in question (e.g., RDNi, RDSr and RDCs) in order to denote the radionuclide as being "repository-derived" separate from the naturally occurring Ni, Sr and Cs. The initial Ra concentration in the system is assumed equal to the deep groundwater; Ra is therefore considered to be repository-derived (i.e., RDRa).

6.2.1 Strontium

The concentration of strontium after 1 000 years of simulation is shown in Figure 6-4. The discharge of repository-derived Sr (RDSr) coincides with groundwater discharge areas (see Figure 6-3 and Section 6.1). The maximum predicted aqueous concentration of RDSr at the surface is ca 1.2×10^{-3} mol·l^{-1}; this is about 50 times higher than the naturally occurring Sr concentration of the pore-water at the surface (Table 2-4). The cross-sections in Figure 6-4 show the distribution of aqueous and sorbed RDSr in the different regolith layers. Two processes affect the transport and retention of RDSr at the regolith: cation exchange within illite (Figure 6-4b) and solid-solution precipitation with the calcite (Figure 6-4c).

The highest concentrations of aqueous RDSr (1.6×10^{-3} mol·l$_{water}^{-1}$) are found in the till (Figure 6-4a). The presence of aqueous RDSr in the uppermost layers is only significant in the water discharge areas (southern and central parts of the sections) where the vertical flow facilitates upwards migration (see Figure 6-3.

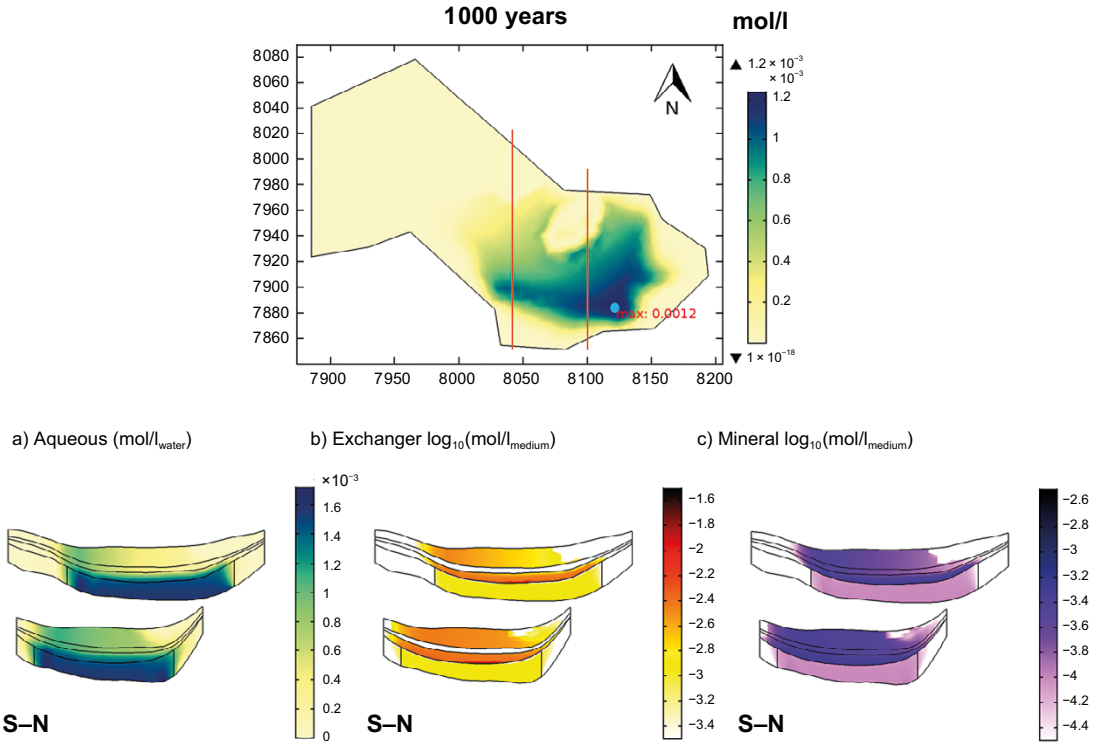

Figure 6-4. *Aqueous RDSr (mol·l$_{water}^{-1}$) at the ground surface of the model after 1 000 years. The maximum concentration location (light blue circle) and value (red text) is shown. The cross-sections A and B indicated in the top figure are plotted below showing the concentration of a) aqueous RDSr (mol·l$_{water}^{-1}$), b) RDSr in the exchanger (log$_{10}$ mol·l$_{medium}^{-1}$) and c) RDSr as solid-solution (log$_{10}$ mol·l$_{medium}^{-1}$).*

The maximum concentration of RDSr in the illite exchanger (2.1×10^{-2} mol·l_{medium}^{-1}) occurs at the boundary between the till and the glacial clay (Figure 6-4b). In the glacial gyttja-peat layer RDSr is present only in the water discharge areas. No RDSr is retained in the postglacial sand due to the absence of illite in its mineralogical composition. The maximum precipitation of RDSr solid-solution (Figure 6-4c) occurs, also, in the glacial clay (5.2×10^{-4} mol·l_{medium}^{-1}). The precipitation of the (Ca,RDSr)CO_3 solid-solution is significant in the postglacial sand and the glacial gyttja-peat layers as well. The accumulation of (Ca,RDSr)CO_3 is of the same order of magnitude in all three layers. Most of the RDSr is retained in the illite exchanger (Figure 6-4b). Concentrations here are between one and two orders of magnitude higher than the aqueous RDSr and the RDSr precipitated as solid-solution. The glacial clay layer accumulates most of RDSr. The system arrives to a steady state in less than 100 years of simulation time (see Figure D-1).

6.2.2 Cesium

The concentration of cesium after 1 000 years of simulation is shown in Figure 6-5. The discharge of RDCs at the surface coincides with the groundwater discharge areas (see Section 6.1). The maximum aqueous concentration of RDCs at the surface (5.5×10^{-10} mol·l_{water}^{-1}) which is about half the maximum concentration of the naturally occurring Cs in pore-water at the surface (Table 2-4).

Cross-sections in Figure 6-5 show the effect of cation exchange within illite on the transport and retention of RDCs at the regolith. There is no retention process affecting RDCs in the postglacial sand. The highest aqueous concentration of RDCs (2.2×10^{-7} mol·l_{water}^{-1}) is found in the postglacial sand at the contact with the glacial clay (Figure 6-5a) which is at least two orders of magnitude greater than the aqueous concentrations of RDCs in the other regolith materials. The high concentration of RDCs in the postglacial sand is due to the vertical preferential flow paths where glacial clay layer is thin.

The maximum RDCs concentration at the illite exchanger (1.8×10^{-5} mol·l_{medium}^{-1}) occurs at the lower boundary of the glacial clay (Figure 6-5b). In the till and in the discharge areas of the clay gyttja-peat, the illite exchanger also accumulates RDCs concentrations of the order of 10^{-6} mol·l_{medium}^{-1}. The modeled system does not reach a steady state after 1 000 years of simulation (see Figure D-2).

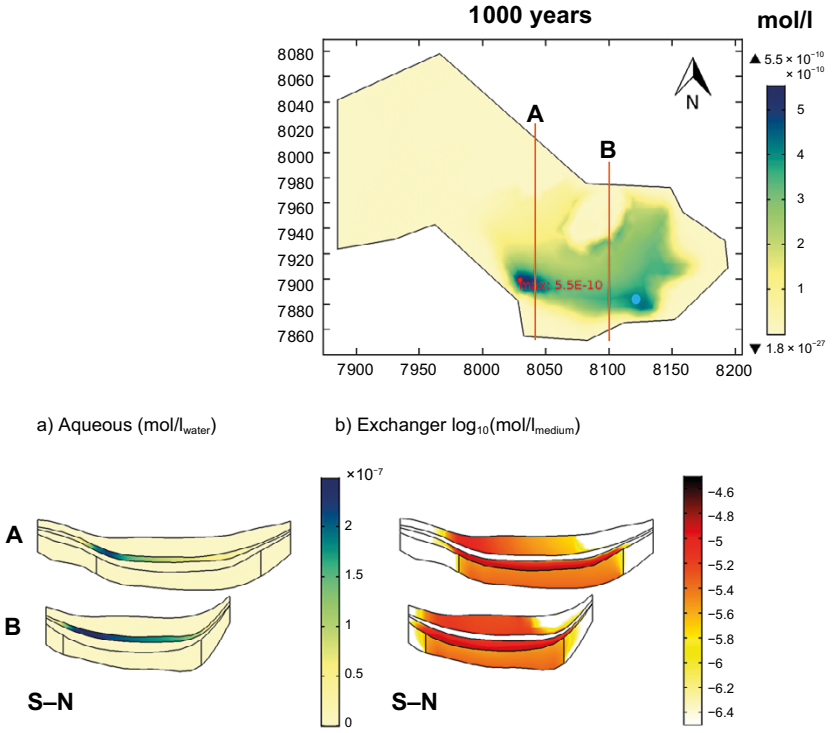

Figure 6-5. *Aqueous RDcesium (mol·l_{water}^{-1}) at the ground surface of the model after 1 000 years. The maximum concentration location and value is plotted in red. The cross-sections A and B indicated in the top figure are plotted below showing the concentration of a) aqueous RDCs (mol·l_{water}^{-1}) and b) RDCs in the exchanger (log_{10} mol·l_{medium}^{-1}). All concentrations are given after 1 000 years. The vertical scale of the cross-sections is exaggerated five times.*

6.2.3 Nickel

The concentration of RDNi after 1 000 years of simulation is shown in Figure 6-6. The maximum concentration of aqueous RDNi at the surface (3.58×10^{-8} mol·l_{water}^{-1}) takes place in the discharge area (see Section 6.1) in the southern part of the domain. This concentration is of a magnitude similar to maximum concentration of the naturally occurring RDNi at the surface (Table 2-4). The higher aqueous concentrations of aqueous RDNi take place in the postglacial sand, where the model assumes that no sorption processes occur (Figure 6-6a). Aqueous RDNi concentration is not relevant in other regolith materials. The concentration on the illite exchange positions (Figure 6-6b) and on illite/ferrihydrite surface sites (Figure 6-6c) show similar patterns. No retention of RDNi occurs in the postglacial sand due to the absence of illite in the ferrihydrite minerals. The maximum modelled RDNi concentrations in the exchanger and on the surfaces are 7.3×10^{-8} mol·l_{medium}^{-1} and 2.5×10^{-5} mol·l_{medium}^{-1} respectively. These concentrations occur at the bottom of the glacial clay.. The system does not appear to be in an equilibrium state after 1 000 years of simulation (Figure D-3).

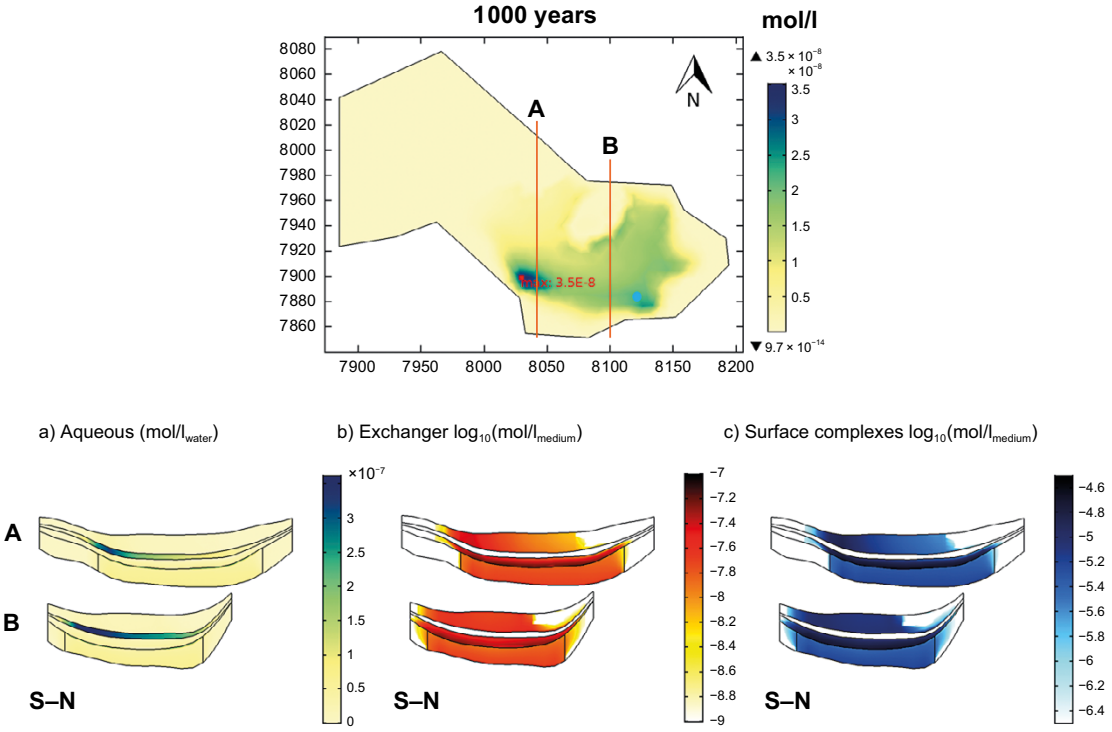

Figure 6-6. *Aqueous RDNi (mol·l_{water}^{-1}) at the ground surface of the model after 1 000 years. The maximum concentration location and value are plotted in red. The cross-sections A and B indicated in the top figure are plotted below showing the concentration of: a) aqueous RDNi (mol·l_{water}^{-1}), b) RDNi in the exchanger (log_{10} mol·l_{medium}^{-1}) and c) RDNi in surface complexes (log_{10} mol·l_{medium}^{-1}). All concentrations are given after 1 000 years. The vertical scale of the cross-sections is exaggerated five times.*

6.2.4 Radium

The concentration of radium after 1 000 years of simulation is shown in Figure 6-7. The maximum aqueous concentration of Ra at the surface (4.8×10^{-11} mol·l_{water}^{-1}) takes place in the discharge area at the south–eastern part of the domain.

The process dominating the retention of Ra in the regolith is precipitation as solid-solution of barite. The highest concentrations of aqueous Ra (9×10^{-11} mol·l_{water}^{-1}) are in the glacial clay (Figure 6-7a). the concentration of aqueous Ra is around one order of magnitude lower in materials overlying the glacial clay. The maximum precipitation of the (Ba,Ra)SO_4 solid-solution (1.2×10^{-9} mol·l_{medium}^{-1}) also occurs in the glacial clay (Figure 6-7b). This result is consistent with the results from a 1D model of Ra retention in the till (Appendix C). The (Ba,Ra)SO_4 precipitates in the till early but as there is no replenishment of Ba-bearing water, barium concentration decreases with time. Therefore, (Ba,Ra)SO_4 precipitation becomes limited and is, eventually, aqueous. In the upper layers of the regolith, the precipitation of (Ba,Ra)SO_4 is constantly growing due to the renewal of clay water with high barium concentration. The system appears to be nearing an equilibrium state after 500–1 000 years of simulation (Figure D-4).

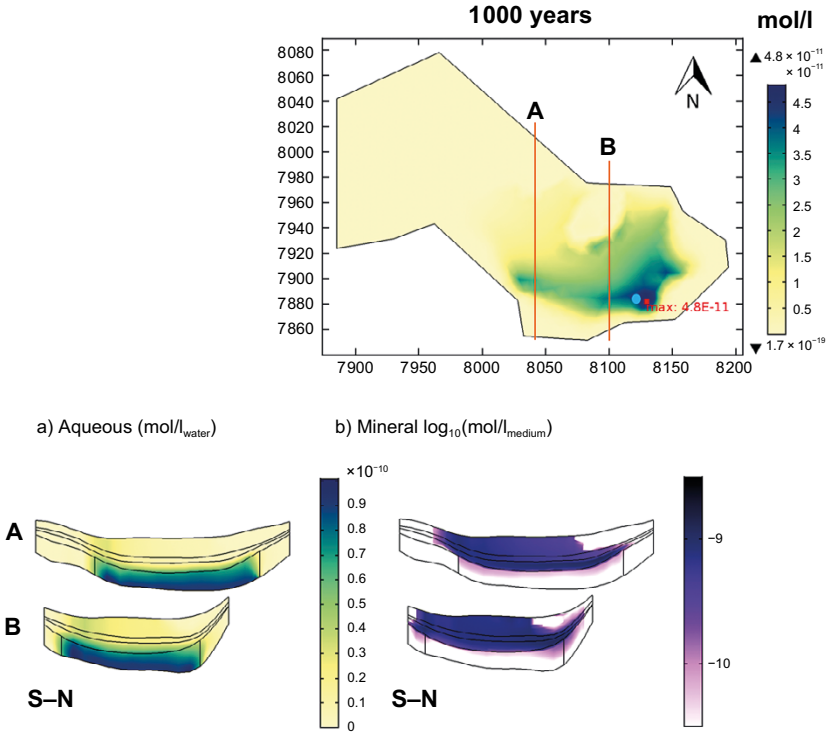

Figure 6-7. *Aqueous radium (mol·l_{water}^{-1}) at the ground surface of the model after 1 000 years. The maximum concentration location and value are plotted in red. The cross-sections A and B indicated in the top figure are plotted below showing the concentration of a) aqueous Ra (mol·l_{water}^{-1}) and b) Ra precipitated as solid-solution (log$_{10}$ mol·l_{medium}^{-1}). All concentrations are given after 1 000 years. The vertical scale of the cross-sections is exaggerated five times.*

6.2.5 Summary and conclusions from the distributed reactive model

According to the distributed reactive model presented in this section, radionuclides reach the surface in the discharge area in the southern and south–eastern parts of the domain as dictated by the simulated groundwater flow-field. The locations of the maximum radionuclide concentrations depend on the controlling retention processes for each of the radionuclides. RDCs and RDNi, which are retained mostly by processes associated with the illite, present their maximum aqueous concentration at the surface in the southern part of the domain. However, RDSr and Ra have the highest aqueous concentrations in the south–eastern part of the discharge zone.

Most of the RDCs and RDNi is retained in the regolith. The maximum aqueous concentrations of the pore-water indicate that greater than 99 % of the RDCs and ca 92 % of the RDNi is removed from solution while traveling through the regolith after 1 000 years of simulation time. Contrary to this, Ra and RDSr migrate with relative ease through the regolith with only ca 48 % respective 23 % being removed from solution by the regolith.

Modeling results indicate that the most effective mechanisms for the retention of RDSr, RDCs are exchange and for RDNi it is surface complexation. Therefore, the layers with high contents of illite (glacial clay and clay gyttja-peat) are predicted to accumulate most of these radionuclides. The postglacial sand interbedded between clay materials contains no illite, and therefore has no retention capacity for these radionuclides. This highly permeable layer, however, is critical in the retention of Ra. It promotes the mixing of lateral and surface recharge waters (enriched with Ba) with the radionuclide-rich groundwater. This mixing leads to $(Ba,Ra)SO_4$ solid-solution precipitation and consequently to Ra retention.

Reactive transport models require well substantiated conceptual models of the chemical reactions affecting the mobility of a given radionuclide which are supported by thermodynamic data as well as a thorough and accurate description of the geochemical background conditions. For Sr and Ni these criteria are judged to be reasonably fulfilled with respect to conditions in the bedrock and some geological materials. However, the interactions with organic matter are not explicitly represented, and thus the simulations of the mobility of Sr and Ni in the upper regolith profile (clay-gyttja and peat) are not realistic.

7 Discussion and conclusions from the two modelling approaches

Two modelling approaches have been presented: (1) a 3D hydrogeological distributed K_d model with a K_d-based retention approach, (2) a smaller scale 3D hydrogeological model with a mechanistic geochemical model of radionuclide transport.

The distributed K_d model evaluates the retention of radionuclides in the regolith using a linear partition coefficient (K_d) which is a lumped parameter that relates the mass retained in the solid phase to its aqueous concentration activity. A basin-scale hydrological model is used to aid in the fate and transport simulations.

The distributed reactive model is applied in a smaller section of the basin-scale hydrogeological model used in the K_d modelling approach. A smaller section of the basin-scale model is used due to the high computational needs of the reactive model relative the K_d modelling approach. The distributed reactive model accounts for various processes to model the retention capacity of the regolith. The radionuclides might be chemically retained by sorption (cation exchange and surface complexes) and by precipitation of solid-solutions. Reactive models require accurate and thorough conceptual models which account for the reactive processes being modelled. These conceptual models should be supported by thermo-dynamic data which is sometimes not available.

The distributed reactive model can help to show the effects of water mixing on the retention processes. For example, when examining the fate and transport of radium, the reactive model indicates that the accumulation of Ra is largely dependent on the availability of other aqueous elements such as Ba (Appendix C). The K_d approach is not capable of capturing this relationship.

When comparing the transport of Cs, Ni and Ra, the distributed K_d model shows higher retentions in the till and glacial clay, which are located in the lower part of the regolith. In contrast, most of the retention processes are linked with the presence of illite, such as glacial clay and clay gyttja-peat, in the distributed reactive model. The discrepancy in the radionuclide's accumulation between the K_d based and the distributed reactive model depends on the actual retention process of each radionuclide. Cesium and nickel are retained by processes (exchange and surface complexation) that behave similarly to the K_d partition coefficient and, therefore, present a relatively similar migration and accumulation in both models.

In Table 7-1 the maximum and average equivalent K_d value for the regolith materials of the distributed reactive model at the final simulation time is compared with the values used in the distributed K_d model. The equivalent K_d distribution is calculated using Equation (7-1):

$$K_d = \frac{1}{\rho_b}\frac{c_{retained}}{c_{dissolved}} \qquad \text{Equation (7-1)}$$

where $c_{retained}$ (mol·l_{medium}) is the concentration of a retained radionuclide, $c_{dissolved}$ (mol·l_{water}) is the concentration of an aqueous radionuclide and ρ_b is the bulk density (kg·l_{medium}). The calculated K_d values have a great variability and the K_d distribution depends on many factors. The maximum K_d values for the Cs and Ni show a relatively good agreement between the two models. The maximum partition coefficient occurs at the glacial clay in both models. On the other hand, the dissolution-precipitation process of Ba solid solutions is highly influenced by the availability of Ba and the water mixing. This leads to a bad correlation between the values of K_d. The equivalent values from the distributed reactive model are at least one order of magnitude lower than in the distributed K_d model.

Table 7-1. Calculated K_d values ($m^3 \cdot kg^{-1}$) the from the distributed reactive model at the final simulation time, compared with K_d values used in the distributed K_d model.

	Distributed reactive model								Distributed K_d model		
	Sr		Cs		Ni		Ra				
	Avg.	Max.	Avg.	Max.	Avg.	Max.	Avg.	Max.	Cs	Ni	Ra
Clay gyttja-peat	0.003	0.011	36.29	51.07	1.5	4.3	0.128	0.559	30	0.46	2.6
Postglacial sand	0.000	0.005	-	-	-	-	0.000	0.220	0.53	0.13	3.1
Glacial clay	0.002	0.021	20.42	68.36	0.49	11.9	0.038	0.744	170	5.08	5.5
Till	0.000	0.002	3.86	9.1	0.07	0.12	0.003	0.242	11	0.75	1.3

Both the mechanistic and the K_d models have their strengths and weaknesses. Both give valuable information on the migration and retention of radionuclides in the regolith. A distributed reactive model could provide a more detailed description of the processes occurring if it is based on relevant chemical reactions and parameters but due to its high computational cost, it can only be applied with high resolution to small domains. Moreover, this type of modelling requires a large amount of information (thermodynamic data) and a previously developed mechanistic model to represent the element retention. For that reason, this approach has not been applied to simulate the retention processes to organic matter as no such model is available. Those retention mechanisms are currently better represented in the K_d-based approach, since the K_d for the organic matter-rich regolith layers have been locally measured.

Due to low amount of computational resources required compared to the distributed reactive model, the K_d model is better suited for examining large areas and long simulation times. Parameter sensitivity analyses are also more easily performed using a K_d approach as are analyses of the effects of stochastic distributions of the K_d values within the regolith materials.

References

SKB's (Svensk Kärnbränslehantering AB) publications can be found at www.skb.com/publications.

Abarca E, Sampietro D, Molinero J, von Schenck H, 2019. Modelling of the near-field hydrogeology – Temperate climate conditions. Report for the safety evaluation SE-SFL. SKB R-19-03, Svensk Kärnbränslehantering AB.

Andersson E, Tudorancea M-M, Tudorancea C, Brunberg A-K, Blomqvist P, 2003. Water chemistry, biomass and production of biota in Lake Eckarfjärden during 2002. SKB R-03-27, Svensk Kärnbränslehantering AB.

Bastviken D, Thomsen F, Svensson T, Karlsson S, Sandén P, Shaw G, Matucha M, Öberg G, 2007. Chloride retention in forest soil by microbial uptake and by natural chlorination of organic matter. Geochimica et Cosmochimica Acta 71, 3182–3192.

Bauer P, Attinger S, Kinzelbach W, 2001. Transport of a decay chain in homogenous porous media: analytical solutions. Journal of Contaminant Hydrology 49, 217–239.

Bosson E, Gustafsson L-G, Sassner M, 2009. Numerical modelling of surface hydrology and near-surface hydrogeology at Laxemar-Simpevarp: site descriptive modelling: SDM-site Laxemar. SKB R-08-72, Svensk Kärnbränslehantering AB.

Bradbury M H, Baeyens B, 2000. A generalised sorption model for the concentration dependent uptake of caesium by argillaceous rocks. Journal of Contaminant Hydrology 42, 141–163.

Bradbury M H, Baeyens B, 2005. Experimental and modelling investigations on Na-illite: Acid-base behaviour and the sorption of strontium, nickel, europium and uranyl. PSI Bericht 05-02, Paul Scherrer Institut, Switzerland.

Bradbury M H, Baeyens B, 2009. Sorption modelling on illite Part I: Titration measurements and the sorption of Ni, Co, Eu and Sn. Geochimica et Cosmochimica Acta 73, 990–1003.

Bradbury M H, Baeyens B, 2011. Predictive sorption modelling of Ni(II), Co(II), Eu(IIII), Th(IV) and U(VI) on MX-80 bentonite and Opalinus Clay: A "bottom-up" approach. Applied Clay Science 52, 27–33.

Cho C M, 1971. Convective transport of ammonium with nitrification in soil. Canadian Journal of Soil Science 51, 339–350.

Cole T, Bidoglio G, Soupioni M, O'Gorman M, Gibson N, 2000. Diffusion mechanisms of multiple strontium species in clay. Geochimica et Cosmochimica Acta 64, 385–396.

COMSOL, 2015. COMSOL Multiphysics. Reference manual. Version 5.1. Burlington, MA: COMSOL Inc.

Duro L, Grivé M, Cera E, Domènech C, Bruno J, 2006. Update of a thermodynamic database for radionuclides to assist solubility limits calculation for performance assessment. SKB TR-06-17, Svensk Kärnbränslehantering AB.

Dzombak D A, Morel F M M, 1990. Surface complexation modeling: hydrous ferric oxide. New York: Wiley.

Elfwing M, Evins L Z, Gontier M, Grahm P, Mårtensson P, Tunbrant S, 2013. SFL concept study. Main report. SKB TR-13-14, Svensk Kärnbränslehantering AB.

Firestone R B, Baglin C M (ed), Chu S Y F (ed), 1998. Table of isotopes: 1998 update. 8th ed. New York: Wiley.

Gelhar L W, Axness C L, 1983. Three-dimensional stochastic analysis of macrodispersion in aquifers. Water Resources Research 19, 161–180.

Gelhar L W, Welty C, Rehfeldt K R, 1992. A critical review of data on field-scale dispersion in aquifers. Water Resources Research 28, 1955–1974.

Hallema D W, Périard Y, Lafond J A, Gumiere S J, Caron J, 2015. Characterization of water retention curves for a series of cultivated Histosols. Vadose Zone Journal 14, 1–8.

Hedenström A, 2004. Forsmark site investigation. Investigation of marine and lacustrine sediment in lakes. Stratigraphical and analytical data. SKB P-04-86, Svensk Kärnbränslehantering AB.

Hedenström A, Sohlenius G, 2008. Description of the regolith at Forsmark. Site descriptive modelling SDM-Site Forsmark. SKB R-08-04, Svensk Kärnbränslehantering AB.

Hummel W, Berner U, Curti E, Pearson F J, Thoenen T, 2002. Nagra/PSI chemical thermodynamic data base 01/01. Radiochimica Acta 90, 805–813. (Also published as Nagra Technical Report NTB 02-16, Nagra, Switzerland.)

Johansson E, Sassner M, 2019. Development of methodology for flow path analysis in the Surface system – Numerical modelling in MIKE SHE for Laxemar. A report for the safety evaluation SE-SFL. SKB R-19-04, Svensk Kärnbränslehantering AB.

Joyce S, Appleyard P, Hartley L, Tsitsopoulos V, Woollard H, Marsic N, Sidborn M, Crawford J, 2019. Groundwater flow and reactive transport modelling of temperate conditions. Report for the safety evaluation SE-SFL. SKB R-19-02, Svensk Kärnbränslehantering AB.

Laaksoharju M, Smellie J, Tullborg E-L, Wallin B, Drake H, Gascoyne M, Gimeno M, Gurban I, Hallbeck L, Molinero J, Nilsson A-C, Waber N, 2009. Bedrock hydrogeochemistry Laxemar. Site descriptive modelling, SDM-Site Laxemar. SKB R-08-93, Svensk Kärnbränslehantering AB.

Lindström M, Lundqvist J, Lundqvist T, 2000. Sveriges geologi från urtid till nutid. 2nd ed. Lund: Studentlitteratur. (In Swedish.)

Lundin L, Stendahl J, Lode E, 2005. Forsmark site investigation. Soils in two large trenches. SKB P-05-166, Svensk Kärnbränslehantering AB.

Lundin L, Snäll S, Jonsson E, Hannu S, Selnert E, Engdahl A, 2007. Oskarshamn site investigation. Characterization of soil samples from three valleys in the Laxemar area. SKB P-07-222, Svensk Kärnbränslehantering AB.

Marques Fernandes M, Baeyens B, Dähn R, Scheinost A C, Bradbury M H, 2012. U(VI) sorption on montmorillonite in the absence and presence of carbonate: a macroscopic and microscopic study. Geochimica et Cosmochimica Acta 93, 262–277.

MDH Engineered Solutions Corp, 2003. Evaluation of computer models for predicting the fate and transport of salt in soil and groundwater: Phase I report, Science and Standards Branch, Alberta Environment.

Nardi A, Idiart A, Trinchero P, de Vries L M, Molinero J, 2014. Interface COMSOL–PHREEQC (iCP), an efficient numerical framework for the solution of coupled multiphysics and geochemistry. Computers & Geosciences 69, 10–21.

Nyman H, Sohlenius G, Strömgren M, Brydsten L, 2008. Depth and stratigraphy of regolith. Site descriptive modelling SDM-Site Laxemar. SKB R-08-06, Svensk Kärnbränslehantering AB.

Outridge P M, Stern G A, Hamilton P B, Percival J B, McNeely R, Lockhart W L, 2005. Trace metal profiles in the varved sediment of an Arctic lake. Geochimica et Cosmochimica Acta 69, 4881–4894.

Parkhurst D L, Appelo C, 2013. Description of input and examples for PHREEQC version 3: a computer program for speciation, batch-reaction, one-dimensional transport, and inverse geochemical calculations. In U.S. Geological Survey Techniques and Methods, Book 6, Chapter A43. Denver, CO: U.S. Geological Survey.

Percival J B, Hunt P, Wygergangs M, 2001. Mineralogical investigations of Canadian till and lake-and stream-sediment reference materials, part 1: Standardized X-ray diffraction and scanning electron microscope methods. Natural Resources Canada, Geological Survey of Canada.

Pintado X, Ledesma A, Lloret A, 2002. Backanalysis of thermohydraulic bentonite properties from laboratory tests. Engineering Geology 64, 91–115.

Piqué À, Grandia F, Sena C, Arcos D, Molinero J, Duro L, Bruno J, 2010. Conceptual and numerical modelling of radionuclide transport in near-surface systems at Forsmark. SR-Site Biosphere. SKB R-10-30, Svensk Kärnbränslehantering AB.

Piqué À, Arcos D, Grandia F, Molinero J, Duro L, Berglund S, 2013. Conceptual and numerical modeling of radionuclide transport and retention in near-surface systems. Ambio 42, 476–487.

Rhén I, Forsmark T, Hartley L, Joyce S, Roberts D, Gylling B, Marsic N, 2009. Bedrock hydrogeology. Model testing and synthesis. Site descriptive modelling SDM-Site Laxemar. SKB R-08-91, Svensk Kärnbränslehantering AB.

Richards L A, 1931. Capillary conduction of liquids through porous mediums. Physics 1, 318–333.

Saaltink M W, Carrera J, Ayora C, 2000. A comparison of two approaches for reactive transport modelling. Journal of Geochemical Exploration 69, 97–101.

Saaltink M W, Carrera J, Ayora C, 2001. On the behavior of approaches to simulate reactive transport. Journal of Contaminant Hydrology 48, 213–235.

Saaltink M W, Ayora C, Olivella S, 2005. User's guide for RetrasoCodeBright (RCB). Department of Geotechnical Engineering and Geo-Sciences, Technical University of Catalonia (UPC), Spain.

Sena C, Grandia F, Arcos D, Molinero J, Duro L, 2008. Complementary modelling of radionuclide retention in the near-surface system at Forsmark. Development of a reactive transport model using Forsmark 1.2 data. SKB R-08-107, Svensk Kärnbränslehantering AB.

Sheppard S, Long J, Sanipelli B, Sohlenius G, 2009. Solid/liquid partition coefficients (K_d) for selected soils and sediments at Forsmark and Laxemar-Simpevarp. SKB R-09-27, Svensk Kärnbränslehantering AB.

Sheppard S, Sohlenius G, Omberg L-G, Borgiel M, Grolander S, Norden S, 2011. Solid/liquid partition coefficients (K_d) and plant/soil concentration ratios (CR) for selected soils, tills and sediments at Forsmark. SKB R-11-24, Svensk Kärnbränslehantering AB.

SKB, 2006. Long-term safety for KBS-3 repositories at Forsmark and Laxemar – a first evaluation. Main report of the SR-Can project. SKB TR-06-09, Svensk Kärnbränslehantering AB.

SKB, 2008. Site description of Forsmark at completion of the site investigation phase. SDM-Site Forsmark. SKB TR-08-05, Svensk Kärnbränslehantering AB.

Sohlenius G, Bergman T, Snäll S, Lundin L, Lode E, Stendahl J, Riise A, Nilsson J, Johansson T, Göransson M, 2006. Oskarshamn site investigation. Soils, Quaternary deposits and bedrock in topographic lineaments situated in the Laxemar subarea. SKB P-06-121, Svensk Kärnbränslehantering AB.

Strömgren M, Brydsten L, 2008. Digital elevation models of Laxemar-Simpevarp. SDM-Site Laxemar. SKB R-08-63, Svensk Kärnbränslehantering AB.

Svensson T, Lovett G M, Likens G E, 2012. Is chloride a conservative ion in forest ecosystems? Biogeochemistry 107, 125–134.

Söderbäck B, Lindborg T, 2009. Surface system Laxemar-Simpevarp. Site descriptive modelling SDM-Site Laxemar. SKB R-09-01, Svensk Kärnbränslehantering AB.

Tournassat C, Gailhanou H, Crouzet C, Braibant G, Gautier A, Lassin A, Blanc P, Gaucher E C, 2007. Two cation exchange models for direct and inverse modelling of solution major cation composition in equilibrium with illite surfaces. Geochimica et Cosmochimica Acta 71, 1098–1114.

Tröjbom M, Grolander S, 2010. Chemical conditions in present and future ecosystems in Forsmark – implications for selected radionuclides in the safety assessment SR-Site. SKB R-10-27, Svensk Kärnbränslehantering AB.

Tröjbom M, Söderbäck B, 2006. Chemical characteristics of surface systems in the Forsmark area. Visualisation and statistical evaluation of data from shallow groundwater, precipitation, and regolith. SKB R-06-19, Svensk Kärnbränslehantering AB.

Tröjbom M, Grolander S, Rensfeldt V, Nordén S, 2013. K_d and CR used for transport calculations in the biosphere in SR-PSU. SKB R-13-01, Svensk Kärnbränslehantering AB.

van Genuchten M T, 1980. A closed-form equation for predicting the hydraulic conductivity of unsaturated soils 1. Soil Science Society of America Journal 44, 892–898.

Villar M V, Martín P L, Bárcena I, García-Siñeriz J L, Gómez-Espina R, Lloret A, 2012. Long-term experimental evidences of saturation of compacted bentonite under repository conditions. Engineering Geology 149, 57–69.

Waite T D, Davis J A, Payne T E, Waychunas G A, Xu N, 1994. Uranium(VI) adsorption to ferrihydrite: Application of a surface complexation model. Geochimica et Cosmochimica Acta 58, 5465–5478.

Yeh G T, Tripathi V S, 1989. A critical evaluation of recent developments in hydrogeochemical transport models of reactive multichemical components. Water Resources Research 25, 93–108.

Yuan-Hui L, Gregory S, 1974. Diffusion of ions in sea water and in deep-sea sediments. Geochimica et Cosmochimica Acta 38, 703–714.

Åkesson M, Börgesson L, Kristensson O, 2010. SR-Site Data report. THM modelling of buffer, backfill and other system components. SKB TR-10-44, Svensk Kärnbränslehantering AB.

Appendix A

Validation of the implementation of the advective-dispersive transport equation with linear sorption and decay

The equations for radionuclide sorption and decay are implemented in COMSOL Multiphysics using the built-in equation for "transport of diluted species in porous media". The following appendix shows two benchmark exercises carried out to test the validity of the implemented equations for solving transport in porous media of a decay chain of radionuclides subject to linear adsorption with K_d. The results of the COMSOL simulation are compared against the analytical solutions detailed in two papers (Cho 1971, Bauer et al. 2001).

Benchmark 1 – Convective transport of ammonium with nitrification in soil (Cho 1971)

Problem description

This paper describes the convective transport of ammonium with nitrification and denitrification in soils. The advection dispersion equation (ADE) with first order reaction rates for nitrogen transformations is used. The proposed problem consists of a source of ammonium entering by the left border. The ammonium (NH_4^+) is degraded to NO_2^- and later NO_2^- is degraded to NO_3^-. In addition to this process, the ammonium is adsorbed in the solid material. It is expected that the concentration of Ammonium will decrease spatially from the origin. This decrease in ammonium will generate an increase in the NO_2^- and the degradation of it an increase in NO_3^-.

This process consists in a first order decay degradation. The solved equations are:

$$\begin{cases} R_1 \dfrac{\delta C_1}{\delta t} = D \dfrac{\delta^2 C_1}{\delta x^2} - v \dfrac{\delta C_1}{\delta x} - k_1 R_1 C_1 \\ R_2 \dfrac{\delta C_2}{\delta t} = D \dfrac{\delta^2 C_2}{\delta x^2} - v \dfrac{\delta C_2}{\delta x} + k_1 R_1 C_1 - k_2 R_2 C_2 \\ R_3 \dfrac{\delta C_3}{\delta t} = D \dfrac{\delta^2 C_3}{\delta x^2} - v \dfrac{\delta C_3}{\delta x} + k_2 R_2 C_2 - k_3 R_3 C_3 \end{cases}$$

where C_i is the concentration of three components, where C_1 is NH_4^+, C_2 is NO_2^- and C_3 is NO_3^- (mol·m^{-3}); D is the dispersion term (m^2·s^{-1}), v the pore velocity of water (u/θ in m·s^{-1}), u is the darcy velocity (m·s^{-1}),θ is the effective porosity and k_i is the degradation rate constant (1·s^{-1}).

The model consists of a 2.2 m length 1D problem with a darcy water velocity of 2.78×10^{-7} m·s^{-1} (0.1 cm·h^{-1}). Additional parameters are $D = 5 \times 10^{-9}$ m^2·s^{-1}; $k_1 = 2.78 \times 10^{-6}$ s^{-1}, $k_2 = 2.78 \times 10^{-5}$ s^{-1} and $k_3 = 0$.

Finally, $R_1 = 2$, $R_2 = R_3 = 1$ where R_i is the retardation factor (-) given by:

$$R_i = 1 + \frac{\rho K_d}{\theta}$$

Here, ρ is the bulk density (kg·m^{-3}) and K_d the solid-water distribution ratio for the ith chain member (m^3·kg^{-1}). A retardation factor of 2 means that the transport velocity of the solute is half of the advective velocity. On the other hand, if R equals 1 there is no adsorption.

Initially, the domain has no concentration of any of the transported species

$$C_i(x, 0) = 0$$

for NH_4^+, NO_2^- and NO_3^-. The boundary conditions are prescribed concentration (Dirichlet type boundary condition) at the inlet (x = 0) and outflow boundary condition at the water outlet (x = L):

$$\begin{cases} C_1(0,t) = 1\dfrac{mol}{m^3} \\ C_2(0,t) = C_3(0,t) = 0\ \dfrac{mol}{m^3} \\ -D_i \nabla C_i = 0 \ \ at\ (L,t) \end{cases}$$

Results

The results show that the concentration of NH_4^+ after 200 hours decreases with increasing depth, while NO_2^- and NO_3^- concentrations first increased and then decreased until they disappear. It should be pointed out that the rate of movement of NH_4^+ is one half of that of NO_2^- or NO_3^- because of retardation effect.

Figure A-1 shows the comparison between the results of the simulation with COMSOL Multiphysics and the results detailed in the paper for a simulation time of 200 hours. The authors calculate these results using an analytical solution (Cho 1971) obtained by derivation of the equation detailed above. It can be observed that COMSOL Multiphysics able to reproduce the sorption of pollutants in solids and the first order decay.

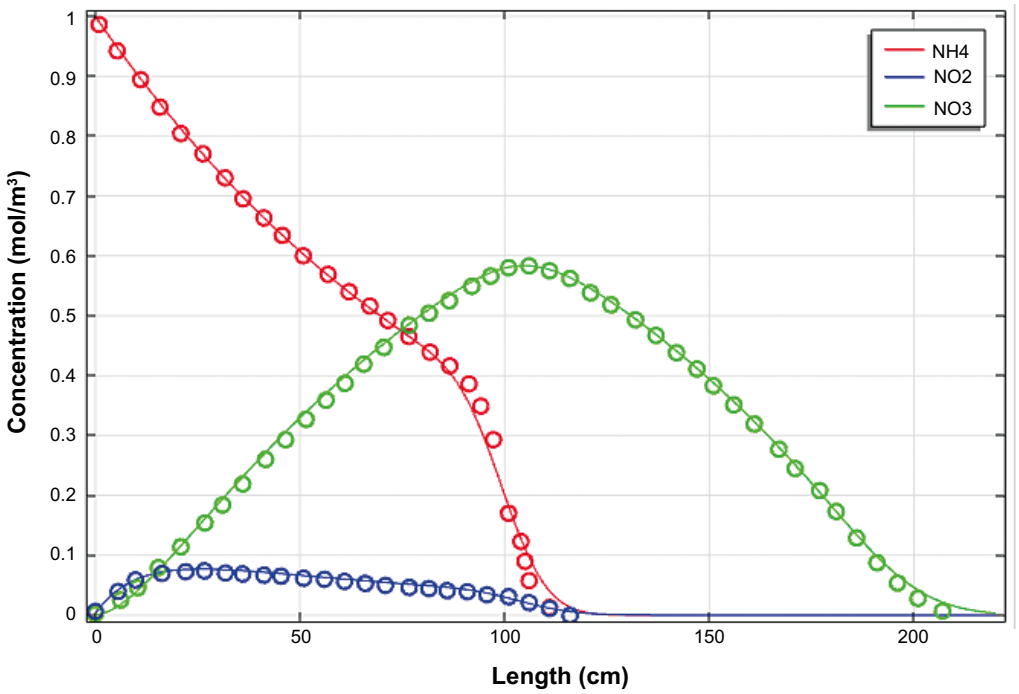

Figure A-1. *Comparison between model (lines) and reference results (dots) reported in Cho (1971) at t = 200 hours.*

Benchmark 2 – Transport of a decay chain in homogeneous porous media: analytical solutions (Bauer et al. 2001)

Problem description

The referenced paper contains a set of analytical solutions for the transport of a general decay chain in homogeneous porous media derived with the aid of integral transforms. Steady-state flow in single and multiple porosity media are considered.

The proposed verification problem considers a series of 4 radionuclides which are coupled by first-order decay processes forming a decay chain. Initially, the system does not contain any radionuclides and only component 1 (C_1) is present at the left boundary of the model. C_1 is degraded to component 2 (C_2) that, in turns, degrades in component 3 (C_3). C_3 also degrades in component 4 (C_4).

The solved equations proposed by the authors are:

$$\begin{cases} R_1 \dfrac{\delta C_1}{\delta t} = D \dfrac{\delta^2 C_1}{\delta x^2} - v \dfrac{\delta C_1}{\delta x} - k_1 R_1 C_1 \\ R_2 \dfrac{\delta C_2}{\delta t} = D \dfrac{\delta^2 C_2}{\delta x^2} - v \dfrac{\delta C_2}{\delta x} + k_1 R_1 C_1 - k_2 R_2 C_2 \\ R_3 \dfrac{\delta C_3}{\delta t} = D \dfrac{\delta^2 C_3}{\delta x^2} - v \dfrac{\delta C_3}{\delta x} + k_2 R_2 C_2 - k_3 R_3 C_3 \\ R_4 \dfrac{\delta C_4}{\delta t} = D \dfrac{\delta^2 C_4}{\delta x^2} - v \dfrac{\delta C_4}{\delta x} + k_3 R_3 C_3 - k_4 R_4 C_4 \end{cases}$$

where C_i is the concentration of the component i ($mol \cdot m^{-3}$), D is the dispersion term ($m^2 \cdot s^{-1}$), v the pore velocity of water ($\underline{u}/\theta$ in $m \cdot s^{-1}$), u is the darcy velocity ($m \cdot s^{-1}$), θ is the effective porosity and k_i is the decay constant ($1 \cdot s^{-1}$).

The model domain is 3 000 m long. The problem is solved in 1D with a Darcy water velocity of 0.042 $m \cdot s^{-1}$ ($1m \cdot day^{-1}$). Additional parameters are $D = 5 \times 10^{-9}$ $m^2 \cdot s^{-1}$, k_i equal to $(0.292, 0.208, 0.1875, 0.158) \times 10^{-4}$ s^{-1} for k_1, k_2, k_3 and k_4 respectively. Finally, R values are 5.3, 1.9, 1.2 and 1.3 for R_1, R_2, R_3 and R_4, respectively, where R_i is the retardation factor (-) given by:

$$R_i = 1 + \left[\frac{1-\theta}{\theta}\right] \rho K_d$$

Here, ρ is the matrix density ($kg \cdot m^{-3}$) and K_d the solid-water distribution ratio for the ith chain member($m^3 \cdot kg^{-1}$). K_d values can be obtained from the retardation factors resulting in 4.336×10^{-4}, 9.076×10^{-5}, 2.017×10^{-5} and 3.025×10^{-5} $m^3 \cdot kg^{-1}$ for C_1, C_2, C_3 and C_4 respectively. The matrix density is related with the bulk density through: $\rho_b = (1 - \theta)\rho_m$.

Initially, the domain has zero concentrations of all transported species

$$C_i(x, 0) = 0$$

for i = 1, 2, 3 and 4.

The boundary conditions are prescribed concentration (Dirichlet type boundary condition) at the inlet (x = 0) and outflow boundary condition at the water outlet (x = L)

$$\begin{cases} C_1(0,t) = 100 \dfrac{mmol}{m^3} \\ C_2(0,t) = C_3(0,t) = C_4(0,t) = 0 \ \dfrac{mol}{m^3} \\ -nD_i \nabla C_i = 0 \ \ at \ (L,t) \end{cases}$$

Results

The resulting concentration distributions after 3 000 days for the four-member decay chain are shown in Figure A-2. One can see that the different member concentrations rise successively to a maximum and then vanish. The maximum concentration of C_1 is located on the boundary and degrades totally to C_2 within the first 1 000 m. The low propagation of C_1 is due to its high retardation factor.

Figure A-2 shows the comparison between the results at t = 3 000 days of the simulation with COMSOL Multiphysics and the analytical solution presented in Bauer et al. (2001). It can be observed that COMSOL Multiphysics is able to reproduce the sorption of pollutants in solids and the first order decay.

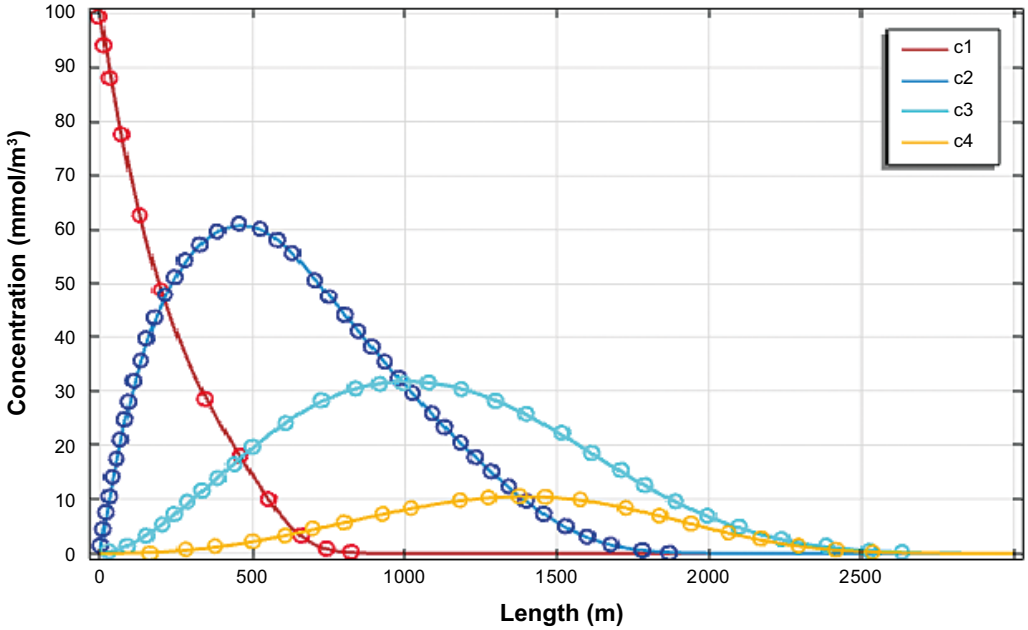

Figure A-2. *Comparison between simulation with COMSOL Multiphysics (lines) and analytical solution (dots) proposed in Bauer et al. (2001) at t = 3 000 days.*

Appendix B

Selected results from K_d model with radioactive decay

The following plots are selected results from the K_d model with radioactive decay. Results examining the distribution of aqueous and sorbed concentrations of radionuclides Chlorine-36, Nickel-59, Cecium-135, Radium-226 and Molybdenum-93 presented.

Vertical, 1D cross-sections at point 1 in object 206 and point 2 in object 210 (see Figure 3-2) are presented in order to show the evolution of the distribution (aqueous and sorbed concentrations) throughout the regolith layers after 1 000, 5 000 and 10 000 years of simulation time. The plots are meant to give an idea of how long the system takes before reaching an equilibrium state where the aqueous and sorbed concentrations no longer change with time.

2D vertical cross-sections in object 206 (see Figure 3-2) are presented in order to give further insight into the vertical distribution of radionuclides in the regolith.

Chlorine-36

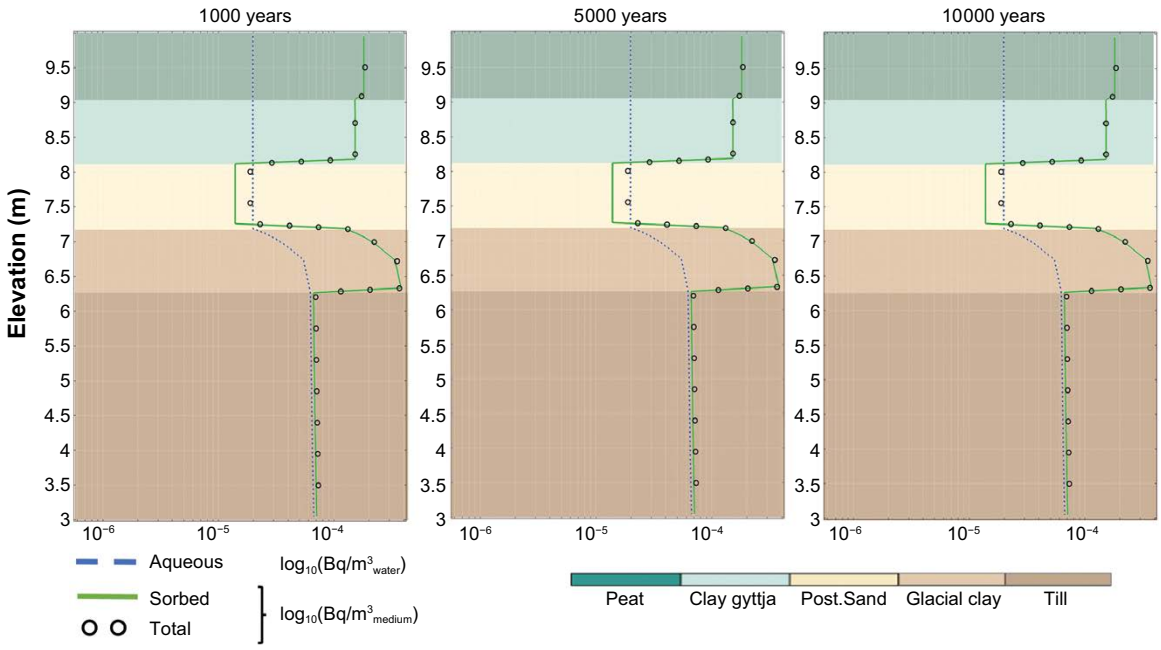

Figure B-1. *Profile of ^{36}Cl activity concentration aqueous, sorbed and total in the 1D vertical profile of point 1 at basin 206 (see Figure 3-2) for simulation times 1 000, 5 000 and 10 000. Note that the x axis is logarithmic.*

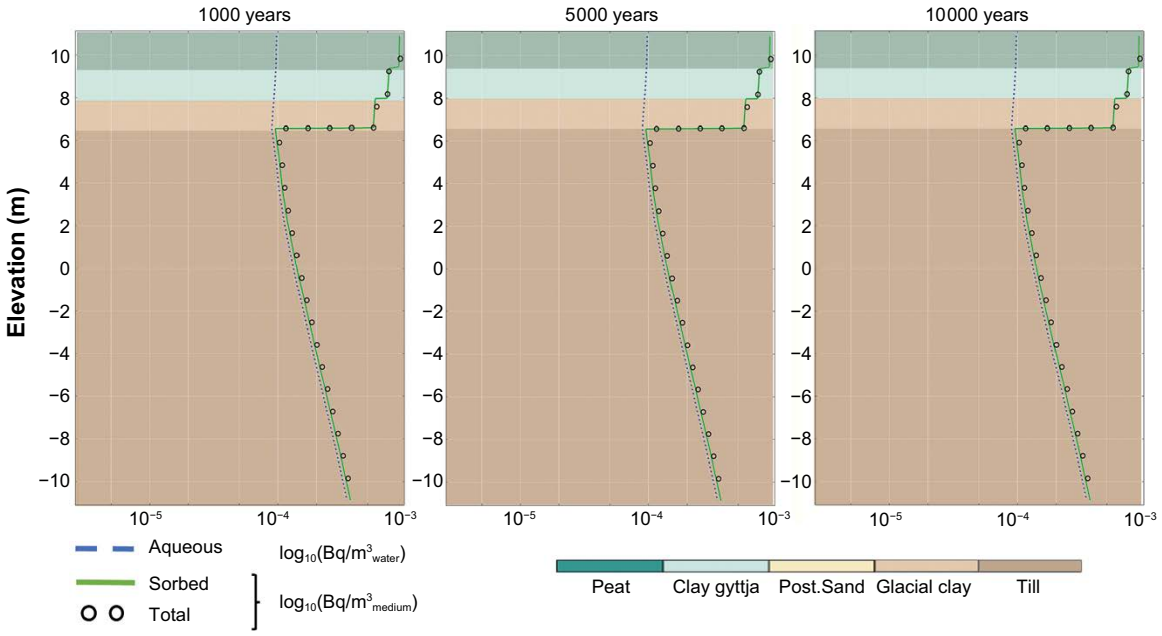

Figure B-2. *Profile of ^{36}Cl activity concentration aqueous, sorbed and total in the 1D vertical profile of point 2 at basin 210 (see Figure 3-2) for simulation times 1 000, 5 000 and 10 000. Note that the x axis is logarithmic.*

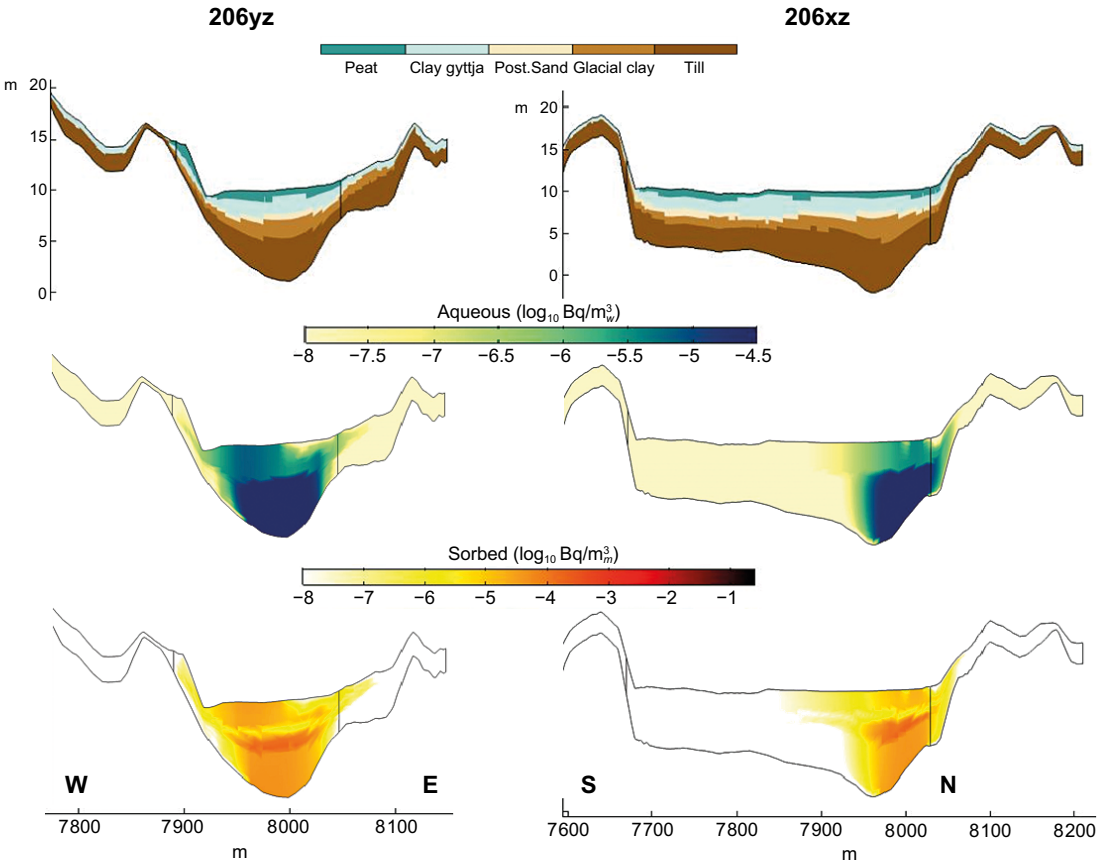

Figure B-3. *^{36}Cl activity concentration in pore water (log_{10} Bq·m$^{-3}_{water}$) and sorbed (log_{10} Bq·m$^{-3}_{medium}$) at 206 yz (left) and 206 xz (right) vertical profiles in basin 206 after 10 000 years. The location of the cross section is shown in Figure 3-2. Regolith materials are shown in the topmost panel. The thin vertical lines delimit the extension of the biosphere object. The vertical axis is exaggerated 5 times. Note that the concentrations are displayed in a logarithmic scale. Coordinates are given in local reference system.*

Nickel-59

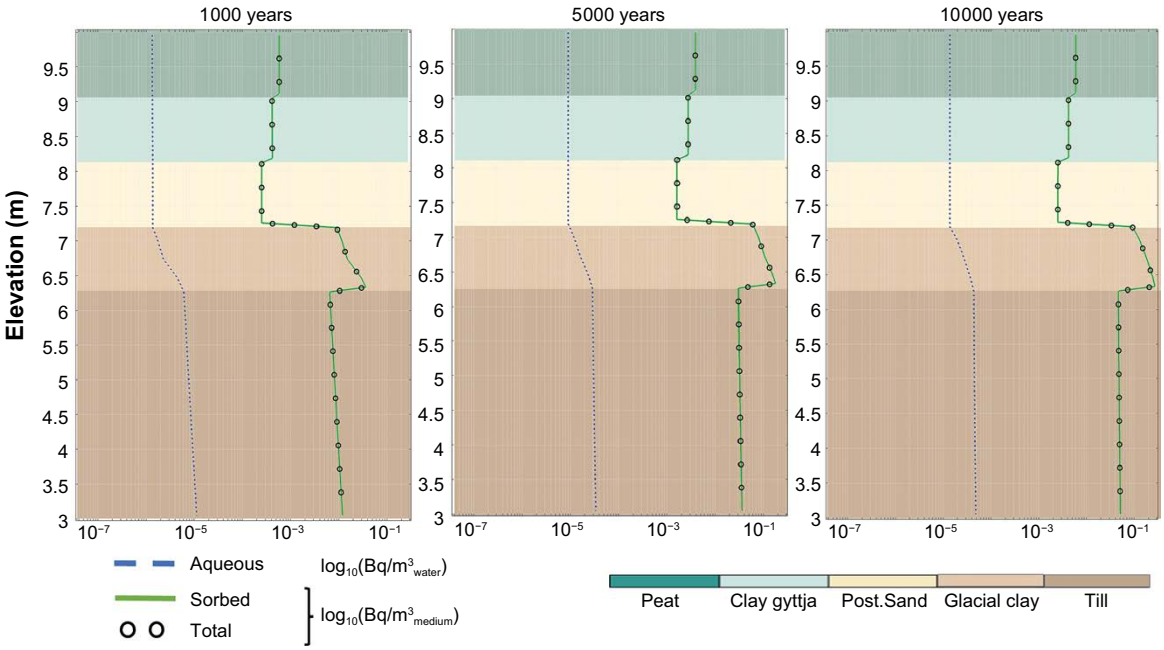

Figure B-4. *Profile of ^{59}Ni activity concentration aqueous, sorbed and total in the 1D vertical profile of point 1 at basin 206 (see Figure 3-2) for simulation times 1 000, 5 000 and 10 000. Note that the x axis is logarithmic.*

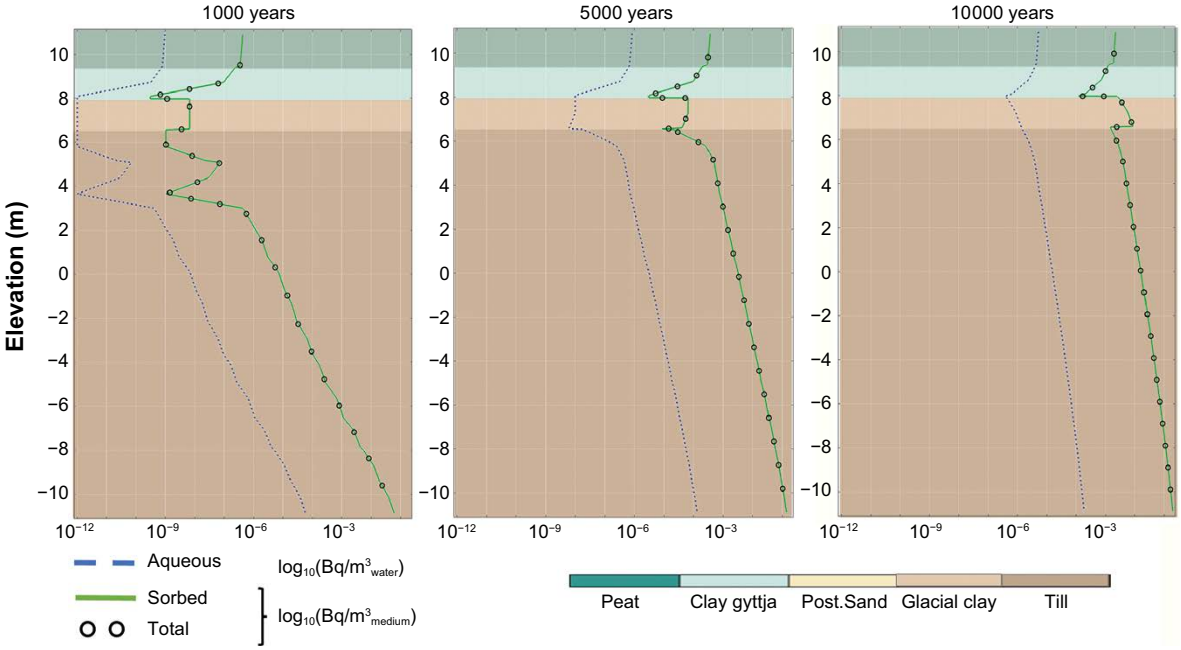

Figure B-5. *Profile of ^{59}Ni activity concentration aqueous, sorbed and total in the 1D vertical profile of point 2 at basin 210 (see Figure 3-2) for simulation times 1 000, 5 000 and 10 000. Note that the x axis is logarithmic.*

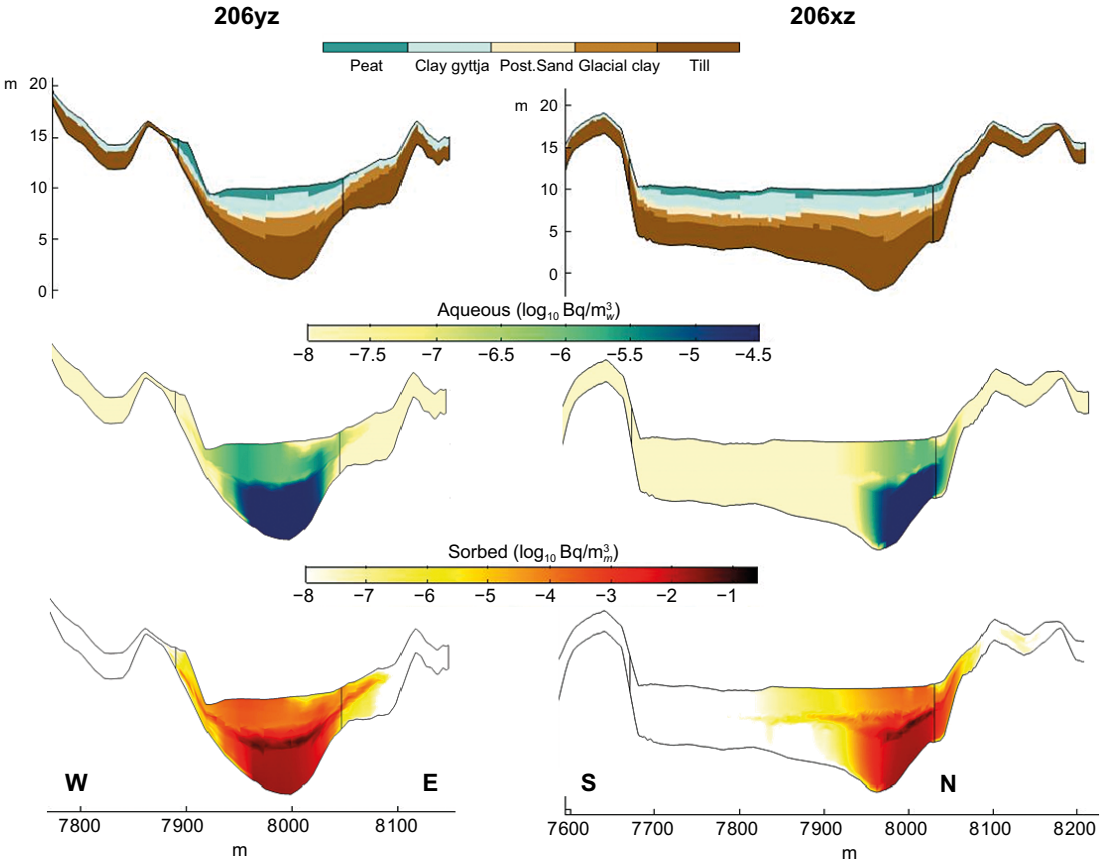

Figure B-6. *Nickel-59 activity concentration in pore water (log_{10} Bq·m^3water) and sorbed (log_{10} Bq·m_m^{-3}) at 206 yz (left) and 206 xz (right) vertical profiles in basin 206 at 10 000 years. The location of the cross section is shown in Figure 3-2. Regolith materials are shown in the topmost panel. The thin vertical lines delimit the extension of the biosphere object. The vertical axis is exaggerated 5 times. Note that the concentrations are displayed in a logarithmic scale. Coordinates are given in local reference system.*

Cesium-135

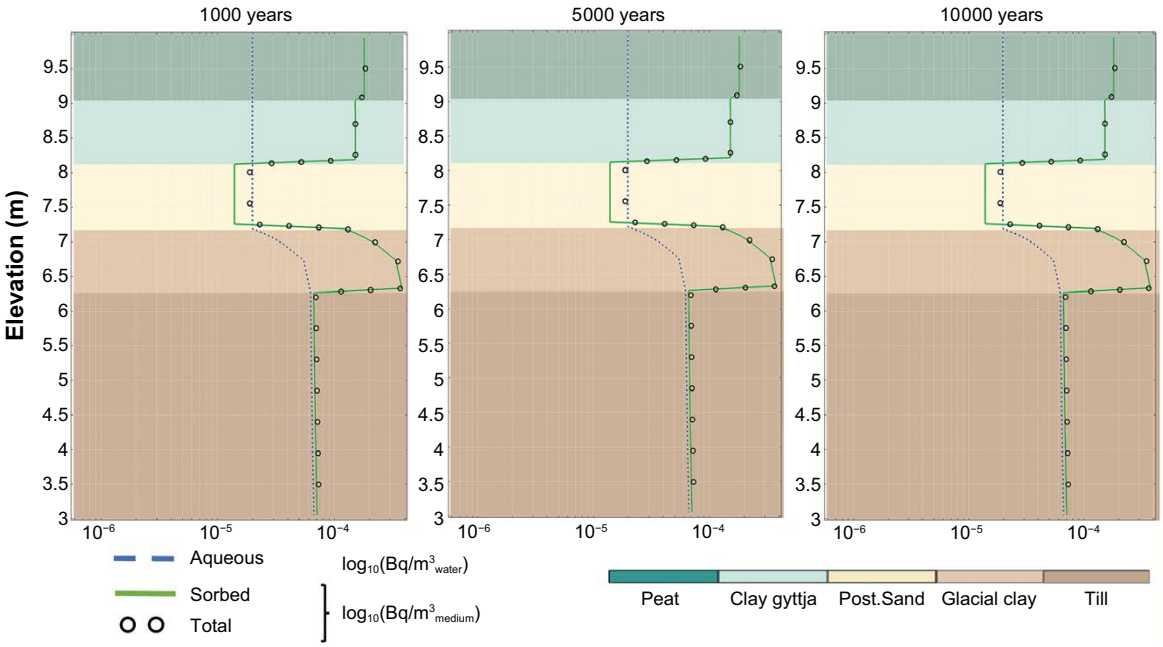

Figure B-7. *Profile of ^{135}Cs activity concentration aqueous, sorbed and total in the 1D vertical profile of point 1 at basin 206 (see Figure 3-2) for simulation times 1 000, 5 000 and 10 000. Note that the x axis is logarithmic.*

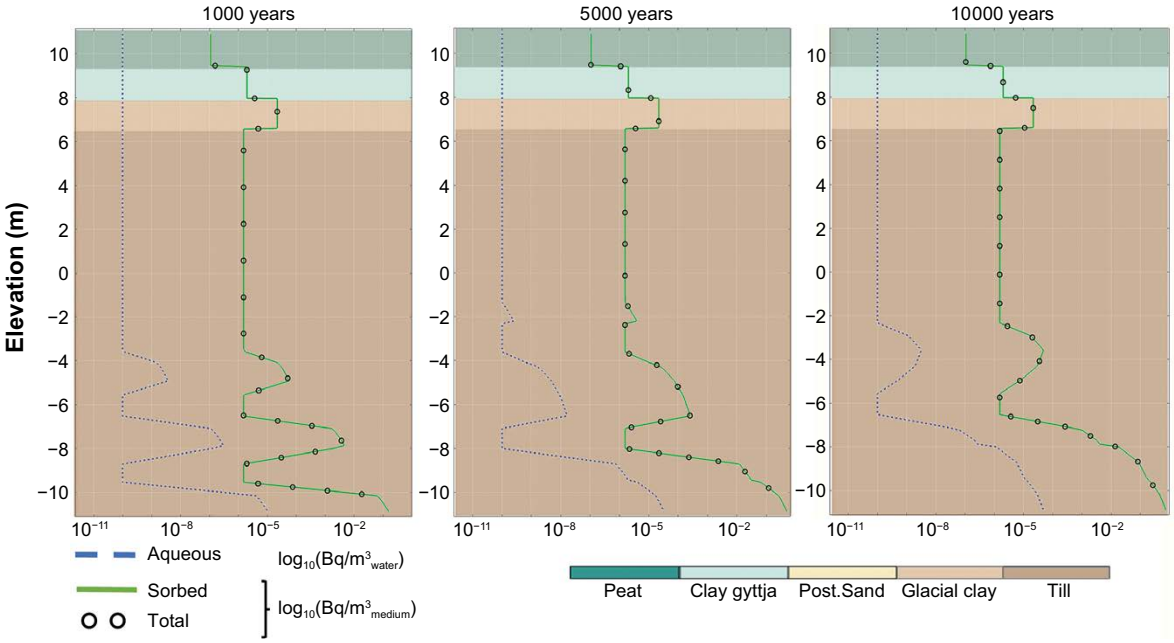

Figure B-8. *Profile of ^{135}Cs activity concentration aqueous, sorbed and total in the 1D vertical profile of point 2 at basin 210 (see Figure 3-2) for simulation times 1 000, 5 000 and 10 000. Note that the x axis is logarithmic.*

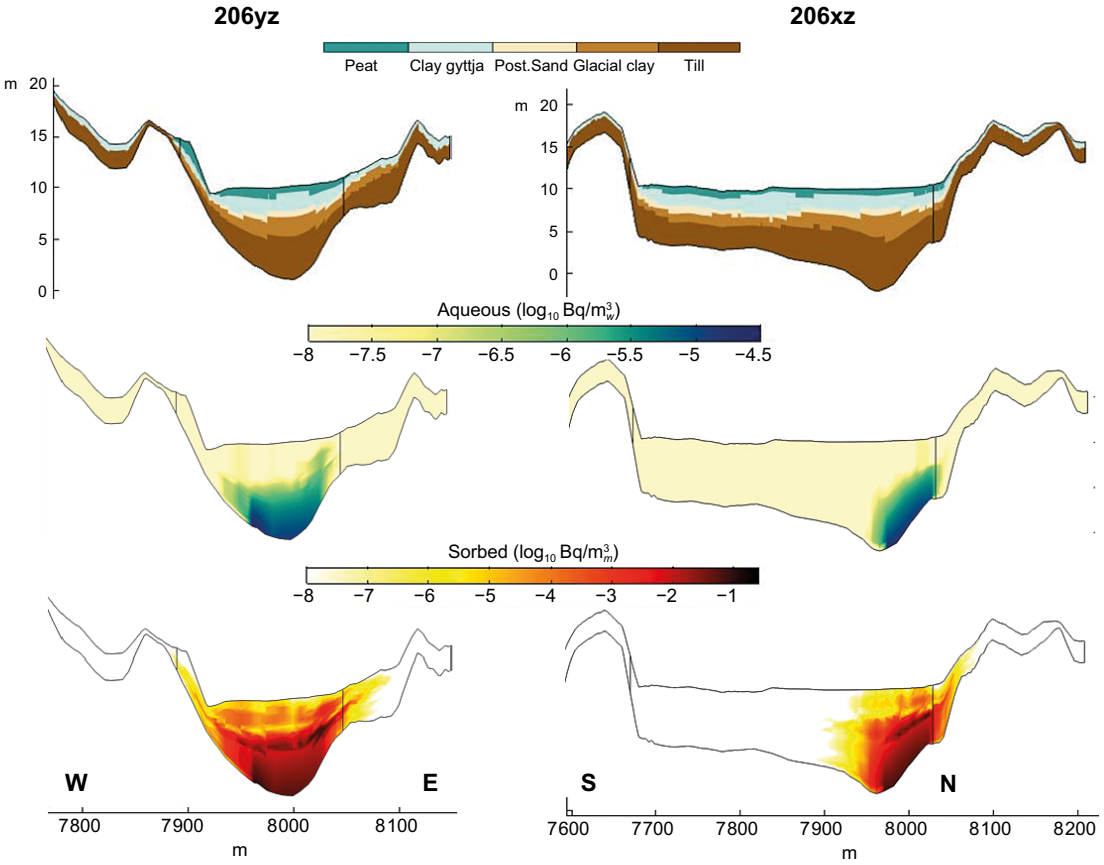

Figure B-9. *^{135}Cs activity concentration in pore water (log_{10} Bq·m^{-3}water) and sorbed (log_{10} Bq·m_m^{-3}) at 206 yz (left) and 206 xz (right) vertical profiles in basin 206 at 10 000 years. The location of the cross section is shown in Figure 3-2. Regolith materials are shown in the topmost panel. The thin vertical lines delimit the extension of the biosphere object. The vertical axis is exaggerated 5 times. Note that the concentrations are displayed in a logarithmic scale. Coordinates are given in local reference system.*

Radium-226

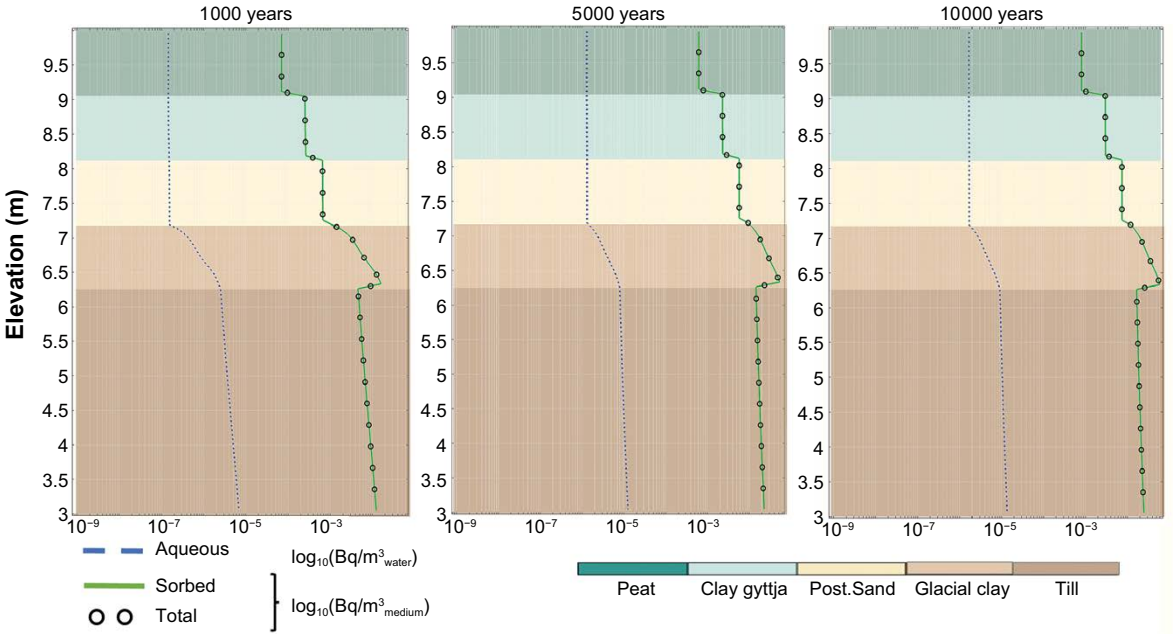

Figure B-10. *Profile of ^{226}Ra activity concentration aqueous, sorbed and total in the 1D vertical profile of point 1 at basin 206 (see Figure 3-2) for simulation times 1 000, 5 000 and 10 000. Note that the x axis is logarithmic.*

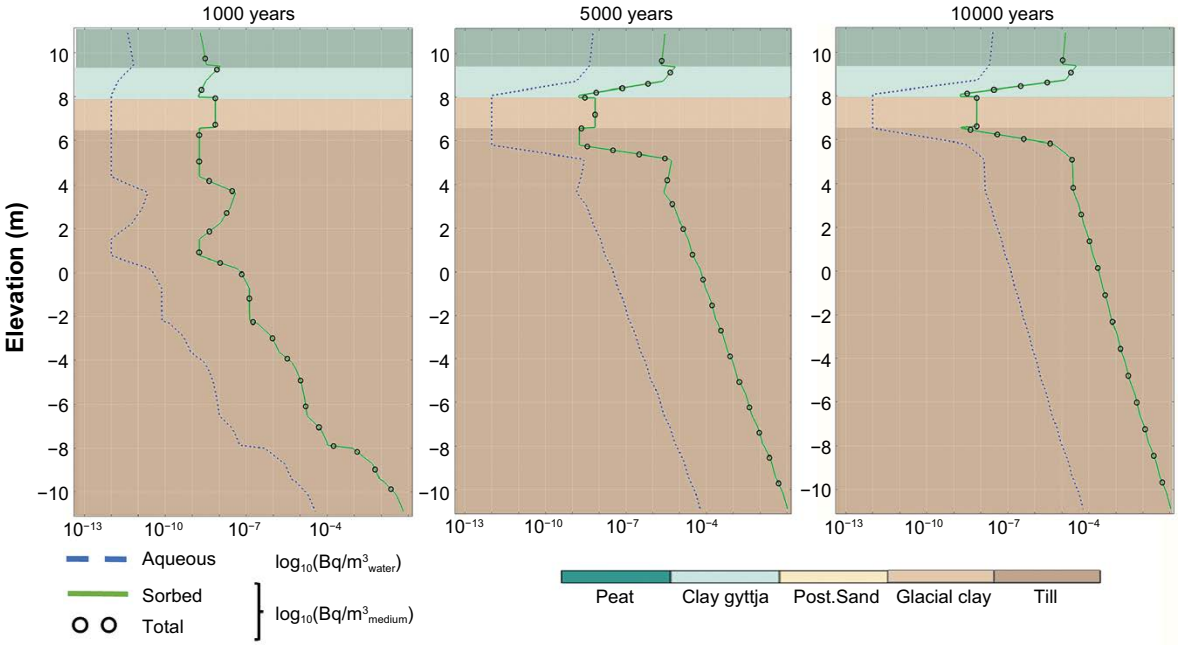

Figure B-11. *Profile of ^{226}Ra activity concentration aqueous, sorbed and total in the 1D vertical profile of point 2 at basin 210 (see Figure 3-2) for simulation times 1 000, 5 000 and 10 000. Note that the x axis is logarithmic.*

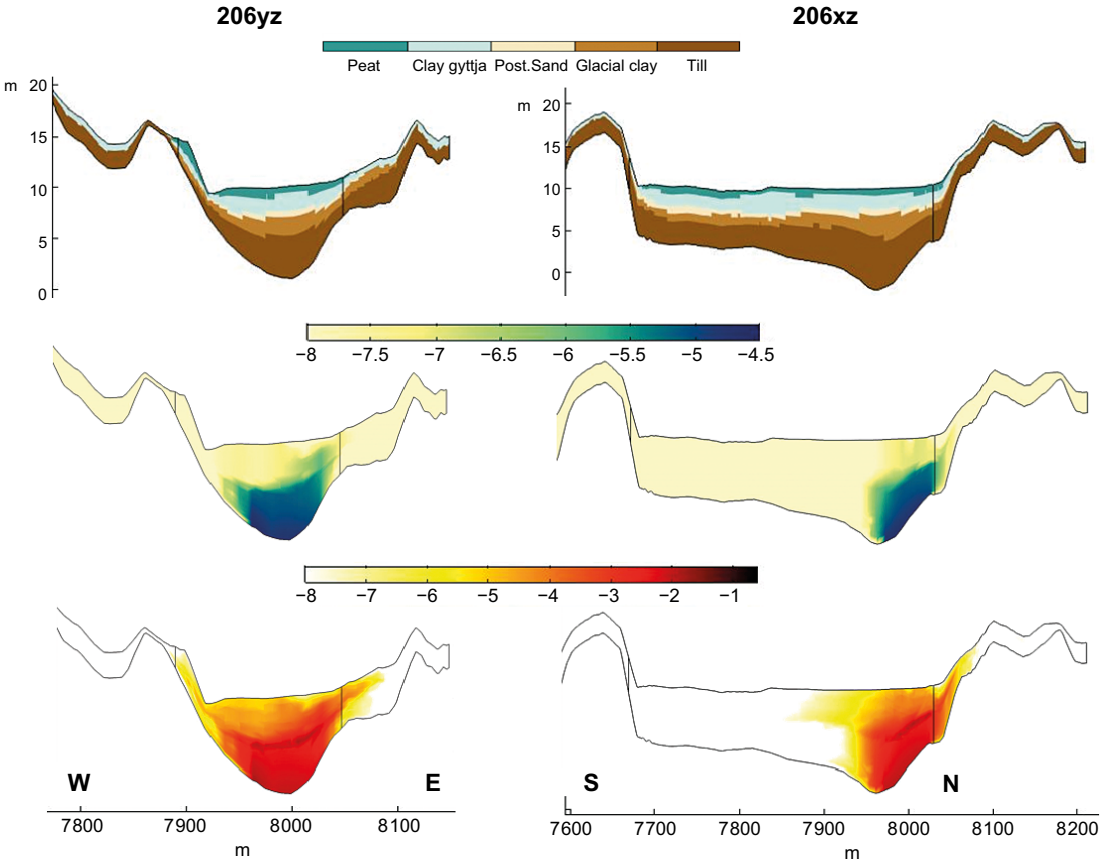

Figure B-12. *^{226}Ra activity concentration in pore water (log_{10} Bq·m^{-3}water) and sorbed (log_{10} Bq·m$_m^{-3}$) at 206 yz (left) and 206 xz (right) vertical profiles in basin 206 at 10 000 years. The location of the cross section is shown in Figure 3-2. Regolith materials are shown in the topmost panel. The thin vertical lines delimit the extension of the biosphere object. The vertical axis is exaggerated 5 times. Note that the concentrations are displayed in a logarithmic scale. Coordinates are given in local reference system.*

Molybdenum-93

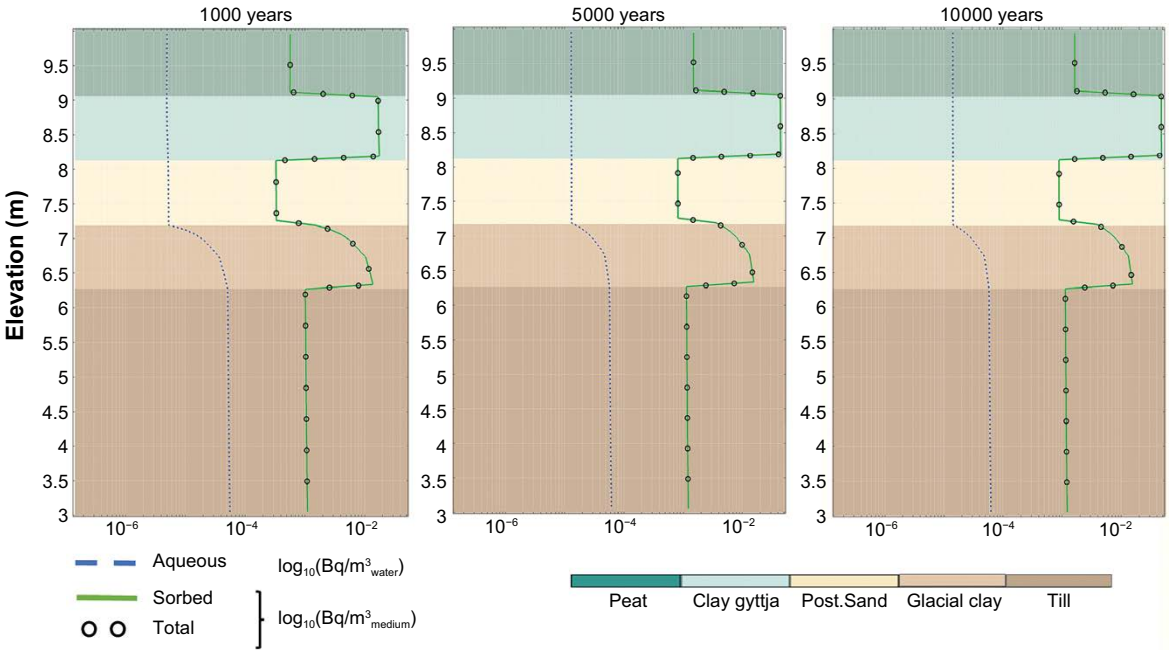

Figure B-13. *Profile of ^{93}Mo activity concentration aqueous, sorbed and total in the 1D vertical profile of point 1 at basin 206 (see Figure 3-2) for simulation times 1 000, 5 000 and 10 000. Note that the x axis is logarithmic.*

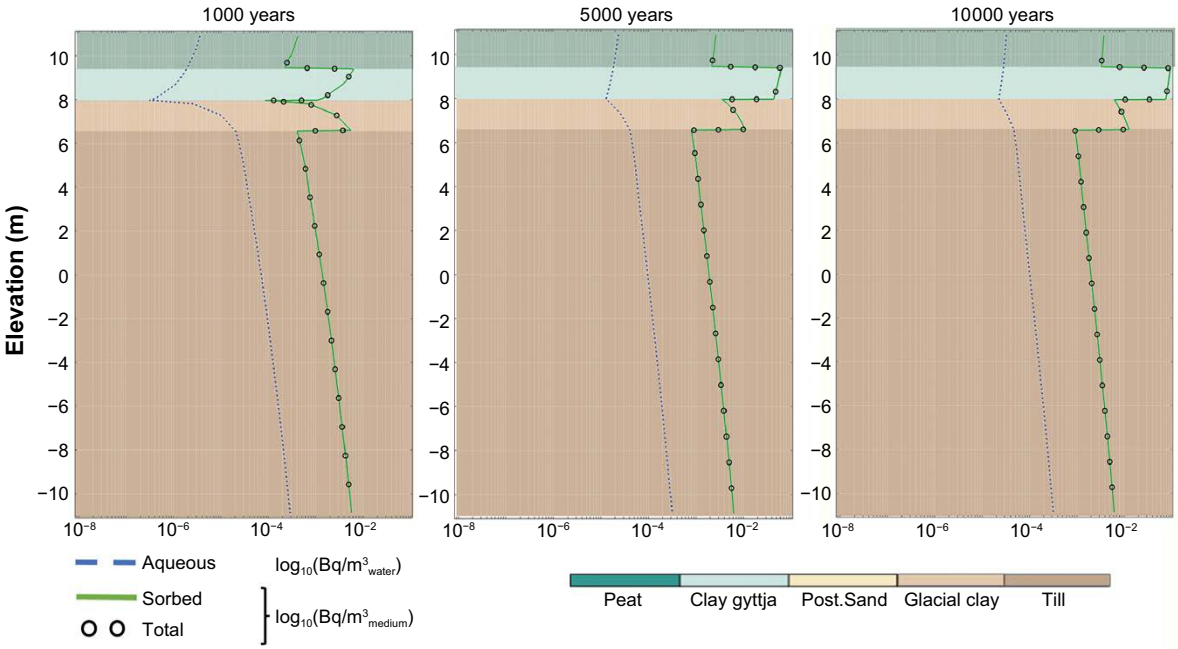

Figure B-14. *Profile of ^{93}Mo activity concentration aqueous, sorbed and total in the 1D vertical profile of point 2 at basin 210 (see Figure 3-2) for simulation times 1 000, 5 000 and 10 000. Note that the x axis is logarithmic.*

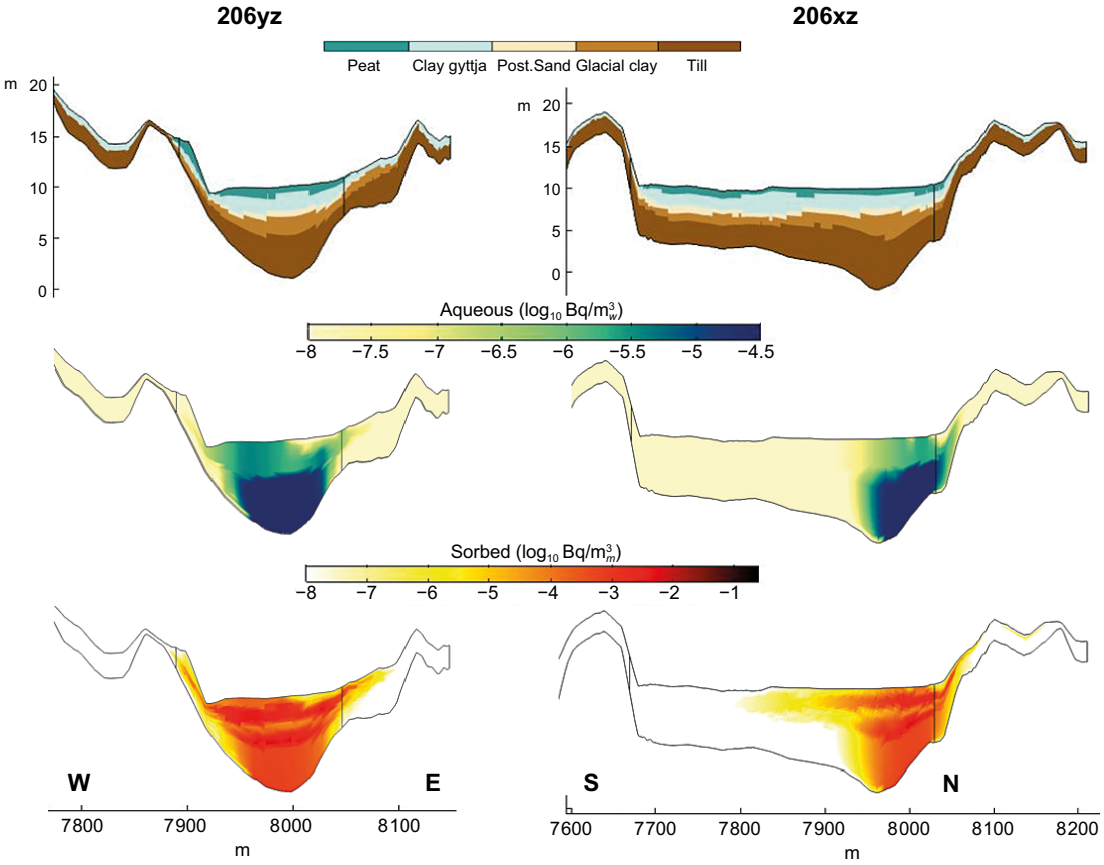

Figure B-15. *^{93}Mo activity concentration in pore water (log_{10} Bq·m^{-3}water) and sorbed (log_{10} Bq·m_m^{-3}) at 206 yz (left) and 206 xz (right) vertical profiles in basin 206 at 10 000 years. The location of the cross section is shown in Figure 3-2. Regolith materials are shown in the topmost panel. The thin vertical lines delimit the extension of the biosphere object. The vertical axis is exaggerated 5 times. Note that the concentrations are displayed in a logarithmic scale. Coordinates are given in local reference system.*

Appendix C

1D distributed reactive model of radionuclides retention processes in the till and clay

Introduction

The geochemical reactions expected when deep groundwater enriched in radionuclides arrives to the regolith are analyzed through 1D models with idealized geometry and hydrodynamics. Till and clay materials are studied separately to better understand the influence of the radionuclide-rich bedrock water.

Hydrogeochemical initial and boundary conditions

The mineralogical compositions of the till and clay systems and the porewater chemistry considered (radionuclides-rich deep groundwater, till and clay) are those explained in Section 2.8.

In the chemical system proposed, radionuclides can be chemically retained by sorption/exchange (in illite or ferrihydrite) or by solid-solutions precipitation ($(Ca,Sr)CO_3$ or $(Ba,Ra)SO_4$) in the chemical system proposed. Deep porewater with radionuclides is the same as deep groundwater (soil pipe SFM0023) but considering the presence of radionuclides as explained in Section 2.8. Till porewater is that resulting of equilibrating the experimental till porewater (from groundwater monitoring well SFM0002 (Tröjbom and Söderbäck 2006)) with calcite and barite solid-solutions, siderite and ferrihydrite. Clay porewater is that resulting from equilibrating the experimental clay porewater (from site PFM000117 (Andersson et al. 2003)) with calcite and barite solid-solutions, siderite and pyrite.

The chemical processes accounted for are described in Section 2.8 (Table 2-5, Table 2-7 and Table 2-8). The initial composition of the exchanger and surface positions of the different minerals are explained in Section 5.4 (Table 2-3, Table 5-3, Table 5-4 and Table 5-5).

Model description

Both models consist of a 0.2 m long column initially filled with water in equilibrium with clay or till. The columns are saturated and have a constant groundwater flow from left to right. The flux has been chosen to maintain a similar solute travel time in both models (the hydrodynamic parameters of the model are shown in Table C-1).

As for the mechanistic 3D model described in Section 4 and 6, the model is implemented with the interface COMSOL-PhreeqC (iCP) (Nardi et al. 2014). The groundwater flow is prescribed, and no flow equations are solved. The equation of conservative transport in porous media to be solved is:

$$\omega \frac{\partial \boldsymbol{c}}{\partial t} = -\psi \boldsymbol{u} \nabla \boldsymbol{c} + \nabla \cdot (\psi \boldsymbol{D_l} \nabla \boldsymbol{c}) - \boldsymbol{c} \nabla \cdot \rho_l \boldsymbol{D_l} \nabla \omega_l^w$$

where $\omega = \theta_s S_l \rho_l \omega_l^w$ and $\psi = \rho_l \omega_l^w$ are auxiliary variables used for notation convenience and c is the concentration vector of all species (mol·kgw^{-1}). The term "kgw" denotes kilogram of pure water. S_l is the liquid saturation (-), ρ_l is the liquid density (kg·m^{-3}), ω_l^w is the pure water mass fraction in the liquid (-), $\boldsymbol{u}$ is the Darcy flow vector (m·s^{-1}) and $\boldsymbol{D_l}$ is the effective diffusion/dispersion tensor (m^2·s^{-1}). In this model no diffusion is considered.

An open boundary condition with the concentration of radionuclide-rich bedrock water is imposed at the left boundary. No flow is allowed through the upper and lower boundaries, while an outflow boundary is prescribed at the right end. The total time of the simulations is 50 days and equal time step (0.25 days) and spatial discretization (1 mm) is used in both models.

Figure C-1. *Conceptual model. The domain is composed by till or clay with waters initially in equilibrium with those materials.*

Table C-1. Hydrodynamic parameters of the models.

Parameter	Till Model	Clay Model	Unit
Effective porosity	0.05	0.25	-
Darcy flow	1.1574×10^{-8}	5.78710^{-8}	m·s
Dispersivity	0.08	0.08	m
Water density	1000	1000	$Kg \cdot m^3$

Results

The results shown in this section are calculated in moles per liter of medium, unless otherwise stated, considering medium as the solid and porous fraction of the aquifer. The temporal evolutions at two points (Figure C-2) are shown for aqueous species together with the concentrations along the domain for different times.

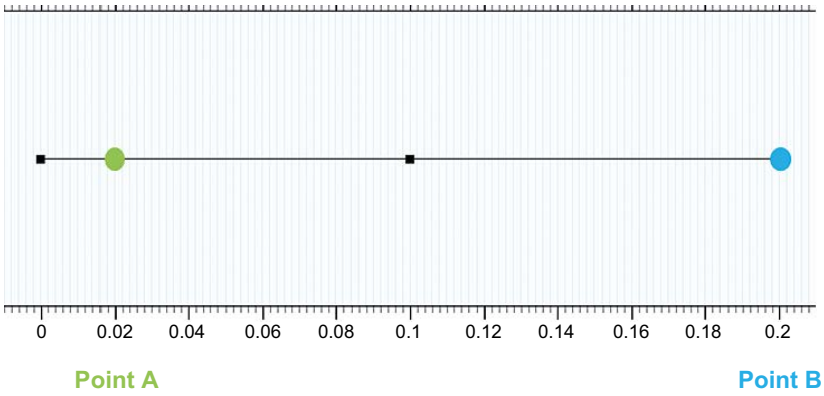

Figure C-2. *Location of the observation points in the 1-D system. Point A is located at the beginning of the domain while point B is located at the end of the domain.*

Till

Results obtained for the evolution of a tracer component (^{36}Cl) in the system are shown in Figure C-3. As seen in the figure, the tracer arrived at the end of the 0.2 m column after 40 days of simulation time.

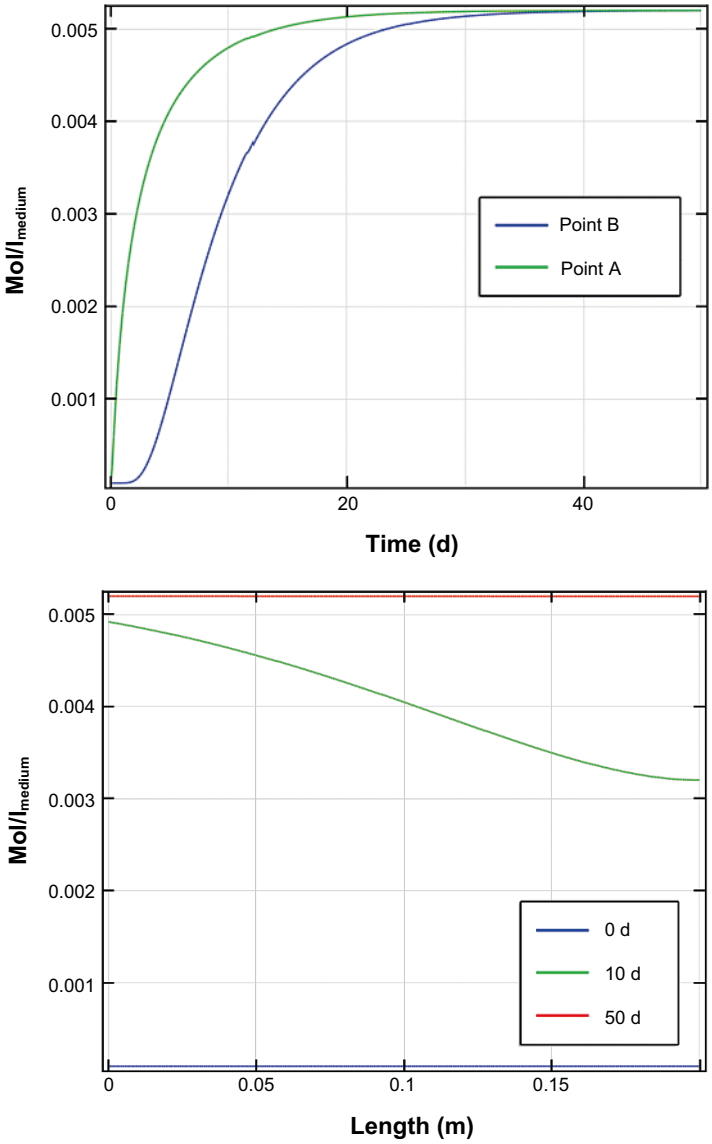

Figure C-3. *Evolution of ^{36}Cl concentration ($mol \cdot l_{medium}^{-1}$) as a function of time on the two different observation points (top), and in the whole domain at three different times (bottom).*

Initial pH conditions in the till (pH ~7.1) are slightly modified by the intrusion of the deep groundwater (pH ~6.8) as seen in Figure C-4. After 50 days of simulation, the till system pH is almost the same as that in the intruding deep groundwater in the whole column.

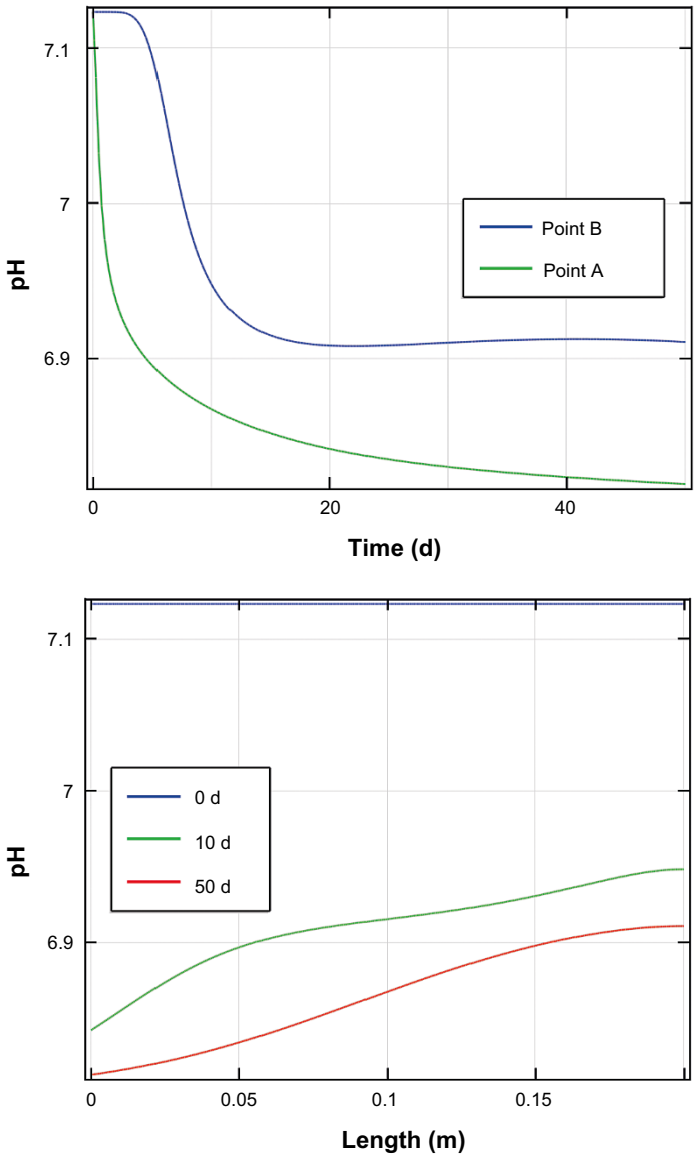

Figure C-4. *Evolution of pH as a function of time on the two different observation points (top), and in the whole domain at three different times (bottom).*

Sodium concentration entering the system ($\sim 10^{-2}$ M) is one order of magnitude higher than the initial sodium concentration in the till ($\sim 10^{-3}$ M). Contrary to non-reactive $^{36}Cl^-$, Na did not reach the inflow solution value at the end of the column after 50 days (Figure C-5). Na intrusion alters the illite exchanger positions (Figure C-6), which become richer in Na while releasing other cations (i.e., Ca).

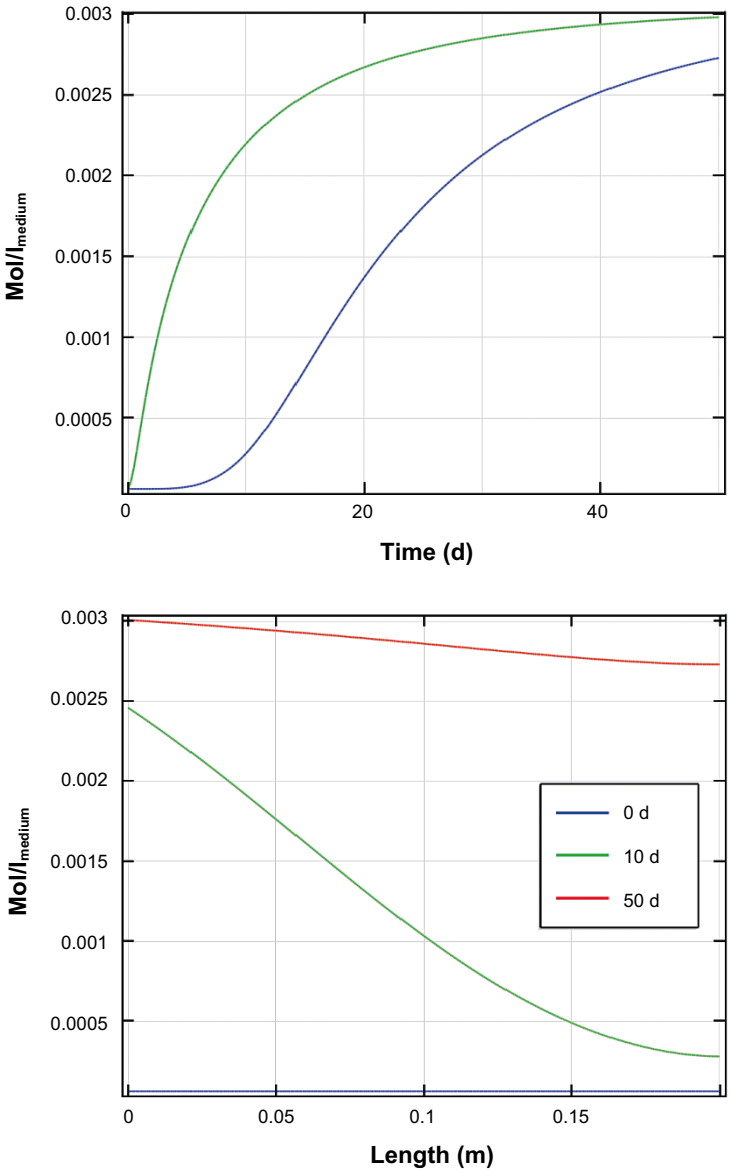

Figure C-5. *Evolution of aqueous sodium concentration (mol·l_{medium}^{-1}) as a function of time at the two different observation points (top), and in the whole domain at three different times (bottom).*

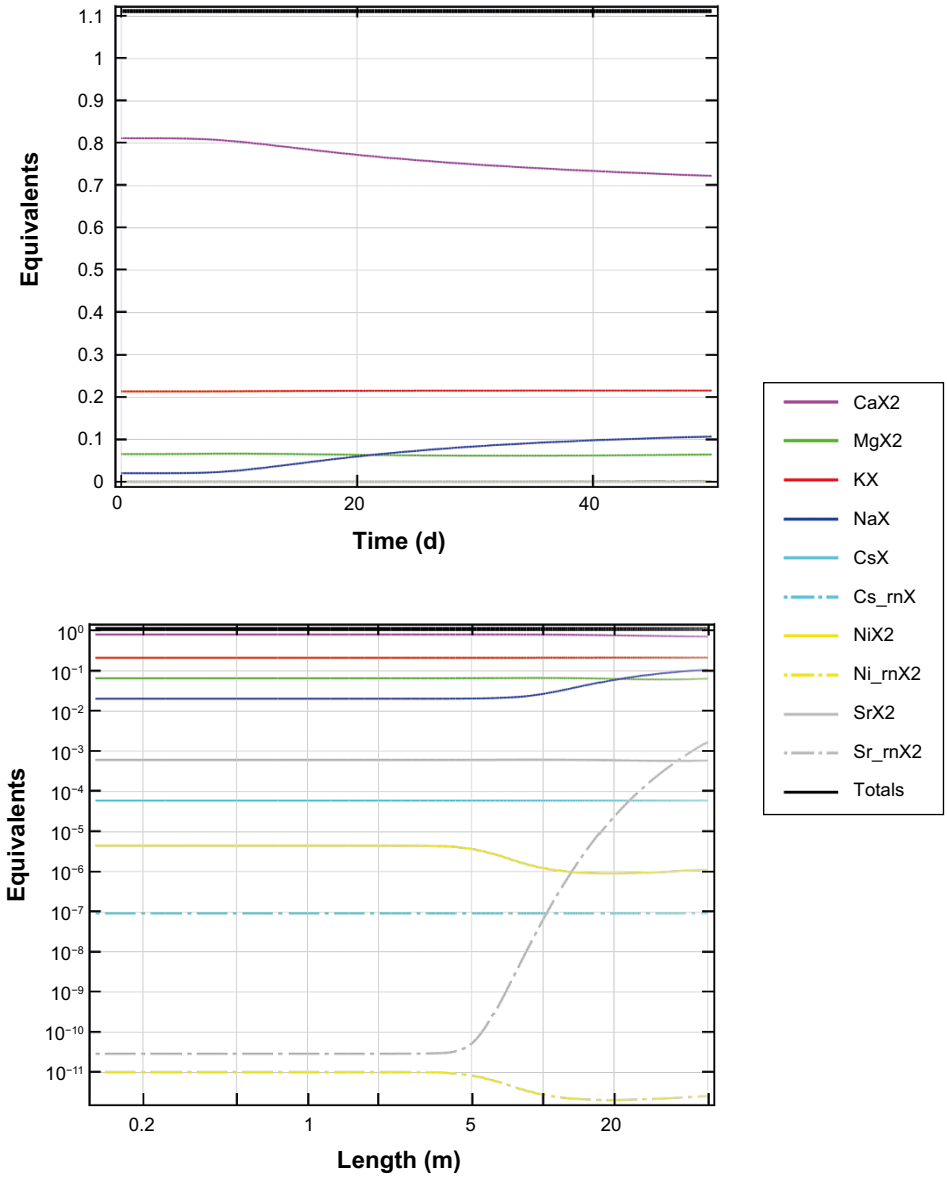

Figure C-6. *Evolution of the illite exchange positions (equivalents·l_{medium}^{-1}) as a function of time in the observation point A: normal scale (top), and log scale (bottom).*

Calcium behavior in the system is somewhat complex as different process are affecting this element (Figure C-7). As for sodium, calcium entering the system is higher than the initial concentration in the till (~1 order of magnitude). Higher Ca concentration together with the slight pH decrease in the till (Figure C-4), produces (Ca,Sr)CO_3 solid-solution precipitation in the whole column (Figure C-8). Note that higher amounts of solid precipitate at the beginning of the column where the effect of the input solution is more relevant.

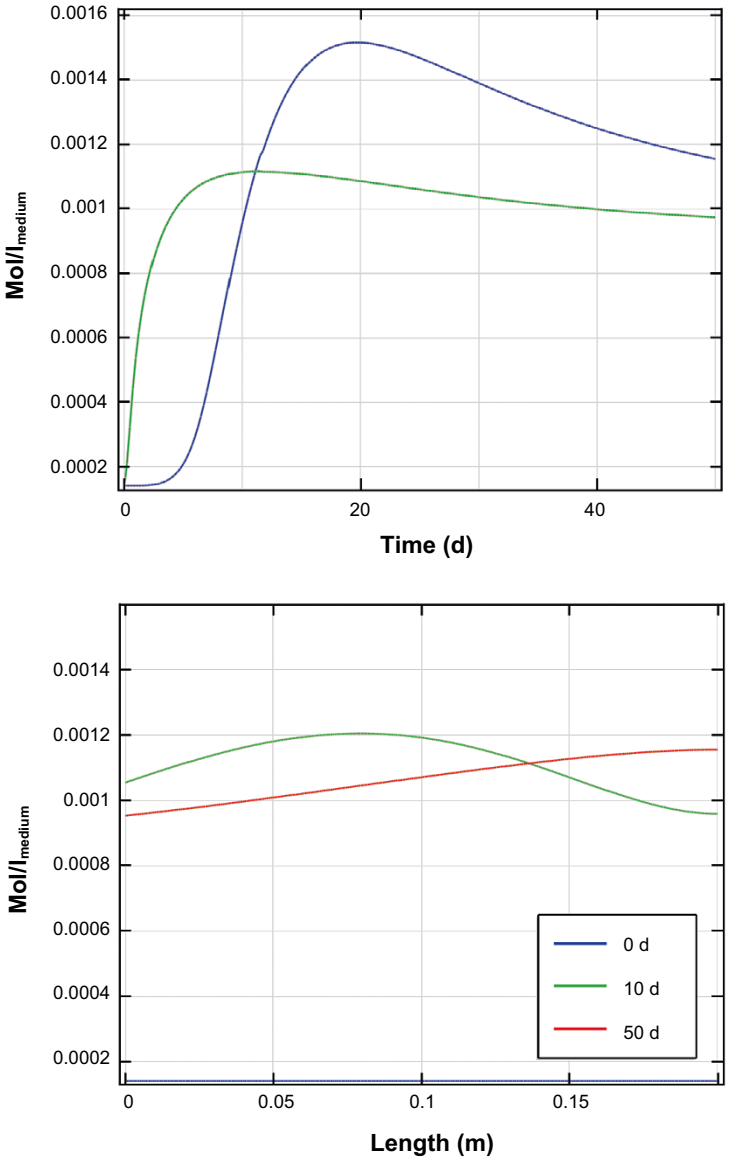

Figure C-7. *Evolution of aqueous calcium concentration (mol·l_{medium}^{-1}) as a function of time on the two different observation points (top), and in the whole domain at three different times (bottom).*

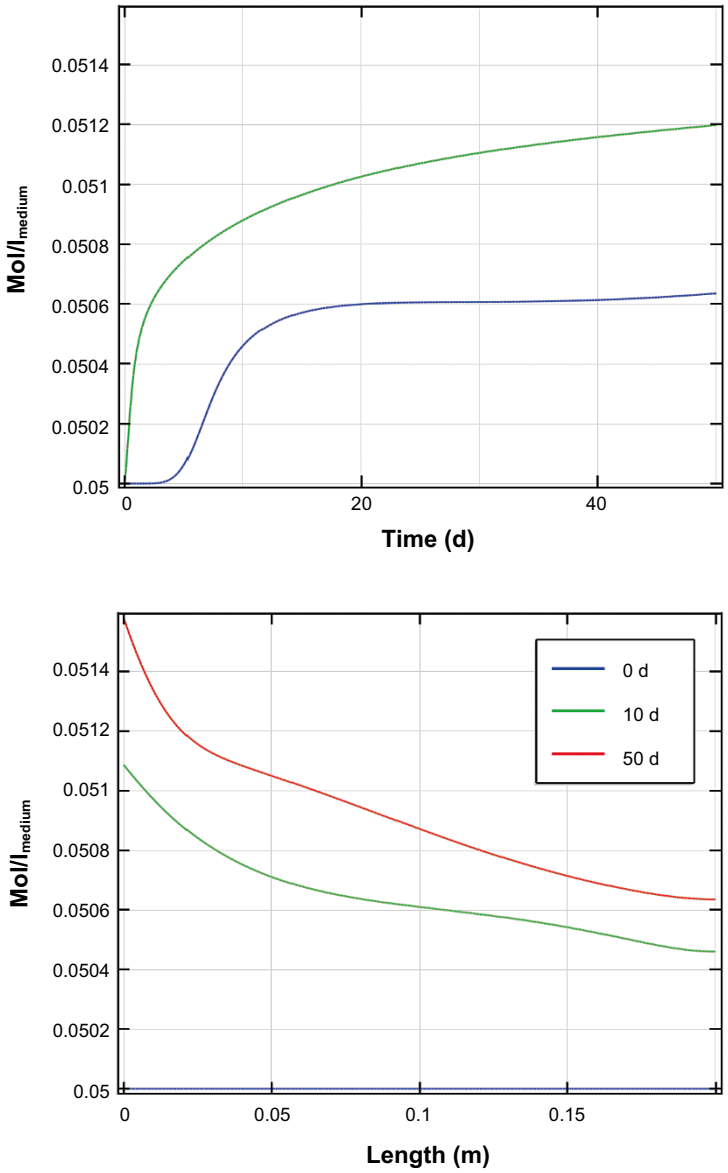

Figure C-8. *Evolution of (Ca,Sr)CO_3 solid-solution (mol·l_{medium}^{-1}) as a function of time on the two different observation points (top), and in the whole domain at three different times (bottom).*

Radioactive strontium entering the till domain is retained through different processes, exchange and solid-solution precipitation, as shown in Figure C-9. The exchange of Sr within the illite sites (species Sr_rnX_2, Figure C-6) is by far the most important retention process, with the exchanged amount of Sr being more than one order of magnitude higher than the precipitated as (Ca,Sr)CO_3 solid-solution (Figure C-9). Overall, the retention processes prevent the rise of the Sr aqueous concentration. After 50 days at the end of the column the aqueous Sr is ~10^{-5} M, while the inflow solution is in the order of ~10^{-3} M (inflow solution detailed in Table 2-4).

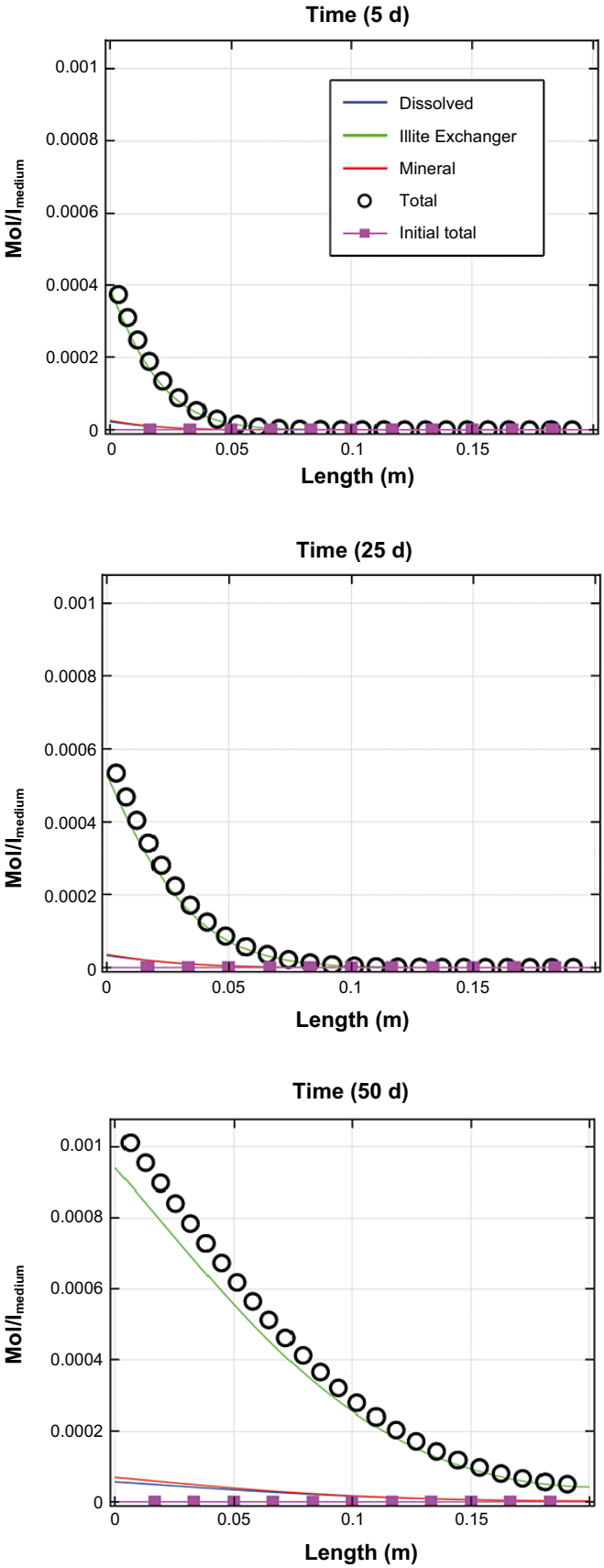

Figure C-9. *Evolution of radioactive Sr (mol·l_{medium}^{-1}), free aqueous species and retained species, in the whole domain after 5, 25 and 50 days of simulation time.*

Cesium (Figure C-10) is almost completely retained in the illite FES exchange positions (species Cs_rnXb = CsX^{FES}, Figure C-6). Contrary to what we observe in the Sr case, Cs is almost completely retained in the first column centimeters (~0.05 m), indicating the strong capacity of the illite surface for uptake of this element. Aqueous concentrations of this element after 50 days of simulation time are down to 10^{-10} mol·l_{medium}^{-1} in the whole column. Nickel performs similarly (Figure C-11), being strongly adsorbed onto the mineral surfaces. Almost the whole amount of radioactive Ni is retained on the illite surface with minor contributions from the ferrihydrite surface. The main difference is that the Ni surface complexation (mainly through the species $\equiv SO^{s}ONi^{+}$) is causing the retention onto the mineral surfaces, while the chemical process that retained the Cs is cationic exchange. Aqueous concentrations of Ni element after 50 days of simulation time are down to ~10^{-8} mol·l_{medium}^{-1} at the end of the 0.2-metre column.

Radium immobilization occurs in the system through the precipitation of a solid-solution with barite $(Ba,Ra)SO_4$ (Figure C-12 and Figure C-13). As seen in these figures at the beginning of the simulation the solid-solution precipitates intensively in the first column centimeters; but, as time passes the maximum precipitation peak is displaced through the column. This is due to the influence of the inflow solution composition. The intruding solution is richer in sulphate but poorer in barium than the till system (Table 2-4). In the beginning of the simulation there is enough barium in the first column centimeters to allow the precipitation of the $(Ba,Ra)SO_4$ solid-solution (Figure C-14). Sulphate is not a reactant limiting element (Figure C-15). As time passes, barium concentration is too low to allow the solid-solution precipitation in the first column centimeters and thus $(Ba,Ra)SO_4$ dissolves (Figure C-12). Therefore, we can conclude that although at short times radium is retained through the solid-solution precipitation, in long-term conditions the solid-solution assemblage re-dissolves releasing radium into the aqueous system again. The Ra aqueous concentration in the whole column decreases from ~2×10^{-11} mol·l_{medium}^{-1} down to ~5×10^{-12} mol·l_{medium}^{-1} after 50 days of simulation.

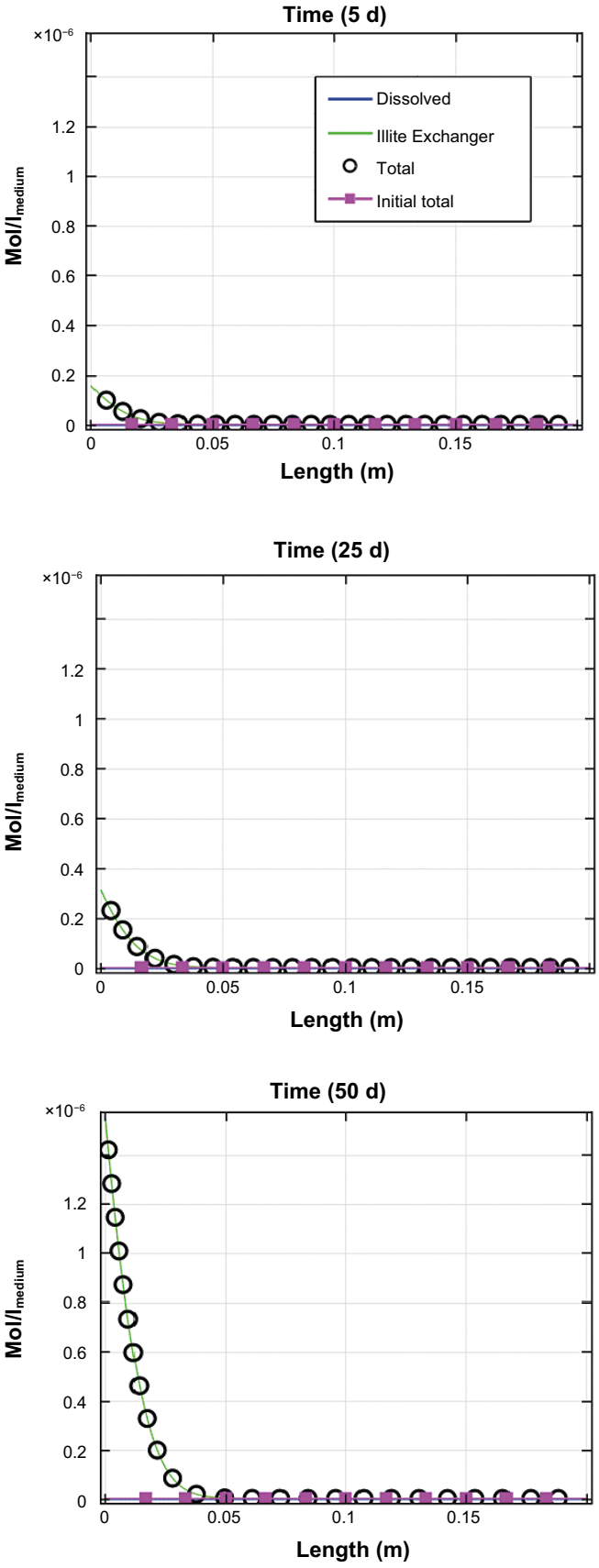

Figure C-10. *Evolution of radioactive Cs (mol·l_{medium}^{-1}) , free aqueous species and retained species, as a function of the distance after 5, 25 and 50 days of simulation time.*

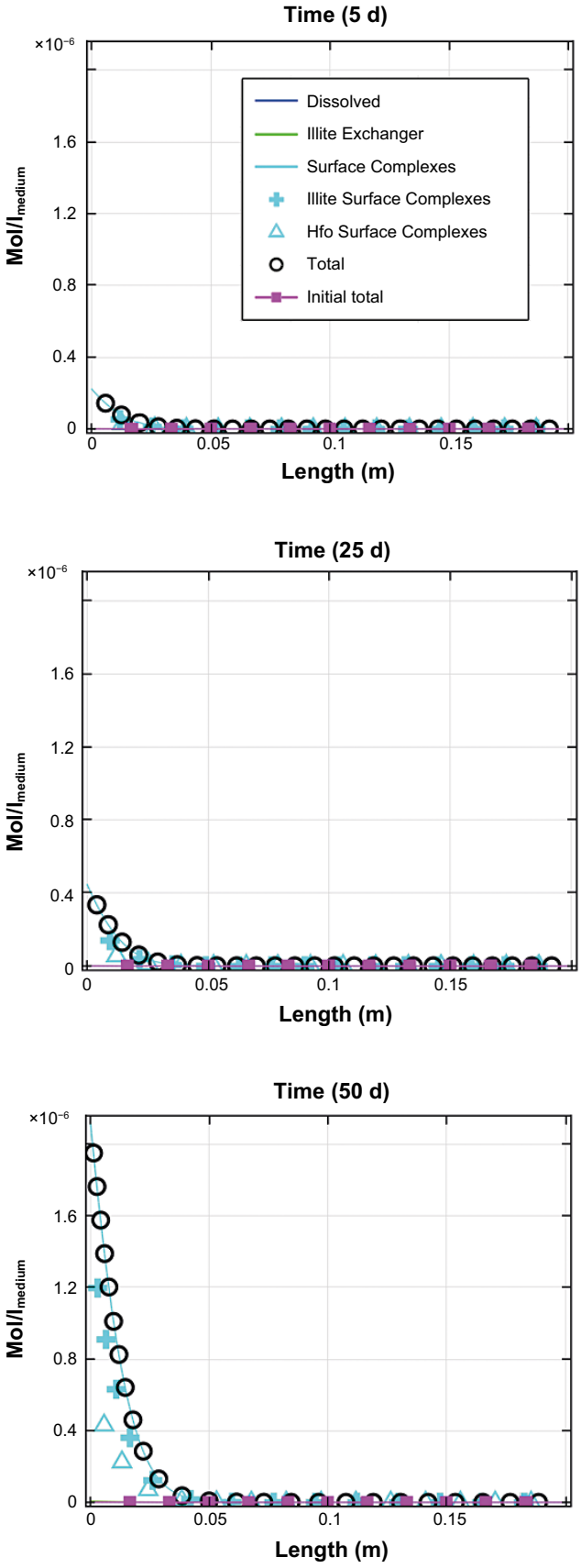

Figure C-11. *Evolution of radioactive Ni (mol·l_{medium}^{-1}), free aqueous species and retained species, in the whole domain after 5, 25 and 50 days of simulation time.*

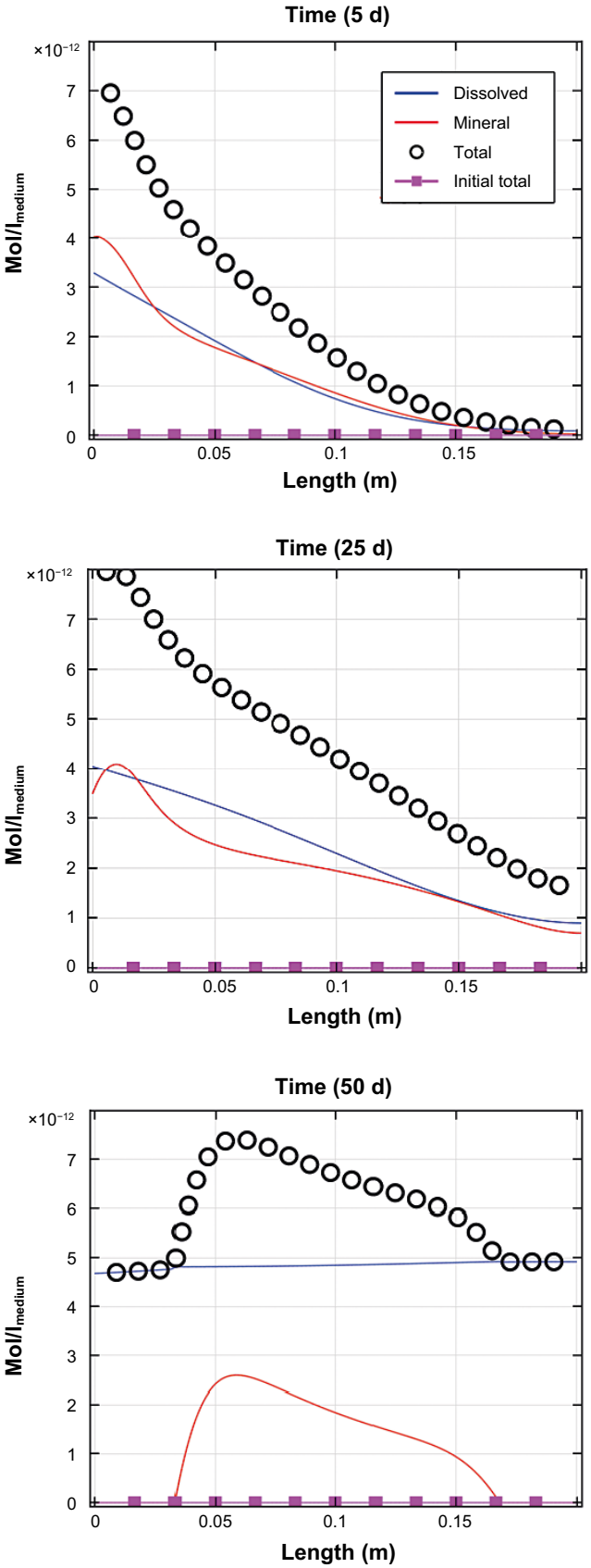

Figure C-12. *Evolution of radioactive Ra (mol·l_{medium}^{-1}), free aqueous species and retained species, in the whole domain after 5, 25 and 50 days of simulation time.*

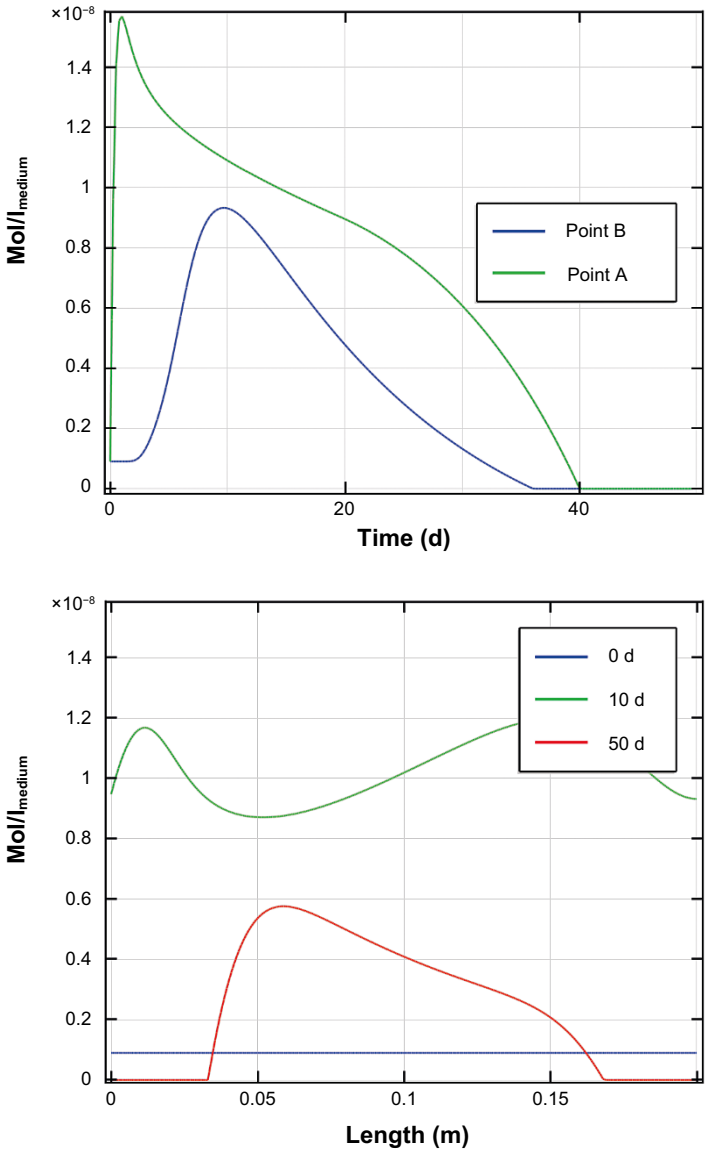

Figure C-13. *Evolution of (Ba,Ra)SO_4 solid-solution (mol·l_{medium}^{-1}) as a function of time on the two different observation points (top), and in the whole domain at three different times (bottom).*

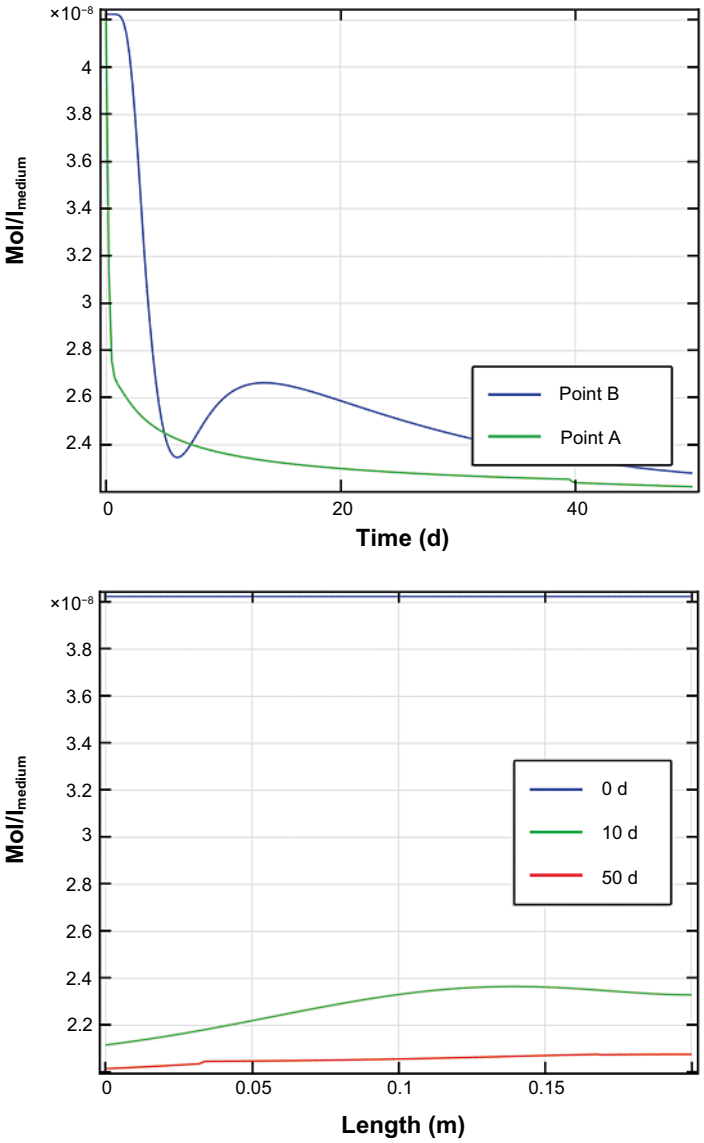

Figure C-14. *Evolution of barium (mol·l_{medium}^{-1}) as a function of time on the two different observation points (top), and in the whole domain at three different times (bottom).*

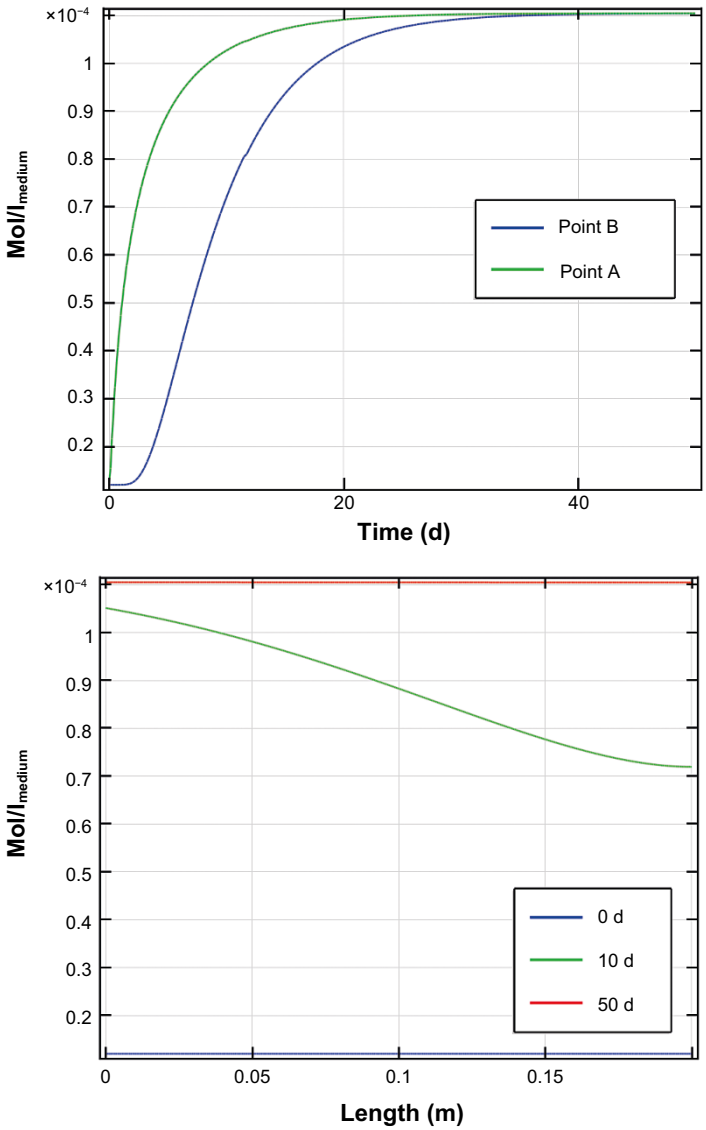

Figure C-15. *Evolution of sulphate (mol·l_{medium}^{-1}) as a function of time on the two different observation points (top), and in the whole domain at three different times (bottom).*

Figure C-16 compares the total amount of radionuclide introduced in the system and the amount of radionuclide present in the system. All the cesium and nickel-59 introduced in the system remain in the till after 50 days. Strontium behaves almost identically to cesium and nickel-59, although a small deviation between the introduced and the remaining amount at the end of the simulation could be seen. Part of the strontium crosses the column of till and is released at the right boundary. On the other hand, radium entering the system seems to be retained up to ~15 days. After that time a clear deviation is observed between the introduced and the retained amount of Ra in the system, indicating that this radionuclide reached is being released out of the till column. At 50 days the amount of radium retained is around 25 % of the total introduced.

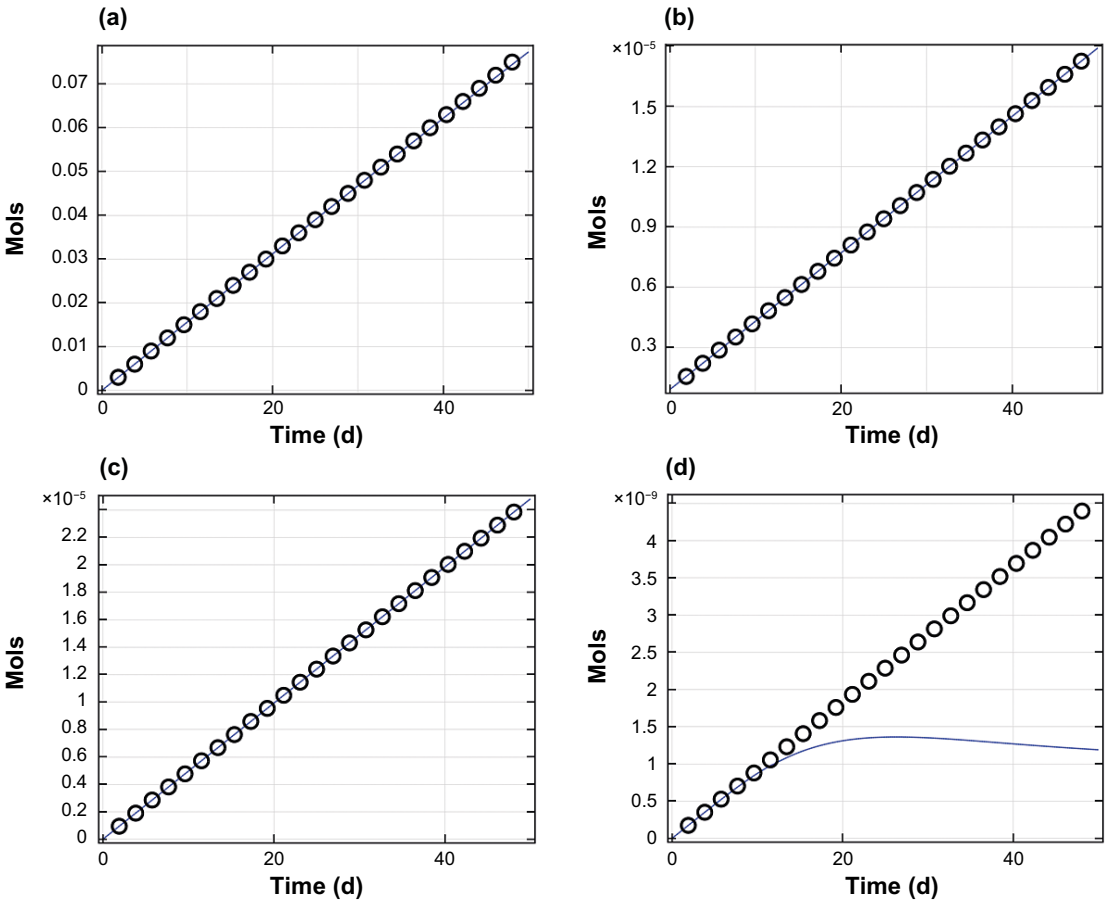

Figure C-16. *Evolution of accumulative amount of radionuclides (mol·m^{-2} system) as a function of time: (a) strontium, (b) cesium, (c) nickel-59, and (d) radium. Circles stand for the total amount of radionuclide introduced while the solid line stands for the amount of radionuclide present in the system.*

Clay

Results obtained for the clay system are very similar to those presented before for the till. The evolution of a tracer component (Figure C-17) does not differ from that presented in the previous model. The tracer arrived at the end of the domain after 40 days of simulation time.

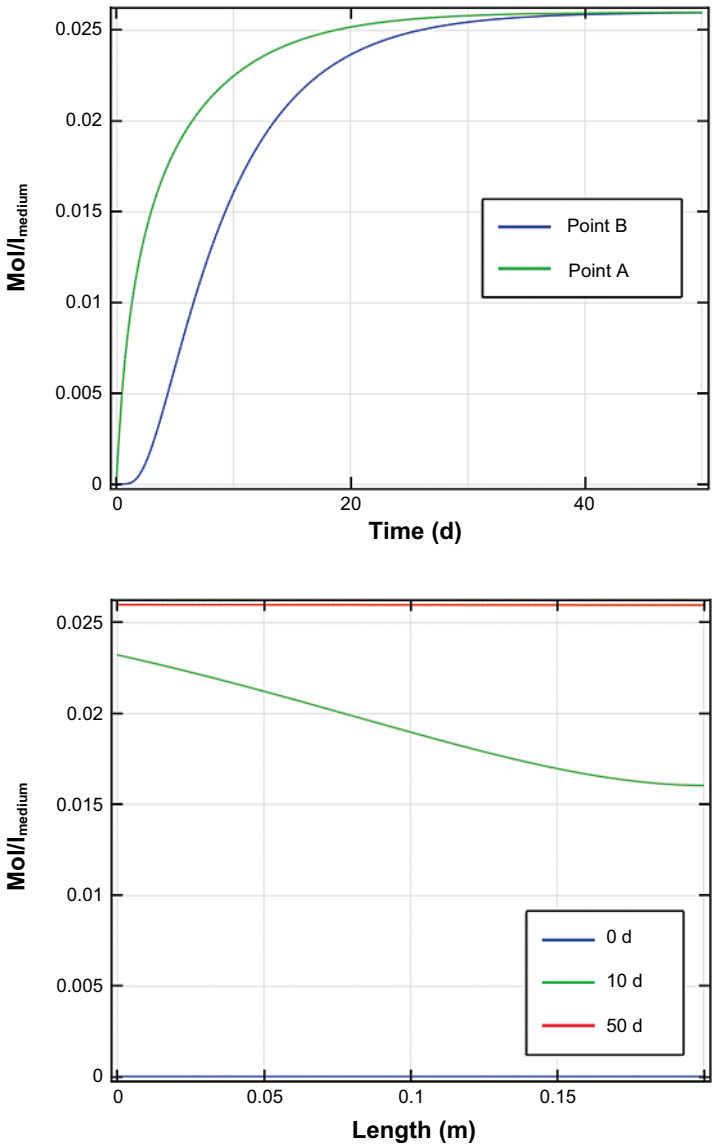

Figure C-17. *Evolution of ^{36}Cl concentration (mol·Kgw^{-1}) as a function of time on the two different observation points (top), and in the whole domain at three different times (bottom).*

The intrusion of the deep groundwater (pH ~6.8) shifts the system pH towards low pH values as seen in Figure C-18. Differently to what we observe in the till case, the clay pH after 50 days of simulation is almost the same as that of the intruding deep groundwater only the first column centimeters. The clay initial pH (pH ~7.8) is higher than the till initial pH (pH ~7.1) and thus a higher amount of deep groundwater is needed to reach the input solution values in the whole column.

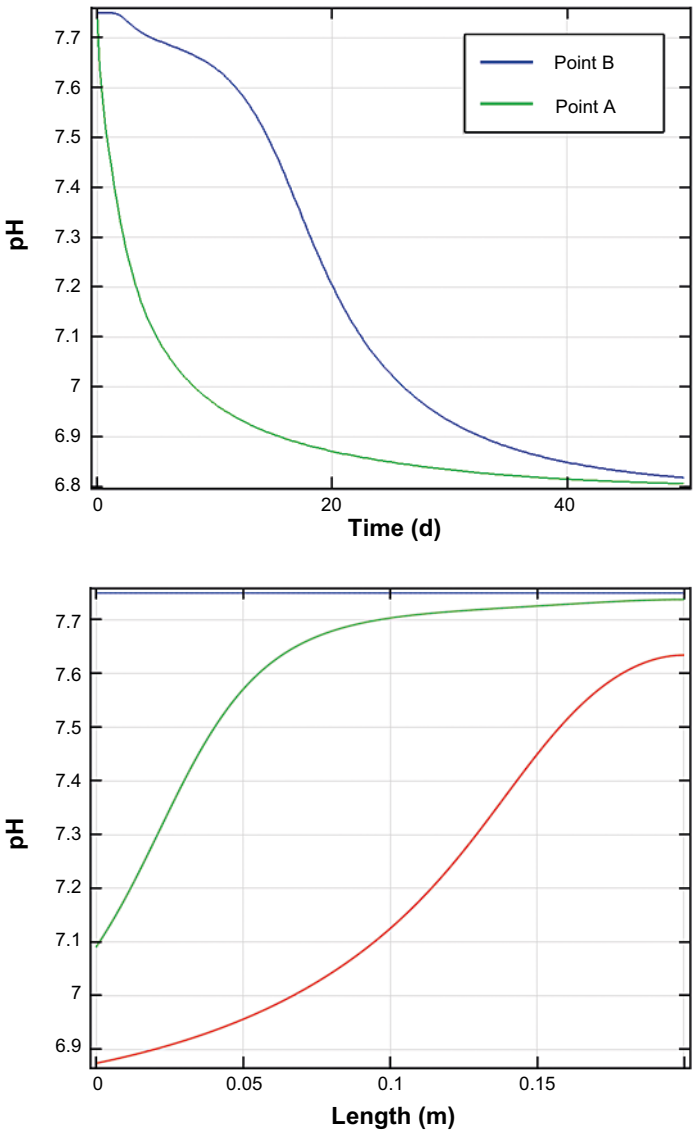

Figure C-18. *Evolution of pH as a function of time on the two different observation points (top), and in the whole domain at three different times (bottom).*

As in the till case, sodium concentration entering the system ($\sim 10^{-2}$ M) is higher than the initial sodium concentration in the clay ($\sim 10^{-4}$ M). This concentration gradient produces an enrichment of the clay solution in terms of sodium (Figure C-19 and Figure C-5) an alteration of the illite exchange positions (Figure C-20), which becomes richer in Na while releases other cations (i.e. Ca). The main difference observed between the till and clay models is that Na concentration ($mol \cdot l_{medium}^{-1}$) is higher in the clay model than in the till. This is due to the porosity of each system. The clay porosity is 5 times higher than the till porosity and thus, the amount of aqueous species introduced in the clay is 5 times higher. It should be taken into account that concentrations expressed as ($mol \cdot l_{medium}^{-1}$) are scaled by this factor.

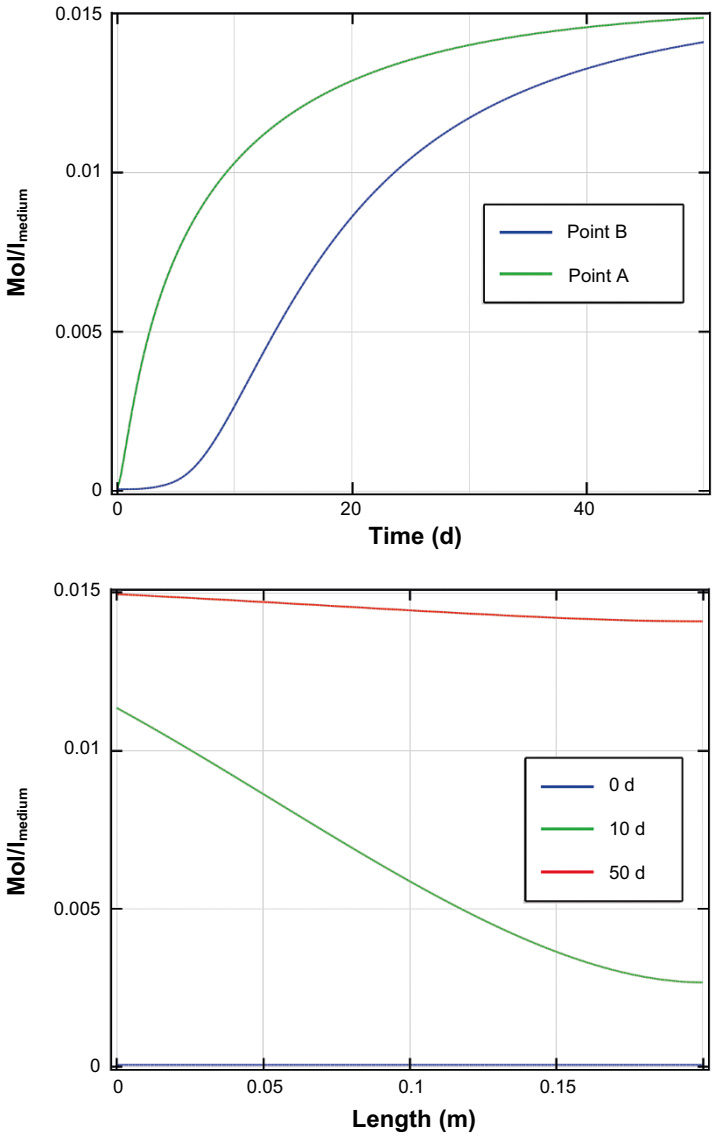

Figure C-19. *Evolution of aqueous sodium concentration ($mol \cdot l_{medium}^{-1}$) as a function of time on the two different observation points (top), and in the whole domain at three different times (bottom).*

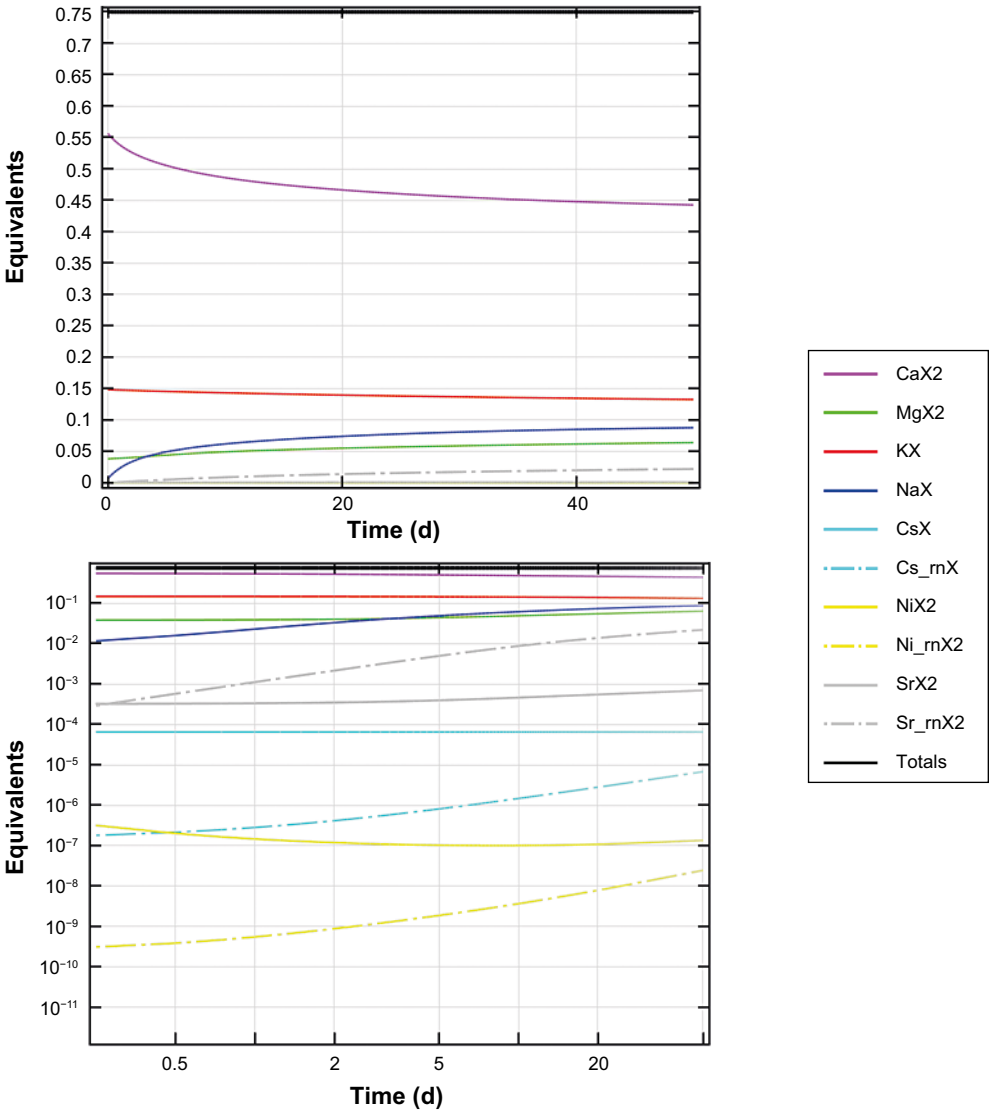

Figure C-20. *Evolution of the illite exchange positions as a function of time in the observation point A: normal scale (top), and log scale (bottom).*

Calcium behavior in the system is close to what we have seen previously in the till model (Figure C-21). The input solution is richer in Ca favoring the precipitation of (Ca,Sr)CO_3 solid-solution in the whole column (Figure C-22). As in the till case, higher amounts of solid precipitate at the beginning of the column where the effect of the input solution is stronger. Note that concentration values (mol·l_{medium}^{-1}) reported in the clay system differ from those reported in the till due to the different porosity assumed in each domain.

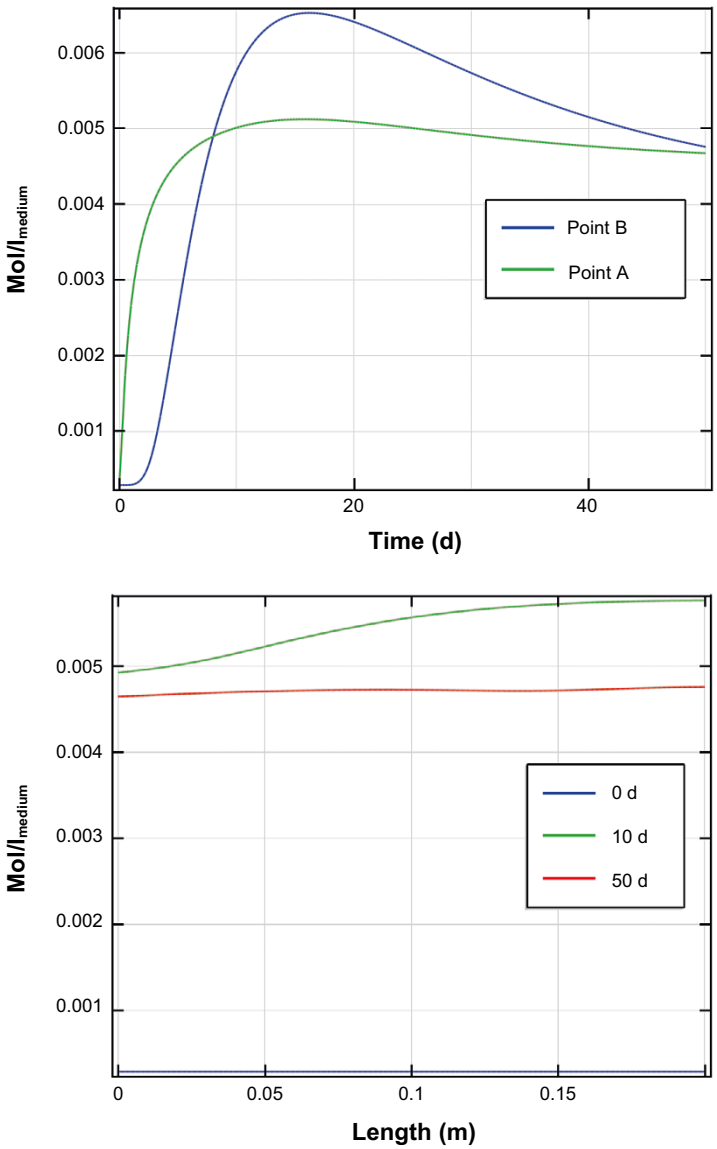

Figure C-21. *Evolution of aqueous calcium concentration (mol·l_{medium}^{-1}) as a function of time on the two different observation points (top), and in the whole domain at three different times (bottom).*

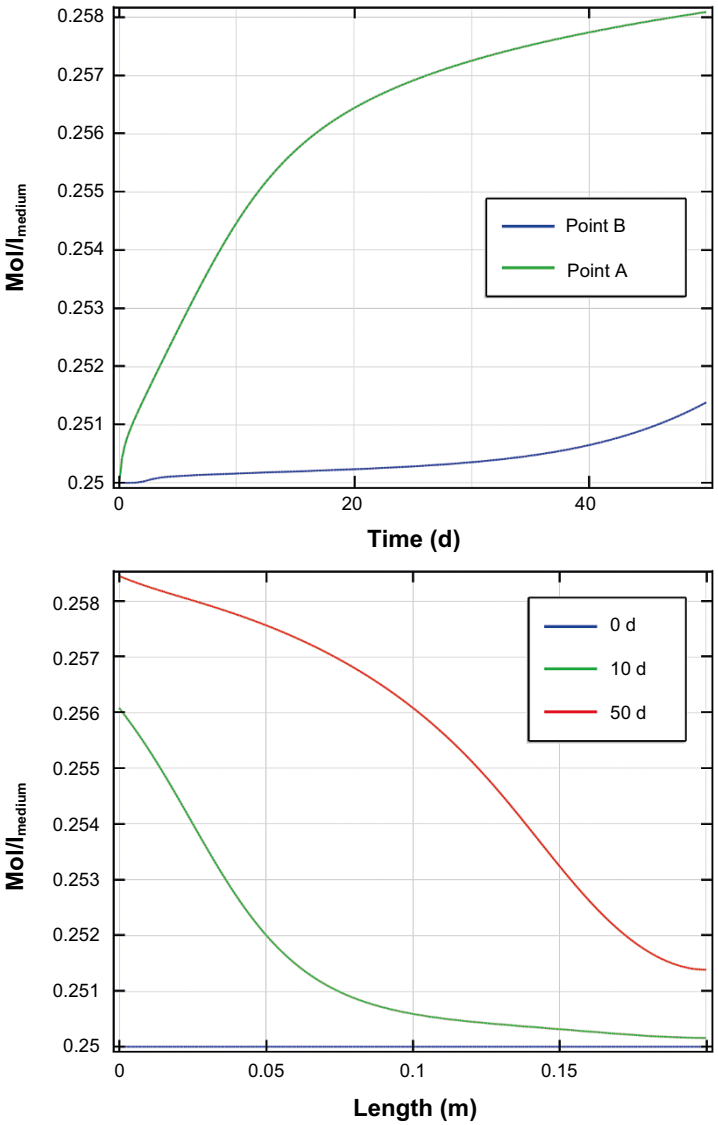

Figure C-22. *Evolution of (Ca,Sr)CO_3 solid-solution (mol·l_{medium}^{-1}) as a function of time on the two different observation points (top), and in the whole domain at three different times (bottom).*

The behavior and the retention mechanisms of the different radioactive elements introduced in the system do not differ from those explained for the till model. Strontium entering the system (Figure C-23, Figure C-9) is mainly retained within the illite exchange positions sites (species Sr_rnX_2, Figure C-20), being the exchanged amount of Sr more than one order of magnitude higher than the precipitated as (Ca,Sr)CO_3 solid-solution (Figure C-9). Overall, the implemented retention processes decreased Sr aqueous concentration from ~10^{-3} M (input solution detailed in Table 2-4) to ~10^{-4} mol·l_{medium}^{-1}.

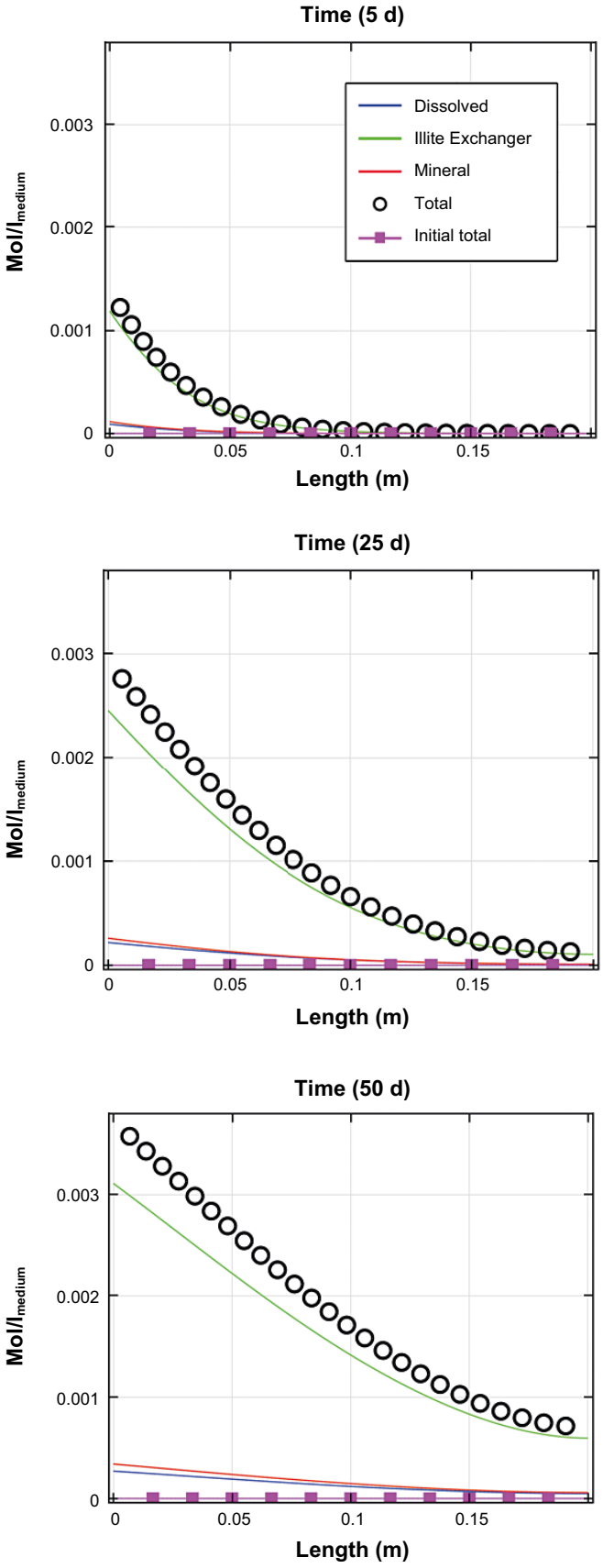

Figure C-23. *Evolution of radioactive Sr (mol·l_{medium}^{-1}), free aqueous species and retained species, in the whole domain after 5, 25 and 50 days of simulation time.*

As in the till model, cesium (Figure C-24) is almost completely retained into the illite FES exchange positions (species Cs_rnXb = CsX^{FES}, Figure C-20) within the first column centimeters (~0.05 m). Aqueous concentrations of this element after 50 days of simulation time are down to 10^{-10} mol·l_{medium}^{-1} in the whole column length.

Similarly, nickel-59 (Figure C-25) is strongly adsorbed onto the mineral surfaces. Illite is by far the main solid responsible for nickel-59 uptake through surface complexation (mainly through the $\equiv SO^{s}ONi^{+}$ specie). Aqueous concentrations of this element after 50 days of simulation time are down to ~10^{-8} mol·l_{medium}^{-1} at the end of the column.

Radium immobilization occurs through the precipitation of a solid-solution with barite (Ba,Ra)SO_4 (Figure C-26 and Figure C-27), as previously shown in the till model. At the beginning of the simulation the solid-solution precipitates intensively in the first column centimeters, but as time passes the maximum precipitation peak is displaced through the column. This phenomenon is the same as previously observed in the till case. However, the transport of Ra in the system is relatively slower in the clay than in the till. The transport delay is due to the amount of aqueous Ba in the system (Figure C-28): higher in the clay (10^{-6} M) than in the till (10^{-7} M). The higher the amount Ba, the higher the amount of precipitated (Ba,Ra)SO_4; slowing down the advance of aqueous Ra in the column. Ra aqueous concentration in the whole column decreases from ~2×10^{-11} mol·l_{medium}^{-1} down to ~1×10^{-12} mol·l_{medium}^{-1} after 50 days of simulation.

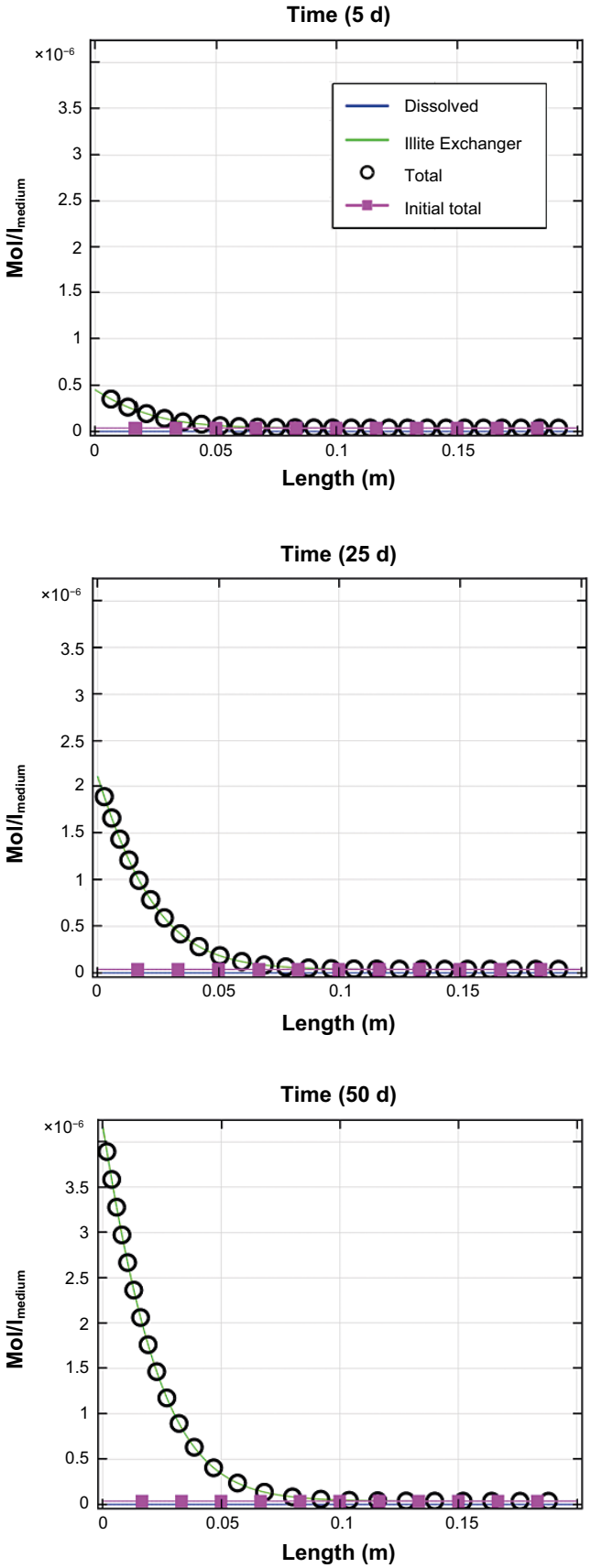

Figure C-24. *Evolution of radioactive Cs (mol·l_{medium}^{-1}), free aqueous species and retained species, in the whole domain after 5, 25 and 50 days of simulation time.*

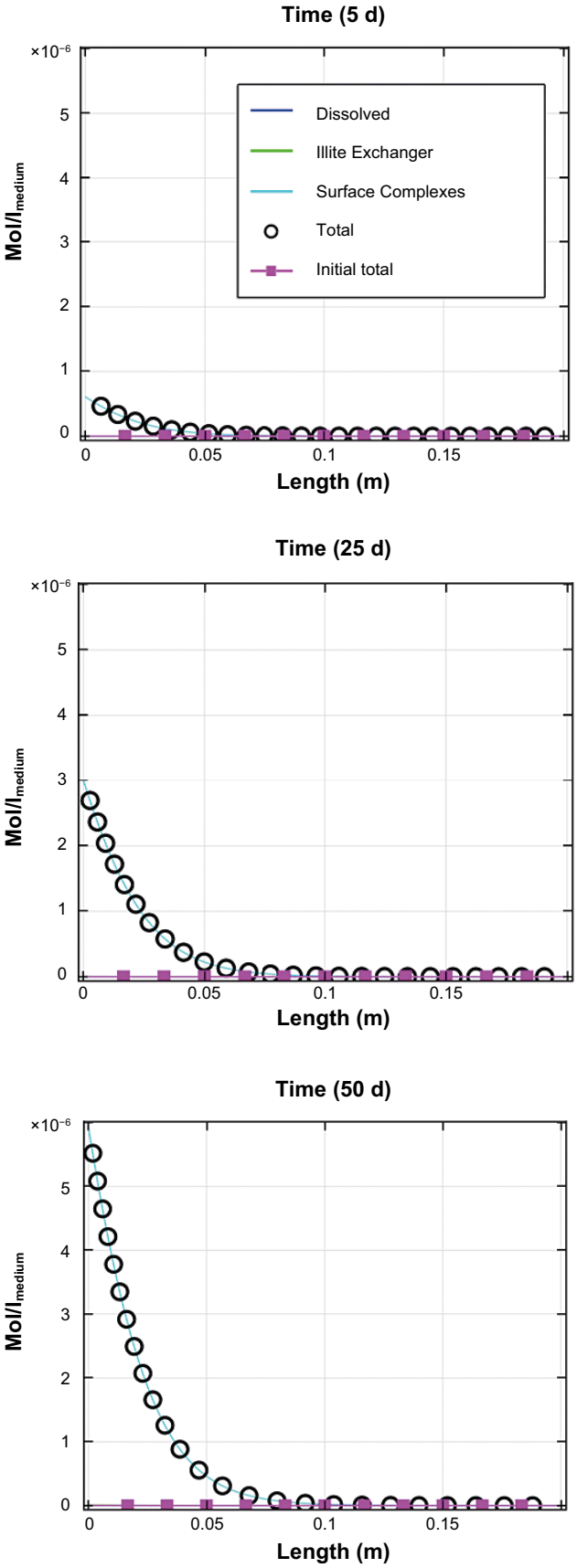

Figure C-25. *Evolution of radioactive Ni (mol·l_{medium}^{-1}), free aqueous species and retained species, in the whole domain after 5, 25 and 50 days of simulation time.*

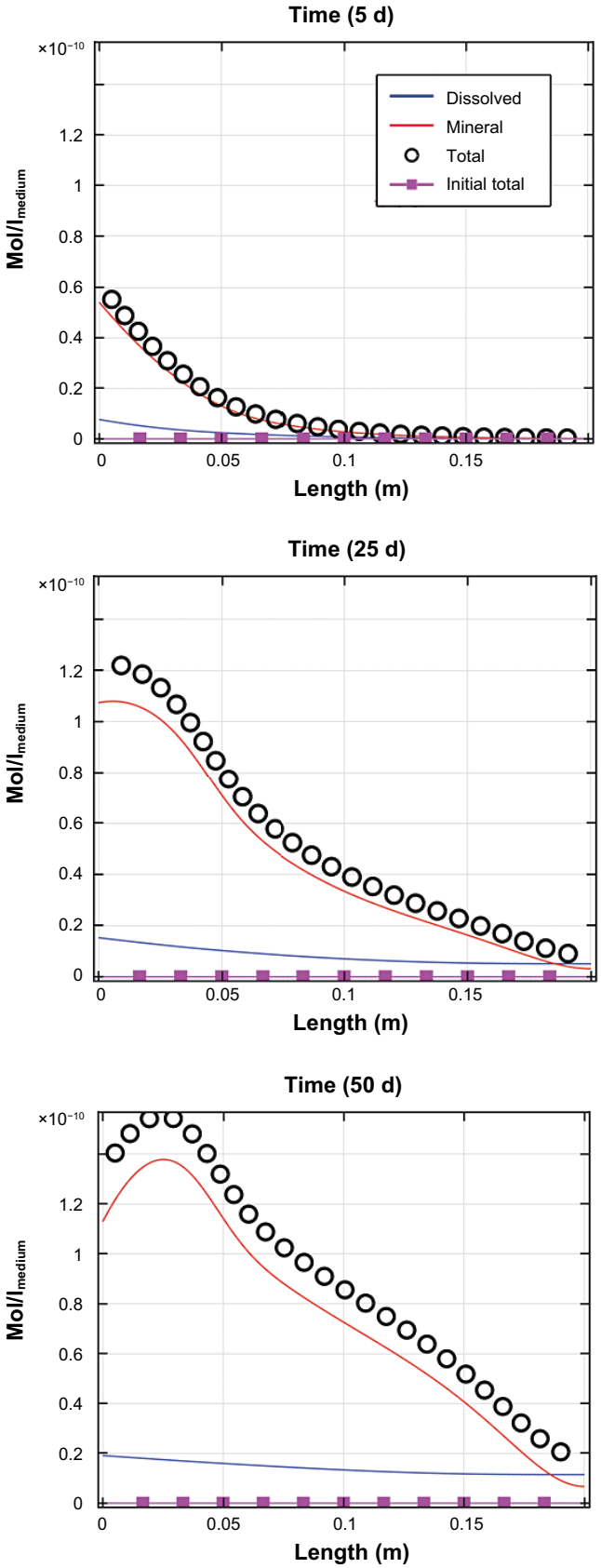

Figure C-26. *Evolution of radioactive Ra (mol·l_{medium}^{-1}), free aqueous species and retained species, in the whole domain after 5, 25 and 50 days of simulation time.*

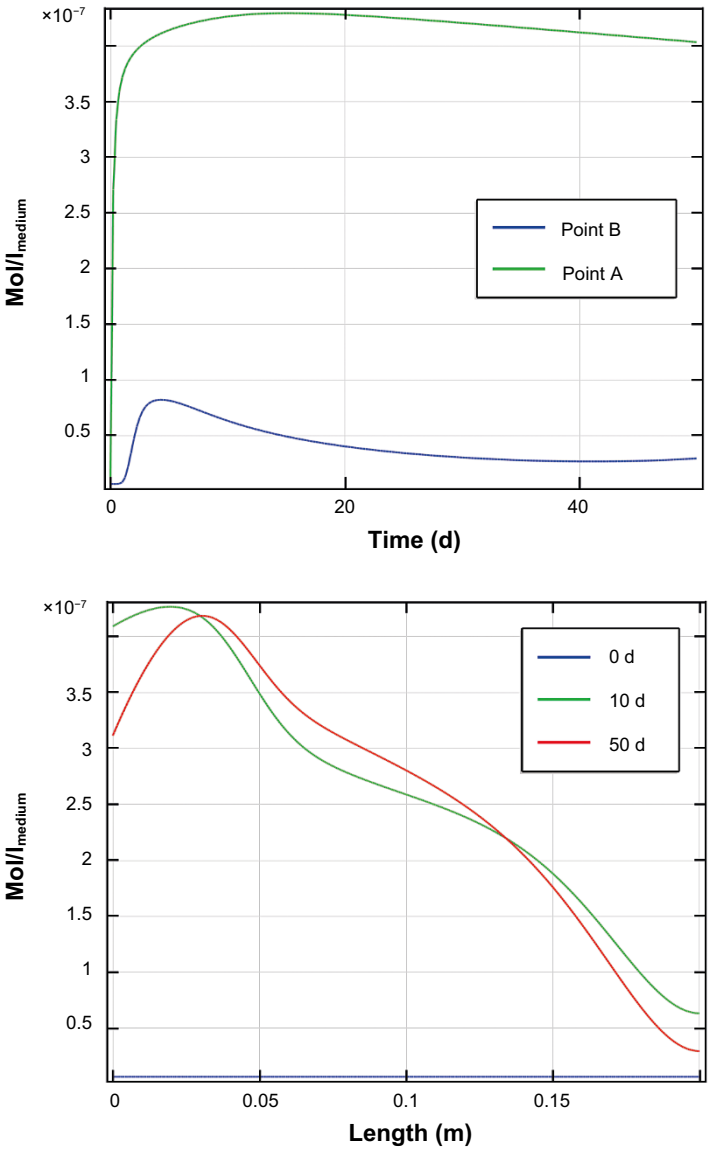

Figure C-27. *Evolution of (Ba,Ra)SO_4 solid-solution (mol·l_{medium}^{-1}) as a function of time on the two different observation points (top), and in the whole domain at three different times (bottom).*

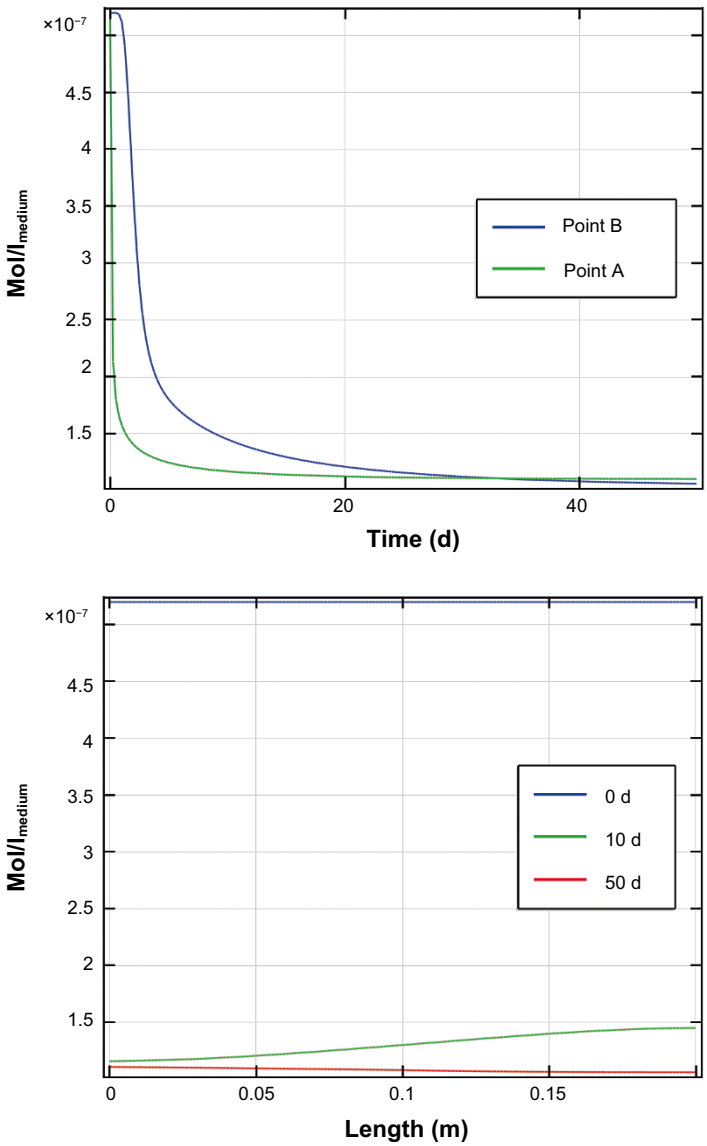

Figure C-28. *Evolution of barium (mol·l_{medium}^{-1}) as a function of time on the two different observation points (top), and in the whole domain at three different times (bottom).*

Figure C-29 compares the evolution of the amount of radionuclide introduced versus the amount of radionuclide present at a given time in the whole system. Results are quite similar as the ones obtained for the till domain. In brief, all cesium and nickel-59 are retained in the system after 50 days; strontium is being released from the system at the end of the simulation (~45–50 days); and radium reached the right boundary of the column being released after ~30 days. As noted previously, in the clay model the transport of Ra is delayed in the time (column release after ~30 days) compared to the till model (column release after ~15 days) due to the higher retention of this element (higher solid-solution precipitation) in the clay model.

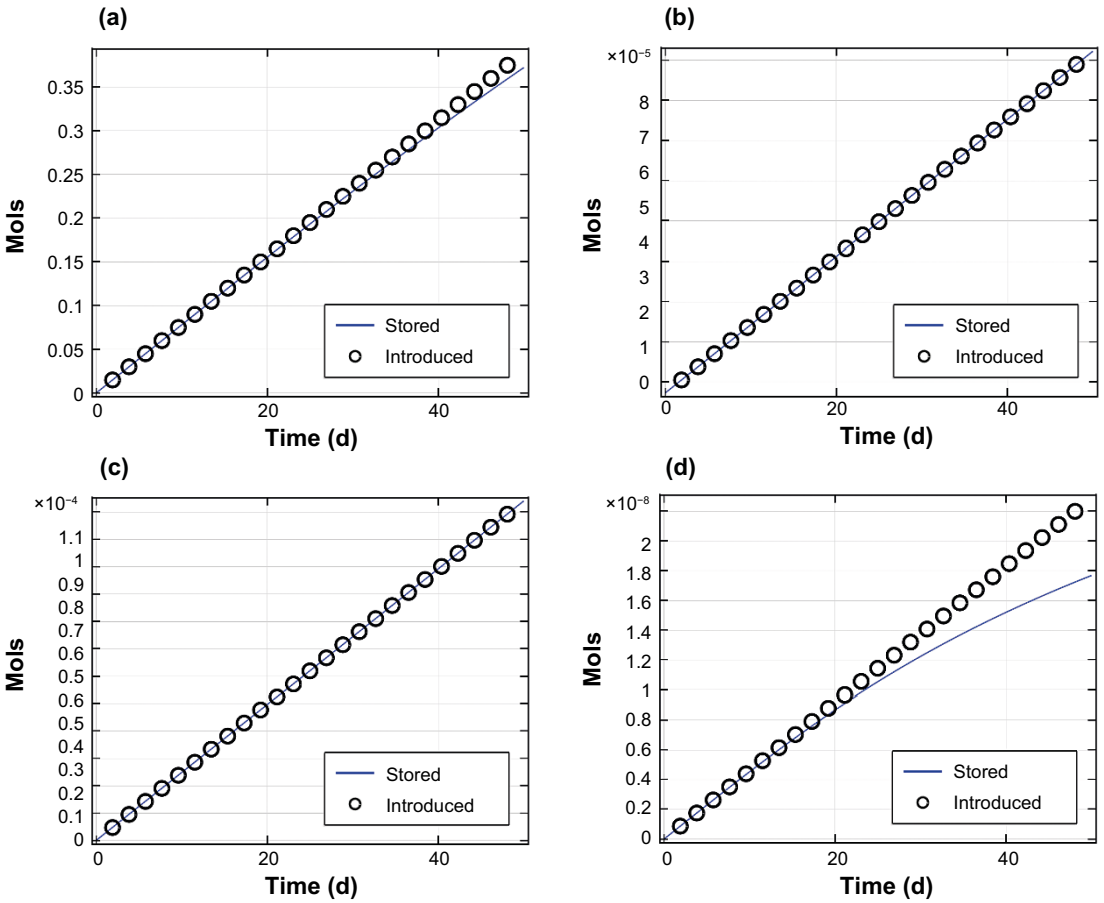

Figure C-29. *Evolution of accumulative amount of radionuclides (mol·m^{-2} system) as a function of time: (a) strontium, (b) cesium, (c) nickel-59, and (d) radium. Circles stand for the total amount of radionuclide introduced in the system while the solid line stands for the amount of radionuclide present in the system at each time.*

Conclusions

1D reactive transport simulations of till and clay systems demonstrated that, in both cases, most of the retention of Sr, Cs and Ni through exchange and surface complexation reactions occurs in the illite. Additionally, solid-solution precipitation ($(Ba,Ra)SO_4$) and ($(Ca, Sr)CO_3$) appears to be an important radionuclide retention process, especially for Ra. No precipitation of radionuclide pure mineral phases occurs in any of the studied systems during the simulation, which is due to the low radionuclide aqueous concentration imposed by the retention processes.

Cs and Ni are the most retained radionuclides in both clay and till systems, being not released from the column after 50 days of simulation. Sr, which is also highly retained in both models, reaches the right boundary of the column after ~45–50 days. Finally, Ra is transported along the column and released out from it after 15 and 30 days in the till and the clay systems, respectively.

Cs and Ni are strongly retained in both the clay and the till system. The regolith can, thus, delay significantly its transport towards the surface. Sr and Ra are also retained but part of the elements reached the right boundary of the column before 50 days. If no extra barium enters the system, Ra would be the first radionuclide reaching the surface, as the precipitation of $(Ba,Ra)SO_4$ is limited by the Ba concentration.

Appendix D

Selected results distributed reactive model

The following plots are selected results from the distributed reactive model. Results examining the distribution of repository-derived strontium, cesium, nickel and radium.

Vertical, 1D sections are presented in order to show the evolution of the element distribution throughout the regolith layers after 100, 500 and 1 000 years of simulation time. The plots are meant to give an idea of how long the system takes before reaching an equilibrium state where concentrations no longer change with time.

Strontium

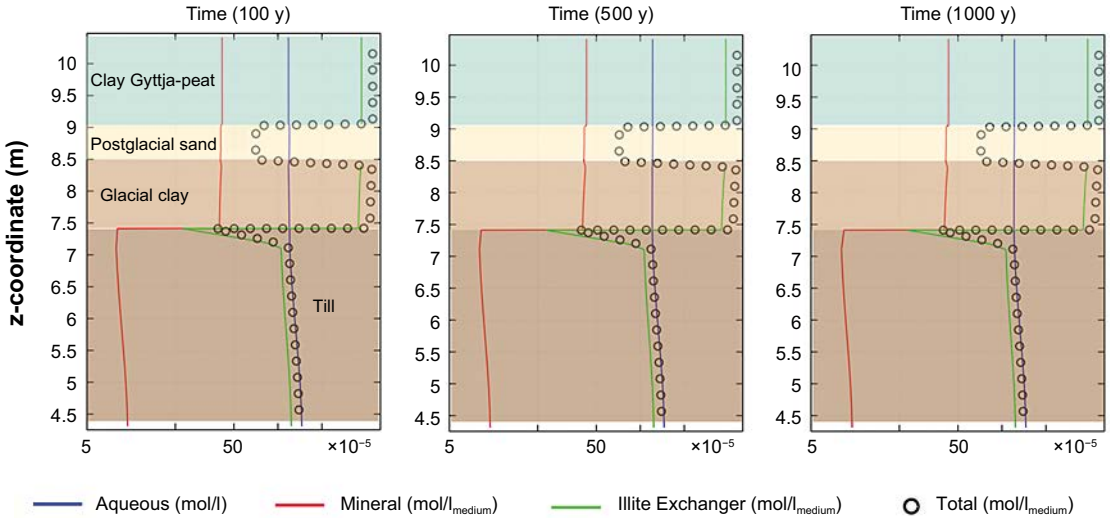

Figure D-1. *Concentration profiles of RDSr at a point in the discharge area (blue point in Figure 6-4) after 100, 500 and 1 000 years of simulation time. Concentration of aqueous RDSr (blue) and retained in solid-solutions (red) and in the exchanger (green). The total concentrations are displayed as black circles. All concentrations are given in mol·l_{medium}^{-1} except aqueous concentration that are given in mol·l_{water}^{-1}. The regolith materials are indicated by the background color: till (dark brown), glacial clay (light brown), postglacial sand (yellow) and clay gyttja-peat (green). Note the logarithmic scale on the x axis.*

Cesium

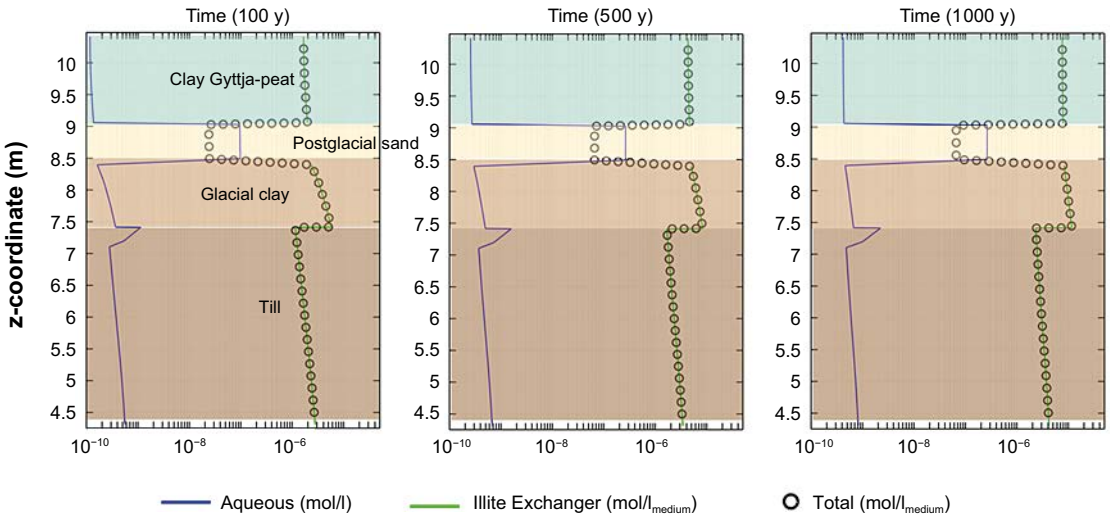

Figure D-2. *Concentration profiles of RDCs at a point in the discharge area (blue point in Figure 6-5) after 100, 500 and 1 000 years of simulation time. Concentration of RDCs aqueous (blue), in the exchanger (green) and total concentration (black circles) are displayed. All concentrations are given in mol·l$_{medium}^{-1}$ except aqueous concentration that are given in mol·l$_{water}^{-1}$. The regolith materials are indicated with the background color: till (dark brown), glacial clay (light brown), postglacial sand (yellow) and clay gyttja-peat (green). Note the logarithmic scale on the x axis.*

Nickel

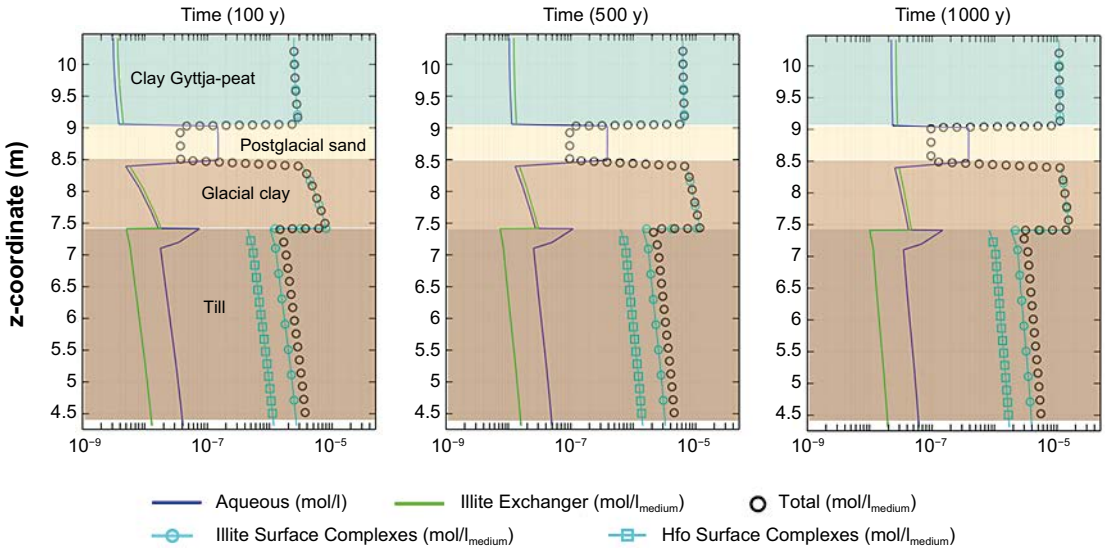

Figure D-3. *Concentration profiles of RDNi at a point in the discharge area (blue point in Figure 6-6) after 100, 500 and 1 000 years of simulation time. Concentration of aqueous RDNi (blue), retained in the exchanger (green) and in surface complexes (light blue). The total concentration is indicated with black circles. All concentrations are given in mol·l_{medium}^{-1} except aqueous concentration that are given in mol·l_{water}^{-1}. The regolith materials are indicated with the background color: till (dark brown), glacial clay (light brown), postglacial sand (yellow) and clay gyttja-peat (green). Note the logarithmic scale on the x axis.*

Radium

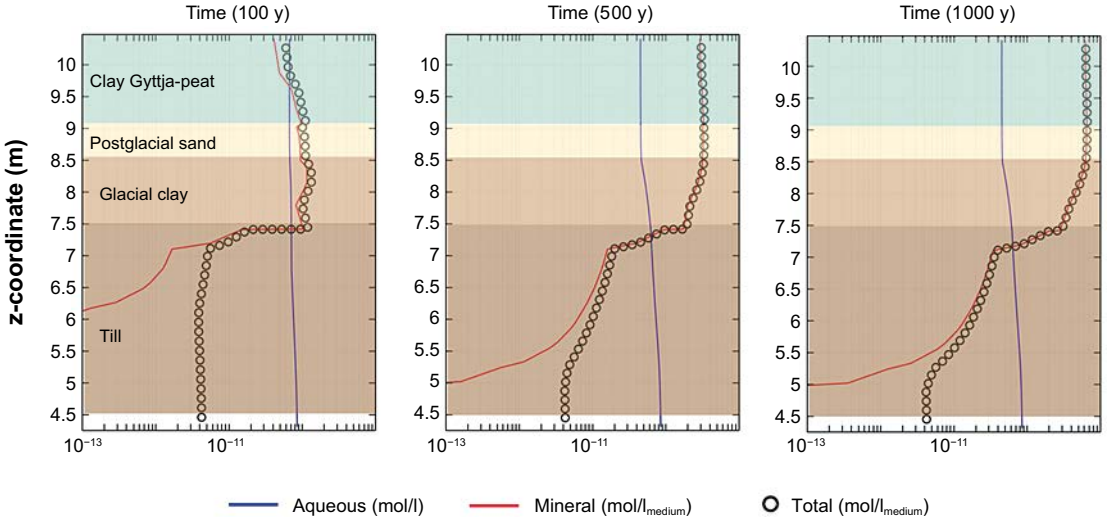

Figure D-4. *Concentration profiles at a point in the discharge area (blue point in Figure 6-7) after 100, 500 and 1 000 years of simulation time. Concentration of aqueous Ra (blue) and precipitated in the solid-solutions (red) are displayed. The total Ra is illustrated with black circles. All concentrations are given in mol·l_{medium}^{-1} except aqueous concentration that are given in mol·l_{water}^{-1}. The regolith materials are indicated with the background color: till (dark brown), glacial clay (light brown), postglacial sand (yellow) and clay gyttja-peat (green). Note the logarithmic scale in the x axis.*

Arkitektkopia AB, Bromma, 2022

SKB is responsible for managing spent nuclear fuel and radioactive waste produced by the Swedish nuclear power plants such that man and the environment are protected in the near and distant future.

skb.se